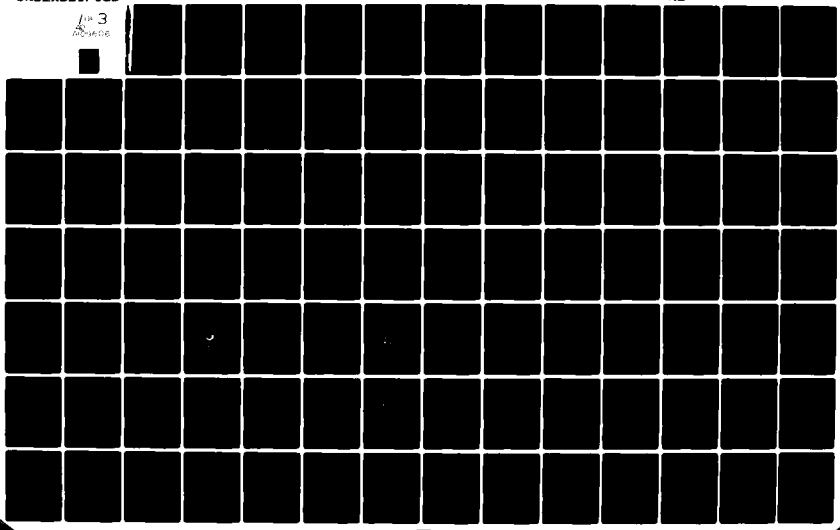


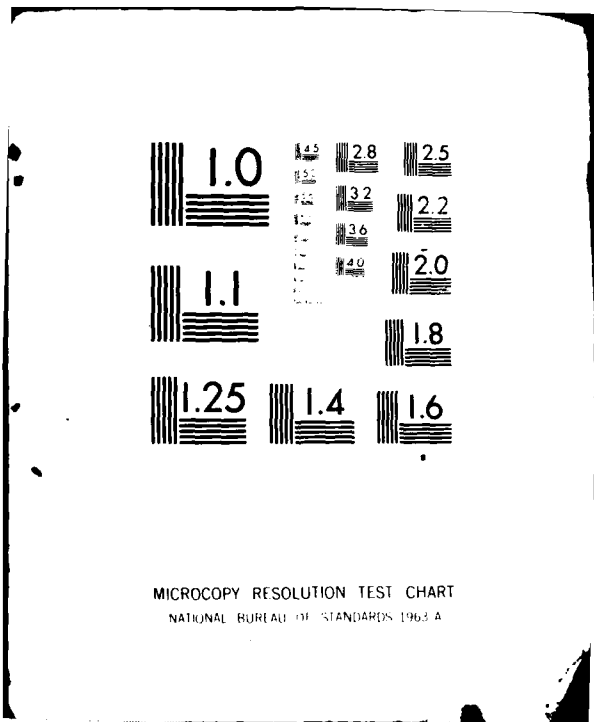
AD-A109 606

LEHIGH UNIV BETHLEHEM PA CENTER FOR SURFACE AND COATINGS ETC F/G 11/3  
CORROSION CONTROL THROUGH A BETTER UNDERSTANDING OF THE METALLI—ETC(U)  
NOV 81 M LEIDHEISER, E M ALLEN, M S EL-AASSER N00014-79-C-0731  
NL

UNCLASSIFIED

4th 3  
ADV-106





**LEVEL**

(1)

A095420

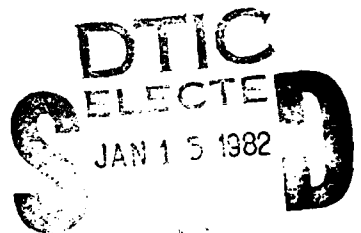
CORROSION CONTROL THROUGH A BETTER UNDERSTANDING  
OF THE METALLIC SUBSTRATE/ORGANIC COATING/INTERFACE

Agreement No. N00014-79-C-0731

Second Annual Report

Covering the Period,

September 1, 1980-August 31, 1981



AD A109606

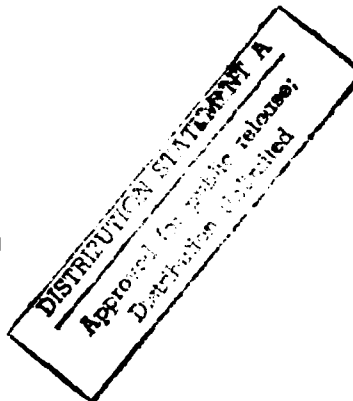
DTIC FILE COPY

Sponsor: Office of Naval Research  
Washington, D.C.

Principal Investigator: Henry Leidheiser, Jr.

Co-Investigators: Eugene M. Allen  
Mohamed S. El-Aasser  
Frederick M. Fowkes  
Michael C. Hughes  
John A. Manson  
Fortunato J. Micale  
David A. Thomas  
Gary W. Simmons  
John W. Vanderhoff

Center for Surface and Coatings Research  
Lehigh University  
Bethlehem, Pa. 18015



November 1, 1981

401155

81 12 23 052

## TABLE OF CONTENTS

	<u>Page</u>
<b>Foreword . . . . .</b>	<b>1</b>
<b>Section 1 - A List of Public Disclosures of the Re-</b> <b>search during the Period September 1,</b> <b>1980-August 31, 1981 . . . . .</b>	<b>2</b>
● Published Papers . . . . .	2
● Papers Accepted for Publication. . . . .	2
<b>Section 2 - The Titles of the Component Programs and</b> <b>the Participants . . . . .</b>	<b>4</b>
● Programs Concerned with Corrosion at	
the Interface. . . . .	4
● Programs Concerned with the Chemistry	
of the Metal/Coating Interface . . . . .	5
● Programs Concerned with the Properties	
of the Coating . . . . .	5
● Programs Related to the Surface Proper-	
ties of Iron Oxides from the Standpoint	
of Their Presence at the Steel/Organic	
Coating Interface and Their Use as	
Pigments . . . . .	6
<b>Section 3 - A Summary of the Experimental Results Ob-</b> <b>tained during the Period, September 1,</b> <b>1980-August 31, 1981 . . . . .</b>	<b>8</b>
Program #1. The Mechanism for the Cathodic Delamination	
of Organic Coatings from a Metal Surface .	15
Program #2. Corrosion Control by Inhibition of the	
Cathodic, Oxygen-Reduction Reaction. . . .	49
Program #3. Optical Studies of Corrosion under Organic	
Coatings . . . . .	55
Program #4. Electrical Properties of Organic Coatings	
and Relationship to Corrosion. . . . .	63
Program #5. Determination of the Acidity of Iron Oxide	
Surfaces . . . . .	79



**CONTENTS Contd.**

	<u>Page</u>
Program #6. Ion Exchange Properties of Iron Surfaces.	91
Program #8. Cathodic Electrodeposition of Epoxy-Curing Agent Latex Mixtures . . . . .	105
Program #9. Drying and Curing of Epoxy Films. . . . .	121
Program #10. Detection of Aggregated Water in Polymer Coatings. . . . . . . . .	127
Program #11. Pigment-Binder Interactions in Corrosion Protecting Films. . . . . . . . .	133
Program #12. Electron Optical Studies of Organic Coatings. . . . . . . . . .	147
Program #13. Preparation of Colloidal Iron Sols by (a) Aqueous Precipitation and (b) by Dispersion. . . . . . . . .	161
Program #14. Mössbauer Studies of Iron Oxides. . . . .	183
Program #15. Characterization of the Surface Properties of Iron Oxides . . . . .	201

## FOREWORD

This report represents the second annual summary of research carried out under Office of Naval Research Contract No. N00014-79-0731. The objective of the research is to obtain a better understanding of the metallic substrate/organic coating/interface system so that improvements may be made in corrosion control of metals by painting. The research during the past year has consisted of 15 different components directed by 10 Lehigh faculty members. These activities may be divided for convenience into those primarily concerned with (a) corrosion at the interface, (b) the chemistry of the metal/coating interface, (c) the properties of the coating, and (d) the surface properties of iron oxides from the standpoint of their presence at the steel/organic coating interface and their use as pigments.

It is recognized that readers of this report will be interested in the contents for different purposes. In an effort to accommodate to these diverse interests, the report is presented in the following format.

- (1) A list of public disclosures of the research reported herein. The references may be useful to those who wish to explore the research in greater detail.
- (2) A list of titles of the 15 component programs keyed to the experimental summaries in (4) and the names of the participants.
- (3) A condensation of the total program. This summary should be useful to those who wish to obtain an overview of the program.
- (4) A more detailed outline of each of the component programs.

## SECTION 1

### A List of Public Disclosures of the Research during the Period September 1, 1980-August 31, 1981

#### Published Papers

"Provocative Questions in Metal/Solution Reactions to Which Mössbauer Spectroscopy Should Be Applied", H. Leidheiser, Jr., Colloque No. 1, Supplément au Journal de Physique 41, C1-351-52 (1980).

"Some Substrate and Environmental Influences on the Cathodic Delamination of Organic Coatings", Henry Leidheiser, Jr. and Wendy Wang, J. Coatings Tech. 53, 77-84 (1981).

"Solid State Chemistry as Applied to Cathodically-Driven or Corrosion-Induced Delamination of Organic Coatings", Henry Leidheiser, Jr., Paper No. 81, Corrosion 81, National Association of Corrosion Engineers, April 6, 1981, Toronto, Canada, 10 pp.

"Solid State Chemistry as Applied to Cathodically Driven or Corrosion-Induced Delamination of Organic Coatings", Henry Leidheiser, Jr., Ind. Eng. Chem. Prod. Res. Dev. 20, 547-51 (1981).

"Mössbauer Spectroscopic Study of the Chemical State of Cobalt in an Electrodeposited Zinc-Cobalt Alloy", H. Leidheiser, Jr., A. Vértes, and M. L. Varsányi, J. Electrochem. Soc. 128, 1456-59 (1981).

"Mechanism of Corrosion Inhibition with Special Attention to Inhibitors in Organic Coatings", Henry Leidheiser, Jr., J. Coatings Tech. 53, No. 678, 29-39 (1981).

"De-adhesion at the Organic Coating/Metal Interface in Aqueous Media", Henry Leidheiser, Jr., Croatica Chemica Acta 53, 197-209 (1980).

#### Papers Accepted for Publication

"Enhancing Polymer Adhesion by Acid-Base Interactions", F. M. Fowkes, Proc. Internat'l. Conf. on Corrosion Control by Organic Coatings, Natl. Assocn. Corrosion Engrs., Houston, Texas, in press.

Papers Accepted for Publication Contd.

"Some Aspects of Cathodic Electrodeposition of Epoxy Latexes as Corrosion-Resistant Coatings", C. C. Ho, A. Humayun, M. S. El-Aasser, and J. W. Vanderhoff, Proc. Internatl. Conf. on Corrosion Control by Organic Coatings, Natl. Assocn. Corrosion Engrs., Houston, Texas, in press.

"New Studies of the De-Adhesion of Coatings from Metal Substrates in Aqueous Media — Interpretation of Cathodic Delamination in Terms of Cathodic Polarization Curves", Henry Leidheiser, Jr., Lars Igetoft, Wendy Wang, and Keith Weber, Proc. 7th Intl. Conf. in Org. Coatings Sci., in press.

"<sup>57</sup>Fe Mössbauer Spectroscopic Study of the Thermal Decomposition of Fe( IO<sub>3</sub>)<sub>3</sub>", S. Music, G. W. Simmons, H. Leidheiser, Jr., Radiochem. & Radioanal. Letters, in press.

"Mössbauer Spectroscopic Study of the Formation of Fe(III) Oxy-hydroxides and Oxides by Hydrolysis of Aqueous Fe(III) Salt Solutions", S. Music, A. Vértes, G. W. Simmons, I. Czakó-Nagy, and H. Leidheiser, Jr., J. Colloid Interface Sci., in press.

"Rate-Controlling Steps in the Cathodic Delamination of 10-40 Micron Thick Polybutadiene and Epoxy-Polyamide Coatings from Metallic Substrates", H. Leidheiser, Jr. and W. Wang, Proc. Internatl. Conf. on Corrosion Control by Organic Coatings, Natl. Assocn. Corrosion Engrs., Houston, Texas, in press.

"An AC Impedance Probe as an Indicator of Corrosion and Defects in Polymer/Metal Substrate Systems", M. C. Hughes and J. M. Parks, Proc. Internatl. Conf. on Corrosion Control by Organic Coatings, Natl. Assocn. Corrosion Engrs., Houston, Texas, in press.

## SECTION 2

### The Titles of the Component Programs and the Participants\*

#### Programs Concerned with Corrosion at the Interface

- (1) The Mechanism for the Cathodic Delamination of Coatings from a Metal Surface

Principal Investigator: Henry Leidheiser, Jr.,  
Professor of Chemistry

Associates: Lars Igetoft, Visiting Scientist  
Wendy Wang, Graduate Student

- (2) Corrosion Control by Inhibition of the Cathodic, Oxygen-Reduction Reaction

Principal Investigator: Henry Leidheiser, Jr.,  
Professor of Chemistry

Associates: Y. Momose, Visiting Scientist  
R. D. Granata, Research Scientist

- (3) Optical Studies of Corrosion under Organic Coatings

Principal Investigator: David A. Thomas, Professor  
of Metallurgy and Materials  
Engineering

Associate: Dale E. Zurawski, Graduate Student

- (4) Electrical Properties of Organic Coatings and Relationship to Corrosion

Principal Investigator: Henry Leidheiser, Jr.,  
Professor of Chemistry

Associates: Michael C. Hughes, formerly Assistant  
Professor of Chemistry; Adjunct Professor of Chemistry since January 1, 1981.  
Jeffrey Parks, Graduate Student

\*Note: Many of the programs involve close cooperation between 2 or more principal investigators. The name listed in the summary is the faculty member with prime responsibility for the program.

Programs Concerned with the Chemistry of the Metal/Coating Interface

(5) Determination of the Acidity of Iron Oxide Surfaces

Principal Investigator: Frederick M. Fowkes,  
Professor of Chemistry

Associate: Sara Joslin, Graduate Student

(6) Ion Exchange Properties of Iron Surfaces

Principal Investigator: Gary W. Simmons,  
Professor of Chemistry

Associate: Bruce Beard, Graduate Student

(7) The Use of the Laser Raman Microprobe in Studies of  
the Metal/Coating Interface

Principal Investigator: Eugene M. Allen,  
Professor of Chemistry

Associate: André Sommer, Graduate Student

Note: The instrument has been assembled and test spectra  
have been generated. No substantive results have  
been obtained by the end of the present report  
period.

Programs Concerned with the Properties of the Coating

(8) Cathodic Electrodeposition of Epoxy-Curing Agent Latex  
Mixtures

Principal Investigator: M. S. El-Aasser, Associate  
Professor of Chemical Engineering

Associates: C. C. Ho, Visiting Scientist  
O. Shaffer, Technical Associate  
K. Earhart, Research Associate  
J. A. Hadley, Graduate Student  
A. Humayun, Graduate Student

Programs Concerned with the Properties of the Coating, Contd.

(9) Drying and Curing of Epoxy Films

Principal Investigator: M. S. El-Aasser, Associate Professor of Chemical Engineering

Associates: J. W. Vanderhoff, Professor of Chemistry  
C. Silebi, Assistant Professor of Chemical Engineering  
Babatunde E. Aremu, Graduate Student  
Ata-Ur Rahman, Graduate Student

(10) Detection of Aggregated Water in Polymer Coatings

Principal Investigator: Henry Leidheiser, Jr., Professor of Chemistry

Associate: Douglas Eadline, Graduate Student

(11) Pigment-Binder Interactions in Corrosion Protecting Films

Principal Investigator: John A. Manson, Professor of Chemistry

Associates: Michael Heffelfinger, Graduate Student  
A. Tiburcio, Graduate Student

(12) Electron Optical Studies of Organic Coatings

Principal Investigator: David A. Thomas, Professor of Metallurgy and Materials Engineering

Associate: Yale West, Graduate Student

Programs Related to the Surface Properties of Iron Oxides from the Standpoint of Their Presence at the Steel/Organic Coating Interface and Their Use as Pigments

(13) Preparation of Iron Oxide Sols by Aqueous Precipitation and by Dispersion

Principal Investigator: J. W. Vanderhoff, Professor of Chemistry

Associates: M. J. Cantow, Visiting Scientist  
L. M. Bennetch, Consultant  
O. L. Shaffer, Technical Associate  
T. C. Huang, Graduate Student  
M. H. Kang, Graduate Student  
D. W. Timmons, Graduate Student

Programs Related to the Surface Properties of Iron Oxides from  
the Standpoint of Their Presence at the Steel/Organic Coating  
Interface and Their Use as Pigments, Contd.

(14) Mössbauer Studies of Iron Oxides

Principal Investigator: Gary W. Simmons,  
Professor of Chemistry

Associate: S. Musić, Visiting Scientist

(15) Characterization of the Surface Properties of Iron Oxides

Principal Investigator: F. J. Micale, Associate  
Professor of Chemistry

Associates: C. C. Yu, Graduate Student  
J. Lavelle, Technician

### SECTION 3

#### A Summary of the Experimental Results Obtained during the Period, September 1, 1980-August 31, 1981

A detailed summary of 14 of the 15 component programs that compose the overall program is presented in SECTION 4. This section represents a consolidation of all the research carried out during the past year in an executive-summary style. It is an attempt to give an overview of the program and to weld the individual tasks into a coherent whole.

Corrosion beneath an organic coating is electrochemical in nature with some areas of the metallic substrate serving as cathode and other areas serving as anode. The anodic regions tend to be smaller than the cathodic regions in the early stages of corrosion but the cathodic areas are specially damaging to the protective nature of the coating because they lead to delamination. Thus, the phenomenon of cathodic delamination is important in (a) understanding the corrosion process and (b) understanding the factors that control delamination when cathodic protection is superimposed on the protective coating as an additional safeguard against corrosion in damaged areas.

Cathodic delamination of a coating, damaged with a pin prick, is a function of the nature of the electrolyte, the concentration of the electrolyte, the amount of dissolved oxygen in the electrolyte, the cathode potential, the temperature, the metal, the surface treatment given to the metal before the application of the coating, the type of coating, and the thickness of the coating. The critical factor in the delamination process is the rate at which the species, water, oxygen, cation, and electrons arrive at the periphery of the delaminating front. The catalytic activity of the surface for the cathodic reaction,  $H_2O + 1/2O_2 + 2e^- = 2OH^-$ , is another important factor. Any of these species, as well as the catalytic activity of the surface, may be involved in the rate controlling step. The organic coating also plays an important role since the reactant species reach the delaminating front largely by diffusion through the coating. Five practical means exist for minimizing cathodic delamination: (1) No bare metal, or superficially oxidized metal, should be present at the coating/substrate interface. (2) There should exist at the coating/substrate interface a layer which is a very poor conductor of electrons. (3) The interfacial layer at the coating/substrate interface should be a poor catalyst for the cathodic reaction. (4) The boundary between the substrate and the coating should be rough in order to provide a tortuous path for lateral diffusion. (5) The interfacial region should be resistant to alkaline attack.

The importance of the cathodic reaction that occurs under the coating in the rate of deterioration of polymer-coated metals indicates that control of the cathodic reaction is a practical means to extend the lifetime of the coating. Previous work has shown that pretreatment of zinc (galvanized steel) in solutions containing cobalt or nickel ions leads to an altered oxide on the surface of zinc such that the surface was a poor substrate for the cathodic oxygen reduction reaction. Work during the present report period has identified another system in which there is striking inhibition of the oxygen reduction reaction on zinc. Samples of chromated zinc were subjected to cathodic treatment in 0.5M NaCl for short periods of time. These cathodically-treated samples were catalytically inactive for the oxygen reduction reaction. The activity was restored by continued immersion in the NaCl solution for an hour or more.

Microscopic studies have been initiated of the early stages of corrosion using a transparent coating (polybutadiene) on a steel substrate immersed in flowing water or salt solution. Corrosion was hastened by contaminating the surface with  $\text{KHSO}_4$  before application of the coating. The corrosion reaction first became visible in one hr. Areas delineated by optical reference rings appeared in an annulus around the contamination spot. These areas grew in diameter with time. The cathodic and anodic areas were separate and could be distinguished because of the blue color that was associated with the anodic areas. Information about liquid volume in the corrosion zone, changes in location of anodes and cathodes with time, earliest stages of coating delamination, and secondary processes that occur was obtained by time lapse photography.

Electrical methods are beginning to be accepted as a useful tool for studying organic coatings. Such methods, when properly used, provide information about the amount of water in the coating, the glass transition temperature of the coating, the presence of conductive paths in the coating and corrosion of the metal substrate. The electrical studies during the past year have focused on the use of impedance techniques to provide information about the coating integrity as a function of time of exposure to an aggressive electrolyte. Different coatings have different impedances and the impedance is a function of the coating thickness. In order to normalize the results so that different types and thicknesses of coatings could be compared, the data were treated in the following way. The ratio of the imaginary and real components (Tangent  $\theta$ ) of the complex impedance was plotted as a function of time. Coatings in which there is little or no deterioration exhibit Tangent  $\theta$  values of the order of 1. When the coating deteriorates and corrosion begins, the value of Tangent  $\theta$  drops by several orders of magnitude. The method appears to be a candidate for predicting the lifetime of coating systems on bare metal. It remains to be determined if the method is applicable to systems in which the metal surface has been phosphated or chromated.

The adherence of a coating to a metal substrate or to pigments or fillers in the coating is presumed to be determined by the interaction of acidic and basic sites at the interface. Efforts to quantify the acidity of iron oxide surfaces are being made by measuring the adsorption from organic solvents of compounds such as pyridine. Such adsorption measurements have been made on  $\text{Fe}_3\text{O}_4$  and  $\alpha\text{-Fe}_2\text{O}_3$  using flow calorimetry. It was found that traces of water in the pyridine competed with the pyridine for surface sites. The surface energies of  $\text{Fe}_3\text{O}_4$  and  $\text{Fe}_2\text{O}_3$ , whose surfaces were largely devoid of adsorbed water, were very similar, i.e., 80 and 83 erg/cm<sup>2</sup>, respectively.

Auger spectroscopy and X-ray photoelectron spectroscopy are being utilized to characterize the sites on metal surfaces that may be available for adhesive bonding. The technique is simple in concept but difficult in execution. Steel, surfaced in a standard way, is immersed in a medium, the pH of which is closely controlled, and the amount of a constituent in the medium present on the surface is determined. One of the systems that has been studied extensively is the exchange of potassium ions with surface hydroxyls on an oxidized steel surface. The amount of potassium up-take by the steel surface increases dramatically in the pH range of 10-11. The  $K_a$  for the hydrated iron oxide on steel is calculated to be 10.8. This number may be important in selecting polymers that have the maximum adhesion to steel surfaces. The major difficulty in generating information about additional systems is the perturbing influence of carbon contamination.

Most of the critical questions regarding the performance of organic coatings in protecting a metal from corrosion relate to the chemistry of the interfacial region and the homogeneity of the coating. Techniques are being sought for carrying out chemical studies in a non-destructive manner. Two candidate techniques, infrared spectroscopy and Raman spectroscopy, were considered and the latter technique was selected because of the availability of a new instrument which utilizes a laser source and generates information from an area of 1  $\mu\text{m}^2$ . A laser microprobe has been purchased and will be applied to studies of the coating and the coating/substrate interface. Preliminary experiments indicate that the instrument has the required capabilities.

One of the coating methods which is exhibiting good corrosion protection performance is cathodic electrocoating in which the polymeric material is deposited on the cathode when a voltage is applied across an aqueous dispersion in the electrolysis chamber. A coherent coating is obtained after baking. The procedure has proven so effective that 85% of the automobiles manufactured have some portion of the vehicle electrocoated. The kinetics of the cathodic electrocoating of epoxy-polyamine mixtures have been studied with the purposes of (a) understanding better the electrodeposition process and (b) developing

electrocoats of the same epoxy-polyamine that can be prepared from an organic solvent. Data have been generated on the mass of polymer deposited per unit time, the coulombic efficiency, the effect of the magnitude of the current and applied voltage, the temperature of the cathode, and the epoxy/amine ratio.

The character and properties of organic coatings are dependent in no small measure on the manner in which the coating dries. This statement is particularly pertinent to coatings that are formed from dispersions (latexes). The mechanism of drying of coatings is thus important in understanding the protective nature of a coating. A gravimetric technique was used to measure the evaporation rate of water or organic solvent from thin films cast from epoxy-amine systems on flat glass plates. Drying conditions were 10-52% relative humidity, 0-76 cm/sec air velocity, and 25-40°C. The drying rates were calculated from the weight loss and determination of the wet portions of the film. The drying rates of the solvent-based systems ranged from  $4.5 \times 10^{-5}$  at the beginning of the drying operation to  $0.5 \times 10^{-5}$  g/cm<sup>2</sup>-sec per g. moisture content at the end of the experiment. The aqueous-based systems were characterized by an initially relatively low and constant rate ( $1 \times 10^{-5}$  g/cm<sup>2</sup>-sec per g. moisture content) followed by an increased flux of the order of  $10^{-4}$  g/cm<sup>2</sup>-sec per g. moisture content. The drying behavior of an aqueous-based solubilized system was intermediate between those of the solvent-based and aqueous-based systems. An explanation of the reasons for the differences observed in the drying characteristics of the different systems was given based on the phenomenon of skin-formation.

Corrosion beneath an organic coating is dependent on the presence of an aqueous phase at the interface. Without an aqueous phase the electrochemical corrosion process does not occur. Capacitance measurements have proven to be a useful method to detect the amount of water taken up by a coating exposed either to a humid environment or to an electrolyte. However, these measurements do not distinguish between water that is dispersed throughout the coating in a gas-like form from water that has aggregated to form a condensed phase. Techniques are thus being sought that will differentiate between dispersed (or mobile) water and aggregated water. Since liquid phase water exhibits a relaxation at high frequencies which is not exhibited by gaseous water, it has been decided to explore high frequency (10<sup>9</sup> c/sec) dielectric measurements in the hope that the two different forms of water can be differentiated when they are present in an organic coating. Equipment to make such measurements based on time domain spectroscopy has been assembled and computer programs for data handling have been developed.

Coatings based on zinc pigments are recognized as being among the most effective in protecting steel against corrosion. Zinc concentrations in a polymer in the range of 85-96% are

typically used. The corrosion mechanism, which is based on a combination of galvanic protection of the steel and the corrosion inhibitor properties of zinc compounds formed on exposure to an aggressive environment, is generally accepted. Important gaps in our knowledge exist in quantitative characterization of the zinc/polymer interaction since a strong interaction is important in restricting liquid water ingress that might occur at breaks in the bond. Studies of mechanical behavior, curing and drying properties, and electronmicroscopic appearance indicate that the adhesion between zinc and an epoxy matrix is usually, but not always, low. Corrosion protection will probably be maximized by minimizing acid/base interaction between the zinc and the polymer.

Electron microscopic examinations were made of epoxy coatings subjected to different corrosive environments. The weakest point of the epoxy matrix appeared to be in those areas which were in contact with the metal surface or in contact with a filler particle. This observation was independent of the formulation or the cure conditions. This conclusion was based on exposure of epoxy coatings to  $\text{OsO}_4$  or to strong hydrochloric acid.

Studies of iron oxides were performed with the hope that a better knowledge of the surface character of iron oxides might be helpful in improving the adherence of organic coatings to a steel surface and might be helpful in designing systems for use in painting slightly oxidized or rusted steel. Commercial materials and colloidal sols prepared in the laboratory were used.

Iron corrosion products are amphoteric, i.e., their surfaces comprise both acidic and basic groups as determined by adsorption of basic polymethyl methacrylate and acid chlorinated polyvinyl chloride. The proportion of acidic and basic groups varied significantly from one compound to another. All iron oxides studied to date adsorb substantial proportions of Epon 1001F and Emerez 1511.

A long range program has been initiated to study the nature of the corrosion products formed on steel exposed to the atmosphere. As background information for this study and other studies involving iron oxides, it was decided to accumulate information on oxides prepared by simple hydrolysis. Aqueous solutions of ferric sulfate, ferric chloride, and ferric nitrate were heated at 90°C and the products that formed were studied as a function of time using Mössbauer spectroscopy. Mechanisms of formation of the oxides were proposed and the Mössbauer parameters of the oxides and hydroxyoxides were determined.

Commercial and synthetic iron oxides were characterized by gas adsorption, thermal treatment, and electrophoretic measurements. Both  $\alpha\text{-Fe}_2\text{O}_3$  and  $\text{Fe}_3\text{O}_4$  have surfaces that are hydrophilic in nature. No evidence for dehydroxylation of the  $\alpha\text{-Fe}_2\text{O}_3$

surface was noted at activation temperatures up to 400°C. The concentration of water molecules adsorbed on  $\alpha\text{-Fe}_2\text{O}_3$  decreased from 8.46 molecules/100  $\text{\AA}^2$  for the sample activated at 25°C to 5.38 molecules/100  $\text{\AA}^2$  for the sample activated at 400°C. Electrophoretic measurements were made on iron oxides prepared by hydrolysis at 90°C and the isoelectric point was determined. The isoelectric points of the pure compounds agreed with those determined previously on commercial materials and mixtures of two components yielded values that were calculable from the percentage composition and knowledge of the isoelectric points of the pure components.

Program #1. The Mechanism for the Cathodic Delamination  
of Organic Coatings from a Metal Surface

ABSTRACT

A detailed mechanism of cathodic delamination is presented which takes into account the reactants and how they get to the delaminating front. Oxygen and water pass through the organic coating whereas cations, at least in part, reach the front by lateral diffusion. Five means for minimizing cathodic delamination are suggested: (1) No bare metal, or superficially oxidized metal, should be present at the coating/substrate interface. (2) There should exist at the coating/substrate interface a layer which is a very poor conductor of electrons. (3) The interfacial layer at the coating/substrate interface should be a poor catalyst for the cathodic reaction. (4) The boundary between the substrate and the coating should be rough in order to provide a tortuous path for lateral diffusion. (5) The interfacial region should be resistant to alkaline attack.

INTRODUCTION

Areas of a metal surface covered with an organic coating may become sufficiently cathodic to catalyze the cathodic reaction beneath the coating. This cathodic nature may be purposely induced or it may be corrosion induced because of separation of the anodic and cathodic areas. The cathodic reaction, or the products of the cathodic reaction, adversely affect the bond between the coating and the substrate and the coating separates from the metal [1-3]. Such separation is termed "cathodic delamination" and is the subject of this paper.

Cathodic delamination has special pertinence to systems such as ships, pipelines, and underground structures which are cathodically protected and there is an ASTM test [4] which appraises the resistance of coating/substrate systems to cathodic delamination. The blistering of paint on vehicles or metallic structures exposed to the atmosphere often is caused by an injury to the coating such that the substrate is exposed. The exposed area becomes the anode and the adjoining area becomes the cathode. The spread of the corrosion and the blistering of the paint is a consequence of the cathodic delamination that

occurs and is followed by incursion of water and salts on alternate wetting and drying during service. A standard test [5] is also used to appraise the sensitivity of coating/substrate systems to this type of deterioration. The coating is scratched through to the substrate and the scribed panel is then exposed in a salt spray cabinet. The distance of creepback from the scribe during a fixed time period is used as a comparative measure when ranking different systems.

We have been interested in cathodic delamination since the paper with Kendig in 1976 [6]. The present paper has as its purpose to outline a detailed mechanism for cathodic delamination based largely on work done in our laboratory [6-14] and, to a lesser extent, on work done elsewhere. Some early views have been modified on the basis of new information.

#### EXPERIMENTAL METHOD

Three different types of coatings were used. Unpigmented polybutadiene coatings were prepared from Budium RK-662 from DuPont applied with a centrifugal applicator and cured at 200° for 20 min. In the case of coatings thicker than 20 µm, the coating was applied in 15 µm increments and was cured after each application. The infrared spectra of the uncured and the cured coatings have been published [14].

The alkyd system was applied in the form of two layers of primer and up to 4 layers of topcoat. Each layer was 25-30 µm in thickness. A drying time of 24 hrs was used between each coat and the multicoat system was dried at room temperature for not less than 2 weeks before immersion in electrolyte. The compositions of the primer (Rust-Oleum 7773) and the topcoat (Rust-Oleum satin white 7791) were as follows:

Primer	
Pigment	44.6%
Silicates	15.6%
Yellow iron oxide	7.6%
TiO <sub>2</sub>	2.7%
Calcium borosilicate	18.2%
Bentonite clay	0.5%
Vehicle	55.4%
Linseed Phenolic alkyd resin	20.1%
Aliphatic hydrocarbons	32.6%
Driers and Additives	2.7%

Topcoat

Pigment	53.5%
Silicates	34.7%
TiO <sub>2</sub>	16.7%
Bentonite clay	0.1%
Tinting colors	2.0%
Vehicle	46.5%
Soya/menhaden alkyd resin	17.2%
Aliphatic hydrocarbons	28.8%
Driers and additives	0.5%

The epoxy system was generally applied in two layers to obtain the desired thickness. Drying time between each layer and before use was 7 days. The formulation was standardized in military specification MIL-P-24441/1 (ships) on September 27, 1971. The formulation consists of two components that were mixed 1:1 by volume (1.17:1 by weight) of components A and B. The compositions were as follows:

Component A

	% by weight
Thixotrope (Thixatrol ST)	0.4
Polyamide (Genamid 2000)	1.7
Polyamide adduct (Versamid 280B75)	23.5
Magnesium silicate	42.0
Titanium dioxide	8.4
Butyl alcohol	22.2
Copper phthalocyanine blue	0.084
Yellow iron oxide	1.7

Component B

Thixotrope (Thixatrol ST)	0.5
Epoxy resin	49.4
Magnesium silicate	9.9
Naphtha	25.5
Diatomaceous silica	14.8

The methods of applying the cathode potential and determining the range of the delamination have been described previously [10]. Polarization curves were determined using a PAR 350 Corrosion Measurement Console and a Model K47 Corrosion Cell system and the procedure was that outlined in ASTM G5-72.

Some experiments were carried out in which the environment at a purposely-applied defect in the coating was different from that to which the majority of the coating was exposed. A schematic diagram of the arrangement is shown in Figure 1. A

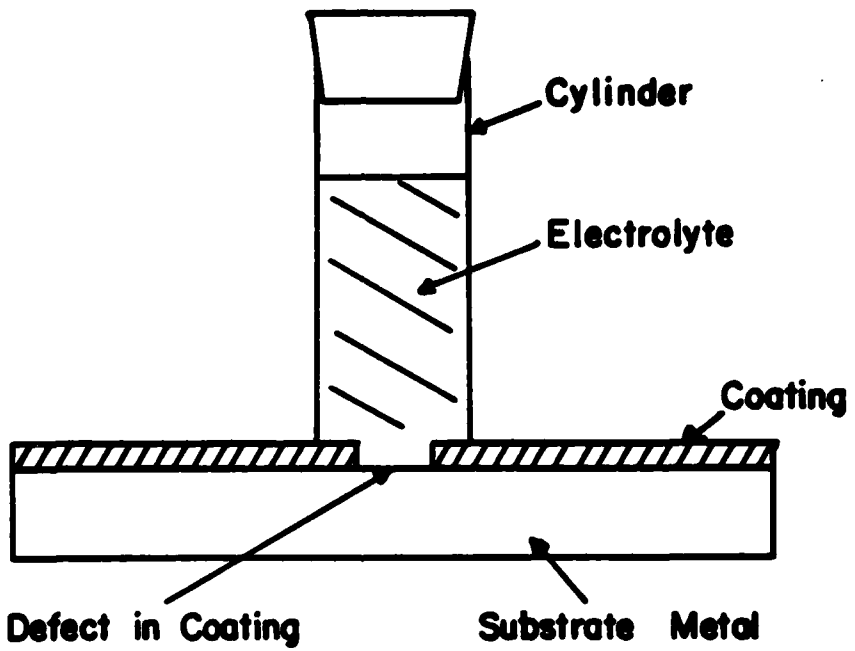


Figure 1. Experimental arrangement utilized in order to expose the coated substrate to two different environments, one inside the cylinder and the other outside the cylinder. Cap was only used when atmosphere in cylinder was controlled.

cylinder, 12 mm in diameter, was fabricated from polyethylene tubing and the end was polished flat. It was cemented to the coating with an additional layer of coating applied after the coated metal had dried. Electrolyte was placed in the cylinder after a defect had been scribed in the coating within the cylinder. The environment external to the cylinder varied depending on the experiment being performed.

Two different lots of steel were utilized during the research, both of which were kindly furnished by Bethlehem Steel. The first, called Lot #1, was 0.73 mm thick and the second, called Lot #2, was 0.41 mm thick. No effort is made to distinguish between these two lots in the text since all comparative experiments were carried out on steel of the same lot. The analysis of the surface of the steel, on the basis of Auger spectroscopy utilizing peak-to-peak intensities and the sensitivity factor for each element, is given in Table I.

Table I  
Surface Analysis of Steels Utilizing Auger Spectroscopy

	Lot #1		Lot #2	
	<u>As-Received</u>	<u>Abrasively Polished</u>	<u>As-Received</u>	<u>Abrasively Polished</u>
Iron	23.1%	34.7%	17.6%	24.9%
Oxygen	44.4	46.5	35.9	46.2
Sodium	--	3.2	--	--
Chlorine	0.3	0.4	--	--
Nitrogen	2.0	2.5	1.4	--
Carbon	29.1	11.9	44.0	28.0
Potassium	0.8	0.4	0.8	0.9
Sulfur	0.3	0.4	0.4	--

It should be emphasized that this analysis should be considered qualitative.

Unless otherwise stated, all panels were abrasively polished with silicon carbide paper, #240 grit, while wetted with distilled water. The grit and metal particles were removed with a paper tissue and the panel was rinsed with hot water, with acetone, and again with hot water. Final rinsing was done with acetone. The panels were dried in air and immediately coated.

## CATHODIC DELAMINATION PROCESS

Relation to Electrochemical Properties of Metal Surface. It is generally believed [6,15] that the major driving force for cathodic delamination in corrosion processes in the presence of air is the cathodic reaction,  $H_2O + 1/2O_2 + 2e^- = 2OH^-$ . When an applied potential is used, the important reaction may be  $2H^+ + 2e^- = H_2$ , if the driving force is sufficient. Figure 2 shows a typical cathodic polarization curve for steel in 0.5M NaCl saturated with air. The regions of dominance of the two cathodic reactions are noted on the figure and the cathodic polarization curve for hydrogen evolution in the absence of oxygen is shown by the dotted line. It is apparent from this figure that at a potential of -0.8 v the dominant reaction is oxygen reduction and at potentials more negative than -1.0 v the dominant reaction is hydrogen evolution. Polarization at -0.8 v of polymer-coated steel containing a defect in the absence of oxygen leads to no significant delamination from the defect, whereas in the presence of air there is significant delamination.

Studies indicate that the pH beneath the organic coating where the cathodic reaction occurs is highly alkaline, as the cathodic equations indicate. Ritter [16] has recently reported that the pH at the delaminating edge is greater than 14 as measured by pH-sensitive electrodes inserted through the metal substrate from the back side. Other studies which integrate the pH over a larger volume of liquid beneath the coating yield values of 10-12. Cathodic polarization curves on steel in 0.5M NaCl at pH values of 6.5, 10, and 12.5 are approximately the same [17] suggesting that the cathodic behavior beneath the coating may be rationalized in terms of the cathodic polarization curve that is applicable at the exposed defect.

The pH at the Delaminating Front. The cathodic reaction which occurs at the delaminating front generates hydroxyl ions which appear to be a major destructive influence on the organic coating/substrate bond. The value of the pH at the delaminating front is determined by the following factors which are discussed here.

(1) The rate at which the cathodic reaction occurs. The rate, as discussed elsewhere in this report, is dependent upon the availability of reactants and the catalytic activity of the surface. The rate determines how many hydroxyl ions are generated per unit time, but the pH is determined by volume effects.

(2) The shape of the delaminating front. The hydroxyl ions are generated at the metal surface and are furnished to the aqueous phase. If the angle between the substrate and the coating

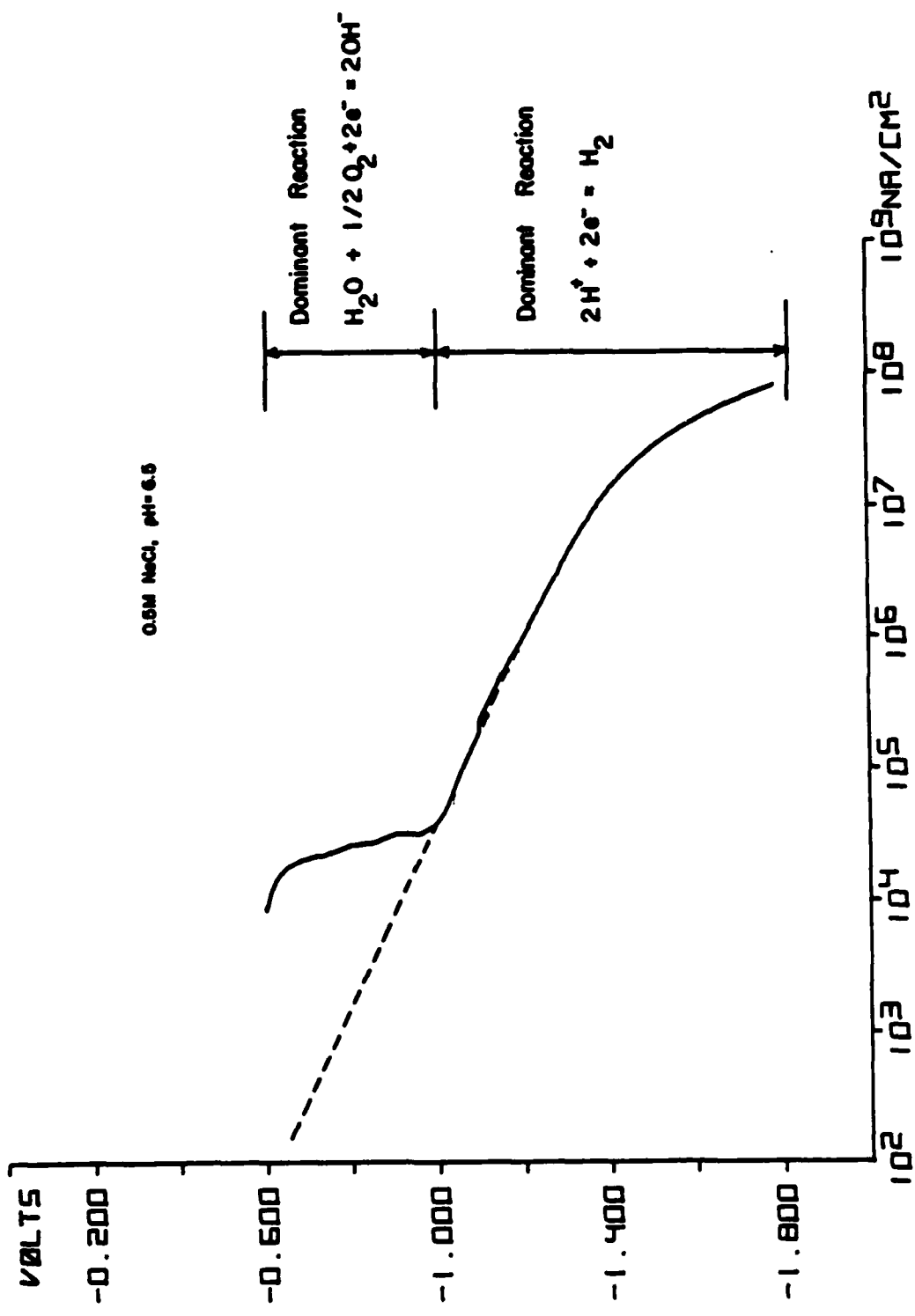
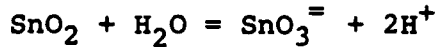
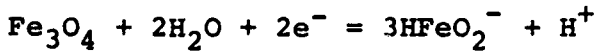
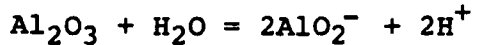


Figure 2. Potentiodynamic polarization curve for steel in aerated 0.5M NaCl. Dotted line represents the extrapolation of the portion of the polarization curve that represents the hydrogen evolution reaction.

is small, the effective volume is small and the pH will be high. If the angle is large, the effective volume of the aqueous phase will be greater and the pH will be substantially lower.

(3) The rate of diffusion of hydroxyl ions away from the delaminating front. The rate of dissipation of the hydroxyl ions away from the region in which they are formed is also a critical factor in determining the pH. This dissipation rate will be determined to some extent by the thickness of the liquid layer immediately behind the delaminating front since diffusion is slower when the dimensions of the layer are small multiples of the ionic diameter.

(4) Buffering reactions. In the cases of aluminum, iron, and tin, hydrolysis reactions at high pH generate hydrogen ions which may neutralize the hydroxyls generated. Typical reactions include:



Other possible buffering reactions include reaction with the polymer with net loss of hydroxyl ions or buffering by environmental constituents.

Mechanism of Delamination. All the evidence presently available indicates that the cathodic delamination process occurs because of the high pH generated by the cathodic reaction. The real question is what is the consequence of a high pH on the interface. The evidence suggests that the strong alkaline environment may attack the oxide at the interface or may attack the polymer. Attack of the oxide has been seen by Ritter [18] using ellipsometric techniques in the case of polybutadiene coatings on steel.

Slight oxidation of the steel surface occurs during oxidative curing of the polybutadiene coatings and the surface develops a faint straw color easily seen through the transparent coating. As delamination proceeds, the straw color disappears and the metallic appearance of iron becomes visible. This observation suggests that the oxide film is destroyed by the alkaline environment but it does not answer the question of whether the destruction is the cause of the delamination or is a result of exposure to the highly alkaline medium after delamination has occurred.

Surface analysis techniques in the hands of Dickie and colleagues [19] give clear evidence that carboxylated species are present at the interface as a result of hydroxyl ion attack of the polymer. Dickie [20] has also recently shown that coatings more resistant to alkaline attack exhibited better performance when scribed and submitted to salt spray.

The Pourbaix diagrams for metals in aqueous solution [21] are a useful source of information on the stability ranges of various species. The metals of interest in the present study all have soluble species at high pH within the potential range of interest. These soluble species are: iron,  $\text{HFeO}_2^-$ ; tin,  $\text{HSnO}_2^-$  and  $\text{SnO}_3^{=}$ ; zinc,  $\text{HZnO}_2^-$  and  $\text{ZnO}_2^{=}$ ; cobalt,  $\text{HCoO}_2^-$ ; aluminum,  $\text{AlO}_2^-$ ; copper,  $\text{HCuO}_2^-$  and  $\text{CuO}_2^{=}$ .

It is proposed that the major mechanism for the delamination process is the solubilization of the thin oxide coating at the interface between the organic coating and the metal. The dissolution of the oxide breaks the bond between the coating and the substrate metal and the high pH leads to localized attack on the polymer at the interface. The presence of oxidized organic species on the metal surface after delamination has occurred may be the result of *a posteriori* adsorption of oxidized species or may be the result of islands of organic left on the surface. The XPS technique used in Reference [19] illuminates a large area and spatial resolution is lacking to determine if the organic material is present over the entire surface or is island-like in nature.

#### Reactants and How They Get to the Reaction Zone.

Water. The coatings used in this study are permeable to water as shown by conventional measurements. The water permeability of the three coatings was determined by the use of aluminum Payne cups. Two methods were utilized: (A) the cups were filled with distilled water, the free film was used as a cover, and the environment exterior to the cup was maintained at approximately 50% relative humidity through the use of a saturated solution of  $\text{Ca}(\text{NO}_3)_2$ ; (B) the interior of the cup was filled with silica gel so as to maintain 0% relative humidity, the free film was used as a cover, and the environment exterior to the film was maintained at 50% relative humidity with the saturated solution of  $\text{Ca}(\text{NO}_3)_2$ . The results of these experiments are summarized in Table II. It has been hypothesized previously [10] that the water reactant for the oxygen reduction reaction reaches the reaction zone by diffusion through the coating. Evidence has now been obtained to support this hypothesis.

The experimental design shown in Figure 1 was applied to the question of the importance of water transmission through the coating in the delamination process. Three different types of experiments were carried out. Steel panels were coated with

Table II

Water Permeability at Room Temperature of Polybutadiene,  
Epoxy, and Alkyd Coatings to Water as Determined  
through the Use of Aluminum Payne Cups

<u>Coating</u>	<u>Water Permeability</u>	
	<u>Method A</u>	<u>Method B</u>
Polybutadiene	0.004 mg-cm/cm <sup>2</sup> -day	0.003 mg-cm/cm <sup>2</sup> /day
Epoxy	0.005	0.001
Alkyd	0.007	0.004

the polybutadiene coating, 33-36  $\mu\text{m}$  thick, or the epoxy coating, 40-47  $\mu\text{m}$  thick. The cylinder surrounded a defect approximately 7 mm in diameter. The cylinder was filled with 0.5M KCl and the coating external to the cylinder was exposed either to distilled water, 100% relative humidity, or 50% relative humidity. Delamination proceeded from the defect and the amount of delamination was determined after 100-200 hrs of exposure. Information on the two coatings is summarized in Table III. In the cases of

Table III

The Effect of Water Concentration External to  
Coating on the Rate of Delamination from a  
Defect Exposed to 0.5M KCl

<u>Type of Coating</u>	<u>Environment External to Cylinder Containing KCl</u>	<u>Delamination Rate in cm<sup>2</sup>/hr</u>
	Distilled Water	0.093
Polybutadiene	100% RH	0.080
	50% RH	0.047
Epoxy	Distilled Water	0.065
	100% RH	0.048
	50% RH	< 0.009

both the polybutadiene and the epoxy coatings the rate was greatest when the coating external to the cylinder was exposed to liquid water, was an intermediate value when exposed to 100% relative humidity, and was the lowest when exposed to 50% relative humidity. Since all systems had water available from the KCl solution at the defect and since the rate decreased with the water concentration above the coating, it is apparent that the delamination process is sensitive to water transmitted through the coating. The lower rate of delamination of the epoxy coating than the polybutadiene coating is probably a consequence of the thicker epoxy coating.

It is not known if water transmission through the coating is exclusively as an uncharged species or if a certain fraction of the water migrates as a cation such as  $H_3O^+$ . The cathodic nature of the delaminating front may favor the transmission of water associated with an ion with a positive charge. Ruggieri and Beck [22] have speculated that the proton is the major charge carrier in the conduction of charge through a polyurethane coating.

Oxygen. At cathodic potentials where the reaction,  $H_2O + 1/2O_2 + 2e^- = 2OH^-$ , is the dominant one, no significant delamination occurs when oxygen is excluded from the system [10]. Additional experiments that confirm this conclusion have been carried out in deaerated 0.5M KCl using an epoxy paint on a steel substrate. No delamination occurred in the absence of oxygen. The question then arises, how does the oxygen reach the delaminating region? Is it through the coating, or laterally from the liquid in contact with the defect? The following experiments were designed to answer this question.

In the first set of experiments, steel panels were coated with the epoxy paint to yield a dry film thickness of 55-59  $\mu m$  and the experimental arrangement shown in Figure 1 was used. A 7 mm defect was formed in the coating within the cylinder. Air-saturated 0.5M KCl was placed in the cylinder and a second liquid with different oxygen solubility was placed exterior to the cylinder. The liquids used and the oxygen solubilities are summarized in Table IV and the delamination rate as a function of the oxygen solubility of the liquid exterior to the cylinder is given in Figure 3. All experiments were run for 79.4 hr and the total delamination was measured after this time.

The data in Figure 3 clearly show that the rate of delamination decreases as the oxygen concentration in the liquid exterior to the cylinder decreases. Thus some of the oxygen furnished to the delaminating zone must come through the coating. However, extrapolation of the line to zero oxygen solubility still yields a finite delamination rate suggesting that some of the oxygen is furnished laterally from the defect in the case of the epoxy coatings. Confirmation of this conclusion is obtained from an experiment in which the 0.5M KCl in

DELAMINATION AS A FUNCTION  
OF OXYGEN CONCENTRATION

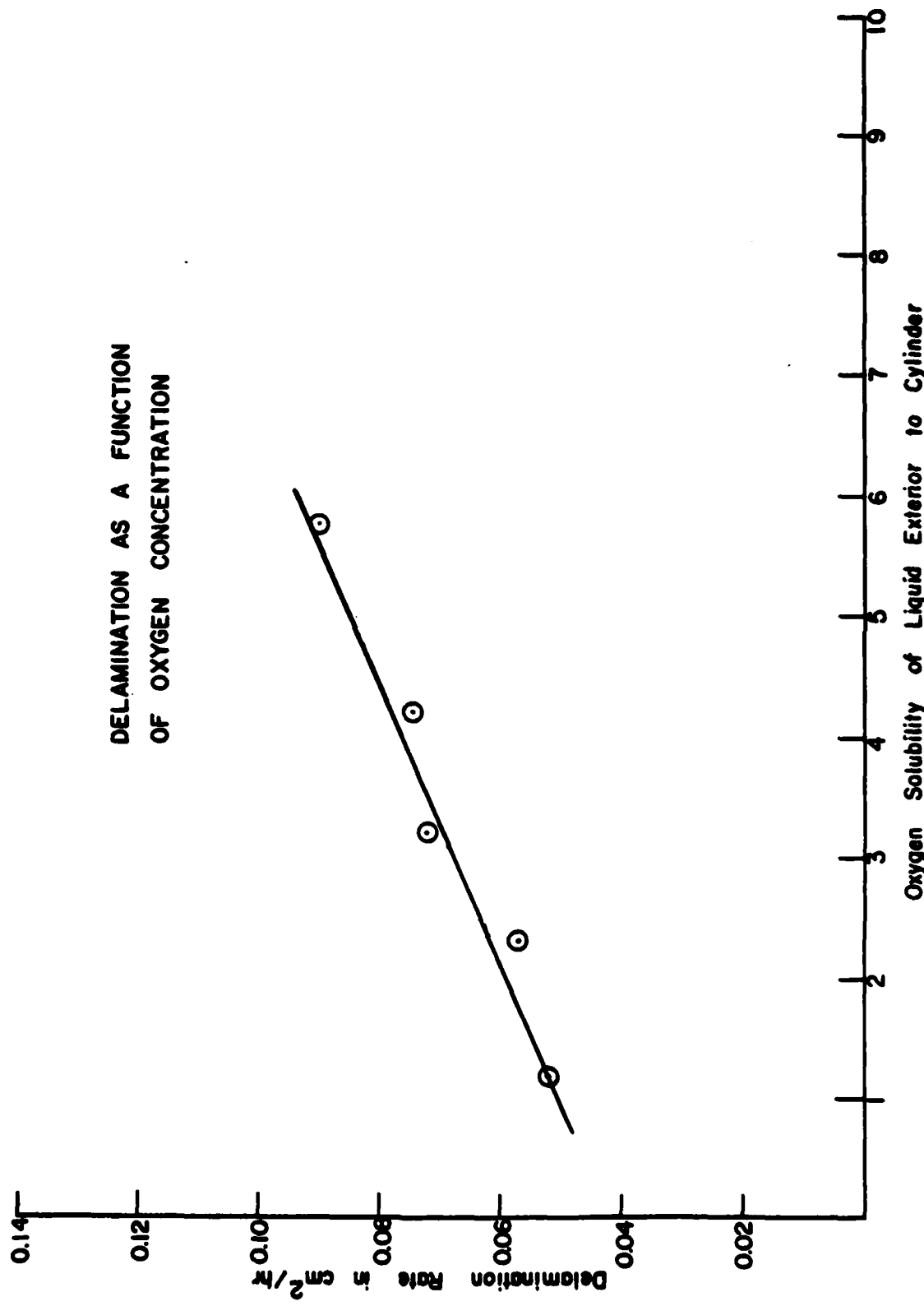


Figure 3. Rate of delamination of an epoxy coating, approximately 57  $\mu\text{m}$  in thickness, as a function of the oxygen solubility of the liquid with which the coating is in contact.

Table IV  
Oxygen Solubility of Liquids in Experiments  
Summarized in Figures 3 and 4

Liquid Exterior to Cylinder	Oxygen Solubility at 25°
Distilled Water	5.78 cm <sup>3</sup> /L
0.125M LiCl	5.63
0.125M sucrose	5.40
0.125M CaCl <sub>2</sub>	5.08
0.5M sucrose	4.39
0.5M KCl	4.18
0.5M CaCl <sub>2</sub>	3.71
2M KCl	3.21
1M sucrose	3.20
0.125M NH <sub>4</sub> Cl	2.31
2M sucrose	1.84
0.25M NH <sub>4</sub> Cl	1.16
1M NH <sub>4</sub> Cl	0.07
16% NaHSO <sub>3</sub>	0

the cylinder was deaerated with argon and sealed and the distilled water exterior to the cylinder was open to the air. No delamination beyond the cylinder occurred under these conditions in a 98 hr period.

In the second set of experiments, steel panels were coated with polybutadiene in two steps to yield coatings approximately 45  $\mu\text{m}$  thick. The cylinder was filled with aerated 0.5M KCl and the liquid exterior to the cylinder was a solution listed in Table IV. The delamination was corrosion induced by the defect within the cylinder and no external potential was applied. The data obtained from this set of experiments are summarized in Figure 4. It will be noted that the delamination rate was very low when the oxygen content in the external cylinder was low and was appreciable when the oxygen content was high. The lack

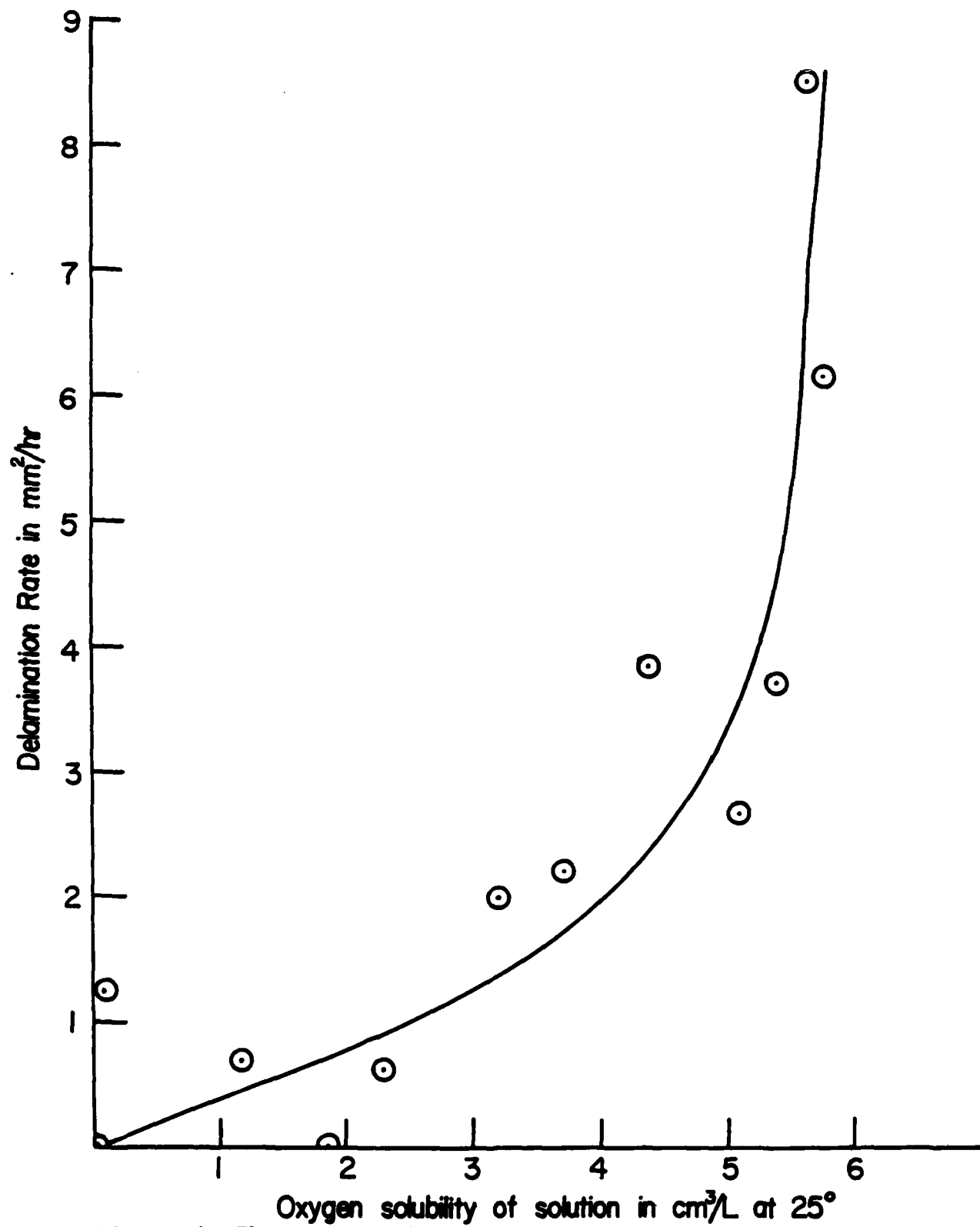


Figure 4. The rate of delamination at the corrosion potential of polybutadiene coatings, 45  $\mu\text{m}$  thick, on steel substrates as a function of the oxygen solubility in the solution in which the panel was immersed. See Table IV for liquids used in this study.

of perfect agreement is probably to be expected because factors other than oxygen solubility may be involved. For example, the concentrated solutions may change the activity of water and the concentrated solution of sucrose may have enough impurities that act as oxygen scavengers to reduce the oxygen concentration to a low value.

Cations for Charge Neutralization. The cathodic reaction that occurs under the coating generates OH<sup>-</sup> ions. Charge balance is maintained by diffusion of cations to the site of OH<sup>-</sup> generation. Metal cations instead of hydrogen ions must be a major diffusing species since the pH under the coating is high. The diffusion of cations to the reaction zone is also shown by the following experiment. Delamination of an epoxy coating from a defect was permitted to occur in aerated 0.5M KCl at the corrosion potential. The coating was removed, the aqueous phase was allowed to dry, and the surface was analyzed by Auger spectroscopy at a point remote from the defect. The relative amounts of the elemental species at this point were:

Iron	13.5 at. %
Oxygen	37.1
Sodium	1.5
Chlorine	1.9
Nitrogen	2.6
Carbon	19.3
Potassium	23.7
Sulfur	0.4

The potassium/chlorine ratio was 12.5, thus indicating the preferential diffusion of cations to the cathodic, delaminating region.

The critical importance of the cation is shown by the data given in Table V. The rate of delamination from a defect, 7 mm in diameter, was determined at the corrosion potential in the system shown in Figure 1, in which the aqueous solution was present in the cylinder and distilled water was present exterior to the cylinder. The substrate in all cases was abrasively polished steel and the coating was a two-layer epoxy, 50-65 µm thick. It will be noted from Table V that the 5 sodium salts yielded approximately the same delamination rates and the rates were very different for the ammonium, calcium, and magnesium salts. The low rate of delamination in the case of 0.5M NaOH is probably a consequence of the low rate of corrosion at the defect and the consequent low driving force for the reaction.

Cations may be provided by two paths: (a) through the aqueous phase immediately at the coating/substrate interface or

Table V

Rate of Delamination of Epoxy Coatings on Steel  
with 0.5M Aqueous Solutions at the Defect and  
Distilled Water Exterior to the Defect in  
System Shown in Figure 1

<u>Solution</u>	<u>Delamination Rate in mm<sup>2</sup>/hr</u>
NaF	4.4
NaCl	3.8
NaBr	3.9
NaI	3.7
Na <sub>2</sub> SO <sub>4</sub>	2.9
NaOH	0.7
NH <sub>4</sub> Cl	0.2
CaCl <sub>2</sub>	0
MgCl <sub>2</sub>	0.9

(b) through the coating from liquid exterior to the interface. Prior to the experiments described below, the evidence to distinguish between (a) and (b) was conflicting.

Much effort was devoted to determining ionic uptake but the difficulties are legion. One set of experiments is mentioned because it does show that ions penetrate the coating when the coating is made the cathode. The experimental design was the following. Panels, 9.5 x 9.5 cm, were coated and were clamped to the other end. The cell was filled with aerated 2M NaCl, the two steel panels were electrically coupled externally, and the system was allowed to stand for 20 days. At the end of this time the panel was wiped clean with tissue and the panel was subjected in another glass cell to circulated triply distilled water. Samples of the liquid were removed periodically and the sodium content of the solution was determined periodically using the flame emission technique of Murray [23]. Results are given in Table VI. The data with the alkyd coating had a consistent time dependence sufficient to permit calculation of a desorption coefficient by the method of Murray. A value of  $2 \times 10^{-15} \text{ cm}^2/\text{sec}$  was obtained after exposure to 2M NaCl and  $2 \times 10^{-12} \text{ cm}^2/\text{sec}$  after exposure to 0.1M NaCl.

A major effort must be expended in order to determine the ionic permeability of the coatings. The data reported are indicative of the fact that sodium ions do penetrate into the coating under conditions where the coated metal is polarized

Table VI

Sodium Desorption from Coatings on Steel after Exposure  
to 2M NaCl for 20 Days While Coupled to a Bare Steel  
Panel of Equal Surface Area

<u>Coating</u>	<u>Thickness</u>	Concn. of Na in Circulating Distilled Water during Desorption	
		<u>After 1 hr</u>	<u>After 312 hr</u>
Polybutadiene	32 $\mu$ m	2.3 ppm	5.6 ppm
Polybutadiene	36	1.0	5.1
Epoxy	71	13.8	18.0
Epoxy	51	16.2	14.5
Alkyd	93	4.2	29.0
Alkyd	94	4.9	27.0

very slightly in the cathodic direction.

The delamination rate of polybutadiene coatings on steel is linearly related to the diffusion coefficient of LiCl, NaCl, KCl, CsCl, and CaCl<sub>2</sub> (see Fig. 5) in aqueous solution [10]. This observation suggested that the supply of cations was provided through the aqueous phase at the interface, although the presence of aqueous pathways through the coating could not be ruled out. The strong dependence of the rate of cathodic delamination on coating thickness [17] suggested that the rate of diffusion of reactants through the coating was the important variable. The inability to interpret these experiments adequately was the motivating force for the following experiments.

Panels were exposed for 174 hr in the arrangement outlined in Figure 1 and the delamination exterior to the central vessel was determined. Data for various combinations of liquids are summarized in Table VII. It will be noted that no delamination occurred, except a minor amount with panel I, when the defect was in contact with distilled water. On the other hand, when the defect was in contact with a salt solution the delamination rate was significant and the delamination extended out beyond the region which was in contact with the salt solution. These experiments prove conclusively that the cations are supplied to the delaminating front through the aqueous phase at the interface under the conditions used.

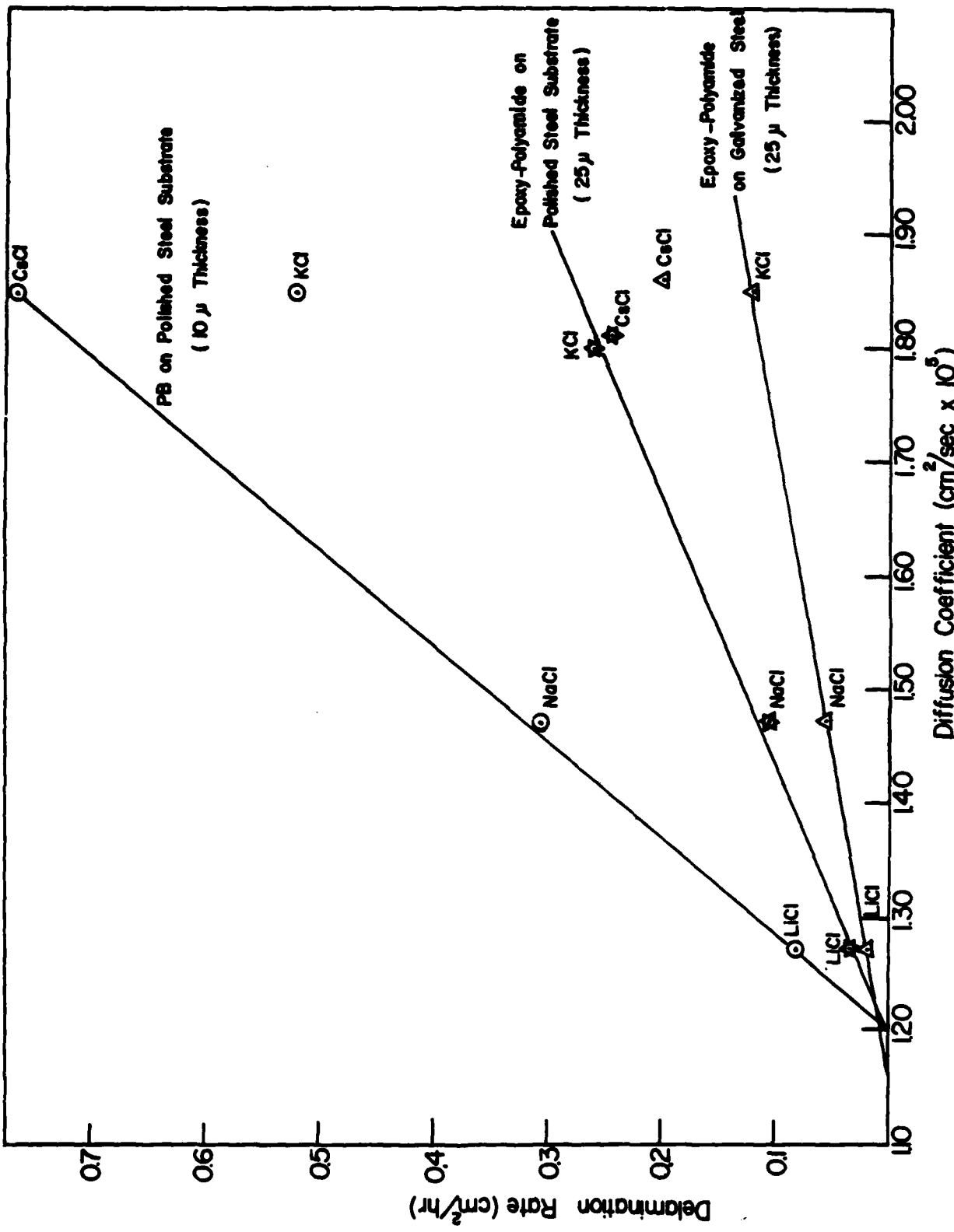


Figure 5. The linear relationship between the cathodic delamination rate and the diffusion coefficient for 4 electrolytes and three different substrate/coating systems.

Table VII  
Delamination Rates Using the Arrangement of Figure 1

<u>Solution in Contact</u>	<u>with defect in exterior to central vessel</u>	<u>Blisters</u>	<u>General Appearance</u>	<u>Delamination</u>	<u>Delamination Rate in cm<sup>2</sup>/hr</u>
<u>without central vessel</u>					
distilled water		none	irregular because of defects in film	0.002	
0.5M KC1		many	entire panel	> 0.16	
0.5M NaCl		some	yes	0.077	
0.5M LiCl		none	yes	0.013	
<u>with central vessel</u>					
distilled water	distilled water	none	no	0	
distilled water	0.5M CsCl	none	no	0	
0.5M CsCl	distilled water	many	yes	0.081	
distilled water	0.5M KC1	none	no	0	
0.5M KC1	distilled water	yes	entire panel	> 0.16	
0.5M KC1	0.5M KC1	some	yes	0.11	
0.5M NaCl	distilled water	few	yes	0.056	
0.5M LiCl	distilled water	none	yes	0.021	

A similar set of experiments was carried out with applied potentials such that the cathode potential was either -0.8 or -1.2 v. These data are summarized in Table VIII. With the exception of the anomalous results shown in the last entry of the table, delamination occurred rapidly when 0.5M KCl was at the defect and distilled water was exterior to the cylinder. Delamination did not occur when distilled water was at the defect and 0.5M KCl was exterior to the cylinder.

In all cases studied to date the delaminated area is linearly related to time at a constant potential. This relationship can be derived under the following assumptions:

- (1) The rate of delamination is determined by the rate at which the cathodic reaction occurs. When the coating is thin and the surface is active catalytically, the rate is determined by the rate of lateral diffusion of cations from the defect area to the delaminating front.
- (2) The concentration of the cation at the defect ( $C_b$ ) is the same as that in the bulk solution.
- (3) The concentration of the cation at the delaminating front is zero.
- (4) The alkali metal ion concentration under the coating changes linearly from the defect to the delaminating front.
- (5) The cations reach the delaminating front by diffusion governed by Fick's Law:

$$F_M^+ = -D(dC_M^+/dr) \quad (1)$$

where  $F_M^+$  is the cation flux, D is the diffusion coefficient,  $C_M^+$  is the concentration of the alkali metal cation, and r is the linear distance from the defect.

- (6) There exists a liquid layer beneath the coating from the defect to the delaminating front.

The thickness of the liquid layer near the delaminating front is d and the radius of the delaminated region is R. The cation diffusion rate at time T,  $M_M^+$ , is thus given by:

$$M_M^+ = F_M^+ A = 2\pi R d F_M^+ . \quad (2)$$

The cation concentration,  $C_M^+$  at a distance r from the defect based on assumption 4 is

$$C_M^+(r) = -(C_b/R)r + C_b \quad (3)$$

Table VIII

Delamination Rates with an Applied Potential of  
-0.8 v. Using the Arrangement of Figure 1

<u>Liquid at Defect</u>	<u>Liquid Exterior to Cylinder</u>	<u>Applied Potential</u>	<u>Delaminated Area in cm<sup>2</sup></u>	<u>Time in hrs</u>	<u>Delamination Rate in cm<sup>2</sup>/hr</u>
0.5M KCl	Distilled water	-0.8 v	10.4	114	0.091
0.5M KCl	Distilled water	-1.2	>36.2	101	>0.4
0.5M KCl	Distilled water	-1.2	>14.3	44.6	>0.32
Distilled water	0.5M KCl	-0.8	0	119	0
Distilled water	0.5M KCl	-1.2	0	92.3	0
Distilled water	0.5M KCl	-1.2	>11.8	102	>0.12

and

$$\frac{dC_M^+}{dr} = -C_b/R . \quad (4)$$

Substituting (4) in (1)

$$F_M^+ = -D(-C_b/R) = D(C_b/R) . \quad (5)$$

Substituting (5) in (2) gives

$$M_M^+ = 2\pi R d[D(C_b/R)] = 2DC_b d . \quad (6)$$

The total amount of cation diffusion from time  $t = 0$  to  $t = T$  can be expressed as:

$$M_T = \int_0^T 2\pi DC_b d dt - 2 DC_b d T . \quad (7)$$

The total amount of cation existing in the electrolyte between the coating and the substrate is

$$M_T = \int_0^R 2\pi r dC_M^+ dr \quad (8)$$

$$M_T = \int_0^R 2\pi r d[(-C_b/k)r + C_b] dr , \quad (9)$$

which on integration yields,

$$M_T = \pi/3 dC_b R^2 \quad (10)$$

equating with (7)

$$\pi/3 dC_b R^2 = 2\pi DC_b d T \quad (11)$$

$$\text{Area delaminated} = 6\pi DT \quad (12)$$

Thus under the above assumptions, the delaminated area is a linear function of time  $T$ . The equation also allows the calculation of the rate of delamination and such data are given in the last column of Table IX. The calculated values are too high by factors of 17-200 indicating that the diffusion of the cations to the reaction zone is not rate limiting under the conditions of these experiments.

Table IX

Rates of Delamination of Coatings from a Steel Substrate at -0.8 v.  
As a Function of the Electrolyte at a Fixed Concentration of 0.5M

<u>Electrolyte</u>	<u>Diffusion Coeff. in cm<sup>2</sup>/sec</u>	<u>Delamination Rate in cm<sup>2</sup>/hr</u>		<u>Calcd. Rate in cm<sup>2</sup>/hr</u>
		<u>Alkyd</u>	<u>Epoxy</u>	
0.5M LiCl	1.27    10 <sup>-5</sup>	0.011	0.018	0.86
0.5M NaCl	1.474    10 <sup>-5</sup>	0.022	0.029	0.95
0.5M KCl	1.85    10 <sup>-5</sup>	0.036	0.072	1.20
0.5M CsCl	1.86    10 <sup>-5</sup>	0.033	0.041	1.20

Effect of Film Thickness. It has previously been shown in the case of polybutadiene coatings that the rate of delamination decreases with an increase in film thickness in the range of 10-20  $\mu\text{m}$ . The thickness range covered with polybutadiene is limited because of the difficulty in getting uniform oxidative curing with thick polybutadiene coatings. It was thus decided to determine the effect of film thickness with the commercial alkyd coating. All studies were carried out in 0.5M NaCl at a cathodic potential of -0.8 v. The delamination rates were determined at times up to 136 hrs. Representative data for a film thickness of 142  $\mu\text{m}$  are given in Figure 6. As described previously [17], the intersection of the linear portion of the curve with the X axis is termed the "delay time". The delamination rates as a function of film thickness are summarized in Figure 7, where it will be noted that the delamination rate dropped to a low value when the thickness of the top-coat only exceeded 90  $\mu\text{m}$ . The delamination rate of the primer plus topcoat did not change greatly with film thickness when the thickness exceeded 50  $\mu\text{m}$ . The primer alone exhibited much better resistance to delamination than the topcoat alone.

The square root of the delay time is plotted vs. the film thickness in Figure 8. A linear relationship with an intersection of approximately 25  $\mu\text{m}$  is obtained.

Electrons. An essential reaction in the cathodic reaction is the electron. The concentration (or rate of supply) of electrons at the delaminating front is an important variable. Covering the metal surface with a non-conducting layer, such as phosphate, reduces the availability of electrons for the cathodic reaction [11]. The representation of the electron availability at various locations within the delaminated region is the polarization curve. As stated previously, the cathodic polarization curve for steel in air-saturated 0.5M NaCl is essentially the same over a pH range of 6.5 to 12.5 and the discussion below assumes that the polarization behavior is independent of pH over the range of concern.

Immediately at the defect the potential is that characteristic of the applied potential and the potential at the delaminating front has an unknown value somewhat negative to the corrosion potential. The value of the potential becomes less negative continuously from the applied potential to the value at the delaminating front. Under the assumption that there is sufficient oxygen in the liquid adjacent to the delaminated region, the rate of the cathodic reaction at each point will be determined by the polarization curve for air-saturated conditions. However, the exact potential at all points within the delaminated region is unknown.

Figure 9 represents the extremes of three types of polarization curves that are observed on metals whose behavior during

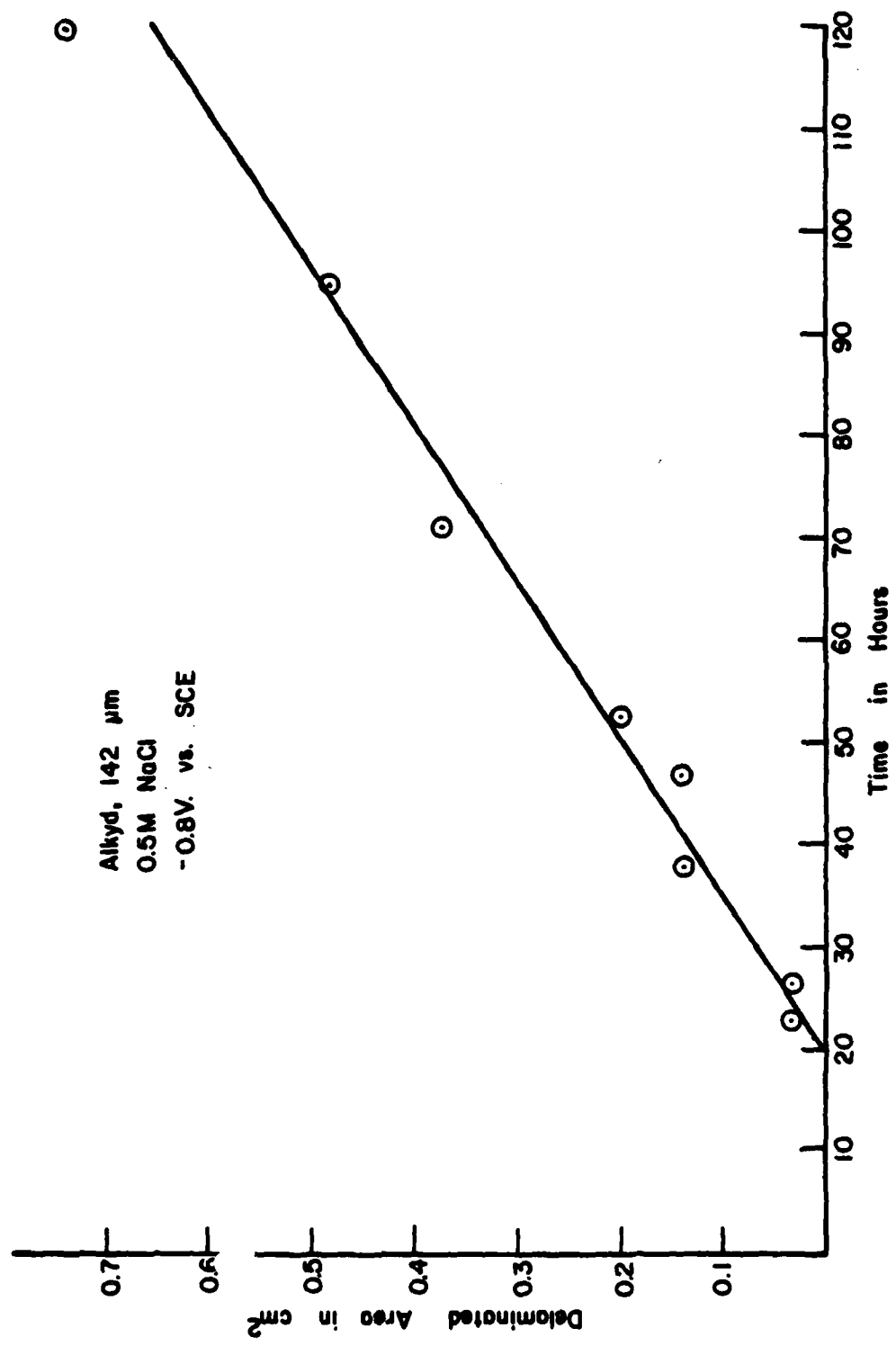


Figure 6. The cathodic delamination at -0.8 v of an alkyd coating, 142  $\mu$ m in thickness in aerated 0.5M NaCl.

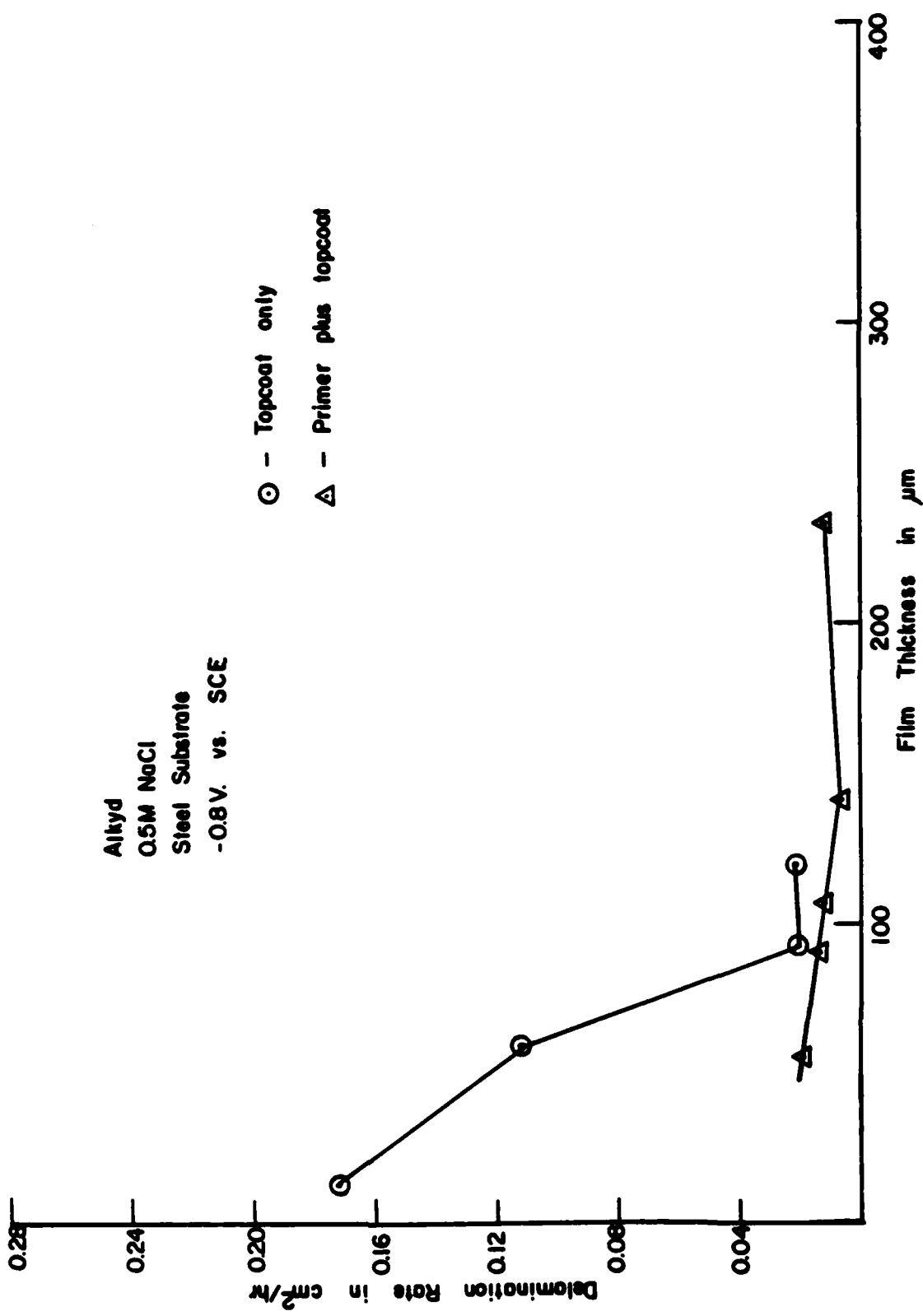


Figure 7. The delamination rates of an alkyd coating on steel polarized at -0.8 v in aerated 0.5M NaCl as a function of film thickness.

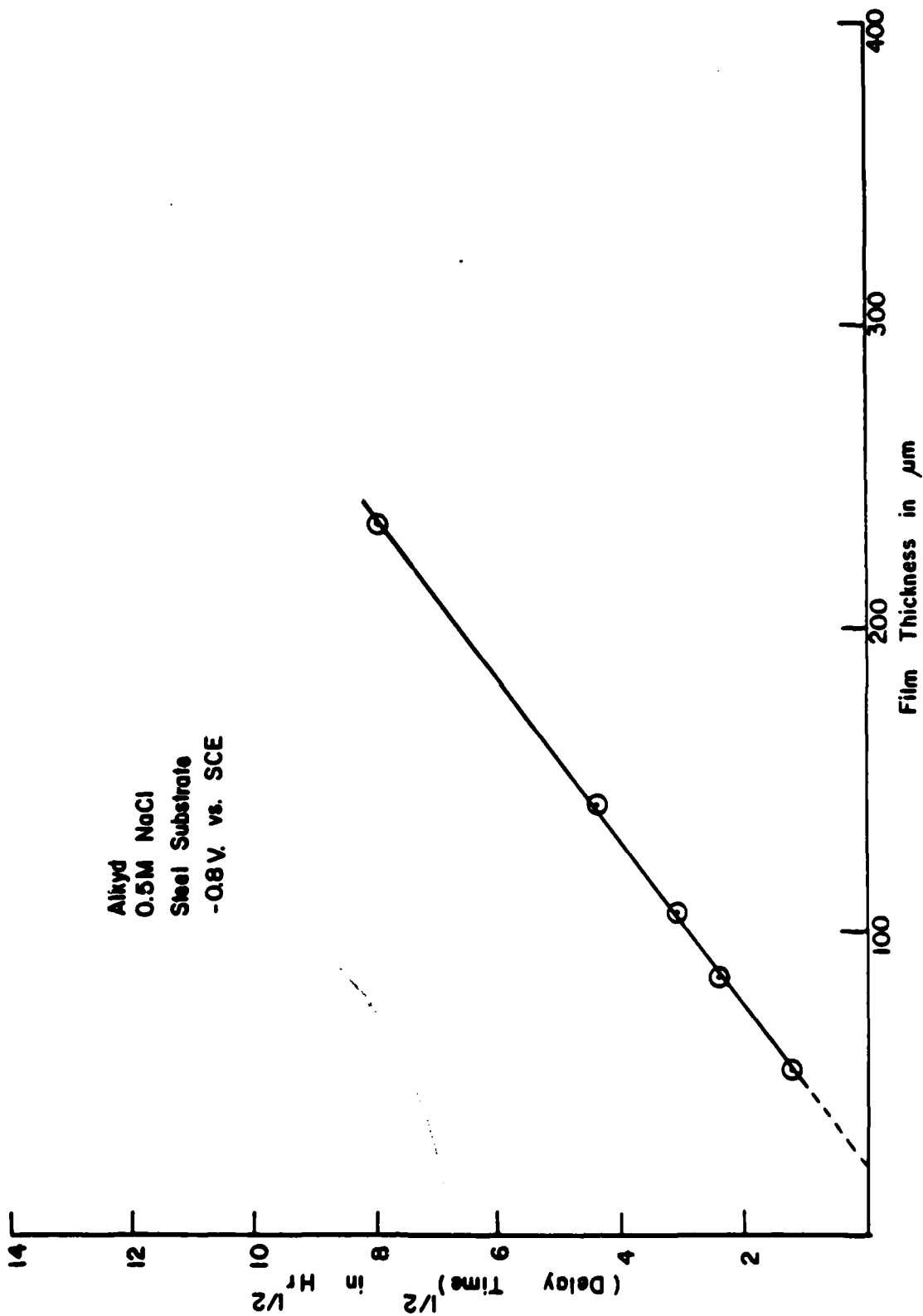


Figure 8. The relationship between the delay time (see text) and the film thickness in the case of alkyd coatings on steel polarized at -0.8 v in aerated 0.5M NaCl.

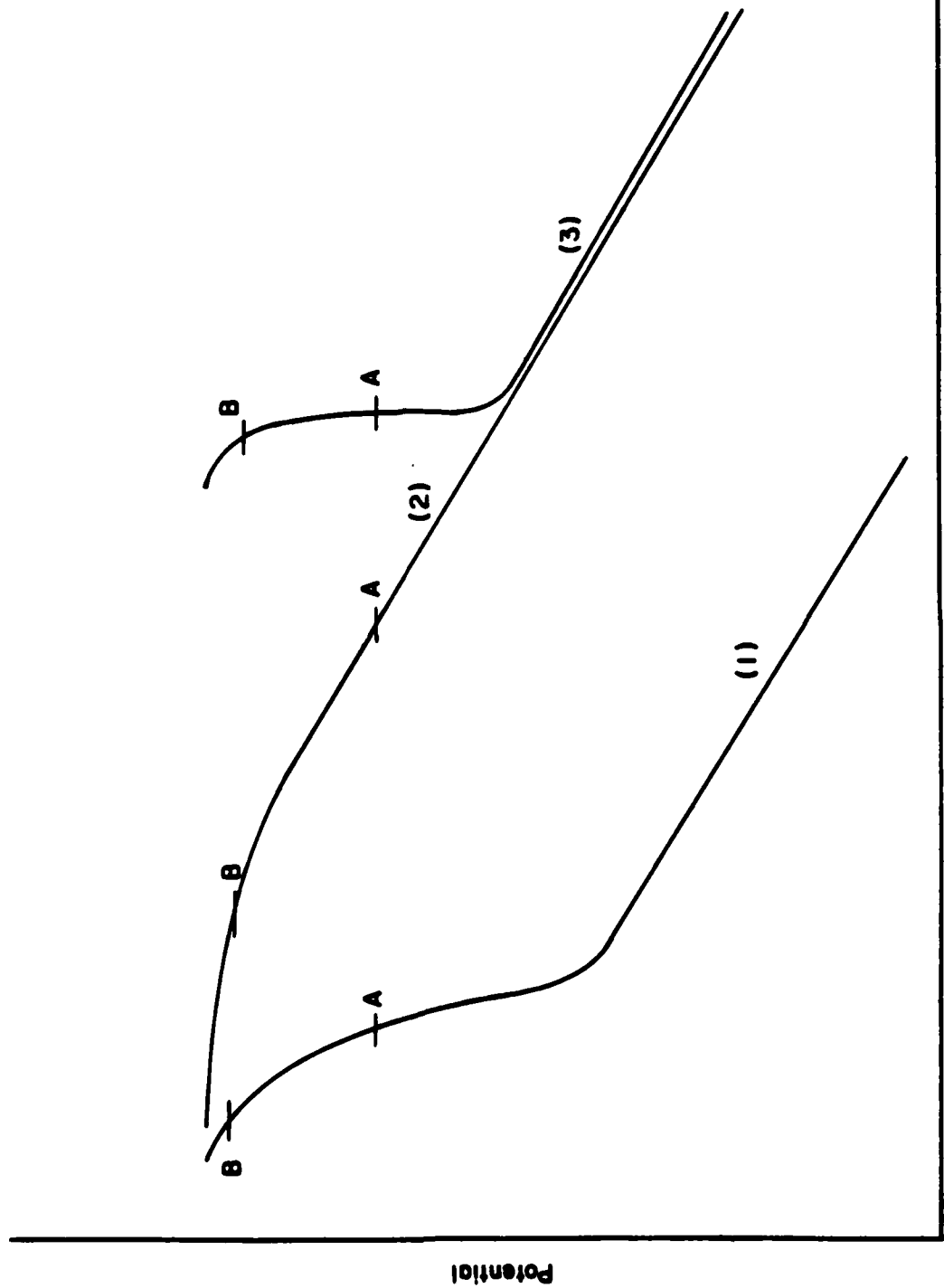


Figure 9. Three types of polarization curves observed on different metals in aerated 0.5M NaCl. Curve (1) is obtained with aluminum, curve (2) with tin, and curve (3) with steel.

cathodic treatment has been studied. Point A on each curve represents the potential at the defect and Point B represents the assumed potential at the delaminating front. Curve (1) has the shape of the polarization curve of aluminum in 0.5M NaCl. The surface is not active for the oxygen reduction reaction and the rate of delamination is low as indicated by the location of Point B. Curve (2) is a hypothetical curve somewhat comparable to the polarization curve for tin in 0.5M NaCl. The curve has a steep slope such that the current density falls off greatly with increase in potential. Thus the current density at the delaminating front is low. Curve (3) is typical of iron and copper in 0.5M NaCl. The oxygen reduction reaction is catalyzed over a wide potential region and the current density remains the same over a considerable potential range. Cathodic delamination occurs at a relatively rapid rate because the current density at Point B is high relative to comparable points on curves (1) and (2).

The effect of the nature of the polarization curve on the delamination rate is shown clearly in the case of thin polybutadiene coatings on copper, steel, and tin substrates. Copper and steel show very similar polarization curves in 0.5M NaCl open to the air [17], and the delamination rate is  $0.016 \text{ cm}^2/\text{hr}$  in the case of copper and  $0.02 \text{ cm}^2/\text{hr}$  in the case of steel when the cathode potential is -0.8 v. The rate of delamination of the polybutadiene coating on tin, on the other hand, is very low at the same potential. This fact is understandable in terms of the idealized polarization curve for tin shown in Figure 9. The current density at this potential is approximately an order of magnitude less and the current density falls off exponentially as the potential decreases radially from the defect. The current at the delaminating front is thus much less in the case of tin than in the cases of copper and steel and the delamination rate is much less.

Catalytic Activity of Surface for Cathodic Reaction. The shapes of the cathodic polarization curves for copper and steel in air-saturated 0.5M NaCl indicate that the cathodic reaction at -0.8 v. is limited by a diffusion process—the rate at which oxygen can reach the electrode surface. At a potential of -0.8 v. it is thus not possible to increase the rate of the reaction by increasing the catalytic activity of the substrate since the maximum rate is limited by oxygen diffusion to the interface. We have been forced, therefore, to concentrate attention on catalytic deactivation of the surface.

Several pieces of evidence are already available that show that the rate of delamination from a surface that has low catalytic activity is indeed low:

(1) As discussed earlier, delamination at potentials several hundred mv. cathodic to the corrosion potentials from both aluminum and tin surfaces is a result of the low activity

of these surfaces at this potential.

(2) Zinc surfaces inactivated by pretreatment in a cobalt-containing solution show lower delamination rates than untreated surfaces [12]. This behavior is explicable in terms of the lower cathodic activity [24].

(3) Surfaces that have been phosphated show low rates of delamination [10]. This result is in accord with the lowered activity of phosphated surfaces for oxygen reduction [25].

Thus the rate of delamination can be decreased by inactivating the surface so that it is ineffective in catalyzing the oxygen reduction reaction.

Effect of Temperature. Data have previously been presented [13] on the effect of temperature on the cathodic delamination of polybutadiene coatings on a galvanized steel substrate immersed in 0.5M NaCl. These data yielded an activation energy for the delamination process of 9,500 cals/mole. Unfortunately, the available data are not sufficient for use in determining the rate-controlling step. The value is in the high range for the diffusion of counterions in ion exchange polymers [26], it is considerably higher than the value for the diffusion of NaCl in aqueous solution, 4100 cal/mole [27] and is lower than the value of 17,000 cal/mole [28] obtained for ionic conductivity in cellulose acetate which had been soaked in 0.1M NaCl. The only conclusion possible at the present time is that the value of 9,500 cal/mole is consistent with a rate controlling step that involves diffusion.

How to Minimize Cathodic Delamination. Many commercial painted metals are specially processed to minimize cathodic delamination. The metal surface is modified chemically by a process known colloquially as "pretreatment". These pretreatments are characteristically based on phosphates, silicates and chromates, and major companies have developed around proprietary processes that have received wide utilization. Most of the processes have been discovered empirically and changes in the process with time have been largely incremental rather than revolutionary. Environmental pressures, cost pressures, and raw materials availability are necessitating changes in pretreatment formulas and entirely new systems are needed. The purpose of the following comments is to outline the characteristics of the interfacial region at the organic coating/substrate boundary that will withstand cathodic delamination. Five characteristics are selected for discussion.

(1) No bare metal, or superficially oxidized metal, should be present at the coating/substrate interface. Slightly oxidized metals such as copper, zinc and steel are good catalysts

for the oxygen reduction reaction. Since the destructive component in the delamination process is the hydroxyl ion, the rate of formation of hydroxyls should be minimized. Any layer at the metal surface should completely cover the metal.

(2) There should exist at the coating/substrate interface a layer which is a very poor conductor of electrons. Electrons for the cathodic reaction are furnished either by an external power supply or by the anodic half of the corrosion reaction. If the electron supply to the interface can be minimized, the reaction rate will be reduced. A non-metallic interfacial layer with poor electron conductive properties is desirable.

(3) The interfacial layer at the coating/substrate interface should be a poor catalyst for the cathodic reaction. The two common cathodic reactions,  $H_2O + 1/2O_2 + 2e^- = 2OH^-$  and  $2H^+ + 2e^- = H_2$ , are both catalyzed reactions that do not occur readily in the absence of a solid. The first reaction occurs most easily on oxidized metals and the latter reaction most easily on bare metal surfaces. Both reactions result in a local increase in pH and both play a role in cathodic delamination. The relative importance of each reaction is dependent upon the potential as well as the nature of the surface.

The interfacial layer should have a chemical nature such that it is inactive catalytically for both the above reactions. Hydroxyl ion generation will not occur if the surface is inactive.

(4) The boundary between the substrate and the coating should be rough. It is standard practice to improve substrate/organic coating adherence by roughening the surface, either by abrasive or chemical attack or by the formation of a reaction product which has a high surface area. A rough surface, however, has another good characteristic to reduce cathodic delamination. It provides a tortuous path for the diffusion of cations to the site of the hydroxyl ion generation. The essential ingredients for the oxygen reduction reaction are (a) water, (b) oxygen, (c) electrons, (d) a catalytically active surface, and (e) cations to provide local charge balance for the hydroxyl ions. It has been shown herein that cathodic delamination in NaCl solution occurs as a consequence of lateral diffusion of sodium cations beneath the coating. Any surface structure that lengthens the path for cation diffusion or makes more difficult the migration of cations to sites of possible hydroxyl ion generation will reduce the rate of the oxygen reduction reaction.

(5) The interfacial region should be resistant to alkaline attack. The delamination process occurs as a consequence of the attack on the surface of the metal and/or the organic coating at the interface. Both components of the interfacial region are probably attacked and which occurs at the faster

rate is a function of the particular system. The ideal interfacial region will include an alkali-resistant coating on the metal and an organic material that is very resistant to hydrolysis or other type of attack by aqueous alkali.

#### REFERENCES

- [1] U. R. Evans, Trans. Electrochem. Soc. 55, 243 (1929).
- [2] W. A. Anderson, Off. Dig. 36, 1210 (1964).
- [3] R. R. Wiggle, A. G. Smith, and J. V. Petrocelli, J. Paint Tech. 40, 174 (1968).
- [4] ASTM Standard G8-72, Annual Book of ASTM Standards 27, 869 (1979).
- [5] ASTM Standard B117-73, Annual Book of ASTM Standards 27, 1, (1979).
- [6] H. Leidheiser, Jr. and M. W. Kendig, Corrosion 32, 69 (1976).
- [7] M. W. Kendig and H. Leidheiser, Jr., J. Electrochem. Soc. 123, 982 (1976).
- [8] H. Leidheiser, Jr. and M. W. Kendig, Ind. Eng. Chem. Prod. Res. Dev. 17, 54 (1978).
- [9] H. Leidheiser, Jr., Croat. Chem. Acta 53, 197 (1980).
- [10] H. Leidheiser, Jr. and W. Wang, J. Coatings Technol. 53, No. 672, 77 (1981).
- [11] R. A. Iezzi and H. Leidheiser, Jr., Corrosion 37, 28 (1981).
- [12] H. Leidheiser, Jr., Ind. Eng. Chem. Prod. Res. Dev. 20, 547 (1981).
- [13] W. Wang and H. Leidheiser, Jr., Proc. Intern. Conf. on Corrosion Control by Organic Coatings, H. Leidheiser, Jr., Editor, Natl. Assocn. Corrosion Engrs., Houston, Texas (1981).
- [14] R. A. Dickie, J. S. Hammond and J. W. Holubka, Ind. Eng. Chem. Prod. Res. Dev. 20, 339 (1981).
- [15] R. A. Dickie and A. G. Smith, Chem. Tech., January 1980, p.31.

- [16] J. Ritter, Proc. Intern. Conf. on Corrosion Control by Organic Coatings, H. Leidheiser, Jr., Editor, Natl. Assocn. Corrosion Engrs., Houston, Texas (1981).
- [17] H. Leidheiser, Jr., L. Igetoft, W. Wang, and K. Weber, Proc. 7th Intern. Conf. on Organic Coatings, Athens, Greece (1981).
- [18] J. Ritter, personal communication, June 1981.
- [19] J. S. Hammond, J. W. Holubka and R. A. Dickie, J. Coatings Technol. 51, No. 655, 45 (1979).
- [20] R. A. Dickie, paper presented at Natl. Assocn. Corrosion Engrs. Meeting, Minneapolis, May 1981.
- [21] M. Pourbaix, "Atlas of Electrochemical Equilibria in Aqueous Solutions", Pergamon Press, London, 1966, 644pp.
- [22] R. T. Ruggeri and T. R. Beck, "A Model for Mass Transport in Paint Films" in Corrosion Control by Coatings, H. Leidheiser, Jr., Editor, Science Press, Princeton, N.J., 1979, pp.455-61.
- [23] J. D. Murray, J. Oil Col. Chem. Assoc. 56, 507 (1973).
- [24] H. Leidheiser, Jr. and I. Suzuki, J. Electrochem. Soc. 128, 242 (1981).
- [25] R. W. Zurilla, "Important Correlations Arising from the Scribe Test for Appraising Paint/Pretreatment/Substrate Systems" in Corrosion Control by Coatings, H. Leidheiser, Jr., Editor, Science Press, Princeton, N.J., 1979, pp. 243-58.
- [26] H. J. V. Tyrrell, "Diffusion and Heat Flow in Liquids", Butterworths, London, 329 pp., (1961).
- [27] D. G. Gillam, Australian J. Sci. Research 4A, 84 (1951).
- [28] J. Crank and G. S. Park, "Diffusion in Polymers", Academic Press, New York, 452 pp., (1968).

**Program #2. Corrosion Control by Inhibition of the  
Cathodic, Oxygen-Reduction Reaction**

It has been proposed previously that the corrosion rate of zinc may be reduced by decreasing the activity of the surface for the cathodic reaction [1]. This proposal was followed by observations that indicated that predipping zinc in dilute solutions of Co(II) or Ni(II) salts decreased the catalytic activity of the zinc surface for the cathodic reaction in aerated NaCl solution [2]. A lower rate of corrosion resulted. We report herein another example of substantial inhibition of the cathodic reaction on zinc using a chromate pretreatment followed by cathodic treatment in NaCl solution at -1.6 v vs SCE.

Commercial samples of galvanized steel were used. No significant differences in behavior were observed among different lots of galvanized steel that were used for comparative purposes in some experiments. All measurements reported herein were made in 3% sodium chloride solution adjusted to pH 5.4 and exposed to air. The counterelectrode was graphite and it was maintained in a vessel separated from the measurement cell by a fritted glass disc. The pH of the liquid in the measurement cell increased to the order of 7-10 during the experiments but independent experiments carried out in this pH range indicated that pH was not a major variable in the interpretation of results. Polarization measurements were carried out using a PAR 350 Corrosion Console and a standard cell assembly. The electrodes were in the form of rectangular pieces, the edges, backside, and contacting wire of which were coated with an epoxy cement. The exposed surface area of zinc was 2.25 cm<sup>2</sup>.

Samples were abrasively polished with aluminum oxide, edge coated with the epoxy, and then exposed in a 10% solution of a proprietary chromating solution known as Granodine® 90 at pH 1.5 for 60 seconds. The pretreated samples were washed with distilled water and immediately immersed in 3% NaCl solution and allowed to stand for 10 min before the polarization was initiated.

A typical set of experiments is summarized in Figure 1. The first cathodic scan yielded a higher cathodic current density than obtained on zinc not pretreated in Granodine® [1], suggestive of the fact that some species on the surface was consuming electrons. The peaks between -1.2 and -1.3 v on the negative-direction scans are probably due to the reduction of zinc oxide, as per prior observation [1]. The scan direction was reversed at -1.6 v and the lower catalytic activity of the reduced surface was noted up to a potential of -1.28 v. At potentials less negative than -1.28 v, the zinc surface behaved anodically and

---

® - Registered Trademark, Amchem Products, Inc.

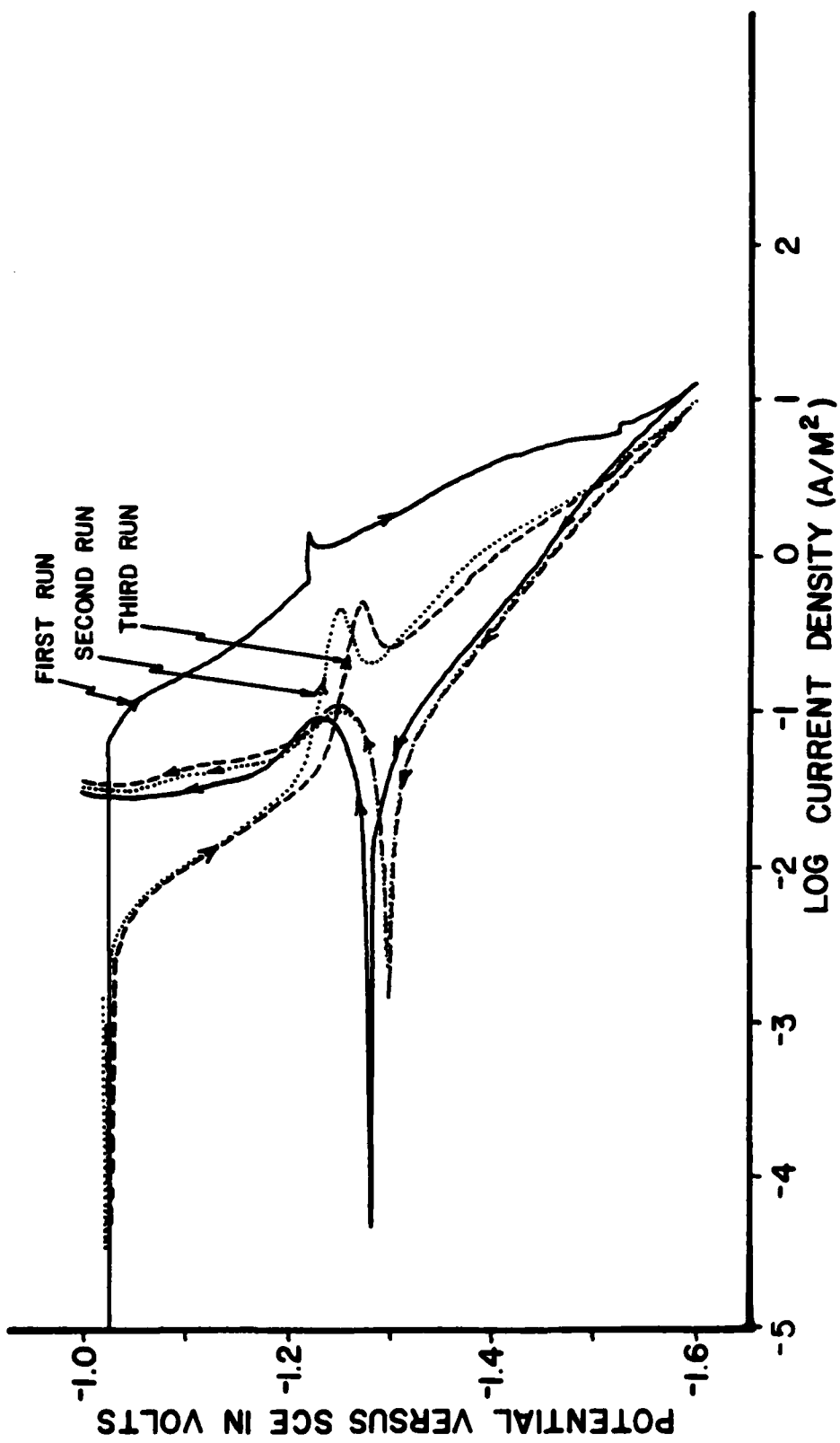


Figure 1. Cathodic polarization in aerated 3% NaCl solution of zinc pre-treated in a chromating solution. The second and third runs were carried out 10 min after the completion of the previous run. Scan speed 1 mv/sec. See text for details of experiment.

an oxide presumably formed on the surface. The potential control was terminated at -1.1 v and the specimen was allowed to remain in the NaCl solution for 10 min, during which time the corrosion potential drifted from -1.1 v to -1.0 v. A second potential scan in the cathodic direction was initiated and it will be noted that the activity of the surface was decreased one order of magnitude in the vicinity of the corrosion potential. The prior cathodic treatment greatly decreased the cathodic activity of the zinc surface.

Repeated experiments of the same type yielded curves essentially the same as that for the second scan so long as the sample remained in the NaCl solution for no more than 20 min after the applied potential was removed. Longer exposure times caused the cathodic curve to move to higher current values until after several hr of exposure, the curve was essentially identical to the first scan.

Experiments of the similar type carried out in 3% NaCl without pretreatment in the Granodine® solution yielded curves such as those shown in Figure 2. The cathodic activity of the zinc surface was approximately the same before and after cathodic polarization at -1.6 v, and up to 1 order of magnitude higher than that observed for the second and third runs in Figure 1.

Unsuccessful attempts were made to understand the chemistry of the zinc surface before and after cathodic treatment at -1.6 v using surface analysis techniques. The elemental composition, largely chromium, zinc and oxygen, was readily determined but no correlation between composition or valence state and catalytic activity was extractable from the data. It is our impression that exposure of the sample to air and to washing prior to insertion into the spectrometer yielded a steady-state condition, reflective of the observation that the cathodic polarization curves obtained after long exposure to the NaCl solution were similar.

Attempts were made without complete success to duplicate the behavior of the proprietary solution using standard chromate solutions. Since our objective was to pursue the concept of cathodic inhibition of zinc, rather than the development of an improved pretreatment solution, we felt it unnecessary to develop a formula which could be published.

In summary, a zinc surface pretreated in a commercial chromating solution exhibits low catalytic activity for the cathodic reaction in 3% NaCl solution after electrolytic reduction at -1.6 v. A higher catalytic activity is regenerated after exposure of the surface to aerated NaCl solution for times in excess of 10 min. These experiments provide additional support for the view that corrosion control of zinc is possible by appropriate control of the composition of the zinc surface with consequent control of the kinetics of the cathodic reaction. It is interesting to point out that commercial electrogalvanized steels

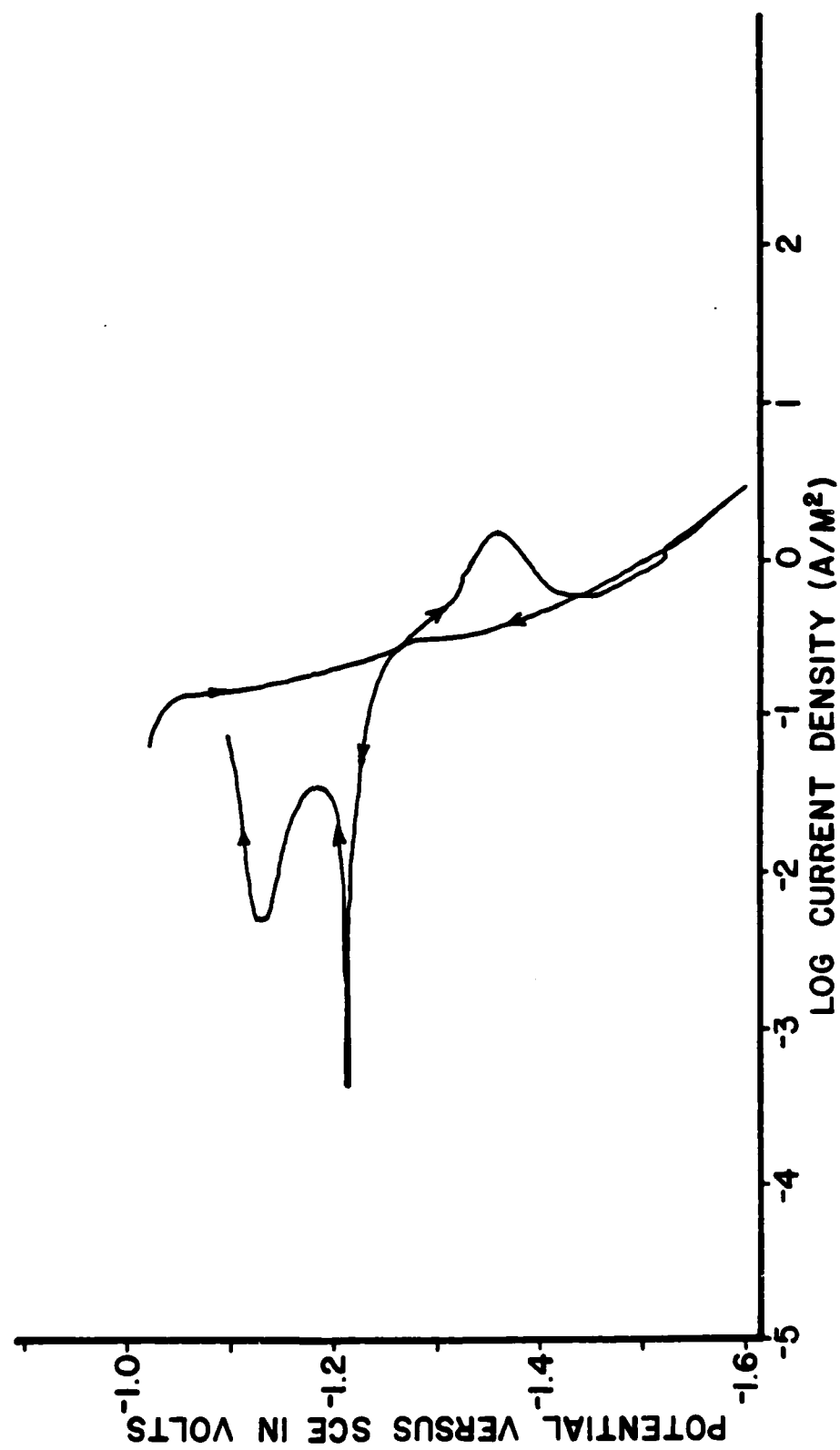


Figure 2. Cathodic polarization of zinc in aerated 3% NaCl solution.  
Compare with Figure 1.

with claimed higher corrosion resistance include chromium as an alloying agent [3].

#### REFERENCES

- [1] H. Leidheiser, Jr. and I. Suzuki, Corrosion 36, 601 (1980).
- [2] H. Leidheiser, Jr. and I. Suzuki, J. Electrochem. Soc. 128, 242 (1981).
- [3] T. Adaniya, Sheet Metal. Ind. 55, 73 (1978).

Program #3. Optical Studies of Corrosion  
under Organic Coatings

This section is based primarily on work performed by the senior investigator while on leave from Lehigh at the Building Materials Group of the National Bureau of Standards, August 1980 to July 1981.

Experimental Method and Initial Results

Light microscopy has received limited use in the study of blistering and corrosion under organic coatings [1-3], but the new method described here permits direct and continuous observation of these processes.

A simple corrosion apparatus has been constructed that operates on the stage of a light microscope. The corrosion test cell is shown schematically in Figure 1. It consists of a 10 mm diameter cell formed from a 3 mm thick layer of silicone rubber placed on a coated steel specimen. Aerated water or salt solution flows through the cell at a rate of 0.1 to 0.2 ml/min, through an inlet and outlet of hypodermic tubing molded into the cell. The cell volume is about 0.2 ml, so this flow rate is slow enough to give smooth flow but it is sufficient to supply a large excess of the dissolved oxygen required for corrosion. The cell is enclosed by a microscope cover glass.

The specimens are observed continuously in a metallurgical (reflected light) microscope by a 10X objective lens with a working distance of 7.6 mm, which provides ample space for the test cell. Glare from the several reflecting surfaces present is overcome by using polarized illumination and an analyzer set 15 to 20° from the crossed position. Observation with completely crossed polars is also helpful in revealing some of the corrosion phenomena. Photography was eventually automated to obtain pairs of 35 mm color slides, bright and dark (crossed polars), at time intervals of one to several hours. Tests typically were carried out for two to four days, often followed by continued exposure to near-100% relative humidity.

Specimens were prepared from cold-rolled, low-carbon steel. The surface was wet ground through 600-grit abrasive paper, washed thoroughly in acetone, distilled water, and ethanol, and then warm-air dried. Polybutadiene was selected as a coating because it is moderately permeable to both water and oxygen [4]. The material used, DuPont's Budium RK 662, was applied by a draw bar or wire-wound rod and then cured at 200°C for 25 min in a

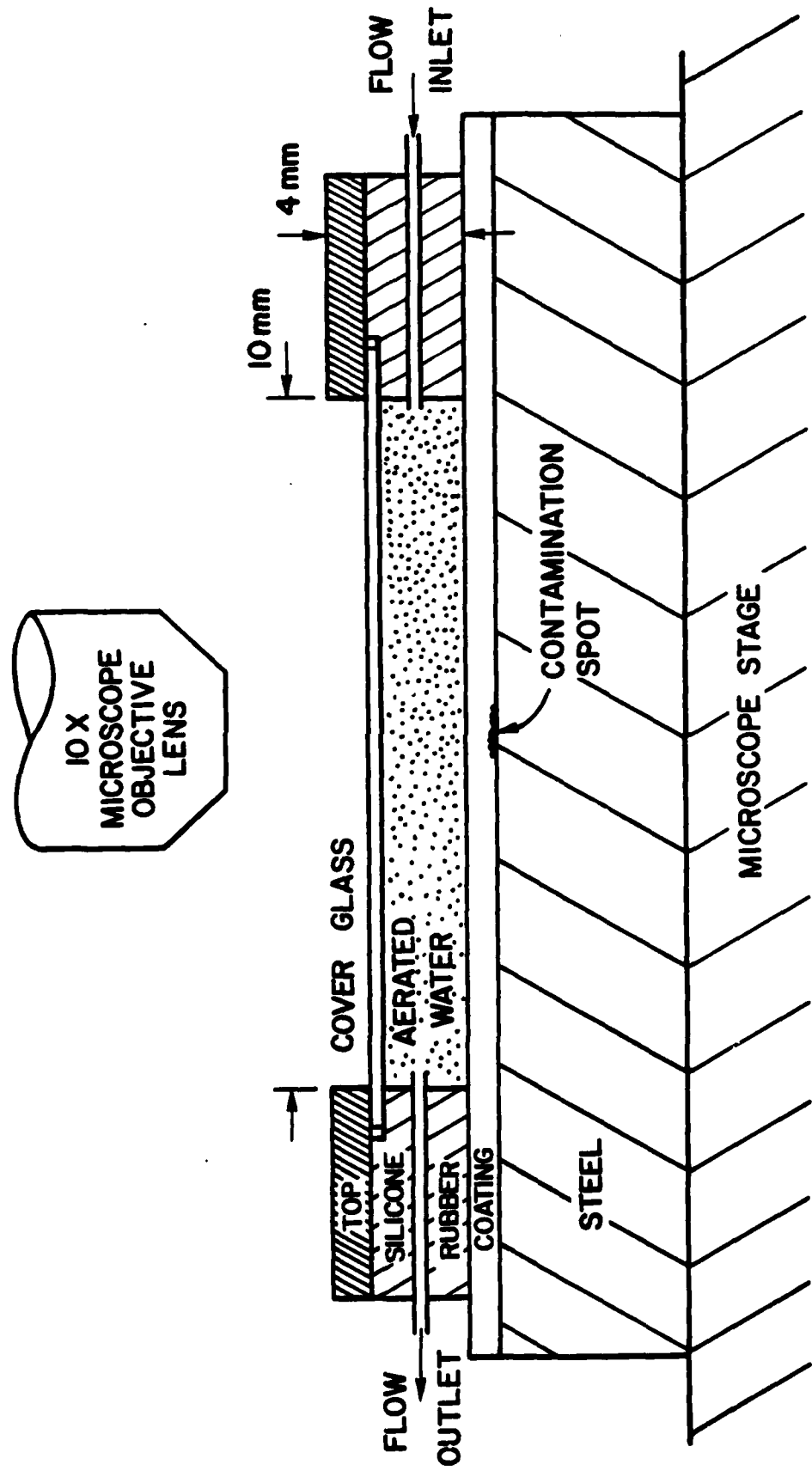


Figure 1. Schematic diagram of corrosion test cell in light microscope.

circulating air oven, to dry thicknesses of about 15 to 30  $\mu\text{m}$ . The cured system is golden yellow in color, but otherwise transparent. Two types of "defects" were introduced in the coated specimens. First, a salt contamination spot was placed on the steel before coating, by drying of a 0.01  $\mu\text{l}$  drop of dilute  $\text{KHSO}_4$  solution to give a spot about 0.6 mm (600  $\mu\text{m}$ ) in diameter, with a calculated average thickness of 0.1  $\mu\text{m}$ . Second, contaminated coating areas were punctured with a needle to make a hole about 60  $\mu\text{m}$  in diameter.

The experimental observations are in general accord with the events included by Masters and Pommersheim in their initial mathematical modeling of corrosion under coatings [5]: permeation of water and oxygen through the coating to the steel, blister formation and growth, and the initiation of corrosion. Most of the observations are qualitative, although some measurements have been made and others will be possible in the future. An example of a simple measurement in the microscope is coating thickness. At high magnification, typically with a 40X objective lens, the depth of focus is small and one can focus successively on the steel surface and on the top surface of the coating (actually on microscopic dirt specks that unavoidably settle on the surface). The coating thickness is the difference in focal positions,  $\Delta h$ , multiplied by the refractive index,  $n$ , or  $t = n\Delta h$ . The refractive index was measured to be 1.549, significantly higher than the literature values of 1.515 to 1.526 [6], so the true thickness is 55% larger than the apparent thickness.

Observations will be described mainly for  $\text{KHSO}_4$  contamination spots under the polybutadiene coating, but similarities will be pointed out when the coating is punctured in an uncontaminated area. The "data" are mainly color micrographs, which cannot be readily reproduced here, so the schematic drawing of Figure 2 will aid in visualizing the results summarized in the following steps:

(1) In an environment of aerated distilled water, the contamination spot becomes visible within one hour. This is attributed to enhanced image contrast from refractive index gradients during transient water permeation. The equilibrium solubility of water in the coating is probably less than 2% [7,8].

(2) Within 2 to 3 hours, areas delineated by optical interference rings appear in an annulus around the contamination spot. Typical diameters of these areas are 80 to 200  $\mu\text{m}$ , and they slowly increase in size, often merging to form larger areas. Subsequent observations suggest that these areas result from the beginning of the cathodic reaction as part of a localized electrochemical corrosion cell.

(3) Within several hours, crossed polars show slight but definite changes in the contamination spot, usually in one or two rounded areas that are 100 to 300  $\mu\text{m}$  in diameter. These develop gradually into prominent blue spots that are the anodes

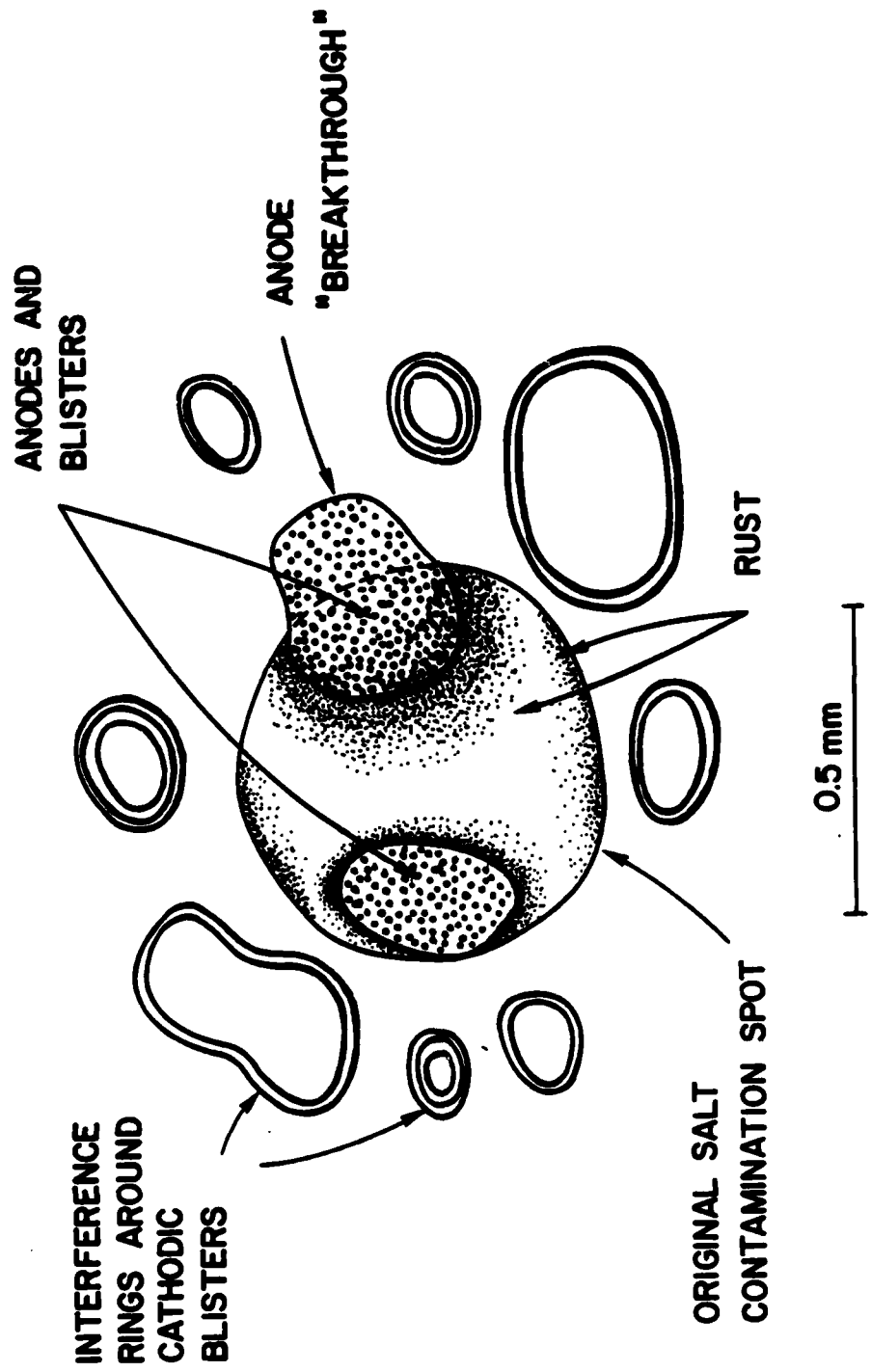


Figure 2. Schematic representation of corrosion at salt contamination spot.

in the electrochemical cell, similar to the appearance of the moving anode in filiform corrosion [9-12].

(4) The anodes develop perceptible depth, which becomes readily recognizable as a blister by about 50 hours. The anodes and blisters are in fact coincident and result from solution of the contaminant in water that has permeated. This creates an osmotic gradient that drives water into the blister and makes it grow. At present, blister height can be measured accurately only after removal of the specimen from the test cell, after 50 to 100 hours. A typical height is 10  $\mu\text{m}$  (about half the coating thickness). The liquid volume in a blister is then calculated to be about 0.0002  $\mu\text{l}$ , which is approximately the quantity required to dissolve all the  $\text{KHSO}_4$  under the blister. Thus, in its early development the blister contains a saturated solution of  $\text{KHSO}_4$ , which is acidic and readily dissolves the anodic product  $\text{Fe}^{++}$ .

(5) There is often a "breakthrough" of the anode outside the original contamination spot, enlarging the anode and the area of the blister. The breakthrough may be caused by two factors: osmotic pressure in the blister, and the tendency of the adjacent cathodic reactions to break the bond at the coating-steel interface (cathodic delamination) [4]. With prolonged exposure to high humidity after the conclusion of the test in the microscope, repeated breakthroughs occur, thus spreading the corrosion.

(6) Iron oxides gradually form, at the periphery of the original contamination spot or immediately around an anode. Oxide formation results from the proximity of the anodic and cathodic reaction products, and the precipitation of hydrated oxides when they meet. The "rust" that is formed is often a striking yellow or red color but is readily observed only when glare is eliminated completely by crossed polars.

(7) The corrosion processes described above proceed very slowly after about 25 hours. The slow rate is probably a consequence of the fact that the cathodic reaction is rate controlling because of the limited amount of oxygen permeating the coating and because the  $\text{OH}^-$  concentration rapidly builds up except where iron oxides can form. The importance of oxygen was demonstrated qualitatively by a test in which the water was saturated with oxygen; anodic action and rust formation were about twice as fast as with air. In another test the water was saturated with nitrogen, largely excluding oxygen; blisters formed as usual, but anodic action was greatly diminished.

(8) When a specimen is tested in aerated  $\text{NaCl}$  solution (0.1 molar), the phenomena are similar to those described already, but faster. This increased rate is attributed to the availability of sodium cations that permeate the coating and act as counter ions for the  $\text{OH}^-$  ions produced at the cathodes.

The explanation remains to be verified by microanalysis on coatings stripped after the test, but the mechanism has been found in other cathodic delamination experiments [13].

(9) When a coating is punctured and then tested in NaCl solution, the bare steel exposed at the puncture is immediately anodic. Cathodic areas develop quickly around the puncture and rust forms (Fig. 3). Within 20 hours, however, anodic action spreads adjacent to the puncture, apparently where some cathodic areas shift to become anodic. A growing annulus of cathodic delamination is apparent, but cathodic blisters with heights of a few  $\mu\text{m}$  continue to exist within the annulus. After the test, the coating can be easily stripped from the anodic and surrounding cathodic areas.

(10) All of the processes described above are localized and take place entirely under the coating, which remains intact. Elsewhere the coating and steel appear unaffected, although the coating must become saturated with water and oxygen. Eventually corrosion is noticed at some additional sites, for reasons that are not yet known.

#### Further Research

Preparations are underway for detailed study of cathodic delamination by light microscopy supplemented by SEM, EDX, and other techniques. The corrosion test cell will be modified to protect the steel cathodically, either by contact with an active zinc anode or by an applied potential. The anodic oxidation of the steel will thereby be suppressed, and the light microscopy will be concentrated on observation and measurement of the cathodic process.

Exploratory EDX analysis on coatings taken from other cathodic delamination tests on this project show that ions from the electrolyte can be detected in the coating at or near the coating-steel interface. In the new experiments, detailed correlation should be possible with the position of the delamination front, by stripping the coating at various positions as observed by light microscopy. Various electrolytes will be used as in previous experiments [4], such as LiCl, NaCl, KCl and CsCl.

A problem in the interpretation of the mechanism of cathodic delamination is that ions may reach the delaminating front either by diffusion through the coating or by migration along the delaminated interface from the original coating defect. It may be possible to distinguish the operative mechanism with substrate salt contamination as reported in the previous section. For example, if  $\text{KHSO}_4$  contamination is used and the electrolyte is a CsCl solution, EDX analysis should readily distinguish which cation is present at the delamination front.

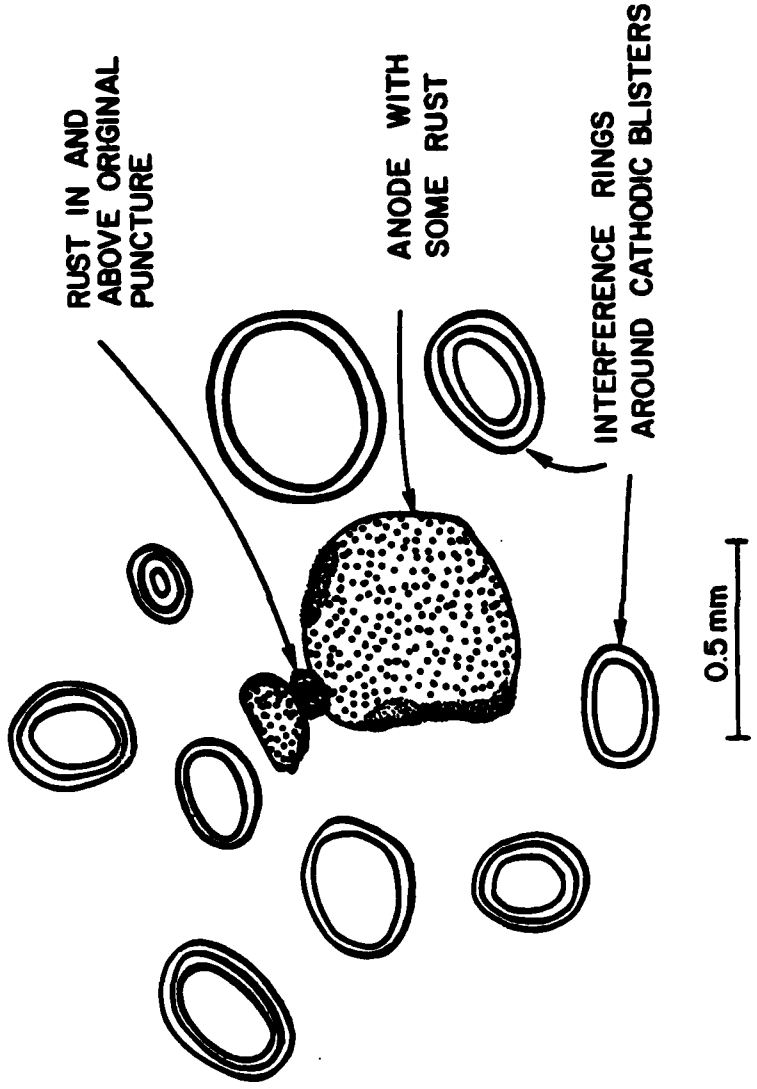


Figure 3. Schematic representation of corrosion at puncture.

Thus it appears that the microscopy method being developed here can contribute to clarifying the mechanism of the very important phenomenon of cathodic delamination.

#### REFERENCES

- [1] L. A. van der Meer-Lerk and P. M. Heertjes, J. Oil Col. Chem. Assoc. 58, 79 (1975).
- [2] L. A. van der Meer-Lerk and P. M. Heertjes, J. Oil Col. Chem. Assoc. 62, 256 (1979).
- [3] W. Funke, Progress in Organic Coatings 9, 29 (1981).
- [4] H. Leidheiser, Jr. and W. Wang, J. Coatings Tech. 53, 77 (1981).
- [5] L. Masters and J. Pommersheim, "Mathematical Models for Formation and Growth of Blisters on Protective Coatings", Preprint Volume, Second International Conference on the Durability of Building Materials and Components, September 1981.
- [6] Polymer Handbook, 2nd Edition, J. Brandrup and E. H. Immergut, Eds., p.V-3, John Wiley & Sons (1975).
- [7] H. Leidheiser, Jr. and M. W. Kendig, Corrosion 342, 69 (1976).
- [8] Solubility estimated to be 1.9% from the refractive index measured after equilibration with 100% relative humidity, 1.545, compared with dry polybutadiene, 1.549, and water, 1.333.
- [9] C. F. Sharman, Nature 153, 621 (May 20, 1944).
- [10] M. Van Loo, D. D. Laiderman, and R. R. Bruhn, Corrosion 9, 277 (1953).
- [11] W. H. Slabaugh and M. Grotheer, Ind. Eng. Chem. 46, 1014 (1954).
- [12] J. D. Sudbury, O. L. Riggs, and F. J. Radd, Materials Protection 1, 8 (1962).
- [13] J. E. Castle and J. F. Watts, "Cathodic Disbondment of Well Characterized Steel/Coating Interfaces", Preprint Volume, N.A.C.E. Conference on Corrosion Control by Organic Coatings, Lehigh University, August 1980.

## **Program #4. Electrical Properties of Organic Coatings and Relationship to Corrosion**

### **INTRODUCTION**

For years organic coatings have been used to protect metals from corrosive environments. The degree of protection provided by such coatings can be attributed to several factors: the permeability to environmental elements (oxygen, water, and ions), adhesion to the substrate, and the electrical resistance of the coating. Classical delamination tests give only a partial picture of the events leading up to localized coating failure and corrosion of the substrate. Recently several authors [1-4] have applied impedance techniques used on bare metals to coated systems in an attempt to achieve a more complete picture of the corrosion process.

We have recently reported on the development of an AC impedance probe [5] used to locate and investigate localized defects in polymer coatings on steel substrates. In the present work the goal is to use this probe to investigate the breakdown of these coatings and to develop predictive criteria for estimating the lifetime of an organic coating.

### **EXPERIMENTAL**

The instrumentation for this study has been described in a previous paper [5]. The AC probe described at that time has been revised to include glass wool rather than a platinum junction between the reference electrode and solution. This change gives better electrical contact and thus a more reproducible response.

Metal samples were conventional 1010 cold-rolled steel supplied by Bethlehem Steel. Auger analysis showed that composition of these panels varied significantly with 1st (23.1: 17.6% Fe, 29.1:44.0% C for first to second shipments). This difference affects coating adhesion properties and is thus noted. The surface was prepared by abrading with medium then fine silicon carbide after degreasing in trichloroethane. Panels were subsequently rinsed several times with distilled water followed by methanol.

Coating systems for this study included commercially available polybutadiene (Budium RK-662), a white alkyd paint (RUST-O-LEUM #7791), a green epoxy-polyamide primer system (Pro-Line Paint QPL No. 24441/114), and Shell Epon 1001-F Emerez 1511 epoxy-polyamide system. In addition, a yellow primer (RUST-O-LEUM #7773) was used with the alkyd paint to study the contribution to coating adhesion and electrical resistance. The alkyd and green epoxy systems were cured at room temperature for about one week per coating layer. Polybutadiene and Epon coating were first subjected to oven curing (200°C, 20 min; 100°C, 1 hr-shorter times for multiple layers) then one week at room temperature. To study the effect of cure-history on electrochemical resistance, the oven-exposure times for the later systems were varied. Coating thickness was varied by applying multiple layers of polymer while allowing for curing for subsequent layers.

Figure 1 shows a typical cell configuration. An AC potential of 2.5 mV was applied to the system, and the applied signal was monitored at the counter electrode (at the scanning amplifier output of the potentiostat). The DC was maintained at 0.00 v (potentiostated) unless otherwise noted in order to keep the DC current below 10  $\mu$ A. The electrolyte was 0.5M NaCl open to the air.

## RESULTS AND DISCUSSION

Figures 2 and 3 show typical impedance plots obtained for uncoated and coated metal samples. Two major differences can be seen. First, the addition of a coating causes an increase in the value of the imaginary component ( $Z''$ ) of the complex impedance. This increase is a result of addition of a capacitance by the coating. The second is the absence of negative  $Z''$  values in the coated system which has been attributed to the presence of a pseudo-inductance when the probe is in close proximity to the metal surface. When a coating breaks down, the impedance response of the system shifts towards that of bare metal. Thus by monitoring the impedance response of coated systems over periods of exposure to electrolyte solution we can characterize the processes leading to corrosion and perhaps predict failure.

Table I lists the coating systems studied and the corresponding delamination rates presently available. Figures 4-12 give the ratio of the imaginary and real components of the complex impedance ( $\tan \theta$ ) as a function of exposure time for some of the systems that were studied. Several distinct regions can be seen in the plots. It is generally accepted that diffusion from the coating is a major rate controlling step in the breakdown mechanism. To determine what processes these steps

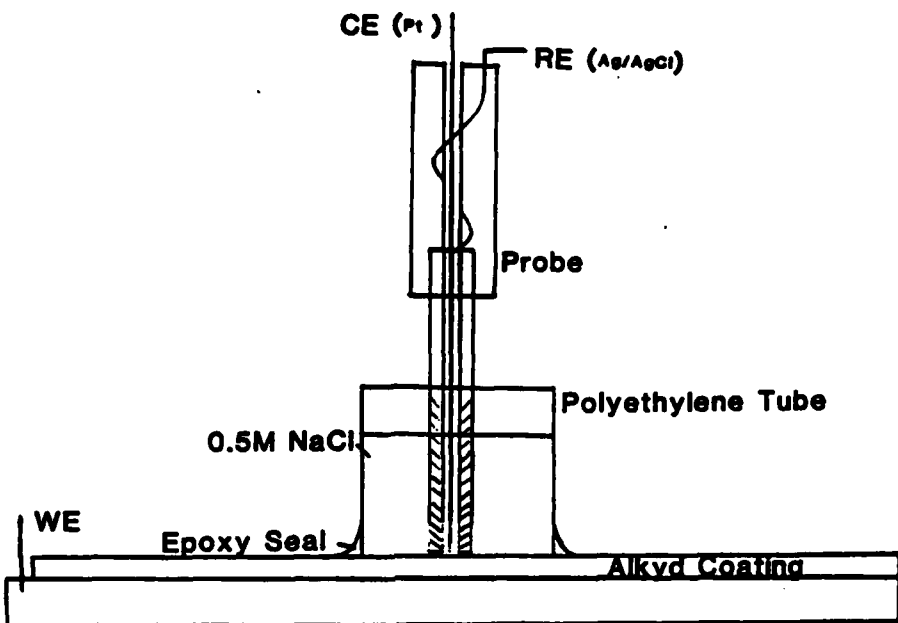


Figure 1. Sketch of measuring system and design of probe.

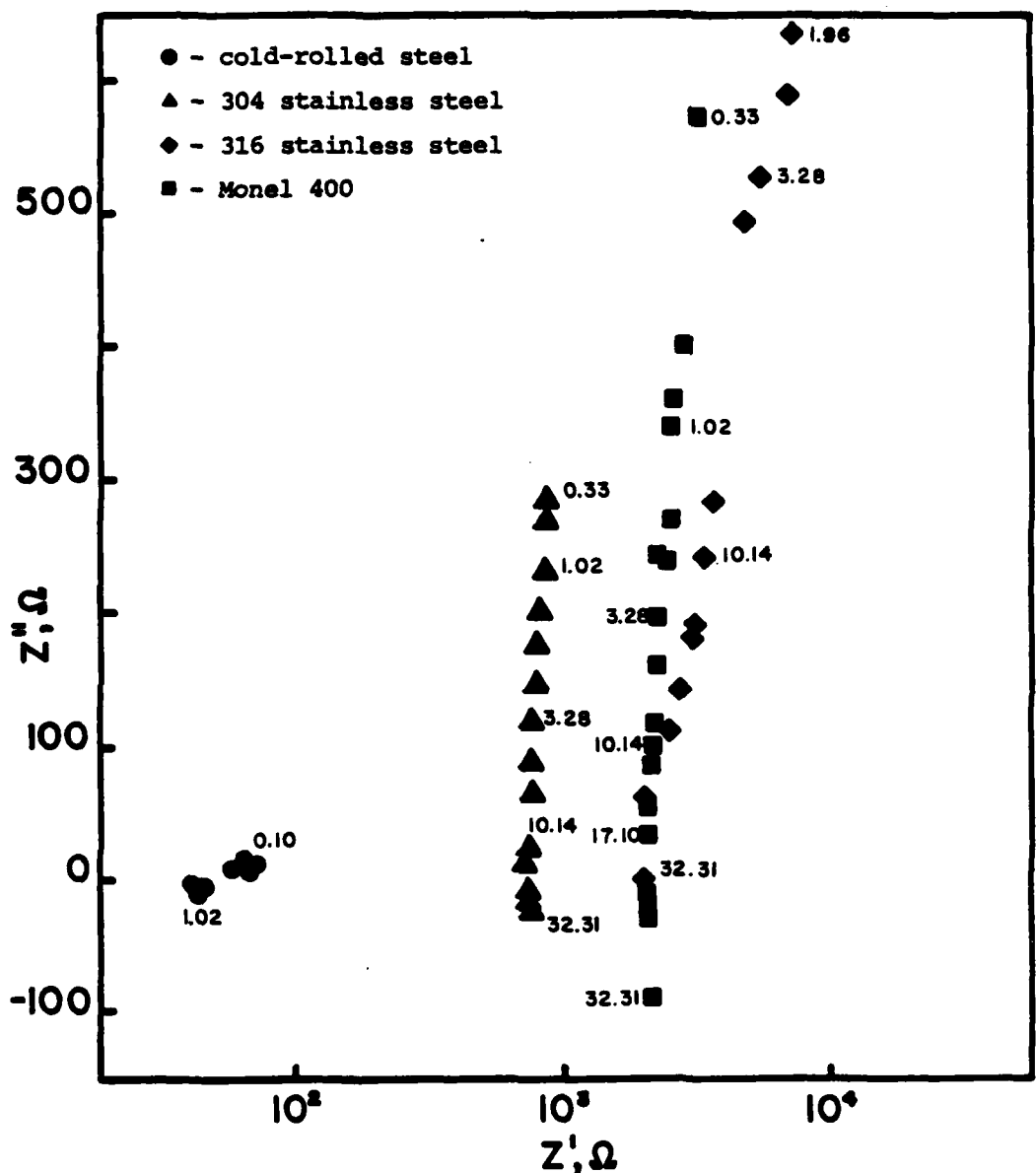


Figure 2. A.C. impedance of uncoated metal samples taken with the probe. Frequencies given in kHz.

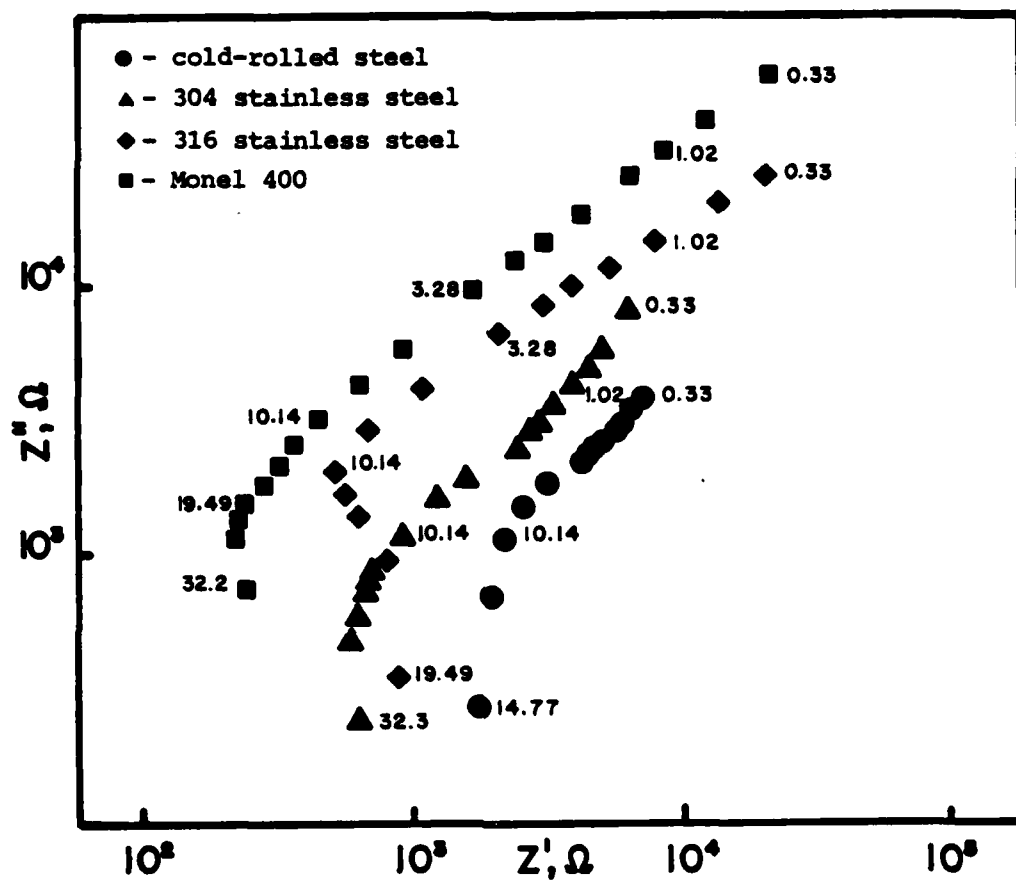


Figure 3. A.C. impedance of coated metal samples taken with the probe. Frequencies given in kHz.

Table I

Coating	Layers	Thickness ( $\mu\text{m}$ )	Time to Failure (Days)	*Delamination Rate ( $\text{mm}^2/\text{hr}$ )
Epon 1001-F/ Emerez 1511	1	15	0.11	(a)
	2	51	1.00	-
	3	51		-
	4	88		-
White Alkyd	1	13	17.85	17.60
	2	68	41.91	11.20
	3	76	52.87	2.01
	4	147	> 67	2.14
Alkyd Plus 2-Layer Primer	1	94	> 50 (b)	1.44
	2	107	"	1.18
	3	115	"	0.66
	4	122	"	1.23
Polybutadiene	1	9.0	> 20	1.51
	1	18.2	"	1.89
	2	29.2	"	0.49
	2	40.3	"	1.96
Green-Epoxy	1	36	> 30 (b)	--
	2	80	"	3.30
	3	107	"	5.49
	4	114	"	3.57
	5	115	"	3.10
Blasted- Surface	2	80	"	2.17
	4	124	"	2.07

\* Delamination rates determined by Lars Igetoft, Visiting Scientist. Measurements taken at -0.8 VDC.

(a) Unable to determine due to overall poor adhesion.

(b) Exposure continuing beyond this writing.

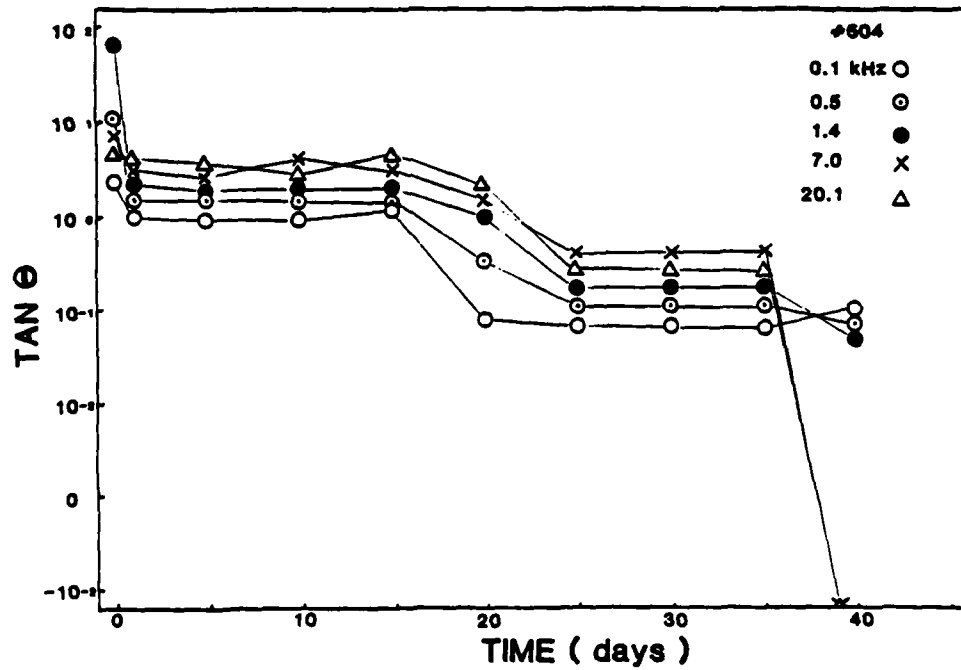
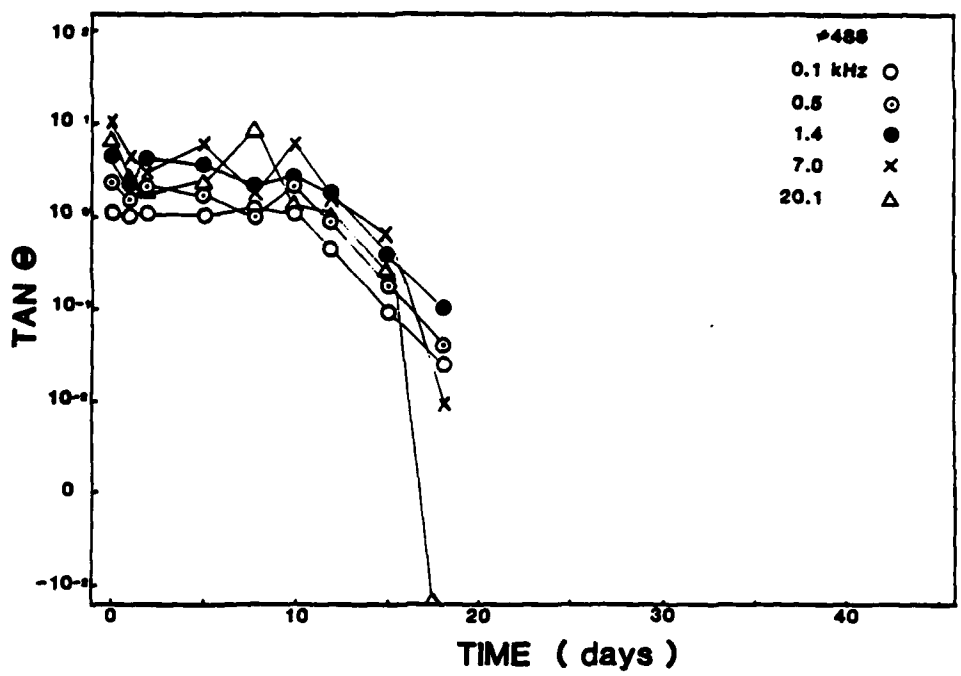
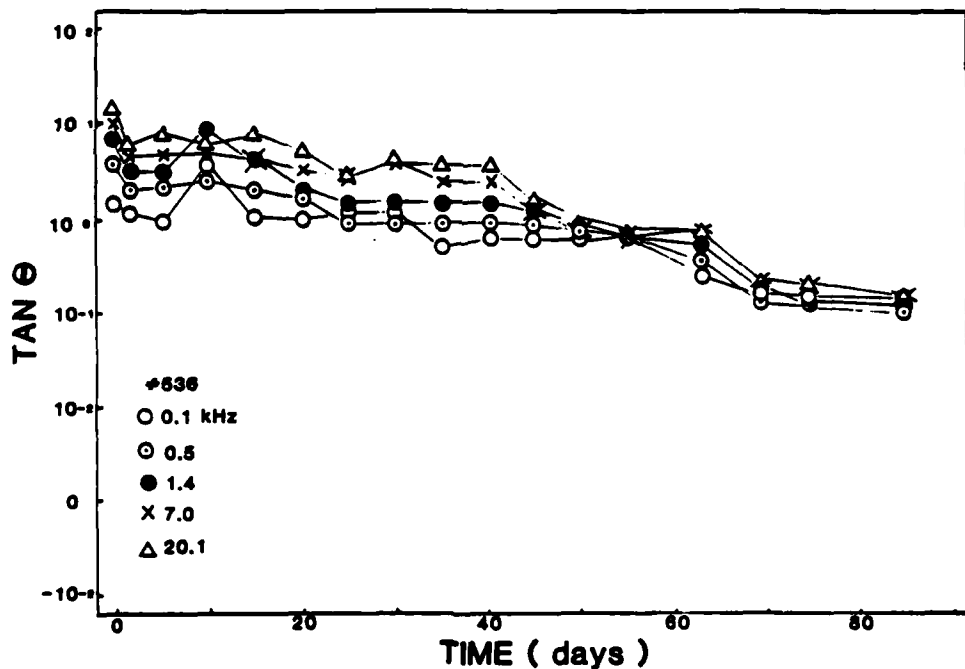
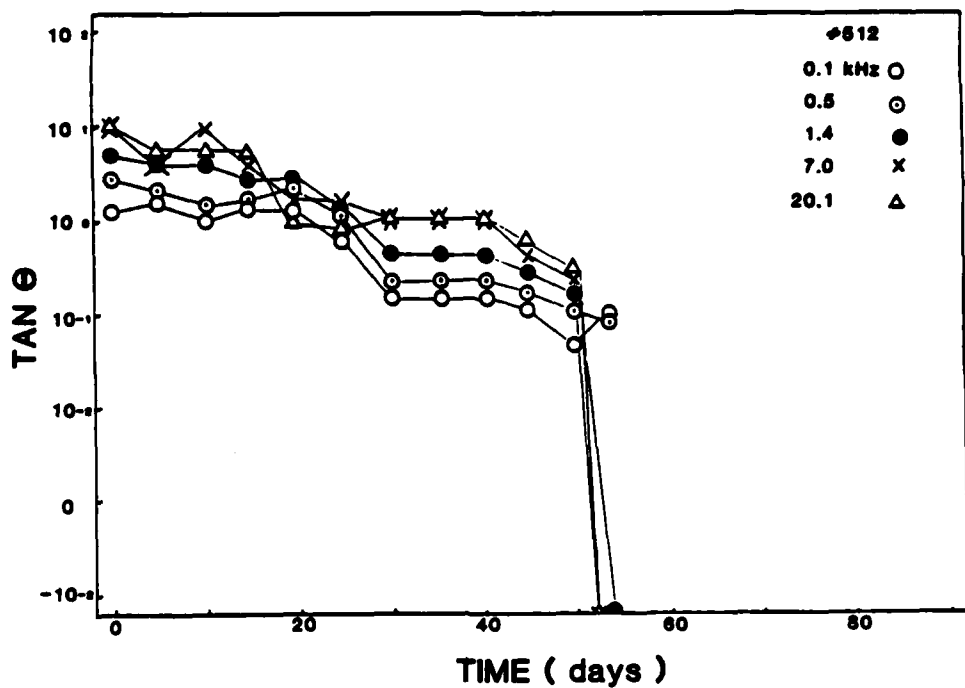


Figure 4. (Top) Tangent  $\theta$  vs. exposure time to aerated 0.5M NaCl for alkyd coating, 13  $\mu\text{m}$  thick, on steel.

Figure 5. (Bottom) Tangent  $\theta$  vs. exposure time to aerated 0.5M NaCl for alkyd coating, 68  $\mu\text{m}$  thick, on steel.



**Figure 6.** (Top) Tangent  $\theta$  vs. exposure time to aerated 0.5M NaCl for alkyd coating, 78  $\mu\text{m}$  thick, on steel.

**Figure 7.** (Bottom) Tangent  $\theta$  vs. exposure time to aerated 0.5M NaCl for alkyd coating, 147  $\mu\text{m}$  thick, on steel.

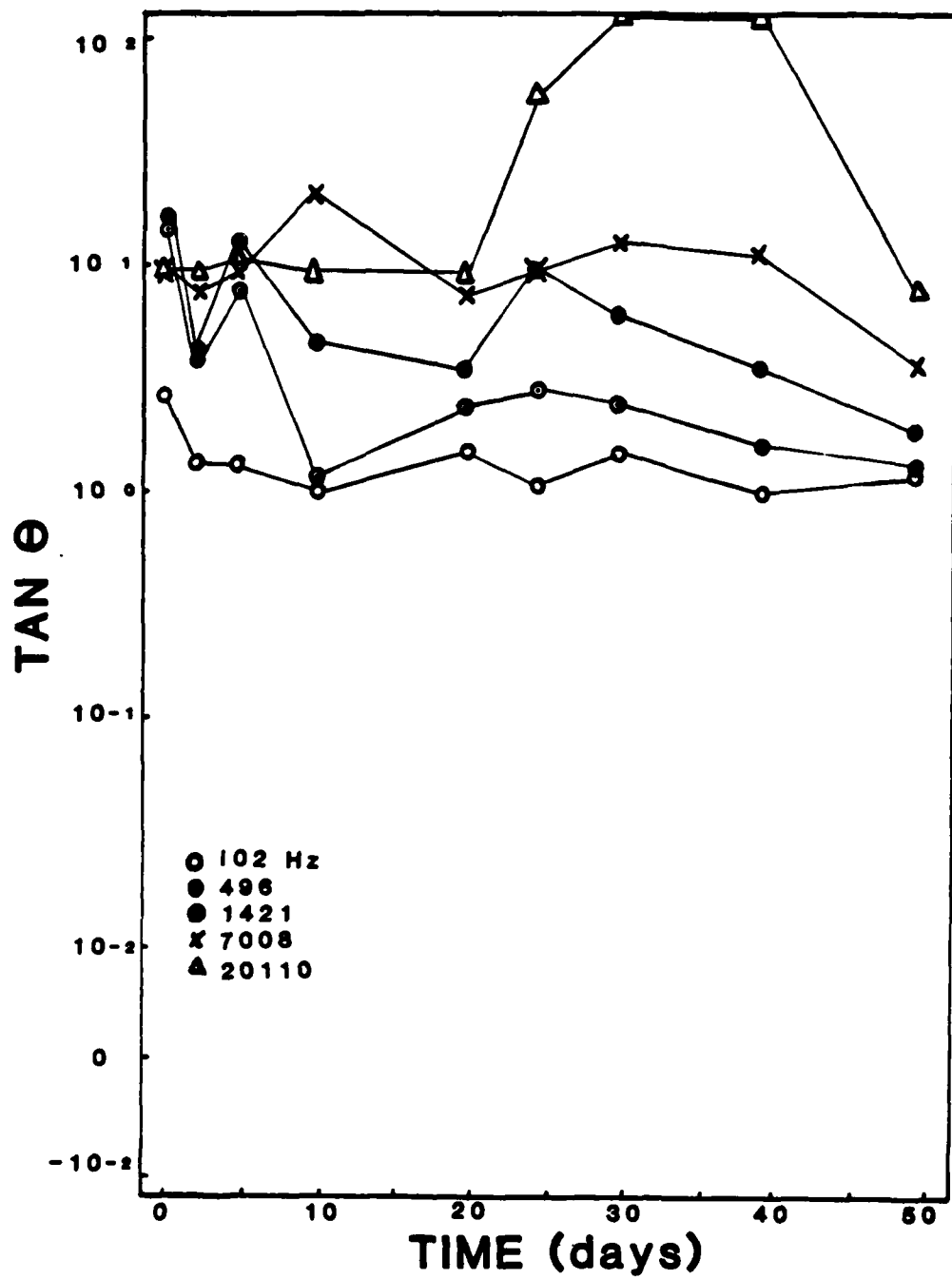


Figure 8. Tangent  $\theta$  vs. exposure time to aerated 0.5M NaCl for alkyd coating plus yellow primer. Total coating thickness was 94  $\mu\text{m}$ .

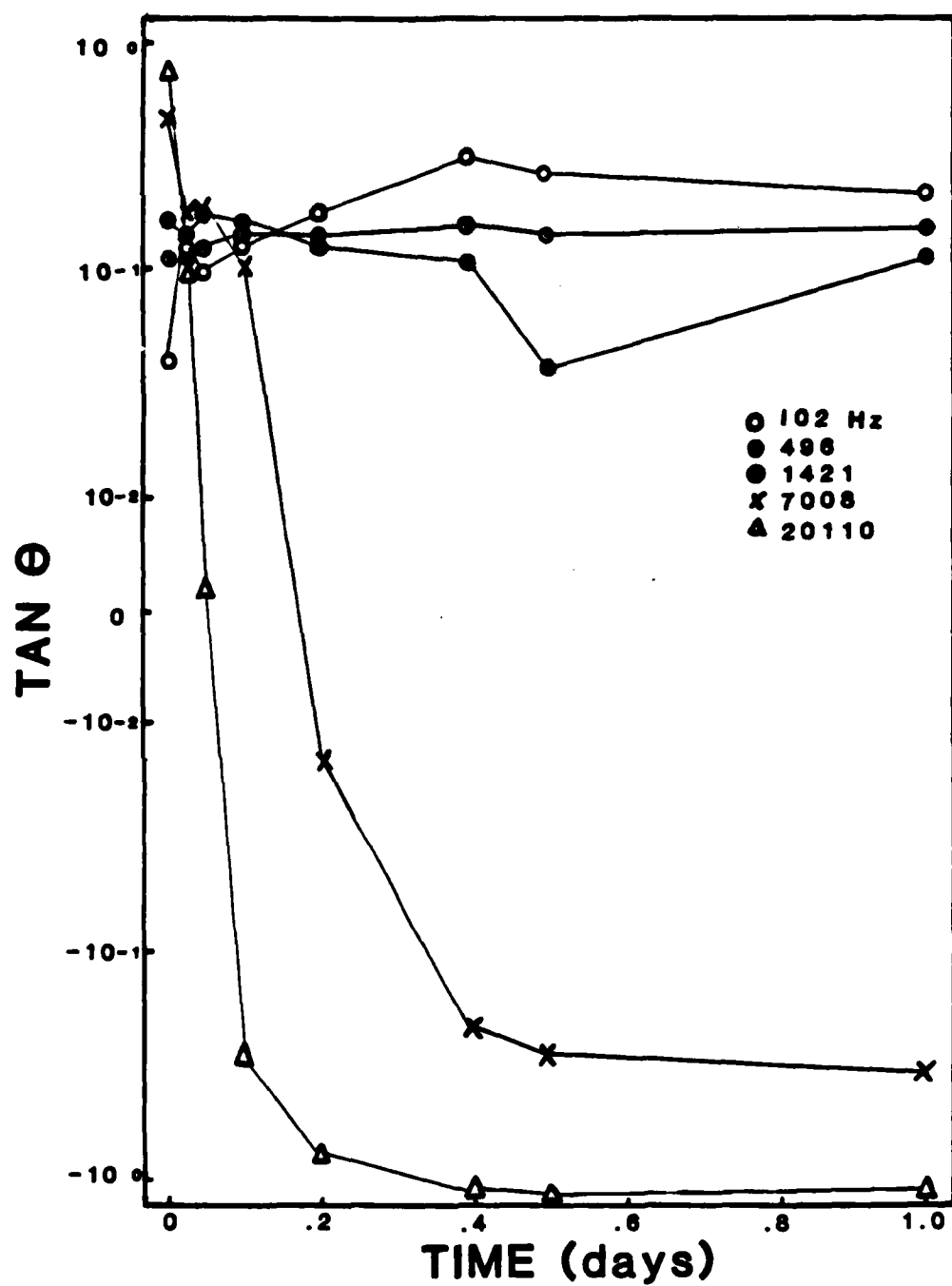


Figure 9. Tangent  $\theta$  vs. exposure time to aerated 0.5M NaCl for Epon 1001-F/Emerez 1511 coating, 15  $\mu\text{m}$  thick, on steel.

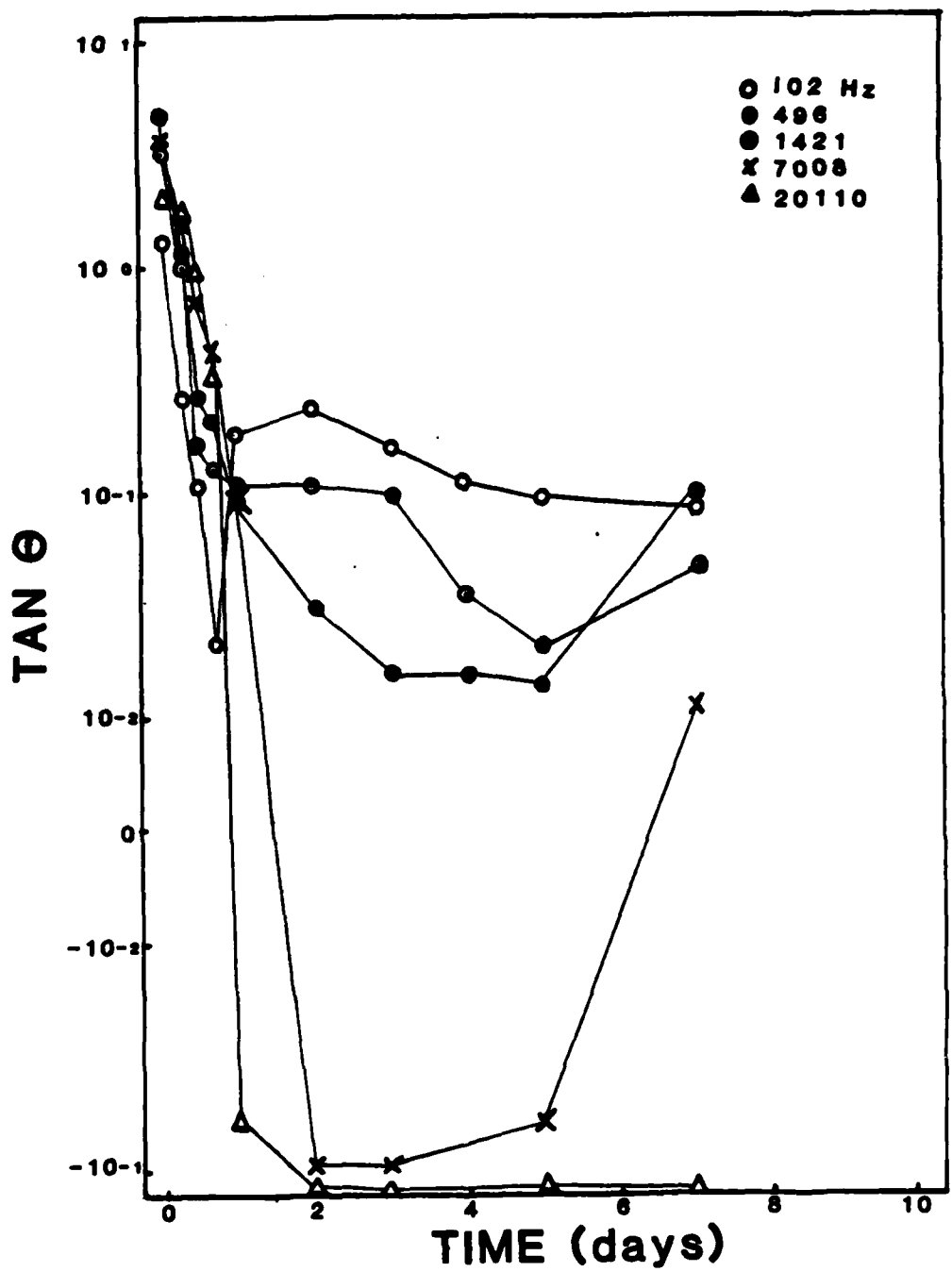


Figure 10. Tangent  $\theta$  vs. exposure time in aerated 0.5M NaCl for Epon 1001-F/Emerez 1511 51  $\mu\text{m}$  thick applied as 2 layers, on steel.

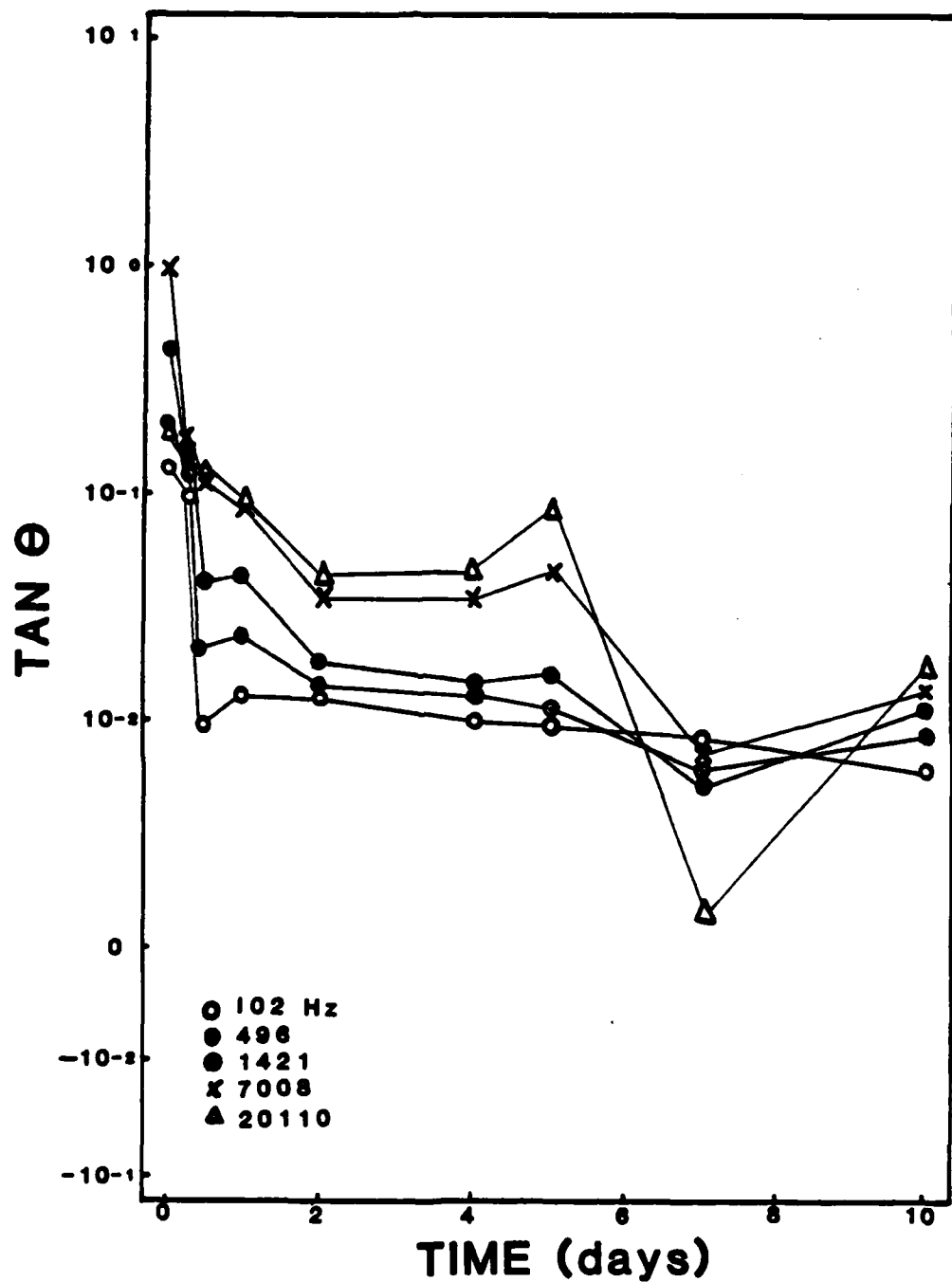


Figure 11. Tangent  $\theta$  vs. exposure time in aerated 0.5M NaCl for Epon 1001-F/Emerez 1511 coating, 51  $\mu\text{m}$  applied as 3 layers, on steel.

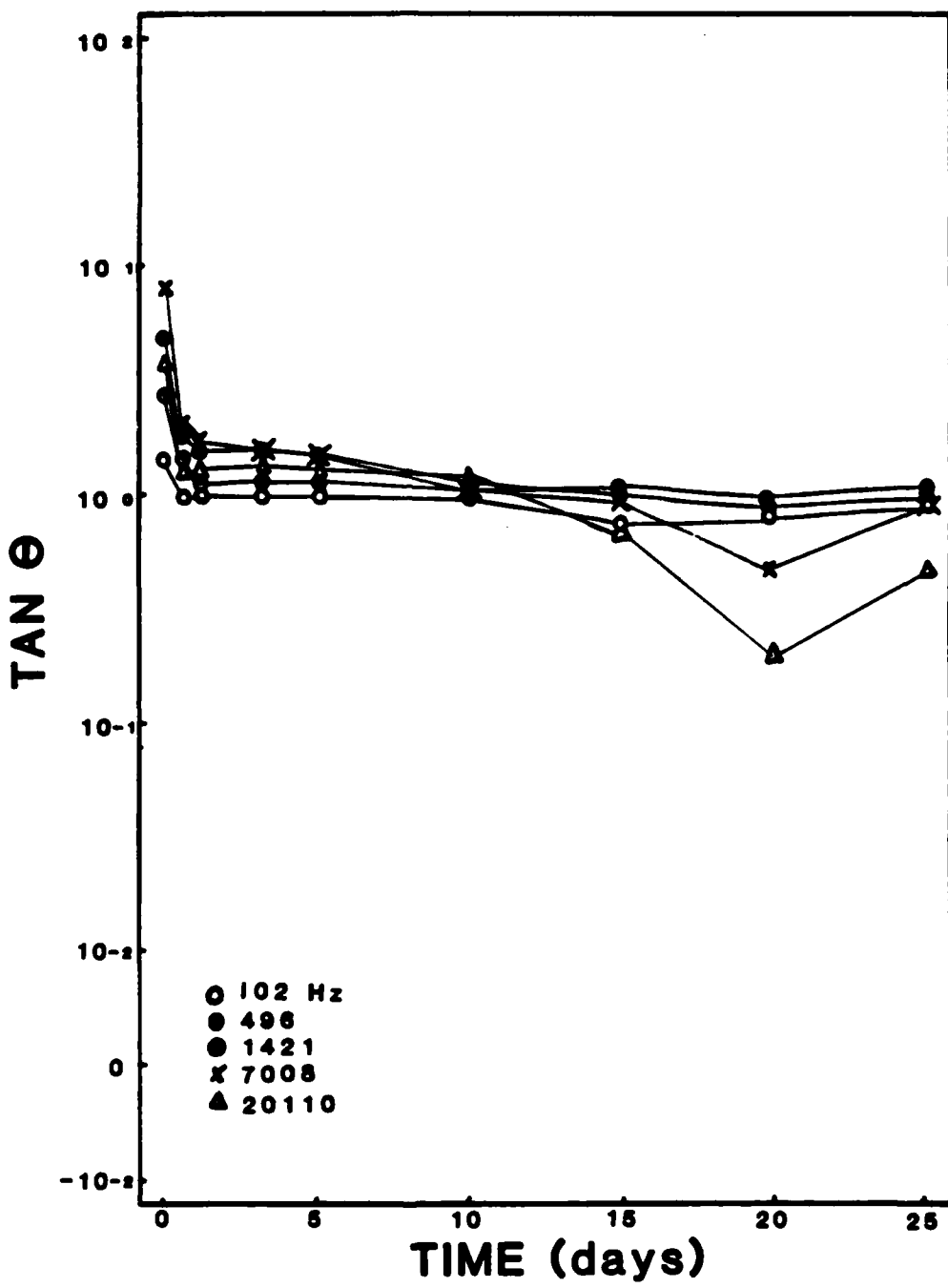
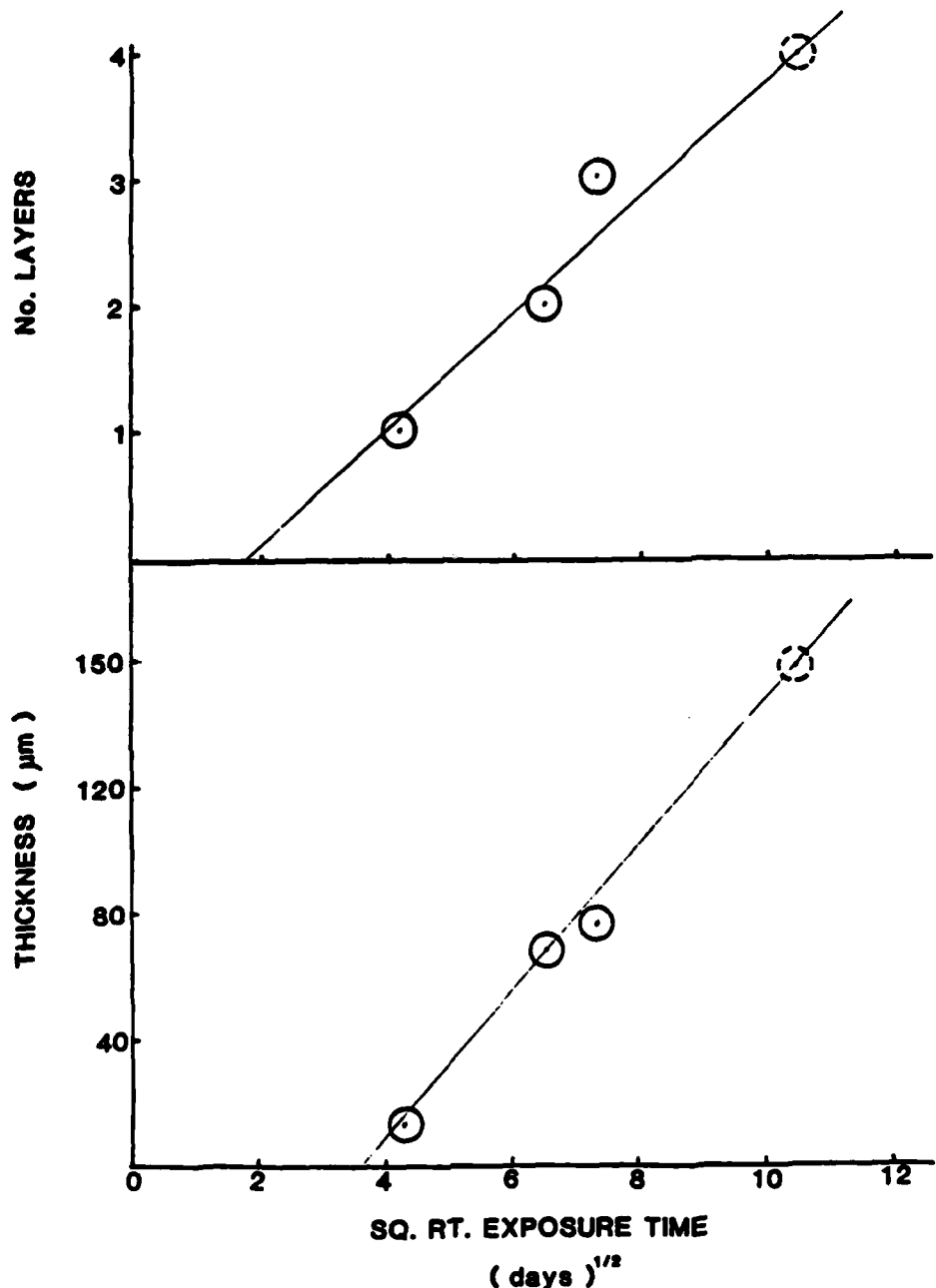


Figure 12. Tangent  $\theta$  vs. exposure time in aerated 0.5M NaCl for Epon 1001-F/Emerez 1511 coating, 88  $\mu\text{m}$  thick, on steel.



**Figure 13.** Relationship between time to failure after exposure in aerated 0.5M NaCl vs. coating thickness for an alkyd coating on steel.

represent, low frequency impedance studies along with other surface analysis techniques are required.

The addition of the yellow primer to the alkyd system showed marked inhibition of the breakdown process, with Tan  $\delta$  values representative of nearly pure capacitive systems. Figures 4 and 8 show the marked difference in the time to failure (crossing to neg Tan  $\delta$  values) for one coat of alkyd paint with and without primer.

Preliminary results for the alkyd system also show a high degree of linearity between the square root of failure time and coating thickness (Fig. 13). These findings may be unique for this system and, thus, should not be extrapolated to other systems. Too many factors (polymer matrix configuration, coating defects prior to testing, etc.) can cause deviations from linearity. Thus, delamination rates (Table I) are helpful in providing another evaluation of the coating.

The coating defect structure and thickness also play an important role in the effect of oven-cure time on impedance response over this frequency range. Since these are two of the major factors controlling coating breakdown, curing effects will only be seen if there is a marked change in coating structure during the curing process. Preliminary results on the polybutadiene system show no measurable difference in impedance response for 10, 20 and 50 minute curing at 200°C after two weeks' exposure to 0.5M NaCl.

#### REFERENCES

- [1] G. Reinhard, K. Hahn, and R. Kaltofen, *Plaste Kautsch.* 22, 522 (1975).
- [2] M. Piens and R. Verbist, "Corrosion Control by Organic Coatings", H. Leidheiser, Jr., editor, Natl. Assocn. Corrosion Engrs., Houston, Texas, in press.
- [3] J. D. Scantlebury and G. A. M. Sussex, "Corrosion Control by Organic Coatings", H. Leidheiser, Jr., editor, Natl. Assocn. Corrosion Engrs., Houston, Texas, in press.
- [4] J. V. Standish and H. Leidheiser, Jr., *Corrosion* 36, 390 (1980).
- [5] M. C. Hughes and J. M. Parks, "Corrosion Control by Organic Coatings", H. Leidheiser, Jr., editor, Natl. Assocn. Corrosion Engrs., Houston, Texas, in press.

## Program #5. Determination of the Acidity of Iron Oxide Surfaces

### INTRODUCTION

The adhesion of organic polymers to inorganic oxides, such as those on steel surfaces and iron oxide pigments, has been shown to result entirely from acid/base interactions between the polymer and the oxide. Hydrogen bonds have been shown to be a sub-set of acid/base interactions and dipole/dipole interactions were shown to be so negligibly small that no experimental evidence for them has yet been found. It therefore becomes important to find a method of measuring and predicting acid/base interactions in the bonding of organic polymers to metal oxide surfaces, especially the oxide layers on steel.

### RESULTS AND DISCUSSION

This year the characterization of the acidity of iron oxide surface by Drago's E and C constants [1] was devoted to investigations of the accuracy and reproducibility of the flow microrimeter, the rate of adsorption, the effect of moisture on the interaction of iron oxide surfaces with bases such as pyridine and triethylamine, and the effect of different hydrocarbon solvents.

The Microscal Flow Microcalorimeter is a very sensitive device for measuring heats of adsorption or desorption as a solution is pumped through a bed of adsorbent, in our case a bed of about 150 mg of iron oxide powder having a surface area of about  $10 \text{ m}^2/\text{g}$ . The unit is calibrated by a resistance heater which generates heat in nearly the same location as the surface of the powder; we find the calibrations are only valid when the bed size is kept within a certain range. Several other variables in the operation of the calorimeter also had to be explored to ensure that the observed heats of adsorption do not include any adventitious effects.

The effect of trace water on the adsorption of pyridine out of cyclohexane onto iron oxide powder was studied in much detail. This was a very necessary part of the overall investigation because the oxide, the cyclohexane and the pyridine always carry trace moisture and the adsorption results are quite different depending upon the degree of dryness. We have chosen to control the moisture content by drying the oxide in a vacuum oven, by drying the pyridine and the cyclohexane over molecular sieves,

and then measuring the ppm of water in the cyclohexane using the Karl Fischer reagent. Powder placed in the calorimeter is also capable of being dried by a vacuum pump to about one torr (4% R.H. at 25°C). The drying and handling of the solvent required construction of an all-glass liquid handling system and the filling of ampoules through septa to facilitate solution preparation. We now have a system capable of dispensing the cyclohexane carrier solvent with a water content of 10 ppm to saturation (99.6 ppm at 25°C) [2].

It was expected that the iron oxide surface would tend to adsorb both water and pyridine and that there would be a competition for the acid sites leading to less pyridine adsorption at higher water contents. Figures 1-3 are recorder traces from the calorimeter run for decreasing water contents. Note that the curves presented in Figures 2 and 3 were run on a more sensitive scale so these areas cannot be directly compared to the areas in Figure 1. The enthalpies of adsorption calculated from these curves are 72, 40 and 52 millicalories (per 150 mg of iron oxide) for Figures 1, 2 and 3, respectively. We will address this apparent anomaly at a later point in this discussion. Figure 1 shows the results obtained without drying either the oxide or the cyclohexane; the adsorption peak is complete in about 5 min and the desorption peak is of equal area; the desorption takes little longer than the adsorption process. In Figure 3, the adsorption is seen to be much slower for this lowest water case. The desorption rate is much more dependent upon the water content, as evidenced by the decreasing area of the desorption peak as compared with the adsorption peak. In Figure 3, only 67% of the pyridine is desorbed in 30 min as compared to 97% of the pyridine in Figure 1, indicating a much stronger interaction occurs between pyridine and the oxide when less water is present.

Equilibrium adsorption isotherms were also determined in some detail as a function of water content. In our prior work using  $\text{Fe}_3\text{O}_4$ , ampoules of weighted iron oxide powder that had been previously dried and stored in a desiccator were contacted with undried cyclohexane solutions and tumbled for two hr to achieve "equilibrium" adsorption at two controlled temperatures (25°C and 45°C). The pyridine remaining in solution was assayed by ultraviolet light absorption at 252 nm. Results for pyridine adsorption on  $\text{Fe}_3\text{O}_4$  using this procedure are presented in Figure 4, where the adsorption is plotted as the straight-line Langmuir isotherm:

$$\frac{C}{\Gamma} = \frac{1}{\Gamma_m K} + \frac{C}{\Gamma_m} \quad (1)$$

In this equation, C is the bulk concentration ( $\text{moles}/\text{m}^3$ ),  $\Gamma$  is the surface concentration ( $\text{moles}/\text{m}^2$ ),  $\Gamma_m$  is the total surface concentration of "adsorption sites", and K is the equilibrium constant for adsorption:

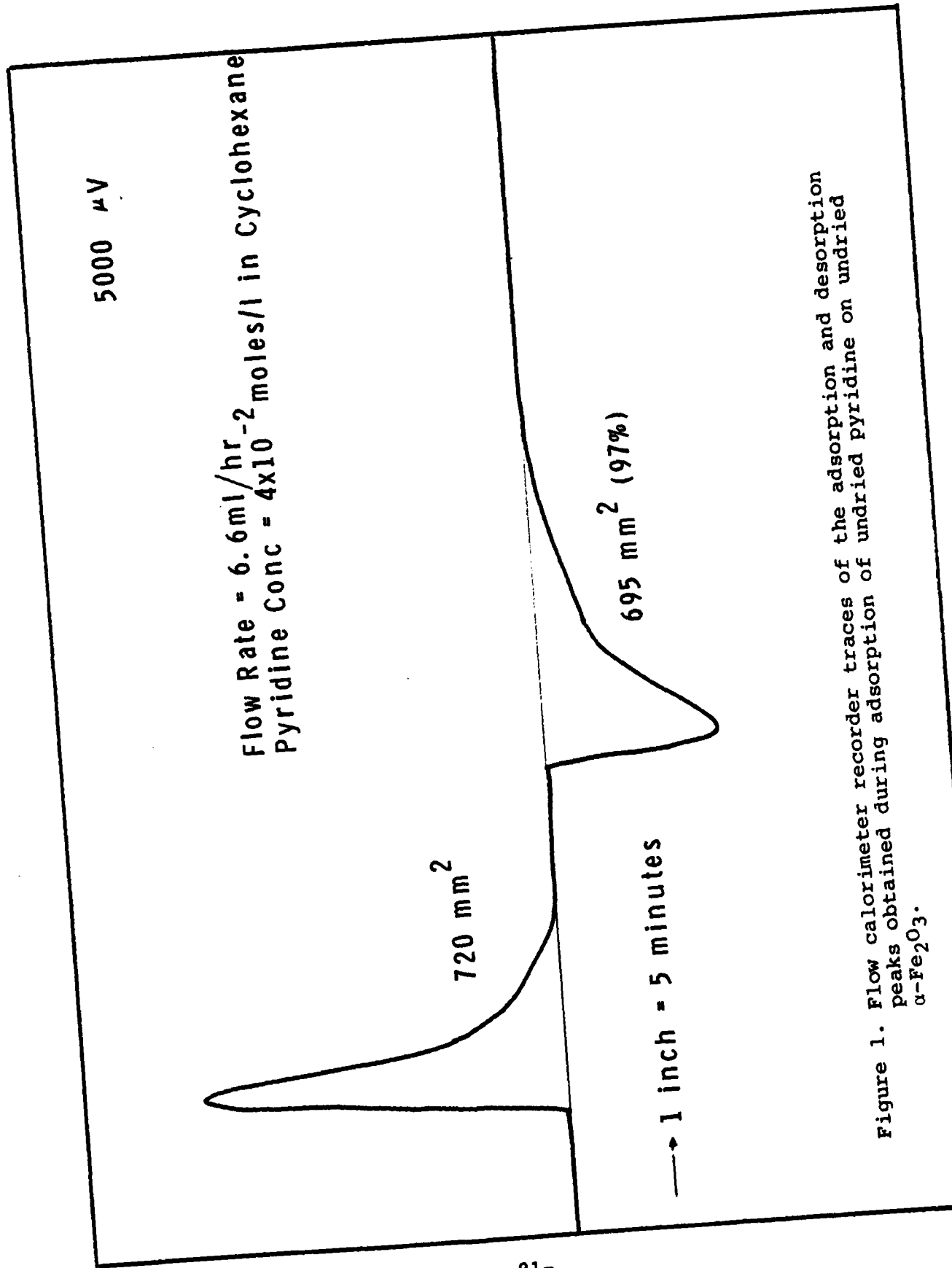


Figure 1. Flow calorimeter recorder traces of the adsorption and desorption peaks obtained during adsorption of undried pyridine on undried  $\alpha\text{-Fe}_2\text{O}_3$ .

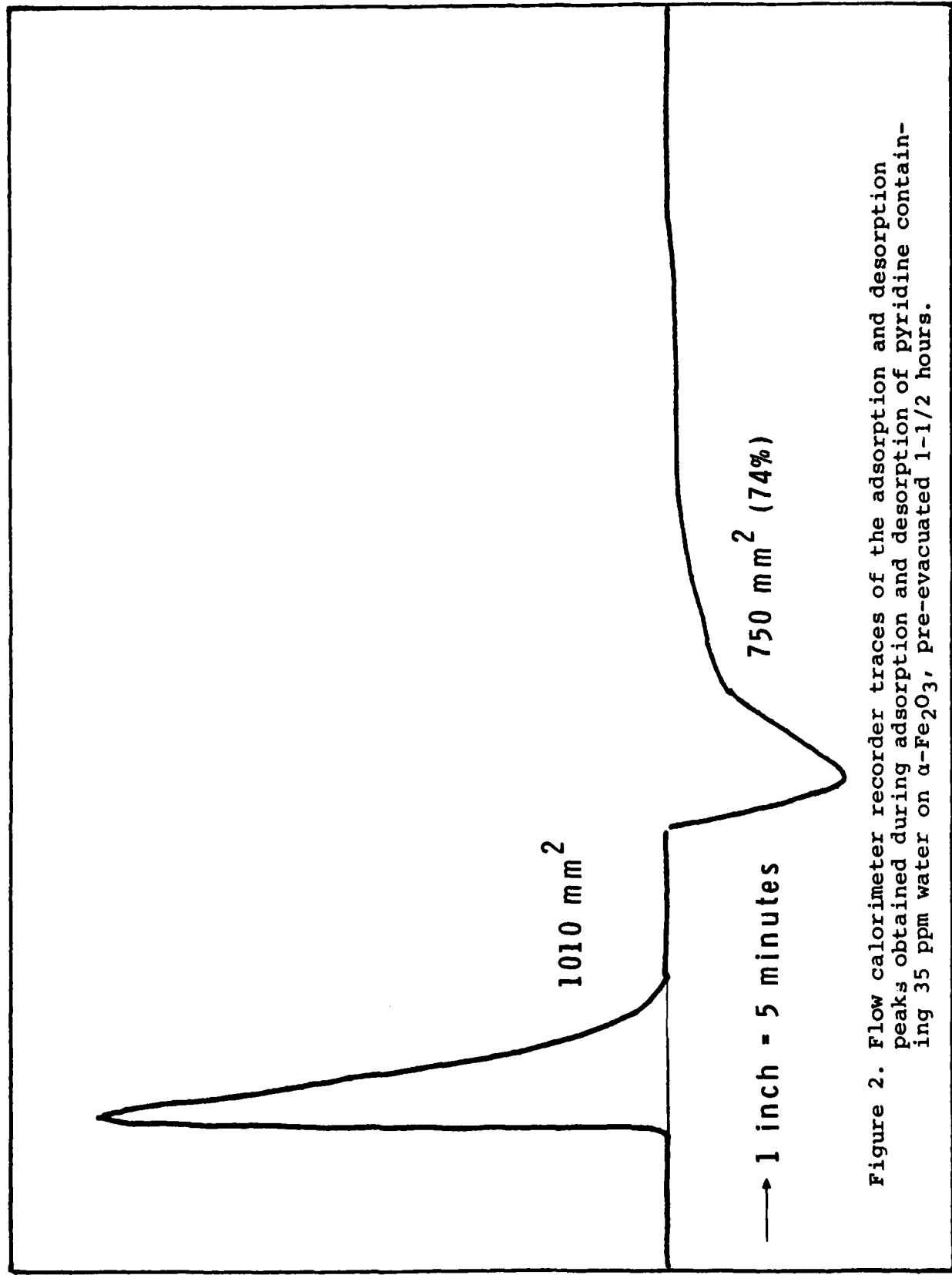


Figure 2. Flow calorimeter recorder traces of the adsorption and desorption peaks obtained during adsorption and desorption of pyridine containing 35 ppm water on  $\alpha\text{-Fe}_2\text{O}_3$ , pre-evacuated 1-1/2 hours.

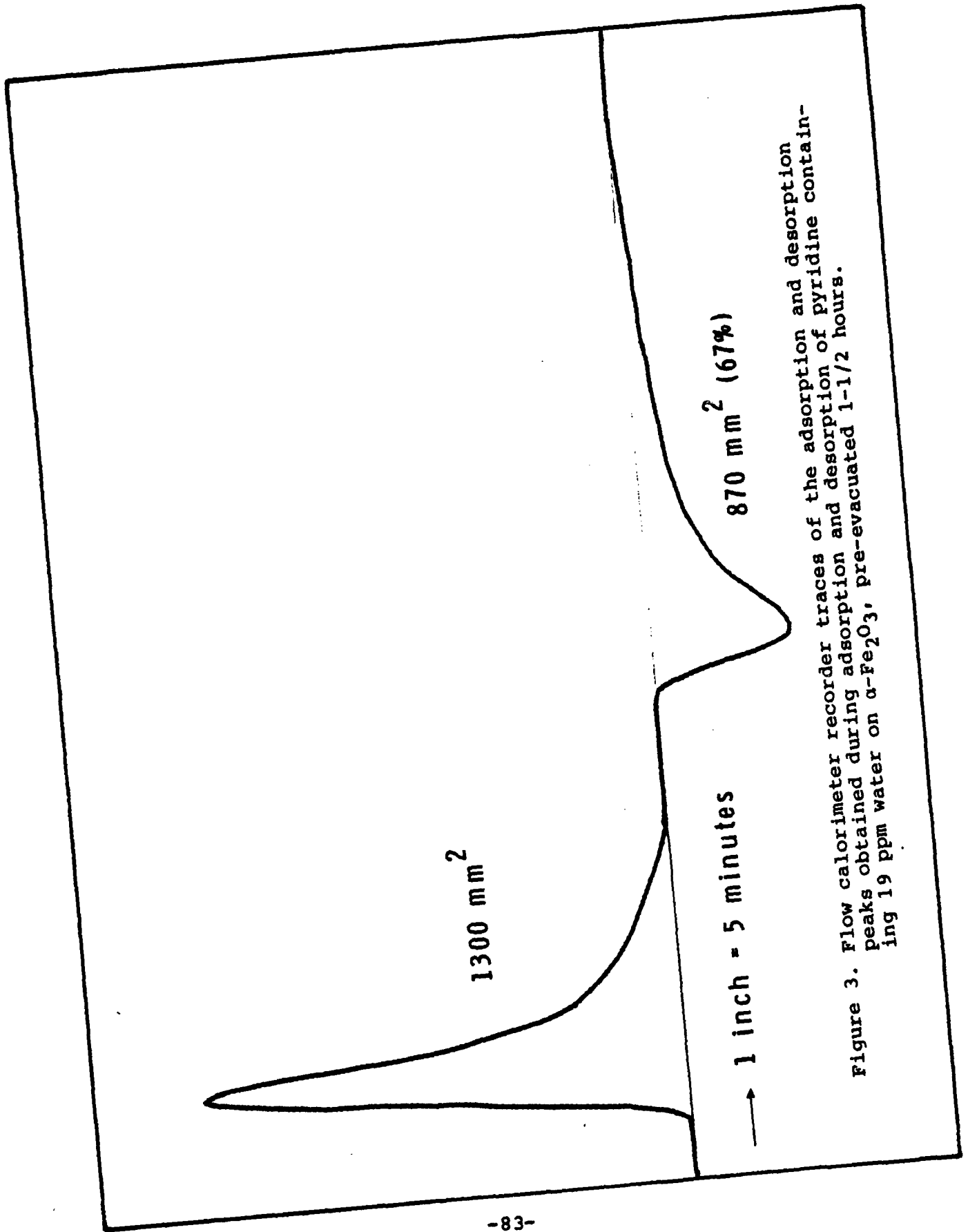


Figure 3. Flow calorimeter recorder traces of the adsorption and desorption of pyridine containing peaks obtained during adsorption and desorption of pyridine containing 19 ppm water on  $\alpha\text{-Fe}_2\text{O}_3$ , pre-evacuated 1-1/2 hours.

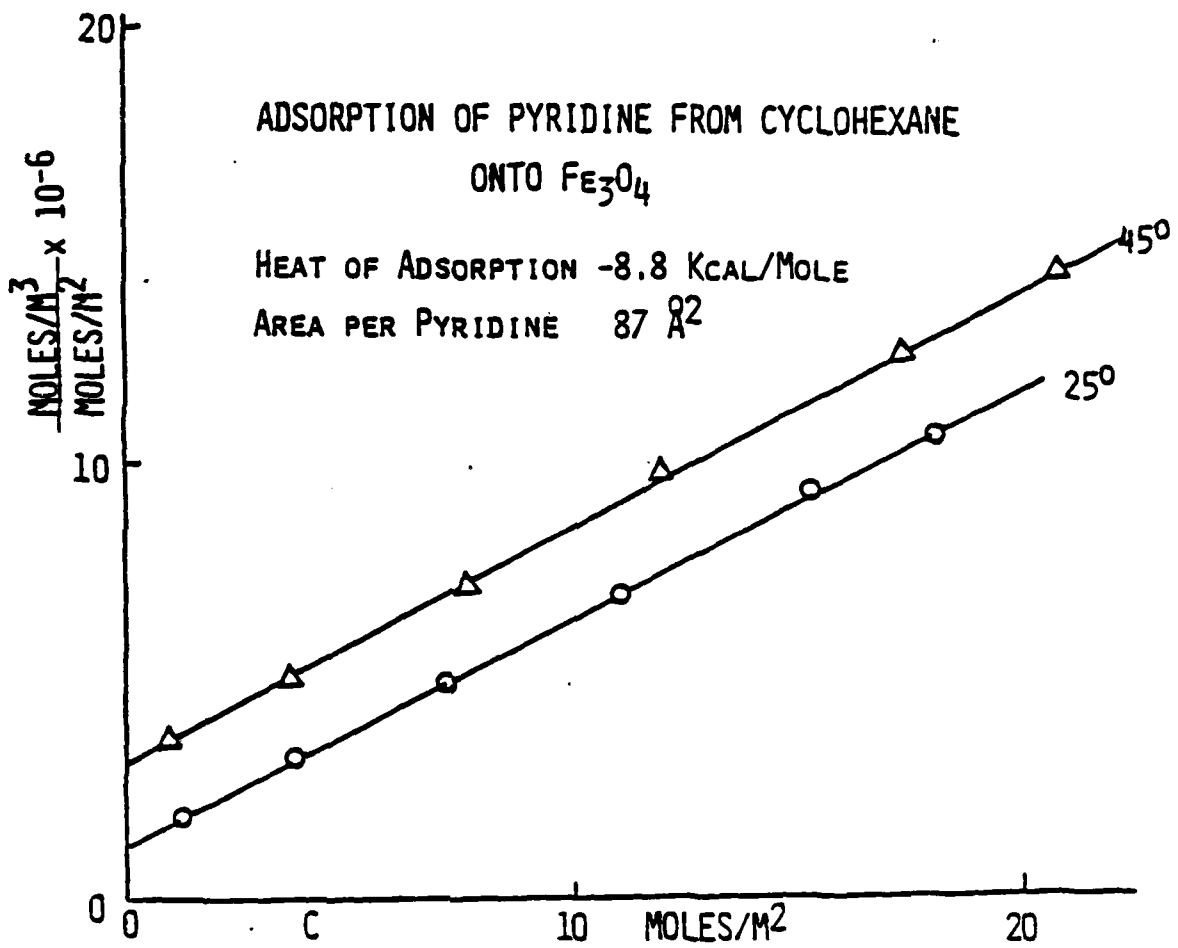


Figure 4. Langmuir isotherm for adsorption of pyridine from cyclohexane onto iron oxide powder.

$$K = \frac{\Gamma}{C(\Gamma - \Gamma_m)} \quad (2)$$

The straightness of the lines shows that all sites bind pyridine with equal energy; this means that all of the adsorption sites are of equal acidity. Such is not always the case; in some of our other studies with silica surfaces using Cab-O-Sil and HiSil there is a distribution of surface acidities which is more marked with Cab-O-Sil, a surface only partly covered with SiOH sites. Iron oxide surfaces are known to be more thoroughly covered with FeOH sites, as evidenced by the work of Micale on this project, so it may not be too surprising that the surfaces are more homogeneous than silica. Heterogeneity in acidity of SiOH or FeOH surfaces results largely from having some of these acid sites close to others (vicinal) where they can form local hydrogen-bonds in which the acidity of the hydrogens is reduced by complexation with neighboring oxygens. The fact that this is not observed with FeOH surfaces may result from denser surface coverage so that there are no isolated FeOH groups as are indeed observed on SiOH surfaces by infrared studies. Another possibility is that since the acidity of FeOH surfaces is nearly twice as strong as SiOH (as evidenced by heats of adsorption), the oxygens of the FeOH sites may be too weakly basic to form hydrogen bonds.

The heat of adsorption can be calculated from the ratio of the intercepts at the two temperatures since the intercepts are inversely proportional to the equilibrium constant K for adsorption, as shown in Equation (2).

$$\Delta H^{\text{ads}} = \frac{RT_1 T_2}{T_2 - T_1} \ln(K_2/K_1) \quad (3)$$

As shown in Figure 4, the heat of adsorption of pyridine on  $\text{Fe}_3\text{O}_4$  is -8.8 Kcal/mole. Similarly, results for triethylamine adsorption onto  $\text{Fe}_3\text{O}_4$  gave a straight line plot and a heat of adsorption of -13.2 Kcal/mole. Considerable effort was spent to verify that these results could be duplicated using the calorimeter. It was determined that good agreement could be obtained if dried cyclohexane was allowed to percolate through the powder bed for 24 to 48 hr prior to solute adsorption. If this procedure was not followed, however, significant variability in the heat of adsorption obtained using the calorimeter occurred which indicates that the state of surface dryness is an important factor in interpreting the results obtained in the flow calorimeter.

More recent studies have concentrated on an  $\alpha\text{-Fe}_2\text{O}_3$  powder since it is stable to oxidation while the  $\text{Fe}_3\text{O}_4$  surface is not. Adsorption isotherms have been determined as a function of water content for iron oxide samples dried in a vacuum oven and capped under a positive flow of dry nitrogen. The pyridine

solutions were injected through the septa and the samples were then agitated for several days in a constant temperature bath. Results of these studies are presented in Figure 5. No effect of trace water in the range of 19 to 35 ppm was observed under equilibrium conditions. As previously stated, these variations in water content of the carrier solvent did result in significant differences in both the rate and amount of pyridine adsorption under flow conditions. A similar study was done for undried iron oxide powder and significantly less pyridine was adsorbed from solution compared to the dried iron oxide, as can be seen in Figure 6. It was found that the degree of agitation was important in determining the amount of pyridine adsorbed on the undried powder while it had no effect when using the dried powder. This is consistent with the existence of water bridges[3] between some of the iron oxide particles which effectively reduce the available surface area for pyridine adsorption on the undried powder. Increased agitation facilitates the dispersal of water into the cyclohexane and thus permits additional sites for pyridine adsorption on the iron oxide surface that had previously been blocked by water molecules.

Returning to the calorimetry work, the unexpectedly large enthalpy observed with the undried powder can be interpreted as the summation of two different interactions: The pyridine-water interaction (water is more readily removed from the iron oxide surface when the pyridine solution is present) plus the adsorption of pyridine on the iron oxide surface. Viewing the data on the pre-dried systems alone, it is apparent that a competition does exist for the acid sites since, when a greater water concentration is present, the measured pyridine interaction is lessened. It is of interest to note that the surface energy determined for the (oxidized)  $\text{Fe}_3\text{O}_4$  and the  $\text{Fe}_2\text{O}_3$  surfaces dried by percolation of dried solvent or by evacuation are quite similar with values of 80 ergs/cm<sup>2</sup> and 83 ergs/cm<sup>2</sup>, respectively.

One very important consideration in this study is the contribution of the dispersion forces of the solvent and the base to the adsorption process. We have therefore adsorbed pyridine from three dried hydrocarbons of differing surface tension: hexane(18.4 dynes/cm), cyclohexane(25.5 dynes/cm), and decahydronaphthalene(31 dynes/cm). The areas per molecule are not very different: 48, 48 and 51 Å<sup>2</sup> per molecule, respectively.

The above findings on the role of trace water on the adsorption of pyridine onto iron oxide are interesting. The fact that the heat evolved per unit area is so constant for two different iron oxides, that the heat per mole of pyridine adsorbed decreases with added water, and that the rate of adsorption increases quite appreciably with more water present are most important considerations in understanding acid-base interactions on iron oxide surfaces. The faster rates of adsorption suggest that the adsorbed pyridine is present as pyridinium ions, for the high surface mobility of ionic adsorbed layers is known to

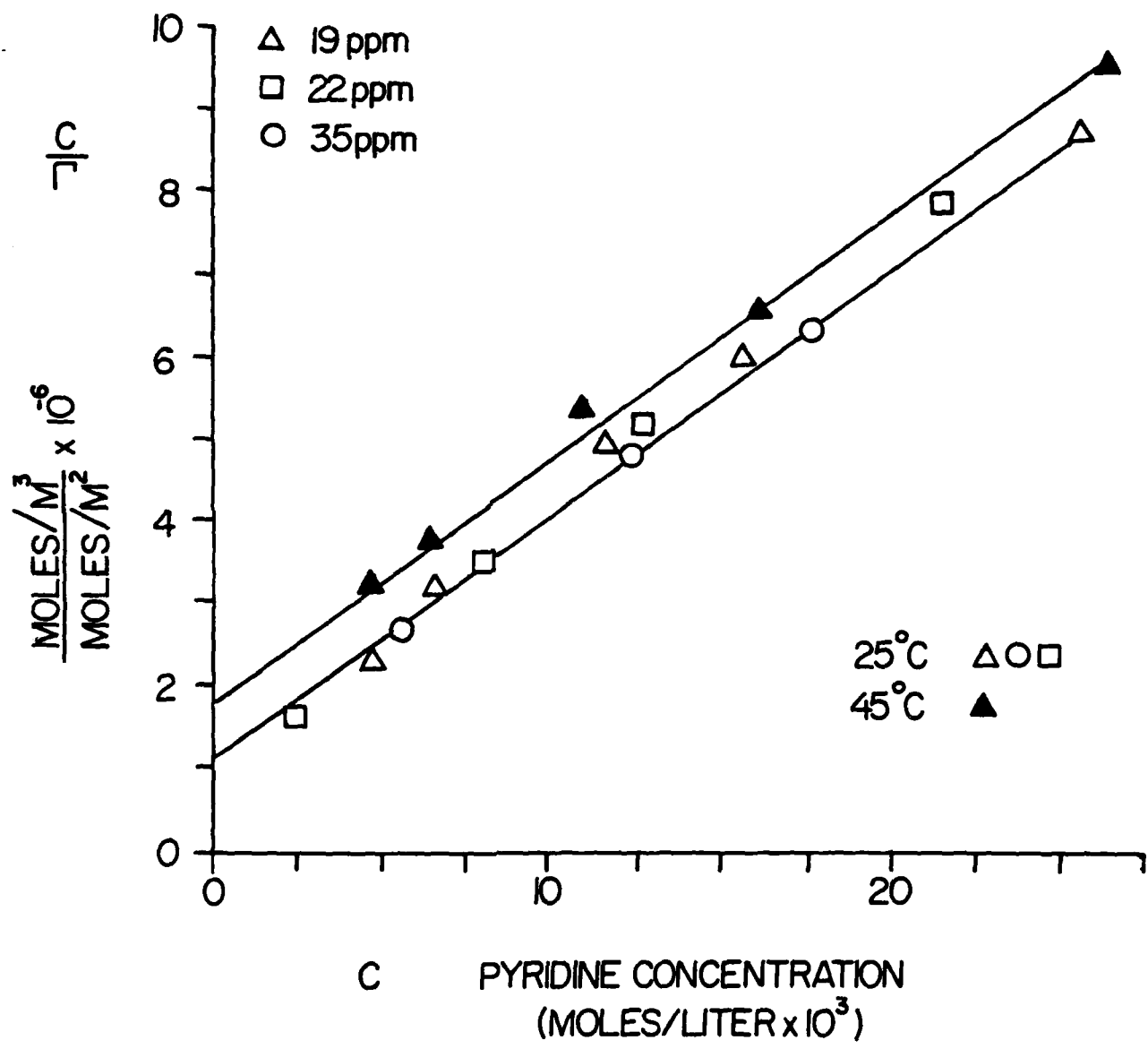


Figure 5. Langmuir plot of the adsorption of pyridine on dried  $\alpha\text{-Fe}_2\text{O}_3$  at  $25^\circ$  and  $45^\circ\text{C}$ .

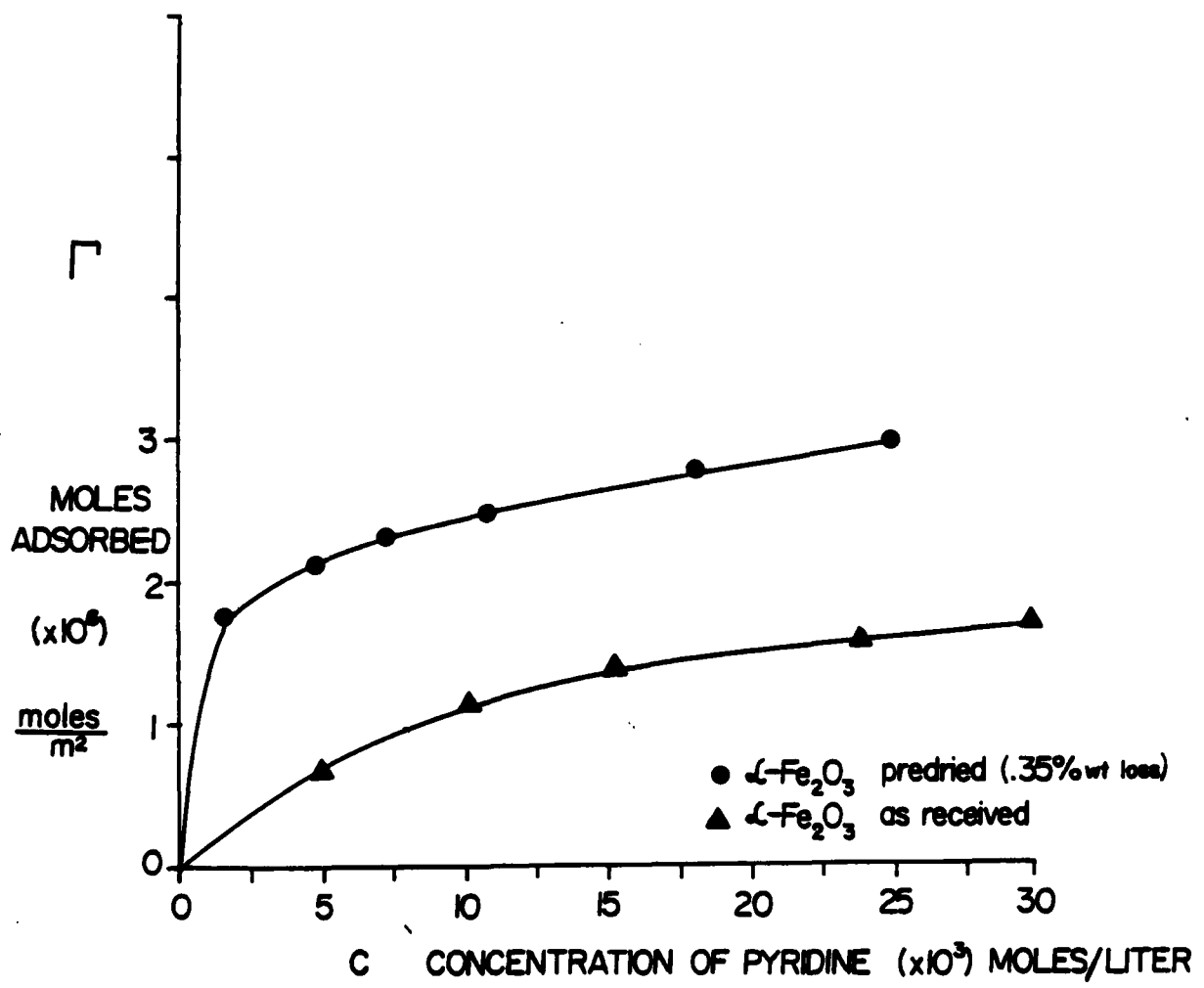


Figure 6. Adsorption of pyridine from cyclohexane onto iron oxide powder as a function of initial powder wetness.

enhance rates of adsorption, and amines adsorbed on iron oxide have been proved to adsorb onto iron oxide out of oil as ions [4]. We might therefore conclude that the presence of trace water at the oxide surface has increased the degree of ionization of the pyridine-oxide acid-base complex. Such ionization could well have increased the area per molecule in the wetter film as observed. A direct measurement of ionization could be made by contact potential differences [4]. If indeed ionization is needed to get rapid adsorption, it is not surprising that in our initial adsorption studies with oxygen bases and sulfur bases we found the rates of adsorption to be extremely slow compared to nitrogen bases.

#### REFERENCES

- [1] R. S. Drago eta al., J. Am. Chem. Soc. 93, 6014 (1971).
- [2] J. H. Hildebrand, Solubility of Non-Electrolytes, 3rd Ed., Reinhold, New York, 1950, p.266.
- [3] M. C. Coelho and N. Harnby, Powder Tech. 20, 197 (1978).
- [4] F. M. Fowkes, J. Phys. Chem. 64, 726 (1960).

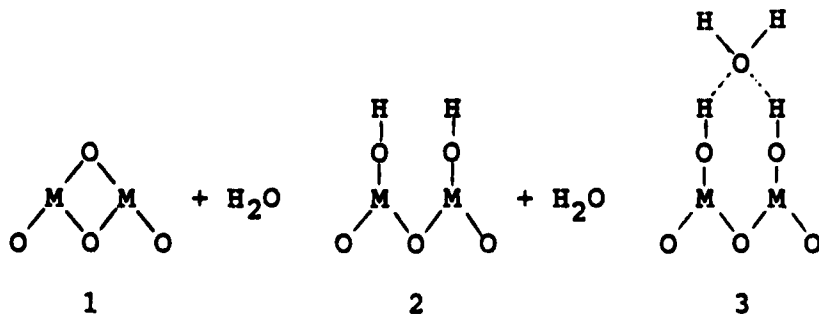
## Program #6. Ion Exchange Properties of Iron Surfaces

### INTRODUCTION

Electron spectroscopic techniques have potential in studies of a number of aspects of adhesion of organic coatings to metal surfaces. Surface analysis of metal substrates as a function of surface preparation can be used to determine the surface composition that either favors or interferes with adhesive bonding. The results of analysis of surfaces that have been produced during adhesive failures may be used to determine whether the failure occurred at the interface or in one or the other of the two phases (i.e., in the surface oxide or in the organic film). Electron spectroscopic studies of the adsorption of simple organic molecules may lead to quantitative measurements of the adhesive bond strength between specific functional groups and the substrate surface. Of these possible applications of electron spectroscopy to studies of adhesion we have chosen to use Auger electron spectroscopy (AES) and X-ray photoelectron spectroscopy (XPS) for characterizing the possible sites on metal surfaces that may be available for adhesive bonding.

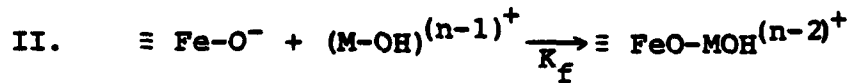
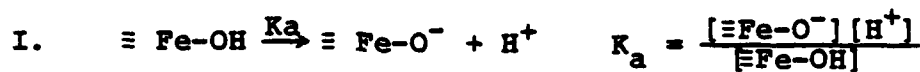
### BACKGROUND

All metals exposed to ambient environments have an oxide film on their surfaces. Furthermore, the surface of this oxide will be hydrated to some extent from either exposure to atmospheric moisture or from previous immersion in aqueous systems that may have been used in surface preparation. Metal surfaces can be realistically considered in terms of an oxide film and its interaction with water as follows:



The adhesion of an organic coating such as a polymer film with a metal must consequently involve this hydrated oxide surface. The intermolecular attractions that contribute to the adhesion of polymers include dispersion forces, dipole interactions and acid-base interactions (including hydrogen bonding). The acid-base interactions are expected to be the dominant interaction for polymers that contain either acid or basic groups. It is therefore important to determine the concentration and relative strengths of the acidic and/or basic sites on metal surfaces.

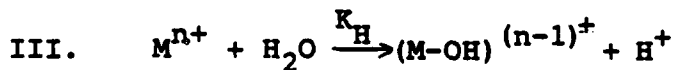
One method of determining the acid-base strength would be to ion exchange the surface hydroxyl as a function of pH. Surface hydroxyls behave in a manner comparable to any amphoteric structure. Based on the results obtained previously and a basic approach to the equilibria involved, the hydroxyl acid-base character can be described as shown below (examples shown for an iron substrate). The equilibria involved in a cation exchange on the surface hydroxyl are given in I, II, and III.



$$K_f = \frac{[\equiv \text{FeO-MOH}^{(n-2)+}]}{[\equiv \text{FeO}^-][(\text{M-OH})^{(n-2)+}]}$$

where,

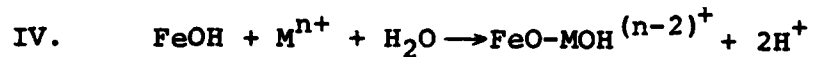
M is any cation with charge n



$$K_H = \frac{[(\text{M-OH})^{(n-1)+}][\text{H}^+]}{[\text{M}^{n+}]}$$

In this representation,  $K_a$  is the surface hydroxyl dissociation constant,  $K_f$  is the formation constant of an exchange surface specie, and  $K_H$  is the hydrolysis constant of the cation.

The overall reaction of the surface hydroxyl with a cation is:



Then

$$\text{V. } K_a \cdot K_f \cdot K_H = \frac{[\text{FeO-MOH}^{(n-2)+}] [H^+]^2}{[M^{n+}] [\text{Fe-OH}]}$$

Let -  $N_o$  = Total number of sites

$$N_o = [\text{Fe-OH}] + [\text{Fe-O}^-] + [\text{FeO-MOH}^{(n-2)+}]$$

$$\text{Define: } \theta = \frac{[\text{FeO-MOH}^{(n-2)+}]}{N_o}$$

Theta ( $\theta$ ) is the fraction of exchanged surface sites.

Rearranging V (assuming  $[\text{FeO}^-] \ll [\text{FeO-MOH}^{(n-2)+}]$ ),

$$\text{VI. } \frac{K_a K_f K_H}{[H^+]^2} [M^{n+}] = \frac{\theta}{1-\theta}$$

Simplifying VI,

$$\text{VII. } \log\{K_a K_f K_H [M^{n+}]\} + 2pH = \log \frac{\theta}{1-\theta}$$

Under the assumption of no cation hydrolysis:

$$\text{VIII. } \log\{K_a K_f [M^{n+}]\} + pH = \log \frac{\theta}{1-\theta}$$

The extent of the surface exchange reaction is readily observed by AES. Samples prepared across the range of pH are studied with Equations VII and VIII as models of the expected behavior. Application of VII and VIII to the results will lead to estimations of the acid-base strength.

The theoretical coverage ( $\theta$ ) can be expressed in a form which allows the prediction of ( $\theta$ ) as a function of pH.

$$\theta \equiv \frac{[\equiv\text{FeO-MOH}^{(n-2)}]^+}{N_0} \approx \frac{[\equiv\text{FeO-MOH}^{(n-2)}]^+}{[\equiv\text{FeOH}] + [\equiv\text{Fe-O}^-]}$$

where

$$[\equiv\text{FeO-MOH}^{(n-2)}]^+ \approx [\equiv\text{FeO}^-]$$

Then

$$\theta = \frac{1}{[\equiv\text{FeOH}] + 1} = \frac{1}{([\text{H}^+]/k_a) + 1}$$

The form of  $\theta$  vs pH is plotted with an assumed  $pK_a = 9.0$  (Fig. 1), as a demonstration of the expected pH dependence of the surface hydroxyl-cation exchange reaction.

Exchange of the surface OH is also followed by the oxygen (1s) photoelectron line. By noting the amount of OH present on each sample, the amount of K can be related to the number of sites present for reaction. From early studies it has been noted that the amount of OH on the surface increases with immersion in solutions with increasing pH.

#### EXPERIMENTAL PROCEDURE

Samples were prepared following a procedure as outlined below. Mild (1010) steel coupons (6 mm x 12 mm x 1 mm) were mechanically polished under flowing water to a final alumina grit size of 0.3  $\mu\text{m}$ , followed by a rinse with 3X distilled water. Each sample was rinsed with ethyl alcohol, dried, and then transferred directly to a 250°C oven for ~ 30 minutes. The oxidized specimens were cooled for ~ 2 minutes and then placed in potassium hydroxide solution. These solutions were prepared from fresh 3X distilled water and A.C.S. certified grade KOH. Individual volumes of this stock solution were adjusted for a specific pH with 0.1M HNO<sub>3</sub> (prepared from fresh 3X distilled

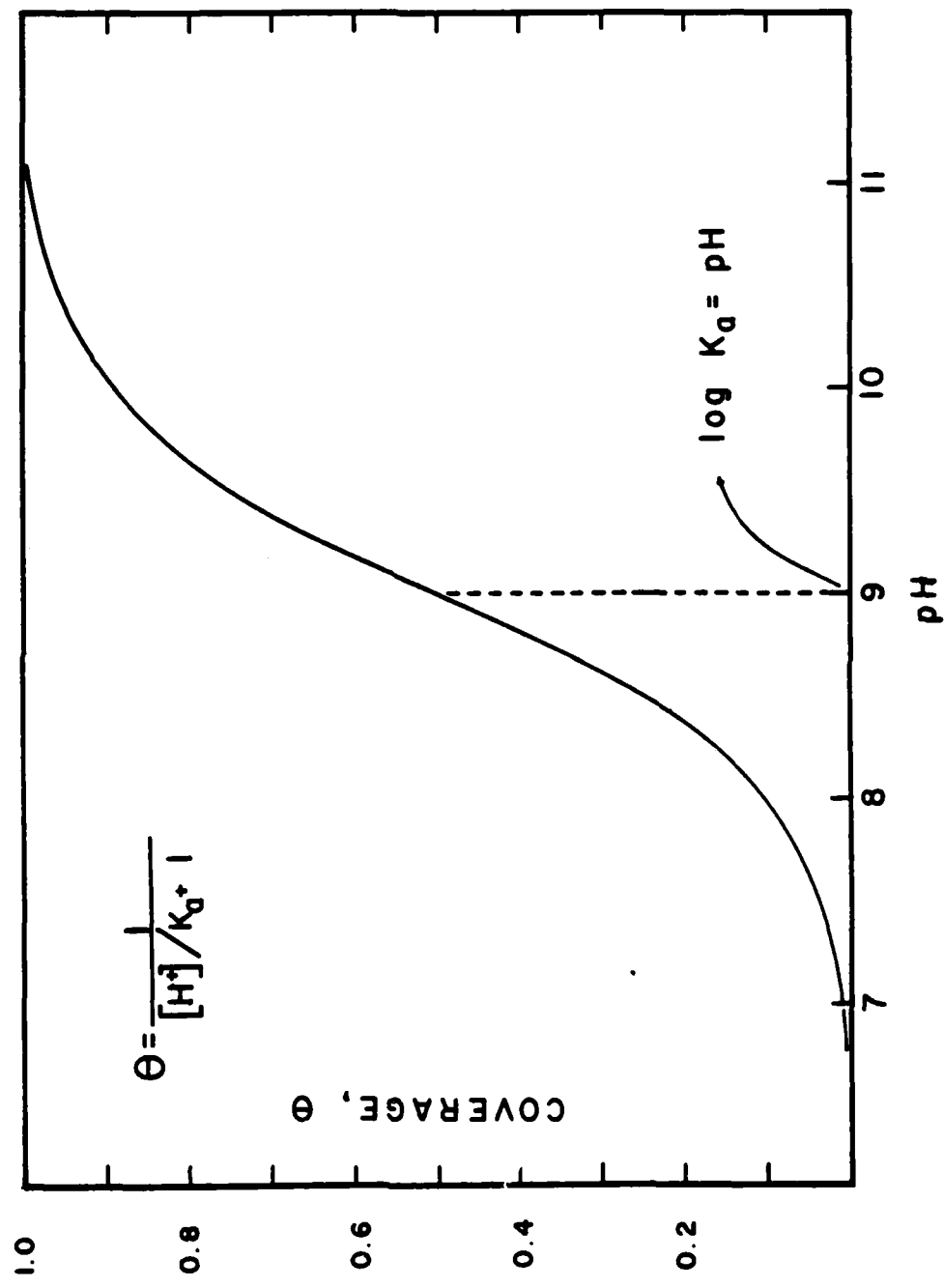


Figure 1. Theoretical coverage curve based on surface acid-base equilibria;  $pK_a$  assumed = 9.0 for demonstration.

water and concentrated  $\text{HNO}_3$ ). Potassium concentration in all solutions was equal. Sample immersion times were 200 seconds, after which the specimens were carefully blotted dry and placed in a desiccator until mounted in the electron spectrometer (<2 hrs).

A change in procedure from the previous report has been made by switching to potassium exchange over calcium exchange. Hydrolysis of  $\text{Ca}^{++}$  at pH's of greater than 10.5 made the study of exchange difficult in the pH range where maximum exchange occurs.

Routine analysis of each sample included an Auger scan for the K surface coverage along with an XPS survey scan and a high resolution XPS scan of the oxygen (1s) line for hydroxide/oxide ratio determination.

#### EXPERIMENTAL RESULTS

Figure 2 is an Auger electron spectrum of a non-exchanged sample carried through the preparation as a control. The spectrum shows the steel is oxidized and has no other surface elements to within the detection sensitivity of the instrument. The X-ray photoelectron oxygen (1s) line of the control sample (Fig. 3) displays the presence of two oxygen types on the surface. The line with the lower binding energy is oxygen in the oxide and a higher binding energy line is attributed to hydroxyl oxygen.

Figure 4 shows an AES spectrum of a sample exposed to a pH = 11.2 potassium hydroxide solution. The large potassium signal at 250 eV is due to potassium that has undergone exchange with the surface. The O(1s) photoelectron line for this sample (Fig. 5) indicates an increase in the hydroxyl line compared to that of the control, Figure 2. The change in the hydroxyl line may be due to hydration of the exchanged cation, or increased hydration of the oxide surface at higher pH's.

The ratio of potassium Auger electron signal to the iron Auger electron signal, K/Fe, is plotted as a function of pH in Figure 6. The increase in potassium at the high pH values is similar to that expected for  $\text{K}^+$  exchange with the surface hydroxyls, cf. Figure 1. This increase in exchange in the pH range 10-11 suggests that the  $p\text{K}_a$  for the hydrated iron oxide on steel has a value of  $\approx 10.8$ .

The results described above were obtained for a "clean" specimen. Auger analyses of most specimens, however, have shown the presence of other elements in addition to those in iron oxide. A spectrum of a specimen that was exposed to  $\text{K}^+$

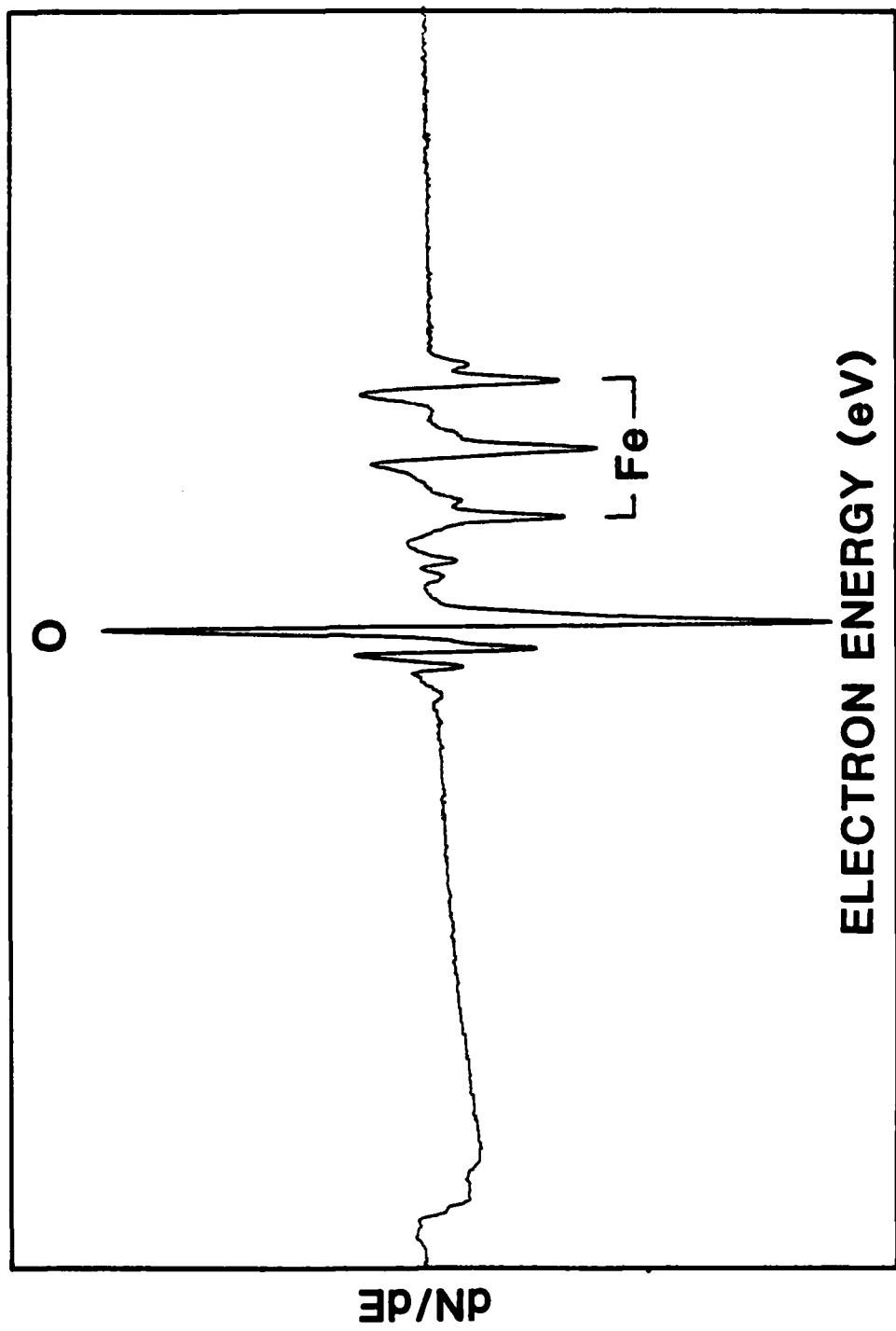


Figure 2. Auger electron spectrum of "clean" control sample.

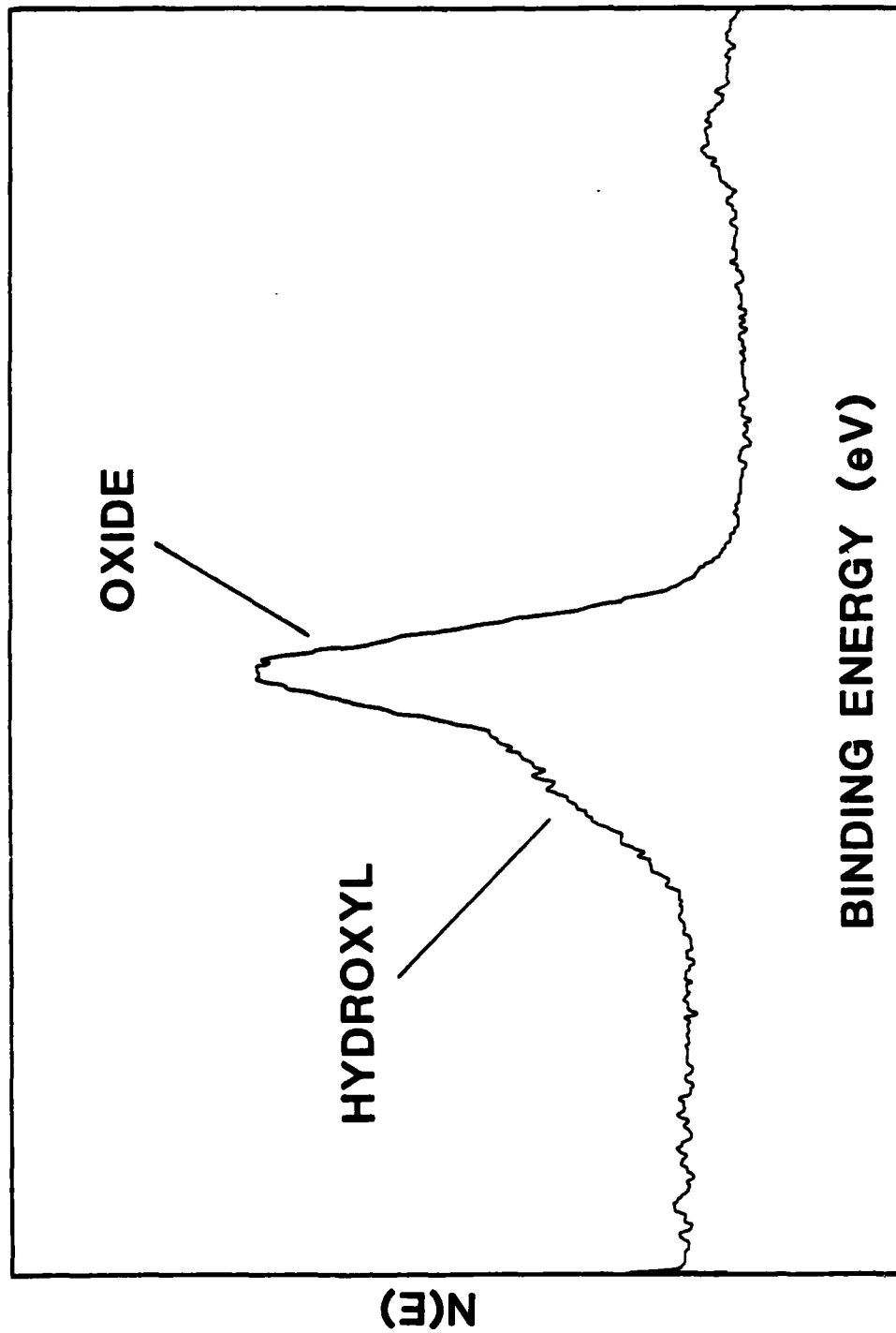


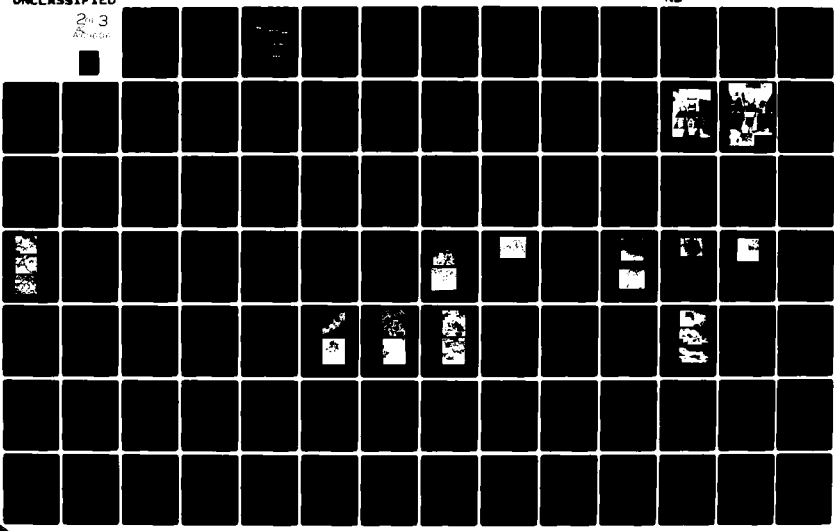
Figure 3. O(1s) X-ray photoelectron line of the "clean" control sample.

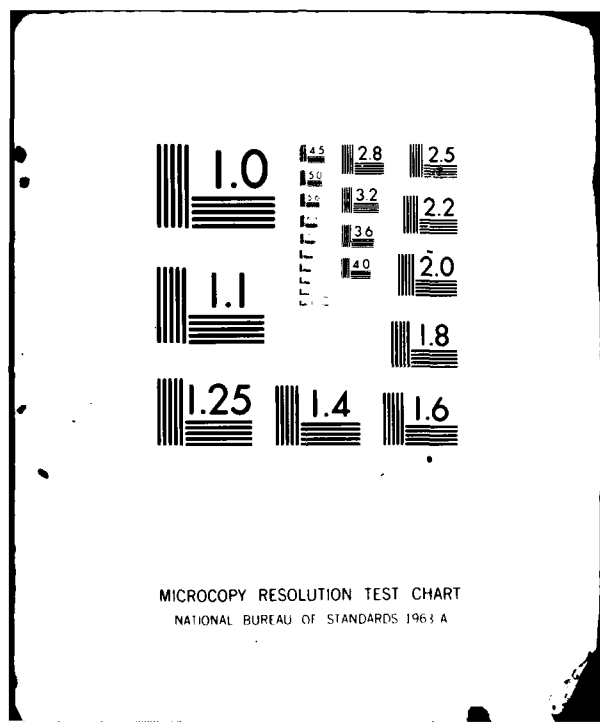
AD-A109 606

LEHIGH UNIV, BETHLEHEM PA CENTER FOR SURFACE AND COATINGS--ETC F/6 11/3  
CORROSION CONTROL THROUGH A BETTER UNDERSTANDING OF THE METALLI--ETC(U)  
NOV 81 H LEIDWEISER, E M ALLEN, M S EL-AASSER N00014-79-C-0731  
NL

UNCLASSIFIED

2n 3  
AB 460





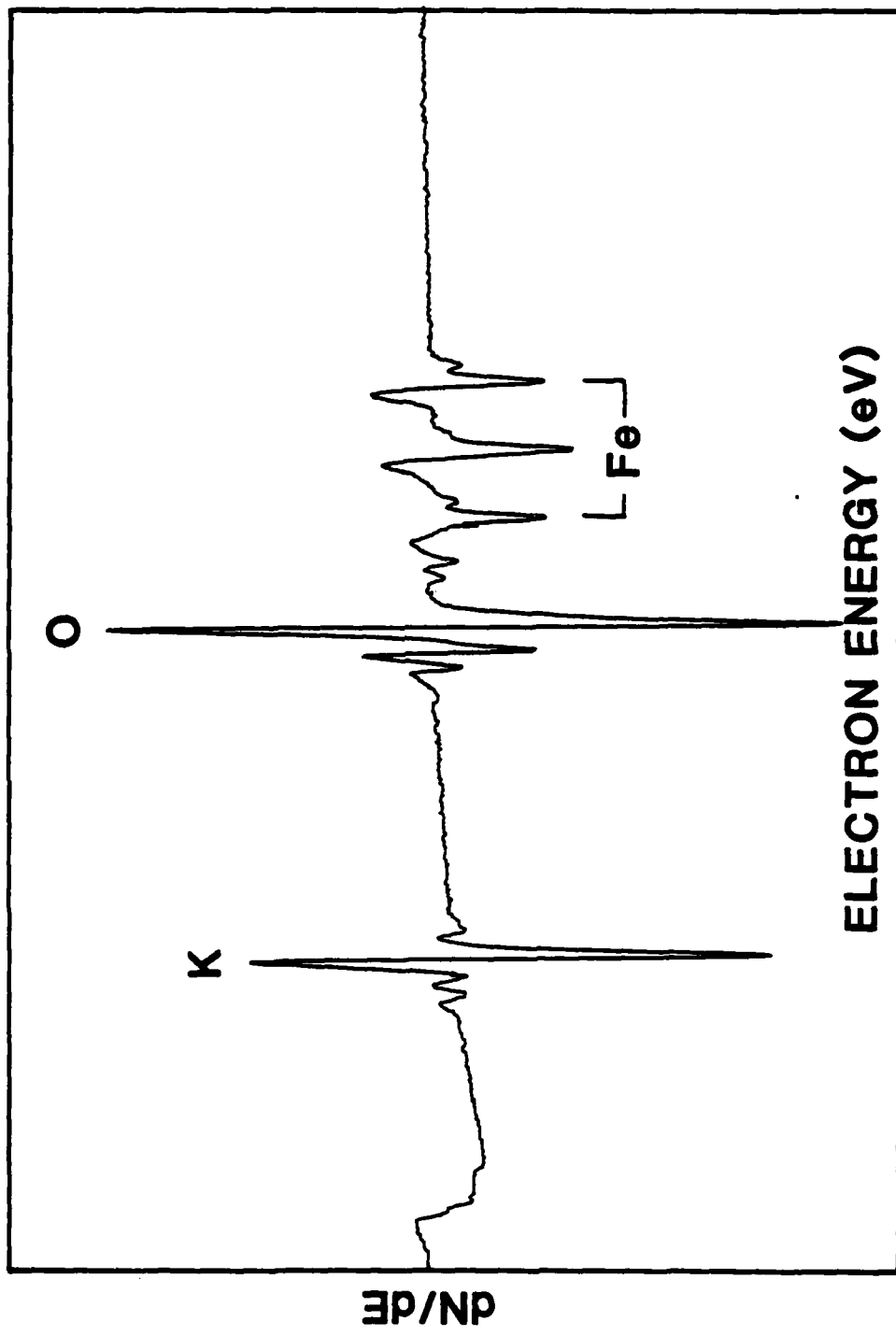


Figure 4. Auger electron spectrum of potassium exchanged surface,  
pH = 11.2.

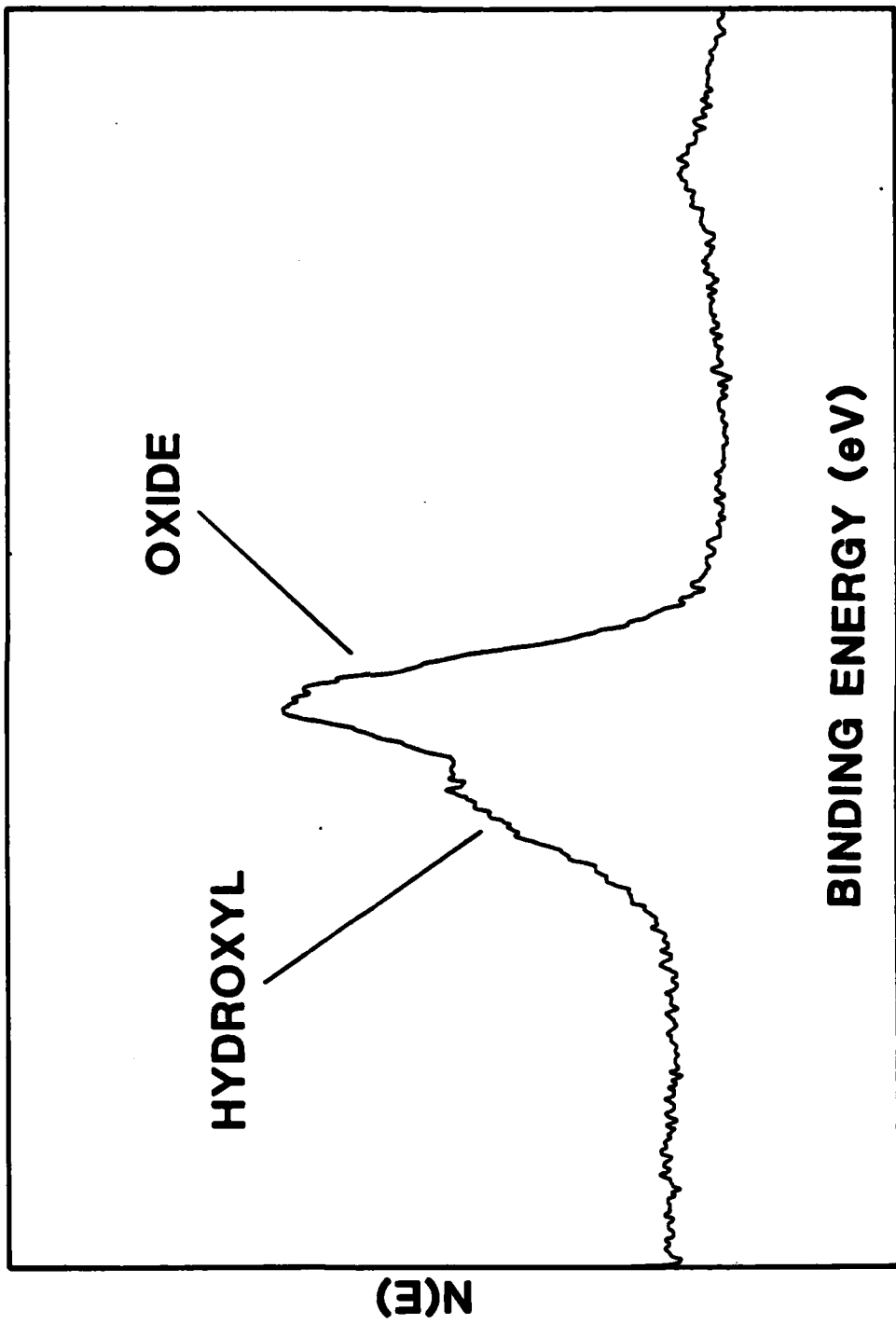


Figure 5. O(1s) X-ray photoelectron line of the potassium exchanged surface, pH = 11.2.

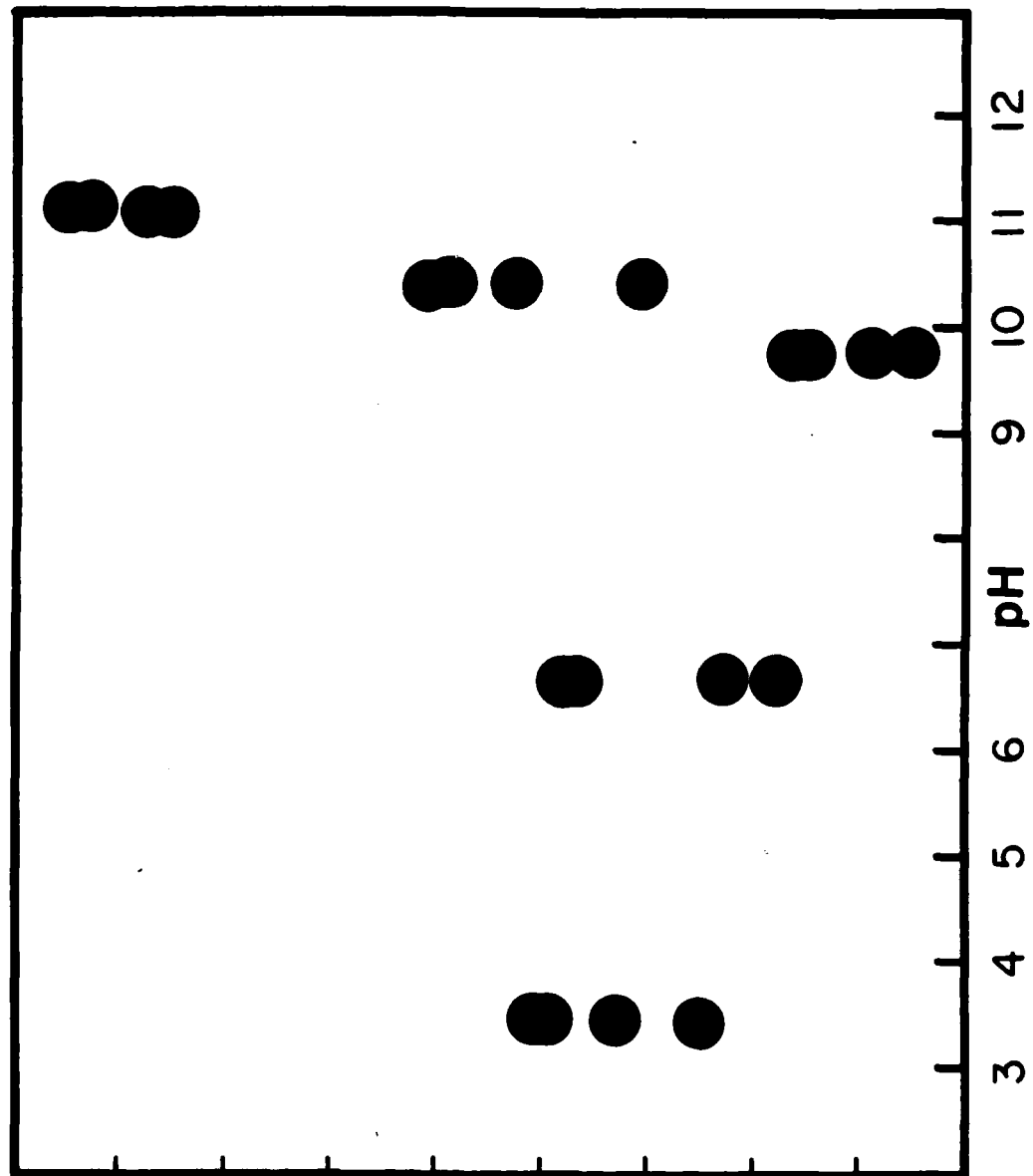


Figure 6. Auger intensity ratio ( $K/Fe$ ) as function of pH.

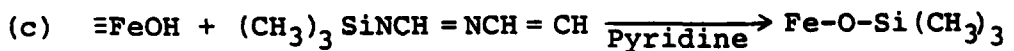
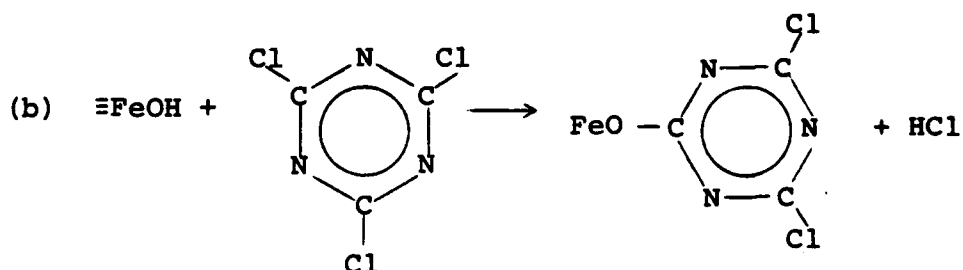
$K/Fe$

at a pH of 11.3 is shown in Figure 7, which shows C, S, Cl, N in addition to K, O and Fe. Carbon was the most often encountered extraneous element.

Once a procedure has been established for the preparation of reproducibly clean samples, studies of the interaction of the surface hydroxyls with various organic functional groups are proposed. Such experiments are of interest owing to their possible implication of the chemistry at a coating substrate interface. Choice of the functional groups can be based on the knowledge of the surface pKa gained from the K exchange experiments. At present, several molecules are under consideration; all have been used in various studies of weak acids or hydroxylated surfaces.



XPS nitrogen (1s) binding energy shifts can be noted relative to  $-\text{NO}_2$  nitrogen allowing for interaction strength study with various R groups.



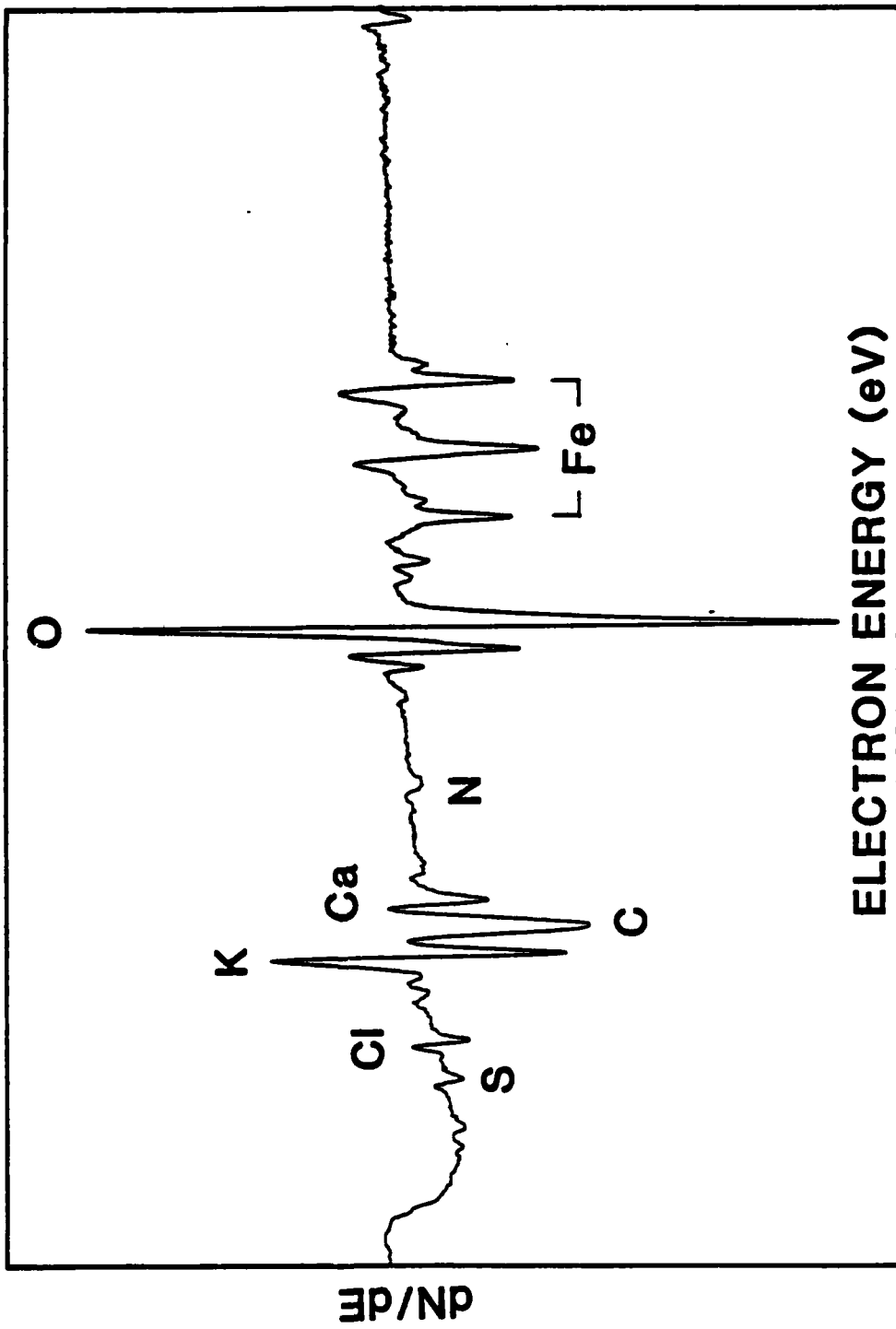


Figure 7. Auger electron spectrum of an exchanged sample which demonstrates the problems encountered in obtaining a reproducible "clean" surface, cf. Figure 4 for comparison.

Program #8. Cathodic Electrodeposition of Epoxy-Curing Agent Latex Mixtures

INTRODUCTION

The kinetics and mechanism of film growth by electrodeposition for the single component epoxy latex system using Epon 1001 (diglycidyl ether of bisphenol A) has been reported previously (First Annual Report pp.99-152). This work was then extended to a two component latex system using an emulsion of an amine adduct as a curing agent with the Epon 1001 latex. Some current-time curves for the two component system, Epon 1001 and Emerez 1511 (polyamide prepared from dimer acids and a diamine) were reported at that time. During the current period, the experimental work for the two component system was completed. The temperature build up in the film during electrodeposition as a function of applied voltage was studied, and so was the effect of agitation during film formation. The data were analyzed to study the kinetics of film formation from the two component system. A preliminary attempt was made to analyze the electrodeposited coat with respect to the unreacted epoxy and amine groups present in the film. The effect of incorporating a reactive diluent in the electrodeposition bath is under investigation. The current-time curves for the two component reactive system reported previously (see First Annual Report) were much different from those for the epoxy latex. The shape of the curve depended not only on the applied voltage but also on the composition and the time of aging of the mixture before deposition. It was therefore imperative to determine an optimum aging time prior to studying the other effects on the electrodeposition. By varying the deposition voltage and aging time after mixing the epoxy and the amine together, it was observed that the best current time curves were obtained for 2½ hr aging time.

RESULTS AND DISCUSSION

Deposited Mass-Time Relationship for Epon 1001-Emerez Latex Mixture

The kinetic data of deposited mass of the film as a function of deposition time, which resulted from the cathodic electrodeposition of the epoxy-curing agent latex mixture, aged for 2½ hr, at five different applied voltages (viz ~ 110 180 220 and

280 volts), were found to follow a linear function as shown in Figure 1. However, when the data were replotted against the square root and the logarithmic function of deposition time respectively, considerable scattering of the data points was noted and no obvious trend was observed as the applied voltage was varied. Thus, it could be seen that the data were best described by a linear deposition time dependency as was already observed in the single component system. According to Uhlig, ("Corrosion and Corrosion Control", p.156, John Wiley, 1963), this linear relationship indicates that the presence of the film does not affect continued film growth.

In contrast to the single component system, only one growth rate was observed for the entire deposition at low applied voltages, i.e., 90 and 140 volts. At higher applied voltages, i.e., 180, 220 and 280 volts, a change in the slope was noted at longer deposition times indicating a transition to a more gradual film buildup after the initial steep rise. The transition to a slower rate at longer deposition time could signify compaction of the coating film and/or more crosslinking, after a certain coating mass was reached, thereby slowing down the rate of further deposition. The initial growth rate was again strongly dependent upon the applied voltage. It varied from  $1.28 \times 10^{-3}$  to  $5.3 \times 10^{-3}$  g/cm<sup>2</sup>/sec; and as expected, higher film growth rates were associated with higher deposition voltages. These rates were comparable to the initial film growth rates for the single component system. The second slower growth rate at longer deposition time was found to vary within a narrow range from  $4.2 \times 10^{-4}$  to  $6.6 \times 10^{-4}$  g/cm<sup>2</sup>/sec in contrast to the single component system where a constant value of  $3.4 \times 10^{-4}$  g/cm<sup>2</sup>/sec was obtained. The absence of a transition to a slower growth rate at lower applied voltages could perhaps be taken as a lack of compaction of the deposited layer.

The initial linear portion of the deposited mass versus time plot for each applied voltage was found to pass through the origin. This result shows that the film growth rate was directly proportional to the deposition time, which would seem to be in agreement with previous observations by other workers on anodic deposition of polymer resins where film deposition starts almost instantaneously under constant voltage conditions. This is in contrast to the behavior of the single component system where an induction time was observed. The two component system is complicated by the simultaneous occurrence of hetero-flocculation and chemical reaction of reactive groups at the particle surface which would have a profound effect on the electrodeposition behavior. Furthermore, a decrease in viscosity as a result of hetero-flocculation could have altered the migration behavior of these particles. All these could have contributed towards the differences observed between the two systems.

When the deposited mass per unit area was converted to film thickness and the data plotted as a function of deposition time, a set of graphs similar to the mass deposited versus time plots

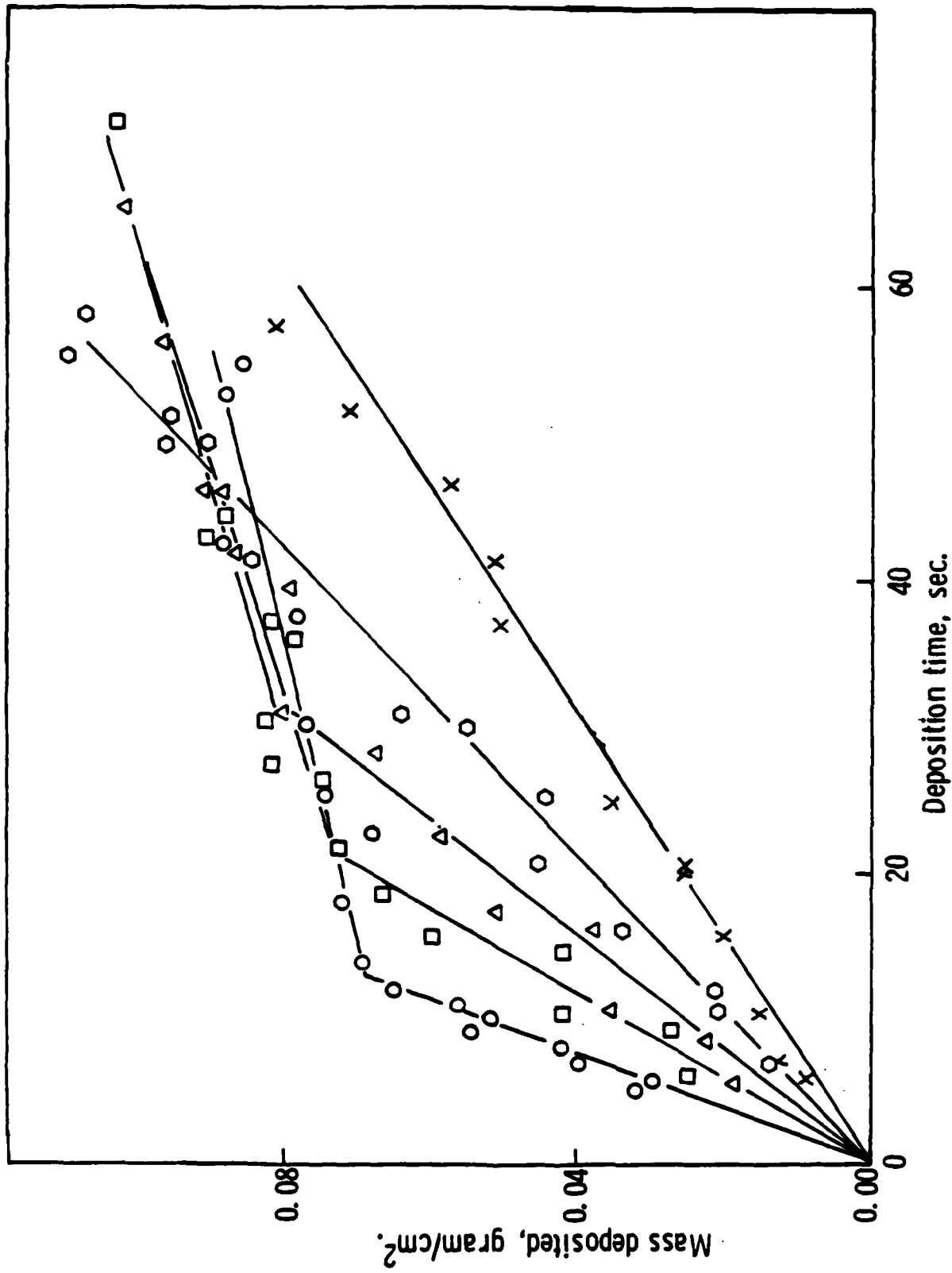


Figure 1. Mass deposited as a function of deposition time for various applied voltages 90 volts (x), 140 volts (O), 180 volts ( $\Delta$ ), 220 volts ( $\square$ ) and 280 volts (O) for stoichiometric latex mixtures of Epon 1001 and Emerez 1511 aged for 2½ hr at room temperature before deposition.

was obtained. In each case, the initial linear portion was strongly dependent upon the applied voltage; the higher the voltage, the higher the gradient, while the second linear portion had a somewhat constant gradient.

Coulombic Efficiency. The mass deposited per coulomb of charge passed for different deposition times at a given applied voltage is shown in Figure 2 for the highest and the lowest voltages used, i.e., 280 and 90 volts, respectively. These experimental data seem to fit a straight line passing through the origin. The gradient of these straight lines gives the coulombic efficiency (in g deposited/coulomb), for the deposition process. The data points for depositions at 140, 180 and 220 volts generally fell between the lines obtained for the depositions at 90 and 280 volts. The gradient of the line obtained for deposition at 90 volts is slightly less than that obtained for the deposition at 280 volts, but the difference is rather small, and so for practical purposes can be taken as constant. The average value for the coulombic efficiency thus calculated for the two component system was 98.3 mg/coulomb, which is higher than those obtained for the single component system (which was found to be in the range of 63 - 85 mg/coulomb).

Effect of Current and Applied Voltage. From the current-time curves at each applied voltage, the current densities at various time intervals were calculated and plotted against time, as shown in Figure 3, for three different applied potential values. Only the descending portion of the current-time curves after the maximum point "Y" on the current-time curves was considered (First Annual Report, Fig. 48, p.113). These plots showed that the maximum current density for all the curves decayed towards a common residual current of approximately  $7 \text{ mA/cm}^2$  regardless of the applied voltage. This value is higher than that obtained for the one component system (ca.  $3\text{mA/cm}^2$ ). However, it is also evident from Figure 3 that there is a marked decrease in current density with time for higher voltage, i.e., 280 volts, while this decrease is more gradual for the lower applied voltage, i.e., 220 volts. In other words, for deposition at higher applied voltage, there is a rapid current cut-off as the film becomes insulating, while for a lower applied potential, the current cut-off is more gradual indicating that the film remains conducting for a longer time. Furthermore, for an applied voltage of 180 or less, after the initial rapid decrease in the current density, a plateau region is reached, followed by a very slow and gradual decrease. This might be the result of different patterns of deposition behavior under low applied potentials; and, perhaps, different film morphology.

The current density-time curves were analyzed according to the treatment of Finn and Hasnip [J. Oil Color Chem. Assoc. 48, 1121 (1965)] where the reciprocal of the inverse square of the current was plotted against deposition time, as shown in Figure 4.

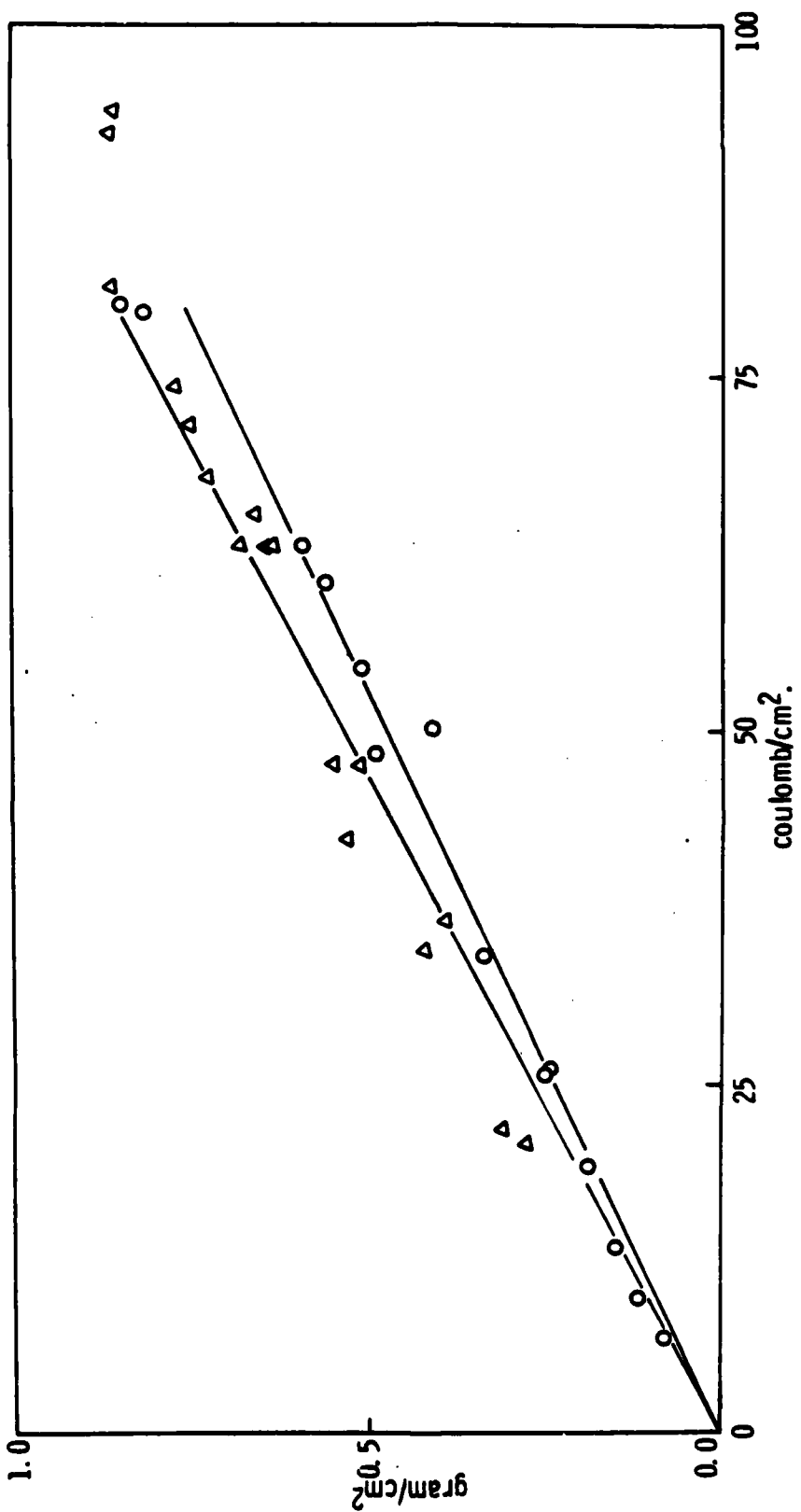


Figure 2. Mass deposited versus coulombs/cm<sup>2</sup> for various deposition times. Deposition voltage: 90 volts (O) and 280 volts (Δ). System: Stoichiometric latex mixtures of Epon 1001 and Emezez 1511 aged for 24 hr at room temperature before deposition.

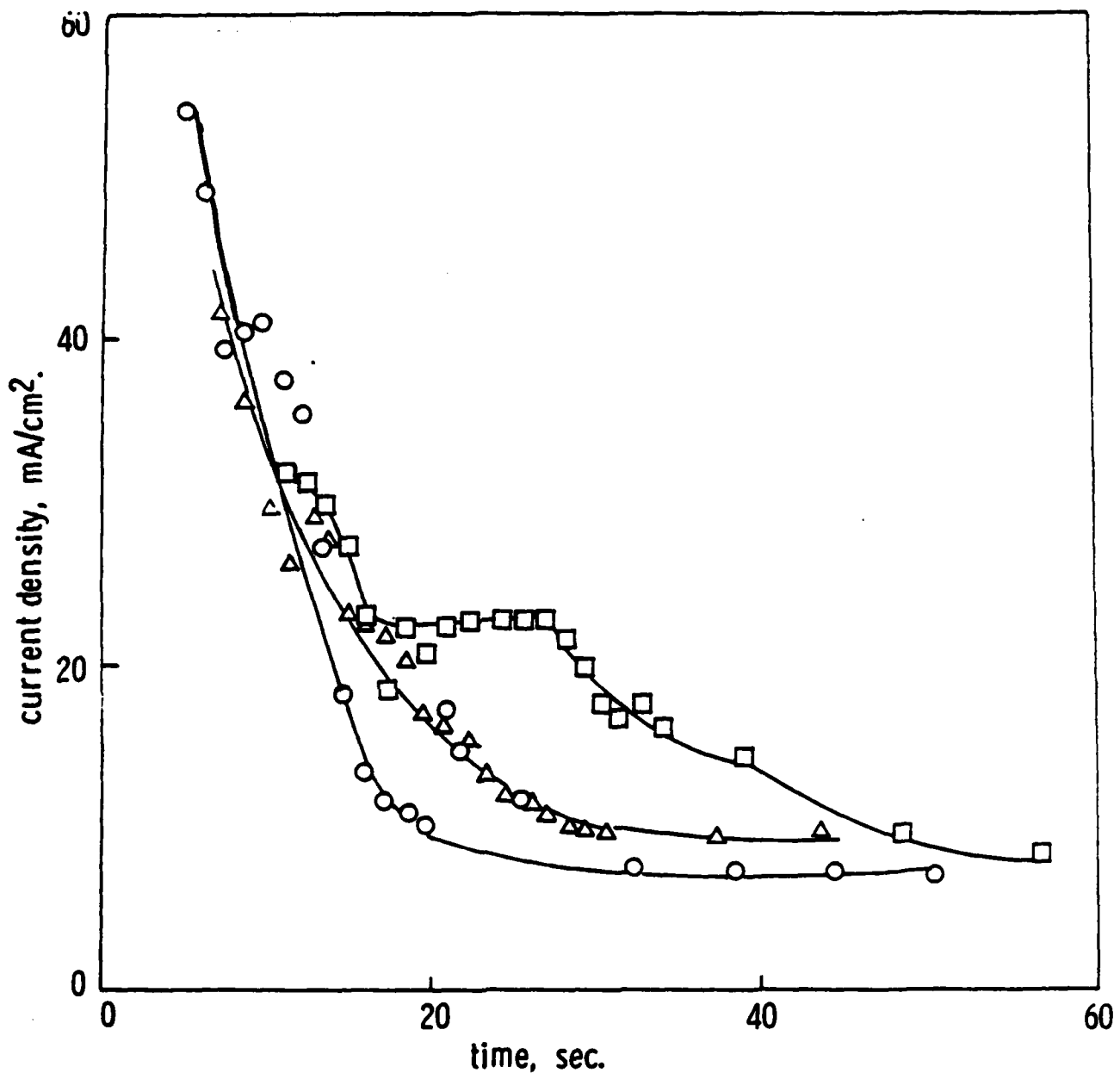


Figure 3. Variation of current density with deposition time for various applied voltages 180 volts ( $\square$ ), 220 volts ( $\Delta$ ), and 280 volts ( $\circ$ ), for stoichiometric latex mixtures of Epon 1001 and Emerez 1511 aged for  $2\frac{1}{2}$  hr at room temperature before deposition.

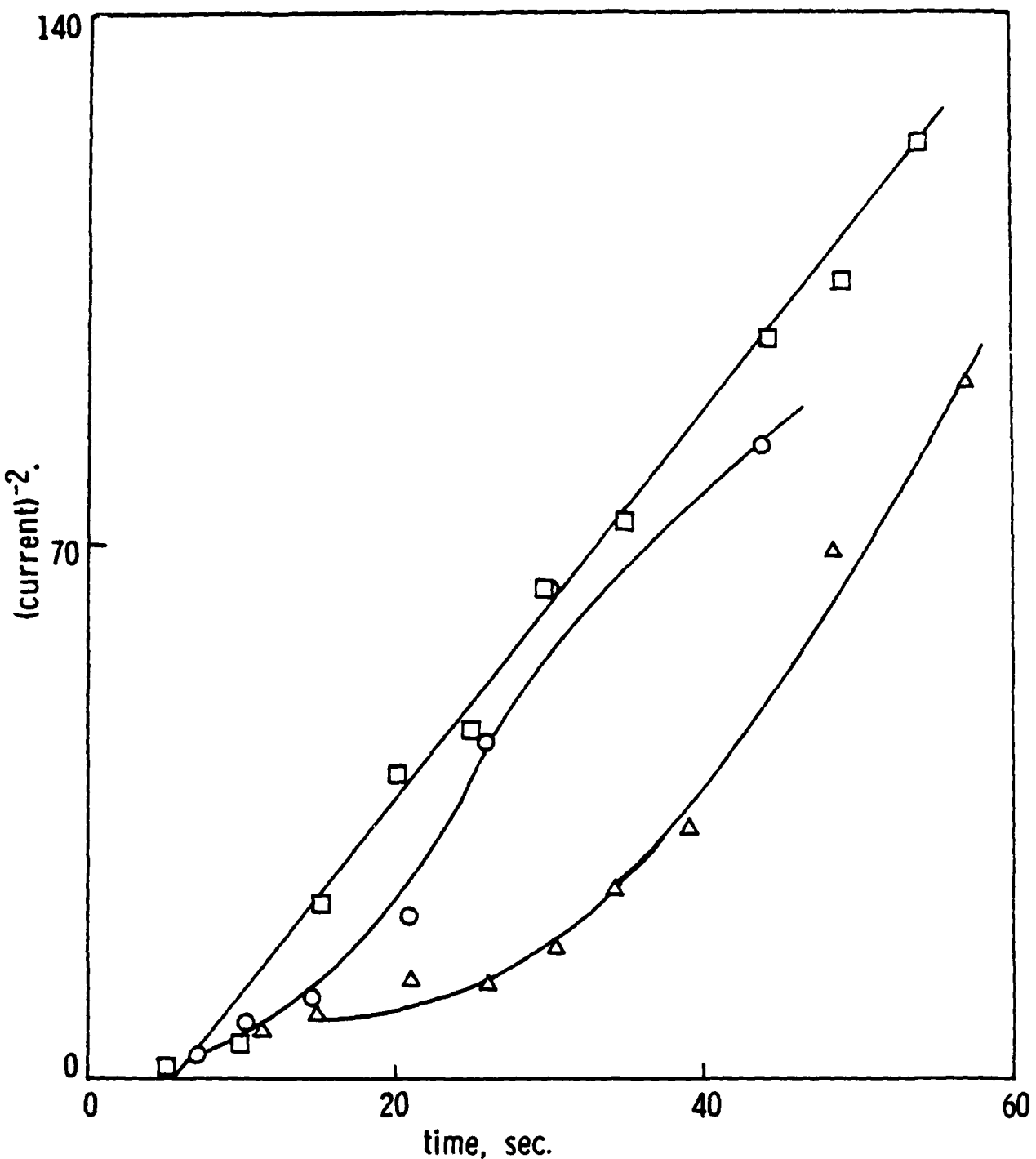


Figure 4. Reciprocal of square of current as a function of deposition time for 180 volts ( $\Delta$ ), 220 volts ( $\circ$ ), and 280 volts ( $\square$ ) for stoichiometric latex mixtures of Epon 1001 and Emerez 1511 aged for  $2\frac{1}{2}$  hr at room temperature before deposition.

For the deposition at 280 volts, a straight line relationship is found to hold indicating that the specific resistance of the film remains constant during the entire deposition period. On the other hand, a curve relationship was observed for deposition at lower voltages. The difference in the behavior of plots may indicate differences in the mechanism of the film build-up under the various applied voltages, and consequently differences in film resistance.

The above analysis points out that two different deposition patterns seem to exist; one at low applied voltage < 220 volts and the second at higher voltages. The deposition pattern should reflect the chemical and physical nature of the coating bath and the depositing film. It has been previously reported (S. Misra, Ph.D. Thesis, Lehigh University 1978) that, upon mixing curing agent latex together with epoxy latex, partial heterogeneous coagulation takes place between the smaller size latex particles (ca. 500A°) of the curing agent and the larger size (ca. 3000A°) epoxy latex particles to give larger globules. Chemical reaction between the epoxide groups and the curing agent will start immediately upon coalescence of the two components in the coating bath. Consequently, upon applying the voltage in the coating bath, the deposition pattern will be determined by the following factors: (i) the relative mobilities of the various species (namely, epoxy particles, curing agent particles and aggregated globules of these two); (ii) the degree of physical compaction at the cathode once deposition takes place; and (iii) the degree of crosslinking as a result of the chemical reaction between the epoxy and curing agent which takes place during aging and mixing in the coating bath as well as after the film deposition at the cathode. The temperature build-up at the cathode has to be considered, especially its effect on the curing reaction which takes place at the cathode.

It is suggested that at the lower applied voltage chemical segregation takes place within the thickness of the deposited film, as a result of differences in the electrophoretic mobilities of the different species in the coating bath. This may result in different degrees of physical compaction as well as differences in chemical composition across the film thickness. On the other hand, at higher applied voltages, perhaps the film is more homogeneous both chemically and physically. Further study of the hetero-flocculation which takes place in the coating bath prior to, and during the course of, deposition is required. Also chemical and morphological analysis of the film during the course of deposition must be conducted.

An attempt was made to calculate the field strength within the film during deposition. The field strength was assumed to be equal to the applied voltage divided by the instantaneous thickness of the film. A plot of current density versus field strength for various voltages (see Fig. 5) indicates that as the film thickness increases, both the field strength and the

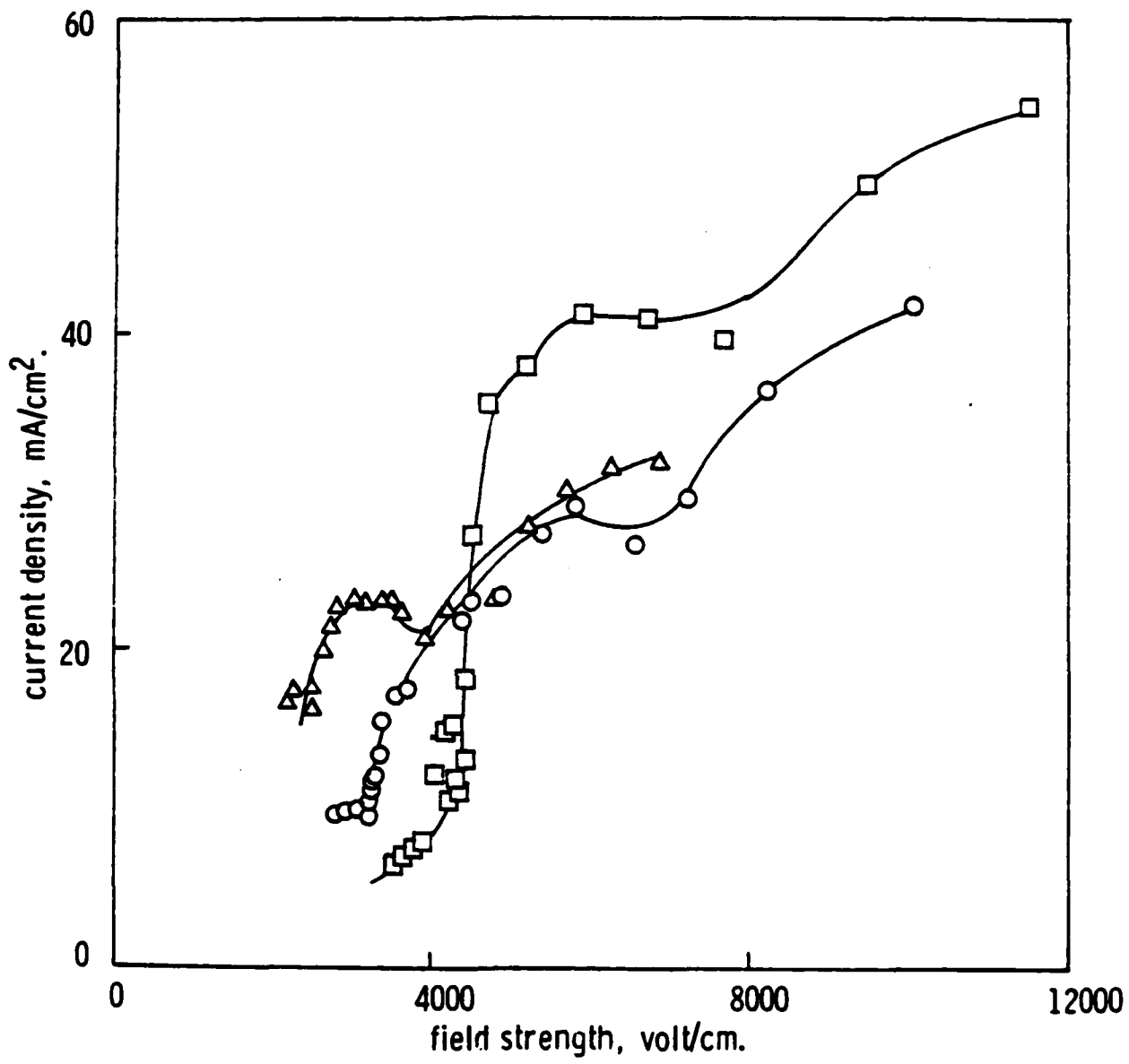


Figure 5. Current density versus field strength for various applied voltages 180 volts ( $\Delta$ ), 220 volts ( $\circ$ ), and 280 volts ( $\square$ ) for stoichiometric latex mixtures of Epon 1001 and Emerez 1511 aged for 2½ hr at room temperature before deposition.

current density decreases. This trend is somewhat similar to that obtained for the one component system. No linear relationship between the current density and field strength was obtained indicating that the current-time relationship was non-ohmic in nature. The field strength operating in the electrodeposition of latex system was found to be in the range of  $3-11 \times 10^3$  volt/cm. This range is about two orders of magnitude smaller than those reported for anodic deposition of solubilized polymer resins (i.e., ca.  $10^5$  volt/cm). The latex system requires less energy consumption for electrodeposition.

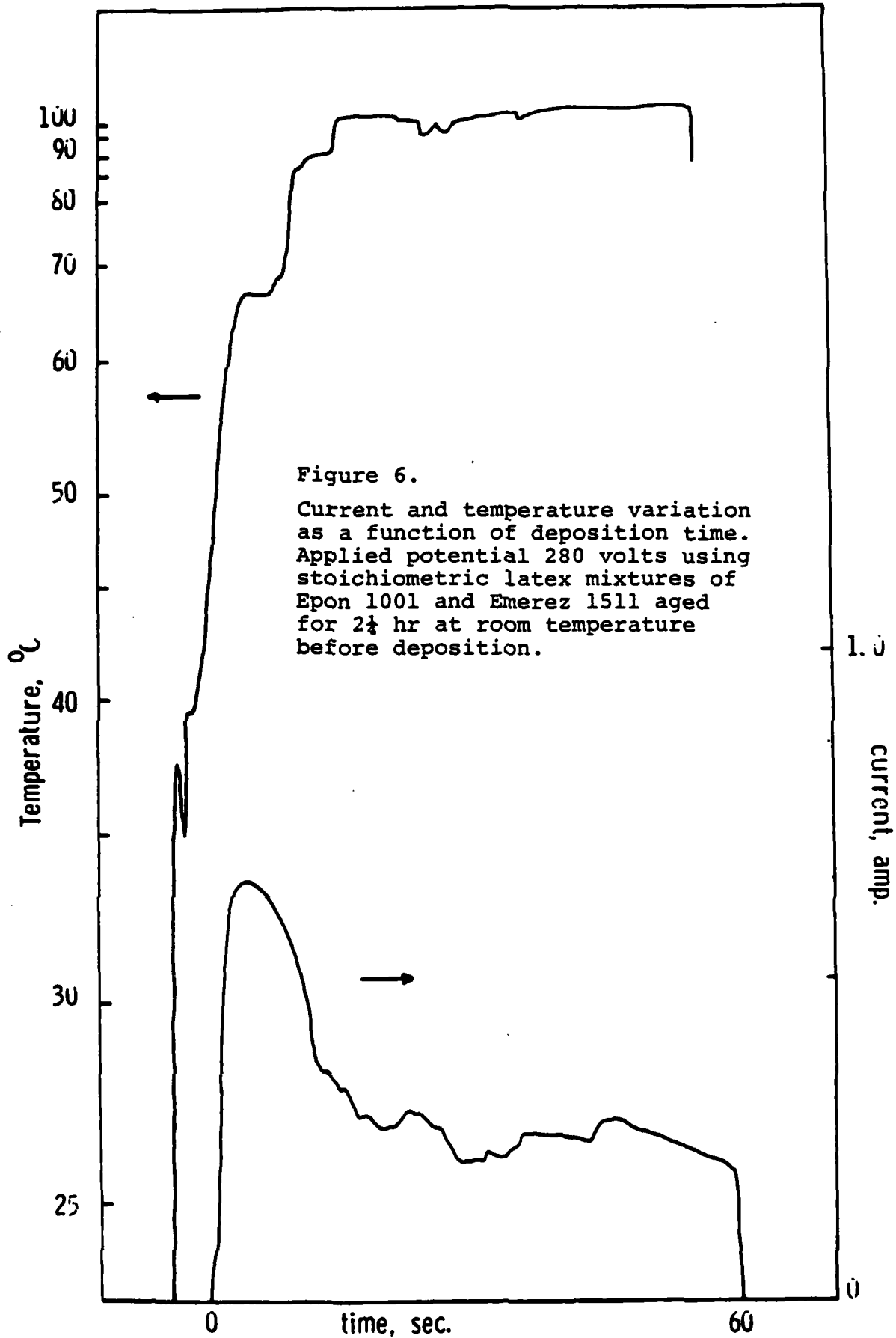
Temperature Build-Up during Deposition. A thermocouple probe was placed very close to the test panel to record the temperature inside the film as it was being formed. The response from the thermocouple was recorded as a function of time and current as shown in Figure 6. The temperature build-up inside the film during electrodeposition was found to reach the maximum value within 5-10 seconds from the beginning of the deposition process. The maximum temperature attained within the film was found to increase with increasing the applied voltage. Table I gives the temperature data as a function of applied voltage. The maximum temperature reached  $100^\circ\text{C}$  for the deposition at 280 volts. This high temperature build-up will have to be considered in analyzing the morphology and the curing properties of the deposited films. This temperature build-up in the vicinity of the cathode should be very important in improving the "flow" required to give coherent film. This will be specially important in case of deposition of materials with higher molecular weight where their  $T_g$  values are higher than room temperature, such as the phenoxy compounds.

To study the effect of agitation, a small magnetic stirring bar was placed inside the cell with current and temperature-time data being recorded as a function of applied voltage. The current-time curves obtained in this case were essentially the same but the maximum temperature developed inside the film was slightly lower.

Table I

Maximum Temperature Developed at the Deposited Film  
As a Function of Applied Voltage during the  
Cathodic Electrodeposition Process

<u>Applied Voltage</u>	<u>Max. Temp. Recorded</u>
280 volts	$100^\circ\text{C}$
220 volts	$81^\circ\text{C}$
180 volts	$58^\circ\text{C}$



Epoxy-Amine Analysis. As shown in previous sections, it is imperative to determine the degree of chemical heterogeneity within the epoxy film during the duration of electrodeposition. Consequently an attempt was made to determine the unreacted epoxy and amine groups present in the film, by potentiometric titration using a method outlined by Bell [J. Polymer Sci. 8, 417-36 (1970)]. The procedure for epoxy groups involves the reaction with pyridinium chloride, followed by titration of the excess pyridinium chloride with a standard base. The difference between the titer and a separate titer for the pyridinium chloride alone is attributed to the epoxy content of the sample. The procedure for amine groups involves the use of carbon disulfide to convert the primary or secondary amine to the corresponding thiocarbamic acid, which is then titrated with the standard base. In the combined method, the epoxy content is measured first and then the carbon disulfide is added, and the titer for the amine is obtained.

Dried electrodeposited films of mixtures of Epon 1001 and Emerez 1511 latex mixtures were filed using a half-round, double cut file. One gram sample of the filed film was used for each analysis. In a round bottomed flask were pipetted 50 ml of 0.2N pyridinium chloride, 50 ml reagent isopropyl alcohol and 25 ml distilled water. The filed sample was placed in the flask and refluxed for 25 minutes under continuous stirring with a magnetic stirrer. The solution was cooled to room temperature and poured into a standard 250 ml beaker, the pH of the above solution was around ca. 5.7. A standardized 0.5N NaOH solution was added in 2 ml increments until the increasing pH (near pH 7.0) indicated approach of the end point. By use of a microburet, 0.2 ml increments were added until the inflection point in ml of NaOH added versus pH was reached (pH ca. 10.5). At this point, 5 ml of carbon disulfide were added with stirring for 2 min before continuing the titration. The titration was continued by adding 0.2 ml of 0.5N NaOH every 2 min until the amine end point was reached. The carbon disulfide reacts with the NaOH in high concentrations of sodium hydroxide, and this is the reason for recording the pH at constant time interval. The amine end point occurs between pH 9.5 and 10.5. The difference in ml of NaOH between the first and second end points is a measure of the amount of unreacted epoxy present in the sample, while the difference between the third and second end points gives the amount of unreacted amine present in the sample. The results of one complete titration, which includes blank, epoxy and amine end points, are given in Figure 7.

The preliminary results of the epoxy-amine analysis in the films deposited over a period of 60 seconds are given in Table II. These results indicate that the amount of unreacted epoxy and amine groups averaged over the total film thickness which is electrodeposited over a period of 60 seconds is independent of the applied voltage. The aging time prior to electrodeposition

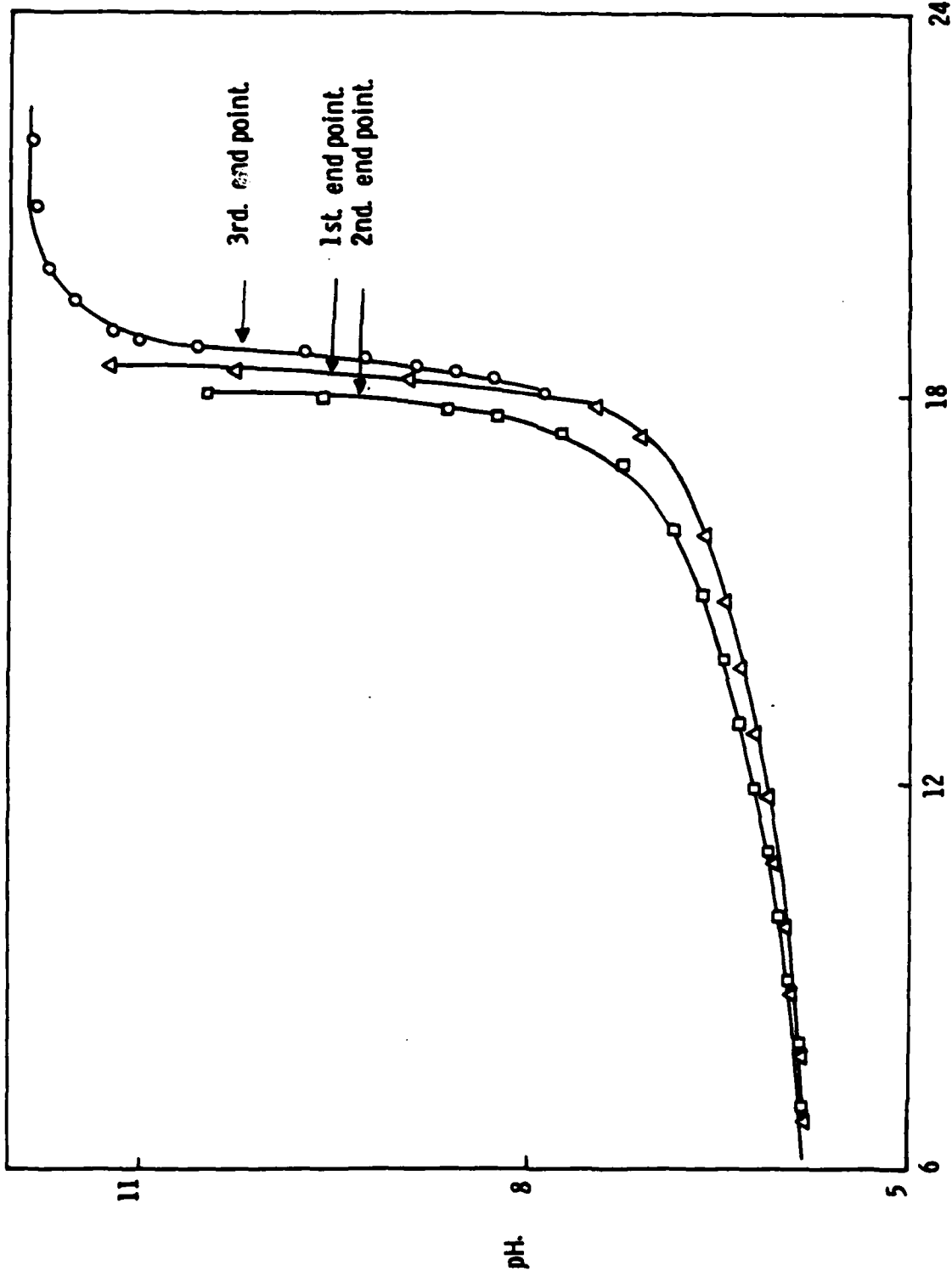


Figure 7. Potentiometric titration for the determination of unreacted epoxy and amine content in films which were cathodically electrodeposited using Epoxy 1001 - Emerez latex mixture. 1st end point for blank solution of pyridinium chloride, 2nd end point for unreacted epoxy, and 3rd end point for unreacted amine.

Table II

Sr. No.	Applied Voltage, Volts	Aging Time	Epon Emerez Ratio	First End Point		Second End Point		Third End Point		Unreacted Epoxy meq/g	Unreacted Amine meq/g
				ml	ml	ml	ml	ml	ml		
<u>0.5N NaOH</u>											
1	170	2	2:1	18.4	17.91	18.7		0.49		0.81	
2	210	2	2:1	18.4	17.9	18.75		0.52		0.88	
3	300	2	2:1	18.4	18.0	18.7		0.50		0.87	
4	230	3	45	2.5:1	21.4	20	20.6	1.26		0.54	
5	230	4	45	2.5:1	21.4	20	20.7	1.05		0.53	

seems to have an effect on the unreacted epoxy content in the deposited film as shown in Table II. This work will be extended to determine the instantaneous film composition as a function of deposition time and the applied voltage.

## Program #9. Drying and Curing of Epoxy Films

The objectives of this work were: (i) to generate drying curves, under different drying conditions, for various formulations of epoxy-curing agent mixtures; (ii) to study the mechanism(s) of drying and curing of epoxy films.

The following mixtures of epoxy-curing agent were studied: (i) Solvent-based Epon 1001 and Emerez 1511; (ii) Aqueous-based Epon 1001 and Emerez 1511 latex mixtures [Lehigh formula]; (iii) Aqueous-based modified Epon 1001 and Emerez 1511 latex mixtures [Lehigh formula]; (iv) Modified water soluble Epi-Rez 510 liquid epoxy resin and Epi-cure W-50-8535 [Celanese formula]; and (v) Modified water soluble Epi-Rez 510 liquid epoxy resin and Epi-cure WC-60-8537 [Celanese formula].

During the past year the drying curves were generated under various drying conditions: relative humidity 10-52%; air velocity 0-76 cm/sec, and temperature 25-40°C. A chemical engineering analysis of these drying curves has been completed.

A Master's thesis (by B. Aremu) has been completed and accepted by the Department of Chemical Engineering. The thesis Abstract is as follows:

"The investigation of the effect of temperature, relative humidity and the flow rate of the drying air on the drying rate of latexes was carried out in an experimental wind tunnel. The gravimetric technique was used to measure the evaporation rate of water and other volatiles from thin films cast from epoxy resin-curing agent systems on flat glass plates. The drying air conditions were at 10.0% to 52.18% relative humidities, 0.0 to 76.2 cm/sec air velocities, and 25.0°C to 40.0°C temperatures. The drying rates were calculated from the weight loss that resulted from the evaporation of water and other volatiles and from the wet area data under the assumption that evaporation occurred only from the wet portion of the film in the period during which experimental data were gathered. This assumption was necessary because of the limitation in the collection of data in the present experimental method.

"In general, the drying rates were observed to increase as the air flow rates and temperatures were increased and to decrease as the relative humidities were increased. Distinct drying behaviors were observed to exist between the aqueous-based latex system

solvent-based system, and the aqueous-based solubilized systems. The drying behavior of the solvent-based system in this study appeared to be in agreement with the generally accepted drying characteristics of solvent-based paint films, i.e., the "wet" stage when the solvent loss is fairly rapid and related to the volatility of the pure system and the "dry" stage. The drying rate (flux) for the solvent-based system ranged between  $4.5 \times 10^{-5}$  (g/cm<sup>2</sup>-sec) per g moisture content at the beginning of the drying operation, and  $0.5 \times 10^{-5}$  (g/cm<sup>2</sup>-sec) per g moisture content at the end of the experimental study. The aqueous-based latex systems displayed a drying pattern characterized by an initial relatively low and constant rate [in the range of  $1.0 \times 10^{-5}$  (g/cm<sup>2</sup>-sec) per g moisture content] followed by an increased flux [order of  $1.0 \times 10^{-4}$  (g/cm<sup>2</sup>-sec) per g moisture content] as the drying operation proceeded. The drying behaviors of the aqueous-based solubilized systems were observed to be intermediate between those of the solvent-based and aqueous-based latex systems.

"An explanation of the reasons for the differences observed in the drying characteristics of the various coating systems based on the phenomenon of skin-formation is suggested."

#### Modification of Wind Tunnel

This work is being continued by Mr. A. Rahman with the following objectives: to extend the drying curves to higher humidity (>50%) and higher temperature (>40°C); to characterize the morphology of the epoxy films dried under different conditions; and to initiate work on the rates of drying of pigmented epoxy systems.

In preparation for this phase of the work, the previous wind tunnel has been modified to improve the drying conditions and increase sensitivity of measurements of temperature, air velocity and relative humidity in the test chamber, as well as the use of a 35 mm camera to record the wet/dry areas in the films during the drying process.

Accurate measurements of the changes in film weight, and reduction in the fluctuations in the specified parameters during the process of drying, are critical to any meaningful interpretation of data particularly while handling thin films. The drying apparatus used previously (B. Aremu, M.S. Thesis, Lehigh University 1981) is modified to further reduce the possibilities of fluctuations in the temperature and relative humidity of the drying air. The plywood control section has been replaced by a 22 x 6.5 x 6 in. plexiglass air conditioning and mixing duct. The control section was divided into two sections:

the air conditioning zone and the mixing zone. The conditioning zone consists of a heater, and air and water vapor supply ducts. The walls of this section are insulated with asbestos to protect them from the heat of the heater and to minimize the effect of environmental conditions. The mixing zone contains baffles to mix air thoroughly before it enters the experimental tunnel. The baffles are arranged to turn the air twice around a horizontal axis and then twice around a vertical axis, when it finally discharges through an orifice into the wind tunnel. This arrangement allows a thorough mixing of air to maintain uniform conditions throughout the wind tunnel. The start-up period usually requires about two hr or more, but operating conditions are steady once they are achieved. Figures 1 and 2 illustrate the system being used.

Other improvements in the experimental drying set-up and techniques include the replacement of thermometers being used for determining the temperature with a set of more accurate ones. Also, the anemometer for air velocity measurements is replaced by a later model of the same type. The water reservoir of the wet bulb thermometer is shifted in the drying tunnel, so that the make-up water supplied to the bulb should be at the wet bulb temperature with the result of reducing the dependence of wet bulb temperature on air velocity. A single lens reflex camera with a close-up lens has been installed on the test section of the apparatus to take pictures of the drying film, for determining the wet area. A variable speed mixer with a glass rod is employed at a constant RPM to mix epoxy and curing agent for greater reproducibility of mixing and curing.

Currently experiments are being carried out to repeat some of the trials performed earlier, using the modified apparatus under identical conditions of specific parameters for evaluating the effect of above-mentioned modifications on the drying rates of epoxy resin-curing agent systems. Experiments will be conducted in order to generate rates of drying curves for the epoxy-curing agent systems to cover humidity ranges above 50% and the drying temperature above 40°C.

Work will be initiated to study the rates of drying of formulated pigmented epoxy-curing agent systems for corrosion protection, and correlate the drying behavior with morphology of coating films and efficiency of corrosion protection.



Figure 1. View of the system being used for studying the drying behavior of epoxy films.



Figure 2. Close-up of system being used for studying the drying behavior of epoxy films.

## Program #10. Detection of Aggregated Water in Polymer Coatings

### INTRODUCTION

The detection of water within organic coatings is of interest since corrosion under coatings is dependent on the presence of water. It may either exist as individual molecules randomly dispersed in the coating (mobile water) or as aggregated "drops" throughout the coating or at the coating/substrate interface (aggregated water). Of special interest is the aggregated form which may eventually lead to corrosion and coating failure. The differentiation and location of these two forms by some analytical means would be very useful in studying the corrosion process under coatings.

The technique that has been selected for initial examination is the dielectric response over a frequency range. Aggregated water will react differently to an applied alternating electric field than will an isolated water molecule. The location of the water aggregate will also determine to some extent the dielectric response. Because water is such a small molecule, no appreciable change in the dielectric value occurs until the giga-hertz region ( $10^9$  c/sec) is reached. Direct frequency measurements in this region become experimentally difficult. The high frequency dielectric response, however, can be obtained in an indirect manner by a technique called Time Domain Spectroscopy (TDS).

#### Time Domain Spectroscopy—Basic Theory

As mentioned, high frequency measurements become difficult using direct frequency measurements. One can, however, ascertain the same information using a time variable or time domain technique. In a time domain measurement the system is perturbed and the response in time is monitored. With time domain information the frequency response can be obtained using a mathematical transform. In this case the transform (commonly called the Fourier Transform) process involves a redistribution of the information from the time to frequency domain.

The time domain response in TDS results from the application of an electrical pulse to the system under test. A typical TDS pulse has an extremely fast rise time ( $20 \times 10^{-12}$  sec) and requires specialized equipment in order to monitor a response. The sample under test is usually placed in a coaxial line which constrains the pulse. When the pulse travels down the coaxial line and encounters a change in dielectric permittivity (sample), it

is partially reflected and partially transmitted. The size and shape of the reflected pulse are the time response of interest. The reflected pulse is mathematically combined with the incident pulse to give a response function which can be related to the frequency dependent dielectric response.

Perhaps the best way to understand a time domain technique is to consider the incident pulse as a combination of all frequencies delivered at once. Thus the reflected pulse contains the response of all the frequencies brought about by the sample. The Fourier Transform process then allows the sorting out of each frequency response. The ability to measure high frequencies with this method requires that a very small time scale be used while in the time domain. Details of how these measurements will be made are given in the next section.

## EXPERIMENTAL CONSIDERATIONS

At the present time there does not exist a commercial domain "spectrometer". Any research in this area requires the experimenter to design and build an instrument based on several fundamental components. A time domain spectrometer can be broken down into three basic sections: data acquisition and processing, high speed pulse measurement, and sample cell arrangement. Descriptions of each section are given below.

Data Acquisition and Processing. Data acquisition and processing are actually two different functions; however, both are best carried out by a computer. The data acquisition system has several responsibilities. First, it must obtain the data in computer-compatible form and store data for later use. Second, it must allow the experimenter to acquire data from different sources and at different rates. Third, based upon data received, it must provide any feedback operations necessary for an intelligent data taking device. Data processing can begin once the data are obtained and stored in the computer. All the mathematical analysis required can be performed at this time.

High Speed Pulse Measurement. Monitoring a TDS pulse requires sophisticated equipment. Fortunately such equipment is available commercially from several sources. The specific device required is a sampling oscilloscope. A sampling oscilloscope is much like a conventional oscilloscope but is constructed so as to permit very fast pulses and reflections to be recorded.

Sample Cell Arrangement. The arrangement of the sample cell is very important in TDS. Since the application of TDS to organic coatings is new, experimentation with the method of sample

cell arrangement will be necessary. Thus it is very important to insure the TDS system works properly before any such experimentation begins.

#### CURRENT STATUS

The effort to initiate TDS measurements commenced in the fall of 1980. A thorough literature investigation was made and visits were made to Bell Telephone Laboratory in Murray Hill, New Jersey, to discuss the best components to use. The following system design resulted.

Data Processing. The complex Fourier Transform will be carried out using the Lehigh computing center. Availability of high level languages and mathematical subroutine packages make the transform process manageable.

Data Acquisition. The real time nature of the data necessitate a dedicated microcomputer. A Rockwell International AIM-65 microcomputer was chosen for its flexibility and superior micro-processing capabilities. Actual interface electronics have been built and the design and writing of appropriate software has been initiated.

High Speed Pulse Measurement. A Hewlett Packard sampling scope consisting of an 1817A remote sampler, 1815B sampler, 1106B tunnel diode pulse generator, and 180C mainframe scope were decided upon.

Sample Cell Arrangement. The sample cell in all likelihood will be of custom design and will be constructed. Appropriate connectors and coaxial lines from GenRad will be used to transmit the TDS signal.

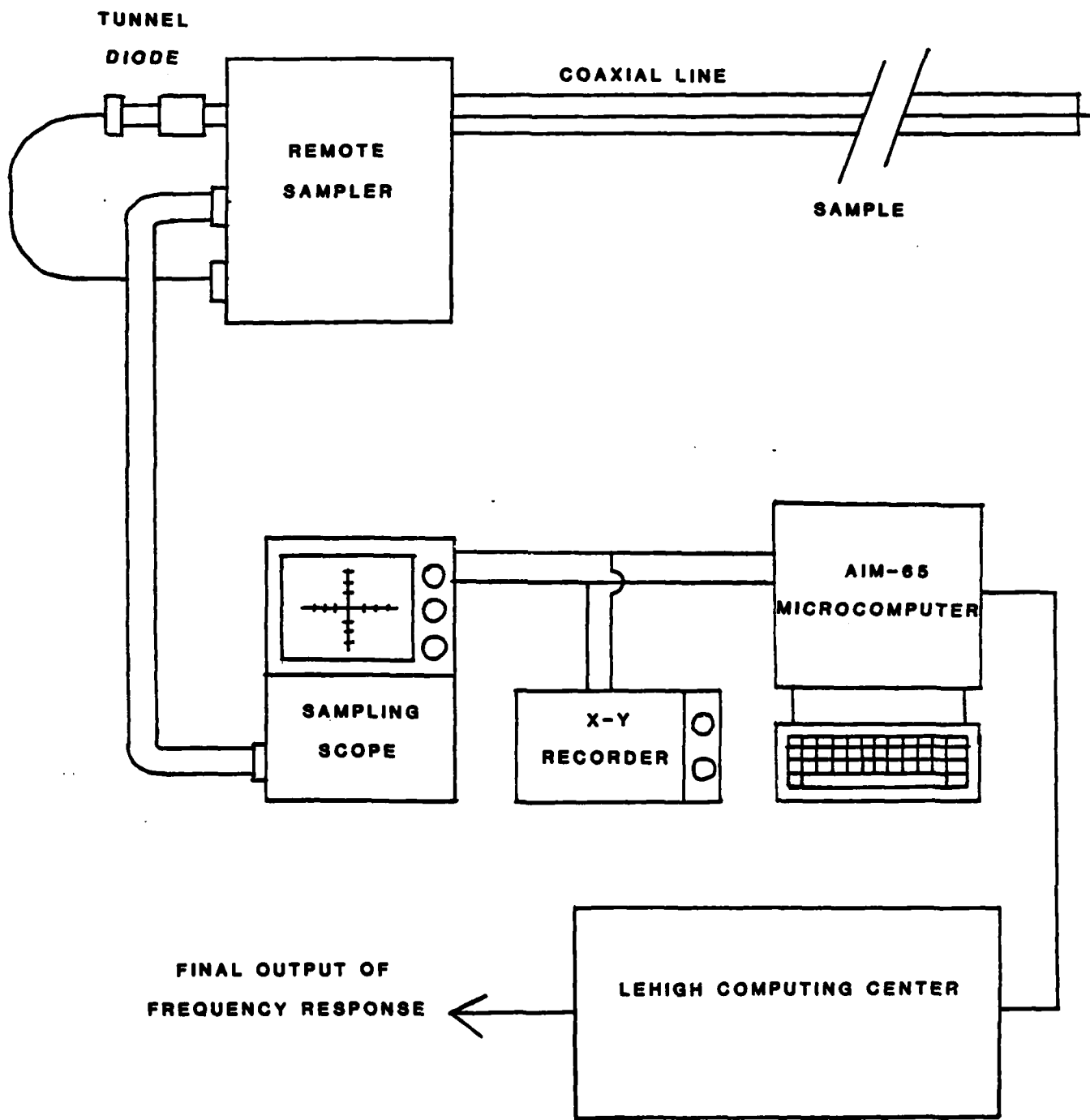
Actual construction and assembly began in the early part of 1981. At the present time the basic TDS system is near completion. The most difficult connection, that between oscilloscope and AIM-65, has been completed along with the successful reading and storing of data from an actual oscilloscope trace. This connection was accomplished by constructing a general purpose interface panel which was then configured to the oscilloscope outputs. Along with the interface electronics a computer card containing more data memory, permanent program memory, and additional input/output lines was developed and constructed.

Upon completion of the electronic interface details a series of computer programs for the AIM-65 were written. The programs perform a variety of functions which are required to obtain,

format, and store data from the oscilloscope. Presently underway is the connection of the AIM-65 microcomputer to the Lehigh computer center via the phone line. Several high level data processing programs needed to perform the mathematical analysis have been completed.

Significant progress towards the successful design and construction of a TDS "spectrometer" has been made. It is anticipated that the flexibility of the system will allow greater ease of experimentation with the sample cell arrangement and eventually in obtaining information which may lead to the detection and better understanding of aggregated water in organic coatings.

## TIME DOMAIN SPECTROSCOPY SETUP



## Program #11. Pigment-Binder Interactions in Corrosion Protecting Films

### INTRODUCTION

Coatings based on zinc pigments are generally recognized as being the most effective in protecting steel against corrosion, e.g. in marine environments. Concentrations of Zn between 85 and 96% are commonly used, the optimum concentration depending on the binder [1-3]. Inert Fe-P alloys, e.g. Fe<sub>2</sub>P, may also be used as extenders [3,4]. While ordinary drying oils are unsatisfactory as binders due to the formation of Zn soaps [5], plasticized or inherently flexible polymers such as polystyrene, vinyl copolymers, chlorinated rubber, and epoxies are suitable. In particular, polyamide-cured epoxies have been of special commercial interest in the form of quick-drying formulations; also, the polyamide itself is believed to have an inhibiting effect on corrosion [6]. With a given formulation, the pigment must be present at a concentration high enough to ensure polarization resistance but not so high as to reduce cathodic protection and minimize self-healing [1].

While the mechanism of protection is evidently complex [1-3], several major phenomena appear to be involved: electrochemical (cathodic) protection and the generation of inhibitive zinc compounds in the pores. The former is important because cathodic alkali is necessary in order to precipitate the Zn compounds. While some researchers hold that these compounds protect by sealing the pores [1,2], there is evidence of specific inhibition by deposition of these compounds on the steel substrate. Since the interfacial aspects of Zn-based coatings have received little attention, we decided to examine the role of pigment-binder interactions in more detail.

### PREVIOUS LEHIGH WORK

In the previous report period, the adsorption of acidic and basic polymers on zinc dust was studied, several Zn-based coatings were studied, preliminary measurements of drying rates and dynamic mechanical response were made, and preliminary observations of fracture surface morphology and of salt diffusion were made. It was shown that Zn dust appeared to possess acidic sites, and the kinetics of drying were established as a function of temperature.

During this period, our graduate student, Mr. M. Heffelfinger, resigned to take an industrial position at the end of 1980, and Mr. A. Tiburcio (a graduate student in Chemical Engineering) joined us in June. Mr. Tiburcio has refined our techniques, and undertaken to complete the work begun on characterization of the drying and curing stages, the morphology, and the mechanical and permeability characterization. Having established base-line properties, he will also begin studies of supported films to obtain correlations between corrosion protection and film characteristics.

## EXPERIMENTAL

### Film Compositions

The formulation reported in a General Mills Technical Bulletin [8] was used to make the 80% zinc-rich epoxy primer. Epon 1001F (Shell and Polyamide 1511 (Emerez)) constituted the binder for this epoxy system. Zinc dust #22 (New Jersey Zinc Co.; 8  $\mu\text{m}$  in av. diameter). After mixing, films were cast on 6" x 6" Teflon-Coated glass plates using a #55 RDS coating rod. The films were allowed to dry for 24 hr at room temperature. This technique yielded flexible, undistorted films, 0.09 to 0.12 mm thick, of excellent and uniform appearance. Curing conditions were varied as in Table II.

### Solvent Retention

The rate of further drying was determined gravimetrically [9-11] using 2" x 3" specimens and was examined under dry and laboratory atmospheres, and at both atmospheric and reduced pressures. Data for 3 specimens were averaged in each case; correction for variations in film thickness was negligible.

### Differential Scanning Calorimetry (DSC)

Specimens were scanned in a DSC unit (Perkin-Elmer, model DSC-1B) at a rate of 20°C/min to obtain glass transition temperatures ( $T_g$ ) and to look for evidence of incomplete curing [12].

### Scanning Electron Microscopy (SEM)

Fracture surfaces were coated with an Au/Pt layer, and examined using an ETEC SEM unit.

Table I  
Formulation [8] of 80% Zinc Rich Primer

<u>Ball Mill Base</u>	<u>Fraction of Component in the Primer</u>
Zinc dust #22 (N.J. Zinc Co.)	0.621
Bentone 27	0.00631
Methanol	0.00291
Epon 1001 F (Shell)	0.101
Xylene	0.0951
Methyl Isobutyl Ketone	0.0388
n-Butanol	0.0573
 <u>Versamid Hardener</u>	
Versamid (Polyamide 1511; Emerez)	<u>0.0776</u>
Total	100%

Table II  
Curing Conditions for Zinc/Epoxy Films

1. Room air ( $T = 24\text{--}28^\circ\text{C}$ )
2. Restricted access to air ( $T = 24\text{--}28^\circ\text{C}$ )  
(in desiccator with open valve)
3. Restricted access to air, but dry ( $T = 24\text{--}28^\circ\text{C}$ )  
(in closed desiccator).
4. Under vacuum (30 in of Hg) ( $T = 27\text{--}28.5^\circ\text{C}$ )
5. Under vacuum (30 in of Hg) ( $T = 38^\circ\text{C}$ )
6. Under vacuum (30 in of Hg) ( $T = 70^\circ\text{C}$ )
7. Under vacuum (30 in of Hg) ( $T = 88^\circ\text{C}$ )

## RESULTS AND DISCUSSION

### Drying Behavior

During the 24-hr pre-drying, an average of 13.4% ( $\pm 1\%$ ) weight was lost, in comparison with the theoretical limit of 15.5% fixed by the formulation. The drying behavior under the various conditions used subsequently is shown in Figures 1 and 2. Significant fluctuations were observed in the early stages of measurement of % weight loss, especially with the specimens dried at atmospheric pressure. Some variation was random, and in one case (condition 3) an initial increase in weight was noted (the cause being unknown). Anomalies were noted in the early stages at 70 and 88°C in the vacuum drying experiments.

With drying at atmospheric pressure (conditions 1, 2 and 3), data conformed reasonably well to a dependence on  $\sqrt{t}$ , where  $t$  = time, once steady-state drying rates were achieved (after ~600 and 1200 min for the closed-desiccator experiments). This dependence is not surprising, for the drying times are long enough that the drying process should be dominated by bulk diffusion rather than by surface evaporation [11]. However, a steady-state concentration of residual solvent has clearly not yet been achieved. Extrapolation of the current data to zero solvent content indicates times of 980, 1120, and 1170 hr for conditions 1, 2, and 3. However, extrapolation of wt loss vs  $1/\sqrt{t}$  suggests that no more than 0.8 to 0.9% could be removed at  $t = \infty$ . These estimations correspond to total solvent losses between 14.2 and 14.3%, in good agreement with the case of vacuum drying (see Table III). To reach the steady-state solvent loss obtained by vacuum drying (~14%, or 90% of the original solvent), from 30 to 40 days would be required. As expected, evacuation and temperature both affect weight loss, though the behavior is complex. At 28, 38, and 70°C a steady state is reached at ~0.7, 0.9, and 14 g wt loss, respectively. However, the behavior at 88°C is anomalous, the wt loss reaching only 0.9 g. Thus, at the highest temperature, either the state of the polymer has been changed due to changes in the degree of curing or in the crosslinked network, or else the entrapment of solvent in the quickly cured network.

In any case, it is likely that up to 10% solvent may be retained, regardless of the rigor of drying. While the experimental error of  $\sim \pm 1\%$  (in absolute wt loss) implies that nearly complete drying (~15%) may have been obtained, the trend in Table 3 suggests that at least a few percent of solvent may be expected. This is not surprising [11] and does not imply a deleterious effect on properties, but obviously any comparison of properties must take into account residual solvent. Gas chromatography is a useful routine method for such characterization, and in addition would define the composition of residual solvent.

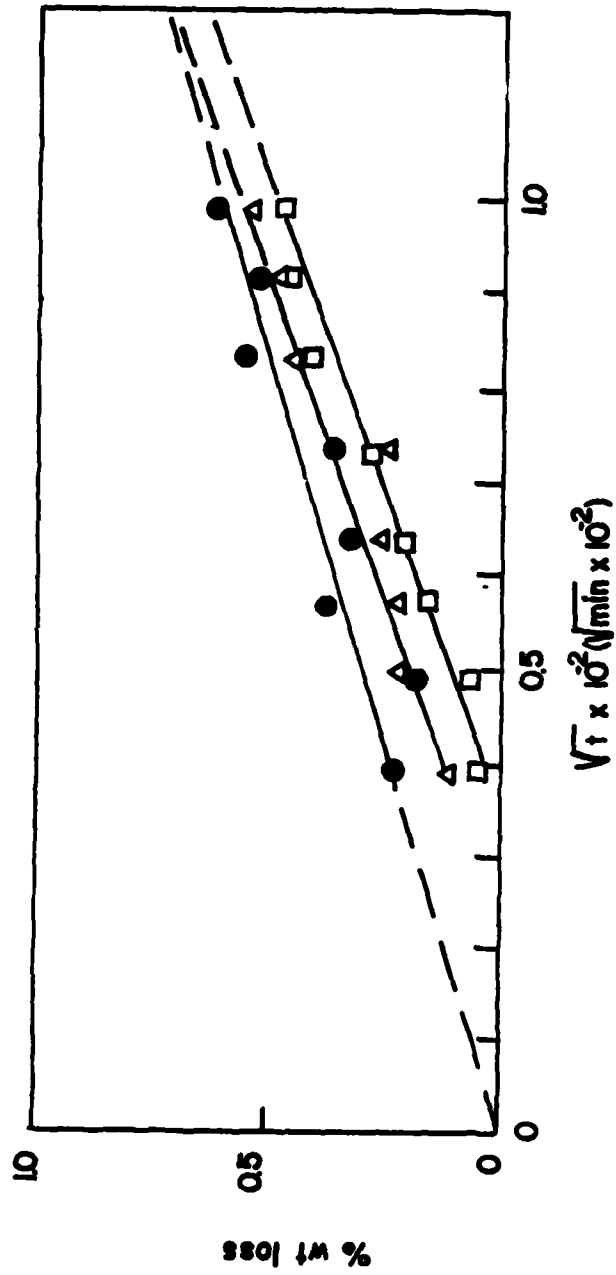


Figure 1. Percent weight loss in zinc/epoxy films as a function of  $\sqrt{t}$  at 28°C, followed by an initial 24 hr of air-drying at 28°C. Drying open to atmosphere (○) or closed (condition 2, △; condition 3, □) as described in Table 2.

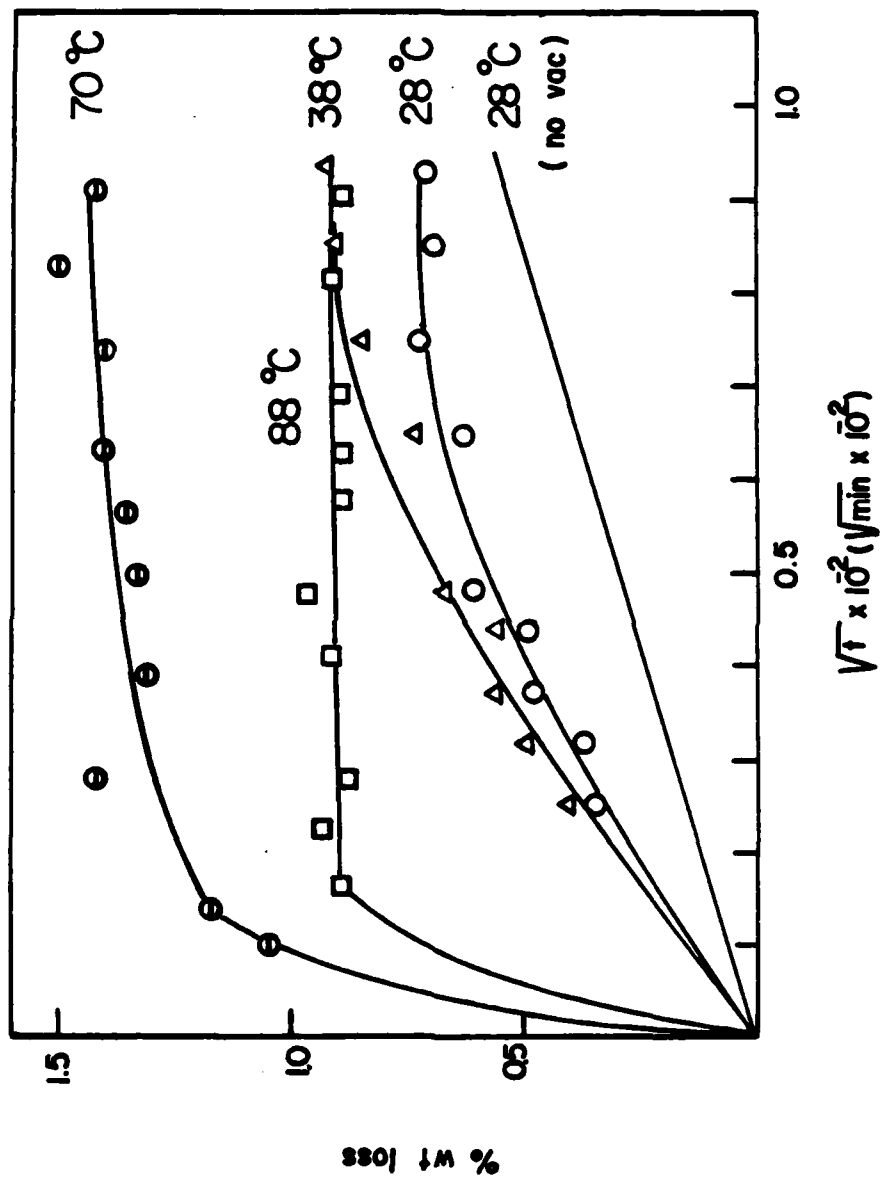


Figure 2. Percent weight loss in zinc/epoxy films as a function of  $\sqrt{t}$  time at various temperatures following an initial 24 hr of air-drying at 28°C. Curve for drying at 28°C with no vacuum included for comparison.

Table III  
Steady-State Weight Loss

<u>Drying Condition</u>	<u>% Wt. Loss</u>	<u>% of Theor.</u> <sup>b</sup>
1. atmospheric, room temp.	-- <sup>a</sup>	
2. covered, room temp.	-- <sup>a</sup>	
3. covered, dry, room temp.	-- <sup>a</sup>	
4. vacuum <sup>c</sup> , T = 28°C	14.0	90
5. vacuum <sup>c</sup> , T = 38°C	14.2	92
6. vacuum <sup>c</sup> , T = 70°C	14.6	94
7. vacuum <sup>c</sup> , T = 88°C	14.2	92

<sup>a</sup>Not yet established, but must  $\leq$  14%.

<sup>b</sup>Theoretical maximum = 15.5%.

<sup>c</sup>30 in of Hg.

#### Curing Behavior

Figure 3 shows a DSC scan for a freshly-cast film (age, 149 min). The exothermic peak between 382 and 410°K (109 and 137°C) corresponds to curing during the scan [12]. However, no such peaks were observed in samples dried for at least 4 hr. The peak in partially cured specimens should appear slightly above the  $T_g$ , which is in the range of 37 to 57°C, depending on curing conditions (see below). This peak location reflects the onset of high segmental mobility above the  $T_g$ , with consequently higher rate of reaction of residual functional groups.

As the temperature rises from room temperature, the heat capacity rises to the peak seen at 382°K in Figure 3. Part of this rise is undoubtedly due to the loss of solvent, but much is associated with the approach to the curing peak, especially at above ~370°K. In fact, the region between 370°K and 410°K resembles curves reported for DSC scans of partially reacted epoxy [12]. With cured specimens (curves not shown), decomposition occurs at high temperatures.

In any case, it is likely that the curing reaction has proceeded to a high degree within a short time, certainly by the time 24 hr has elapsed after casting. Experiments in progress will establish the curing kinetics in more detail.

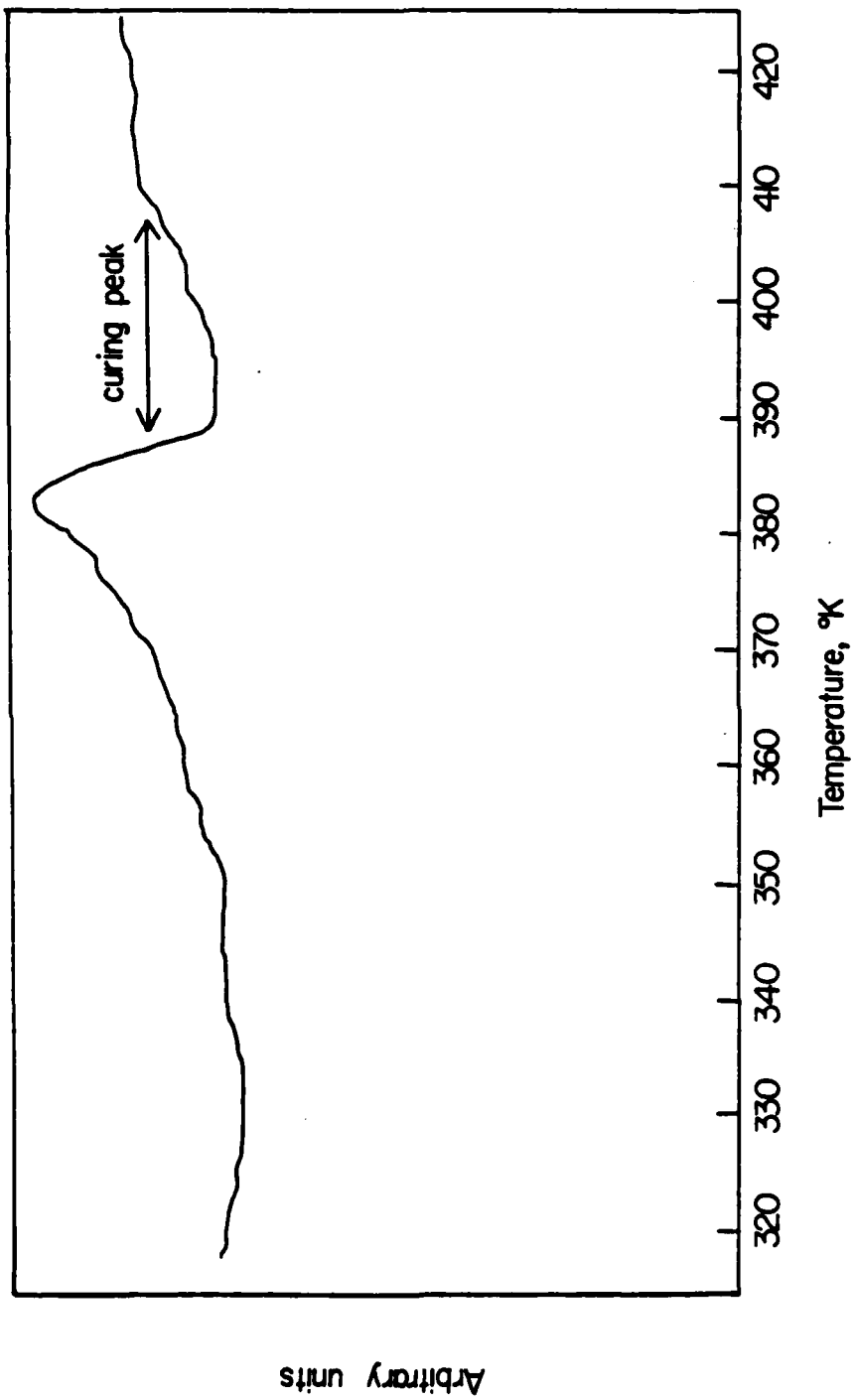


Figure 3. DSC scan of a zinc/epoxy film 2.5 hr after casting.

### Glass Transition Behavior

The  $T_g$  behavior is of interest because it reflects both the type of network formed and the state of cure. Thus the  $T_g$  is expected to be close to the curing temperature [13] and to increase with subsequent heating if the cure is incomplete.

Typical data are summarized in Table IV. Several observations may be made:

1. With ambient curing the first-scan  $T_g$  increased from 310°K to 325°K as time increased from 1.5 to 30 days. A second scan raised the  $T_g$  slightly in the 1.5-day-old specimen, but had no effect on the 30-day-old specimen.
2. With the closed-desiccator drying,  $T_g$ 's after 28 to 35 days resemble those from ambient drying at 30°C, with a small increase in  $T_g$  on the second scan.
3. Vacuum drying at 28, 38, and 70°C also gave values of  $T_g$  (after 7 days) in the same range, also with a small increase in  $T_g$  in repeated scanning. Drying at 88°C gave a slightly higher  $T_g$ , inconsistent with the solvent loss studies.

Table IV  
 $T_g$  Behavior of Zinc/Epoxy Films

<u>Curing Condition</u>	<u>Time, Days</u>	<u><math>T_g</math>, °K<sup>a</sup></u>
1. Ambient	1.5	310, 312
	30	325, 325, 325, 325
2. Closed desiccator (valve open)	28	318, 322, 324
3. Closed desiccator (dry)	35	321, 324, 324
4. Under vacuum ( $T = 28^\circ\text{C}$ )	7	320, 326, 324
5. Under vacuum ( $T = 38^\circ\text{C}$ )	7	318, 320, 319
6. Under vacuum ( $T = 70^\circ\text{C}$ )	7	324, 330, 329
7. Under vacuum ( $T = 88^\circ\text{C}$ )	7	329, 333, 335

<sup>a</sup>By repeated DSC scans, the scan number reading from left to right. Scanning rate: 20°C/min.

These observations suggest that some variations in network character may develop, depending on the curing conditions. There may even be different curing mechanisms, depending on the temperature [15]. However, the trend towards an increasing  $T_g$  with increasing temperature in the vacuum-drying experiments also parallels the trend in increased solvent loss (at least for temperatures up to 70°C).

### Morphology

Typical SEM micrographs of fracture surfaces are shown in Figure 4; the general appearance is similar for all films, whether dried for 1.5 to 2 days under ambient conditions or dried for 7 days under vacuum at 88°C. Several observations may be made:

1. Although most of the zinc particles are relatively smooth and featureless, some present a rough appearance with very small particles attached (Figs. 4a and b). It is not known if there are impurities such as unslaked lime, which is added to a concentration of 0.4% to minimize reduction of the binder.
2. While the binder portions show few pores (at least at the magnifications used), small pores about 0.1  $\mu\text{m}$  in diameter may be seen occasionally (see the lower left of Fig. 4a in the hole vacated by a large zinc particle).
3. In most cases, the pigment-binder adhesion is quite low, as shown in Figures 4a and b. Thus, even though earlier studies [14] showed a slight tendency for zinc to adsorb the Versamid component, the net result is typical of a filler-matrix system possessing a very weak interfacial bond. However, occasional evidence for a higher degree of wetting and adhesion is seen, as in Figure 4c. The reason for the adhesion in this case is not known, but must reflect a difference in the surface chemistry of the zinc concerned. Clearly, characterization of the zinc surfaces would be helpful.

Indeed, Figure 4c resembles a micrograph of a zinc/chlorinated rubber system exhibiting effective wetting [1], while Figures 4a and b are similar to a micrograph of a zinc/polystyrene system exhibiting poor wetting. Since the latter system was shown to be more effective in corrosion protection (at a given zinc content) than the former, it was proposed [1] that the zinc particles bridge together more effectively with the former case, so that the electrical resistance is significantly lowered. In addition, good wetting may hinder the formation of corrosion-inhibiting zinc compounds [2].

An interpretation in terms of acid-base interactions certainly seems warranted. If acid-base interaction between a pigment and its binder is high, dispersion of the pigment and

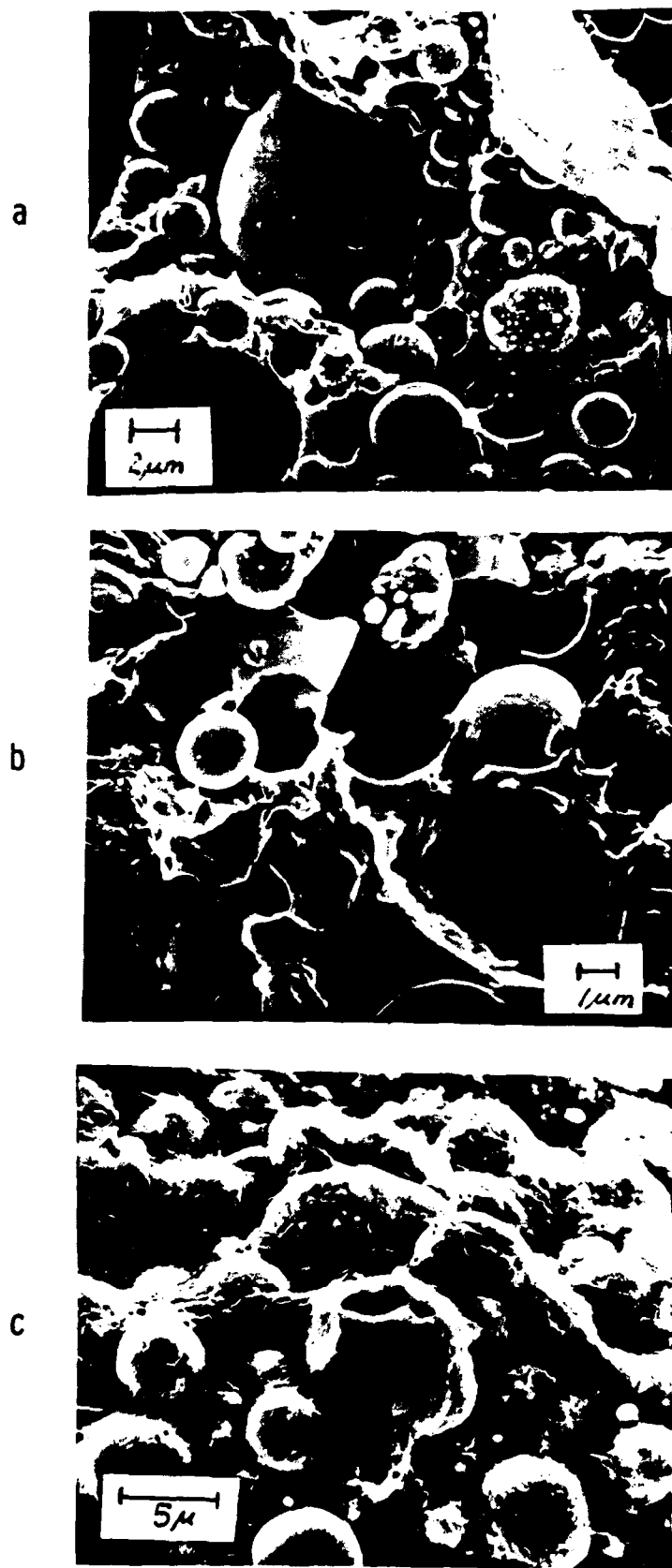


Figure 4.

SEM micrographs of zinc-epoxy primer films (80% zinc). Micrographs a and b are more typical than c.

adhesion are both enhanced, whereas a low degree of interaction leads to agglomeration of the pigment and low adhesion. In fact, electron microprobe studies of the present system confirm a high level of clustering in the zinc particles. Also, adsorption of residual basic solvent (e.g. xylene) in preference to binder would tend to decrease interfacial adhesion.

While in most coatings good pigment dispersion and good adhesion are desirable, in zinc-rich coatings these characteristics appear to be undesirable. Thus it will be of interest to try to maximize the agglomeration of the zinc. Further investigation of the binder/solvent system to minimize acid-base interaction should confirm this hypothesis.

#### CONCLUSIONS AND RECOMMENDATIONS

1. It has been shown that while curing of these zinc/epoxy systems takes place quickly, even under ambient conditions, some further curing may take place at elevated temperatures. Also, while drying takes place in a well-balanced fashion (a function of  $\sqrt{t}$  and temperature, at least up to 70°C), considerable solvent (from 6 to 10%) remains. In any studies of behavior, such retention should be characterized.
2. SEM micrographs confirm that pigment-binder adhesion is usually, though not always, very low. Further characterization of the zinc surface would be desirable.
3. It is suggested that corrosion protection should be maximized by minimizing acid-base interaction between the zinc and the binder. Experiments are planned to test this hypothesis by varying the binder from acidic to basic (in an appropriate solvent).
4. Now that a baseline has been established for drying and curing, research on mechanical and permeability behavior will be timely. Also, extension of research to include correlation of corrosion protection performance with film properties should be started.

## REFERENCES

- [1] F. Theiler, Corrosion Sci. 14, 405 (1974).
- [2] T. K. Ross and J. Wolstenholme, Corrosion Sci. 17, 341 (1977).
- [3] V. P. Simpson and F. A. Simko, J. Oil Col. Chem. Assoc. 56, 494 (1973).
- [4] D. S. Newton and F. G. Sampson, J. Oil Col. Chem. Assoc. 48, 382 (1965).
- [5] E. W. Horvick, Heat., Piping Air Cond. 42, 210 (1970).
- [6] H. Witcoff, Paintindia 14(5), 41 (1964).
- [7] M. J. Marmo, M. A. Mostafa, H. Jinnai, F. M. Fowkes, and J. A. Manson, I&EC Prod. Res. Dev. 15, 206 (1976).
- [8] Technical Bulletin 11-D-3, "Protective and Decorative Coatings Based on Versamid Polyamide Resins", General Mills Chemical Division, 1963, p.19.
- [9] R. A. Scherzinger, Off. Dig. 32, 1197 (1960).
- [10] R. E. Murdock and J. A. Carney, Off. Dig. 181(1961).
- [11] D. J. Newman and C. J. Nunn, Prog. Org. Coatings 3, 221 (1975).
- [12] R. A. Fava, Polymer 9, 137 (1968).
- [13] J. Gillham, Polym. Eng. Sci. 19, 676 (1979).
- [14] J. A. Manson, in First Annual Report, this project, 1980.
- [15] N. Levy, Org. Coatings Plast. Chem. 43, 485 (1980).

## Program #12. Electron Optical Studies of Organic Coatings

### ABSTRACT

Studies have been conducted that show epoxies to consist of primary microgels of 10-60 nm in size. These primary microgels join together to form the secondary microgels which later interconnect to form the macro-gel exceeding as much as 0.5  $\mu\text{m}$  in size. The development of this crosslinked network has led to inhomogeneities in the crosslink density. We believe that these inhomogeneities may serve as paths for the permeation of corroding species.

Scanning electron microscopy with energy dispersive X-ray spectroscopy was used to examine and analyze non-filled and Zn-filled epoxy films, and bulk glass bead filled epoxy samples. These samples were derived from a variety of formulations and cured under various conditions. The films were cast on different substrates and subjected to an assortment of etching conditions.

Regardless of any of the aforementioned variations, formulation, cure conditions, or etching treatment, the results were the same. The area of epoxy in contact with a surface was the most susceptible to attack by a corroding species.

Film samples of epoxy and polybutadiene derived from cathodic delamination experiments were examined in the scanning electron microscope (with an energy dispersive spectrometer). The films showed regional differences in concentrations of permeating ions. Transmission electron microscopy was employed for the study of epoxy thin sections. The use of this instrument proved fruitless due to the problems of sample preparation.

### BACKGROUND

Extensive studies have been conducted relating the morphology of epoxies to their mechanical behavior [1-4]. Epoxies have considerably lower tensile strengths than strengths predicted by either primary bond breakage or van der

PRECEDING PAGE BLANK-NOT FILMED

Various experimental techniques have subsequently indicated morphological inhomogeneities that could explain these low tensile strengths [6-10]. We believe that these inhomogeneities in a polymer film are related to the quality of corrosion control exhibited by that film. These differences or inhomogeneities in the crosslink density may serve as paths for the permeation of corrodents in the initiation and propagation of corrosion.

Electron microscopic evidence indicates that epoxies have a primary morphology consisting of particles or microgels on the order of 10 nm in size [11]. These particles are formed during the initial stages of polymerization and interconnect to form 20-60 nm aggregates. These network entities aggregate to form macrogel particles sometimes exceeding 0.5  $\mu\text{m}$  in size. The macrogel particles are only weakly attached to the surrounding matrix.

Two types of network structure have been observed [12]: regions of high crosslink density embedded in a low crosslink density matrix or a low crosslink density region embedded in a high crosslink density matrix.

In addition to inhomogeneities in the crosslink density, the presence of microvoids must be accounted for when studying structure-behavior relationships [13]. The epoxy monomer present in the partially cured thermoset resin may crystallize in micro-regions. The crystalline monomer may be suspended in a higher molecular weight matrix. Post curing can volatilize the monomer thus leaving microvoids.

Manson et al. has proposed a three-step mechanism for the formation of the microstructural network: formation of the primary microgel, formation of the secondary microgel, and finally the formation of the macrogel (Fig. 1).

During the formation of the primary microgel the reacting epoxy prepolymer diffuses to the nuclei of the curing agent. Throughout this process new nuclei are formed, giving rise to a size distribution of primary microgels (10-60 nm). After a certain concentration has been reached the primary microgels and the growing nuclei join with each other to form the nuclei of the secondary microgel. The secondary microgel is not as coherent as the primary microgel due to the new nuclei growing from the physical forces of a developing network and from the reaction of unreacted groups in the primary microgel.

The experimental gel point is observed at a critical solid concentration where the secondary microgels pack together to form the macrogel. At this stage, phase inversion occurs where the secondary microgels become the matrix and the unreacted prepolymer forms the dispersed phases. The coherence of the interconnections of the secondary microgels determines the final network properties.

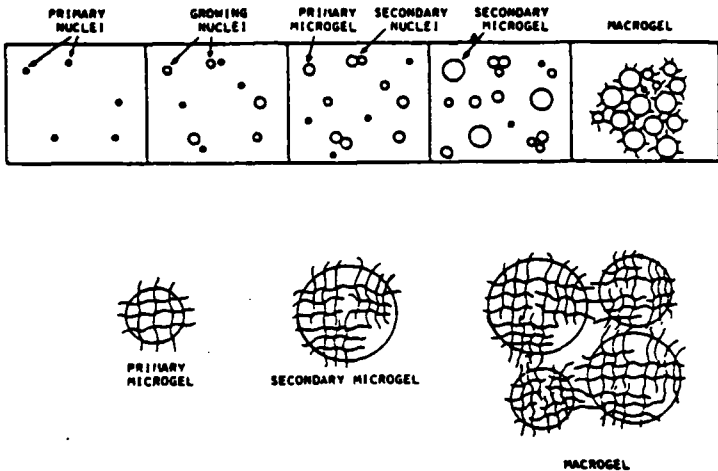


Figure 1. Proposed model for network formation [12].

Intramolecularly crosslinked regions within these phases are caused by the inability of the unreacted epoxy and curing agent, which are attached to the growing domain, to diffuse to other active species in neighboring domains. Therefore they react with active species only in their immediate area.

The size of the crosslinked region depends on stoichiometry, cure conditions, and the proximity of surfaces. High concentrations of curing agent apparently initiate higher crosslink densities both locally and at more sites. This results in a densely packed small nodule [14]. Low concentrations of curing agent generate a morphology of larger, more widely spaced, and less closely packed domains.

There are changes in thermoset properties near interfaces [15]. Free surfaces show a larger morphology than that seen on the bulk fracture surface of the same specimen (due to loss of curing agent at the free surface). Polar adherends attract the curing agent while depleting catalyst away from the interface. Polar materials generate two boundary layers.

Racich and Koutsky [16] studied high and low energy substrates to establish their effects on epoxy morphology. Low surface energy substrates (teflon, silicone rubber) cause little change in epoxy morphology adjacent to the surface, while higher energy substrates show a strong influence on the epoxy morphology, an increase in nodule size. Kardos [17] has observed morphological evidence in glass filled epoxies that could be interpreted in terms of migration of curing agent to the glass-epoxy interface. Kessenikh [18] observed that nodule size increases

with the amount of dissolved foreign material.

Adhesion of a polymer to a substrate depends upon the restriction of vibratory motion of the macromolecules near the surface [19]. Bascom [20] reviews the effects of adsorbed molecular species on the interfacial morphology. He suspects a reduction in molecular mobility (and the subsequent changes in properties) near rigid inclusions. The proximity of surfaces makes the segmental mobilities of the polymer chains less homogeneous. The density at the interface of a film adsorbed on a surface is less than what it would be in the free state.

The decrease in vibratory motion creates a region of decreased or restricted motion whose properties are different from that of the bulk. Kwei [21] and Kumins [22] deduced from water diffusion experiments the existence of a region approximately 1000 Å surrounding a filler particle; the epoxy polymer in this boundary layer has significantly less molecular mobility than that in the bulk.

## RESULTS

Scanning electron microscopy (SEM) with energy dispersive X-ray spectroscopy (EDS) was employed to study both the suitability of electron optical method and the susceptibility of epoxies to permeating species. Zn-filled and non-filled epoxies, derived from a variety of formulation and cure conditions, were prepared. These epoxies were cast on a variety of substrates. Bulk glass-bead-filled samples were also prepared. The film samples which were removed from the substrates, and the bulk samples were subjected to various forms of solvent and solution etching. Included were solvent etching, Cr<sub>2</sub>O<sub>3</sub> etching, and the Zn-filled epoxies were treated with HCl as well. Epoxy and polybutadiene films cast on cold rolled steel and subjected to cathodic delamination were also examined. Transmission electron microscopy (TEM) was also attempted for some samples.

The epoxy samples were prepared from Epon 1001-F (solid, Shell Chemical) and Versamid 115 polyamide (General Mills), where the ratio of epoxy to polyamide was varied from 0.8 to 3.5 (ratios = 0.8, 1.0, 1.5, 2.0, 2.75, 3.5). The epoxy was dissolved in the equivalent weight of butyl cellosolve. The polyamide was dissolved in 65% by weight of xylene and 35% by weight of butyl cellosolve. (Initially the epoxy was dissolved in methyl isobutyl ketone, but it was discovered that the ketone affected the reactivity of the epoxy.) Non-filled, zinc-filled (8 µm diameter spheres) films, and bulk glass-bead-filled (40 µm average diameter spheres) systems were prepared.

The fracture surfaces of both the filled and non-filled systems were observed under the scanning electron microscope (SEM),

Figures 2-4. In the filled systems the filler particles were evenly dispersed throughout the epoxy. At the interface the filler particles were found in higher concentration. This is due to the settling of the filler from gravitational forces. The fracture surface showed that the epoxy encased the filler particles but was not bonded or very weakly bonded to the surface. The fracture surface of the non-filled systems revealed nothing about the morphology of the thermoset resin.

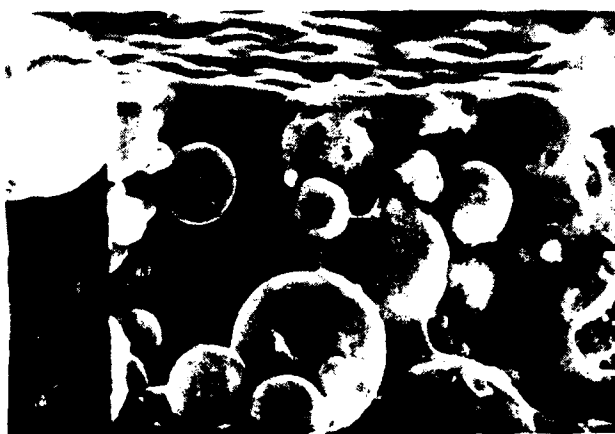


Fig. 2. Zinc particles dispersed in epoxy.

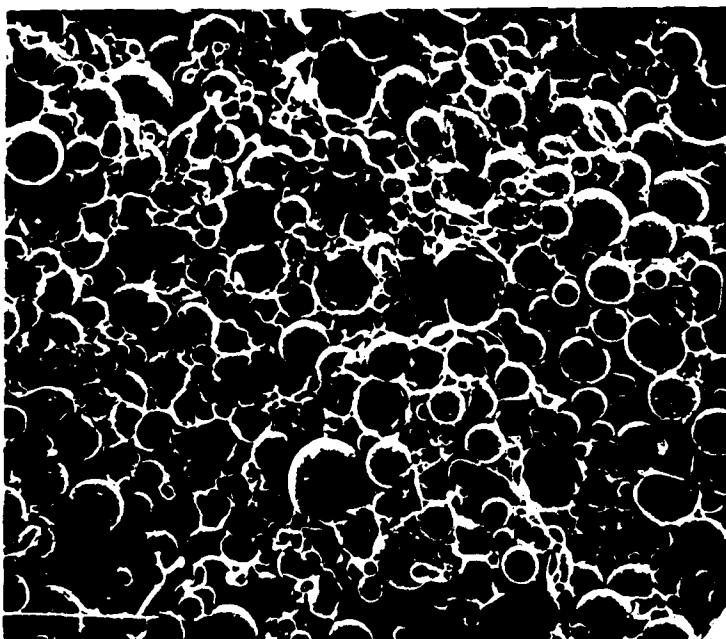


Fig. 3. Glass beads dispersed in epoxy (800X).

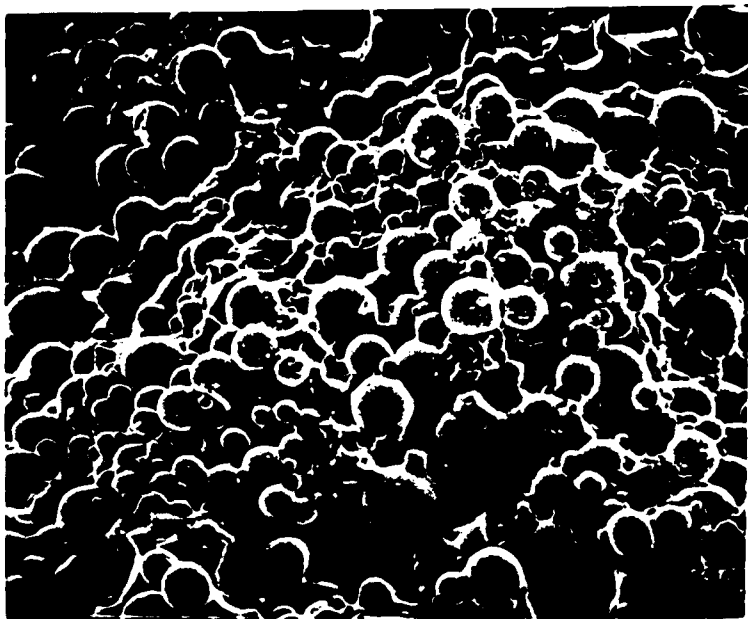


Figure 4. Glass beads dispersed in epoxy.  
Glass beads were added 4 hrs after  
onset of cure, as described later.  
Note region of filler exclusion  
(region E).

The filler particles were added at various times relative to the curing of the epoxy. Some epoxy samples were placed in closed containers and some samples were exposed to the atmosphere during the curing process prior to the addition of the filler. In samples, both film and bulk, where the filler was added at four or more hr after the onset of cure, SEM observation of the fracture surfaces showed that there were regions in the interior where the filler particles were excluded. There are factors to be considered in order to understand this observation. First, in the exposed samples an increase in viscosity due to the loss of solvent through evaporation may have led to an inability of the epoxy-polyamide solution to wet the filler particles, thus preventing bonding to the epoxy matrix. Second, for both the contained and exposed epoxies, the onset of polymerization may have contributed to the exclusion of the filler particles, due to the development of crosslinked regions. These may have served as physical barriers for the filler.

It is believed, based on the following observation, that the latter is the most responsible for the exclusion of the filler particles. A study was conducted concerning the consequences of solvent loss through evaporation during polymerization. Non-filled epoxies were formulated (noting the total weight) and placed in closed containers to prevent solvent evaporation. After 24 hr the result was a partially polymerized sample with no solvent loss (noting total weight). After a week it was evident that the epoxy had undergone additional curing. The samples were

then removed from the closed containers to determine the evaporation of the solvent from the cured epoxy. One month passed before the solvent had totally evaporated (determined by weight loss).

This study shows that a sufficient amount of polymerization can occur before a significant amount of solvent has evaporated. A significant amount may be interpreted as the amount of solvent lost to evaporation needed to cause a high enough increase in viscosity to prevent the wetting of the filler particles.

Both the zinc-filled and the non-filled epoxies were cast on various substrates, with film thickness varying from 20 to 90  $\mu\text{m}$  for the non-filled and 30 to 200  $\mu\text{m}$  for the zinc-filled epoxies. The substrates used were aluminum foil, Teflon sheets, stainless steel, and cold rolled steel. (All substrates were cleaned and degreased by a preliminary wash with Alconox detergent followed by boiling acetone.) The epoxy was easily removed from the aluminum foil and the Teflon sheets. There was some difficulty in separating the film from the stainless steel, but it was not possible to remove the films from the cold rolled steel without damaging the film. Therefore the following studies were on films cast on aluminum foil, Teflon sheets, and stainless steel.

The zinc-filled films and the bulk glass-bead-filled systems were formulated from epoxy to polyamide ratios ranging from 0.8 to 3.5. They were cured at room temperature for 1-2 weeks. These samples were then etched using 1M aqueous solution of  $\text{Cr}_2\text{O}_3$  for 24, 48, 72, and 168 hr at room temperature and for 4-7 hr at 70°C. This solution preferentially attacks regions of low crosslink density. These samples were fractured at room temperature and subsequent electron microscopic observation showed considerable erosion of the epoxy matrix (Figs. 5 and 6). The region near the substrate showed the most erosion and the interior of the film showed the least. This was confirmed for the zinc-filled films by EDS analysis, which showed the strongest Cr signal near the substrate, the weakest in the interior, and a somewhat higher signal near the free surface of the original film.

Non-filled systems were treated and examined similarly. Non-filled systems which were post cured at 120°C for 24 hr were also included. These films, cast on the various substrates, showed the same trend of Cr permeation. The differences between the filled and non-filled systems were the magnitude of the Cr signal, the filled epoxy having a considerably stronger signal. Visual observation showed that erosion was greater in the filled system; the SEM revealed no appreciable attack by the etching solution on the non-filled samples (the substrate side showed some erosion, Fig. 7, but it did not extend into the interior of the bulk epoxy).

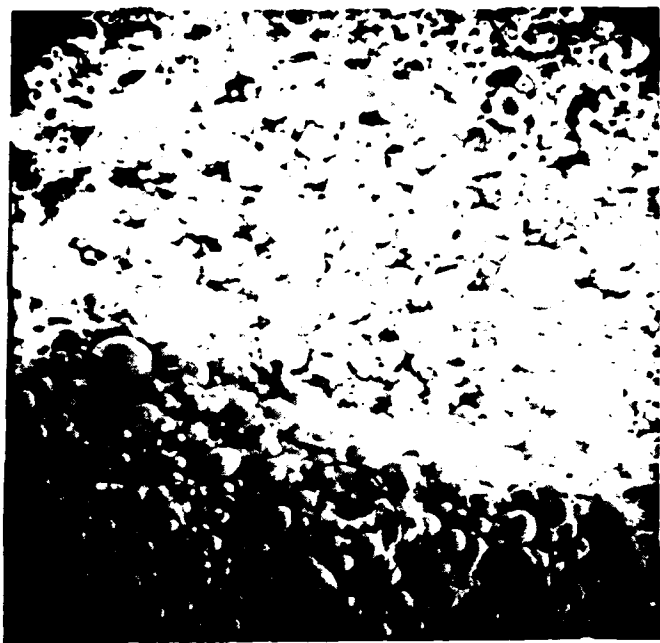


Figure 5. Zinc-filled epoxy etched for 7 hr at 70°C (600X). Area of  $\text{Cr}_2\text{O}_3$  attack is at the top of the micrograph.

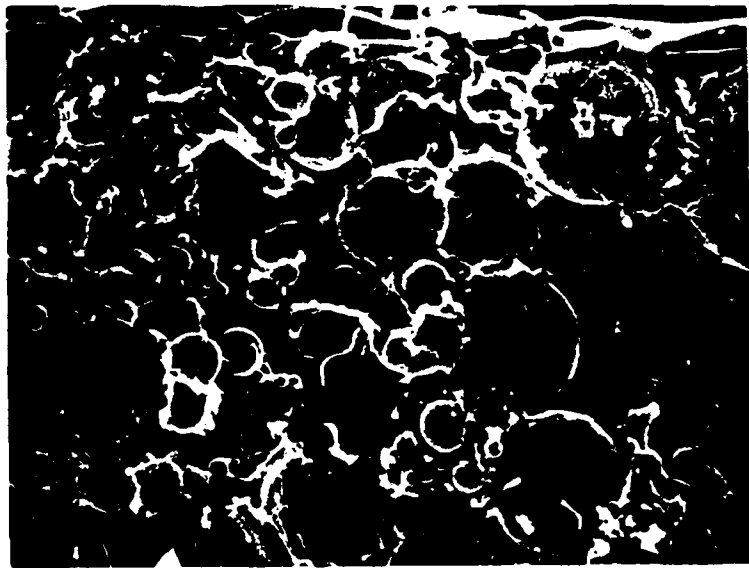


Figure 6. Glass bead-filled epoxy, etched for 7 hr at 60°C (600X).

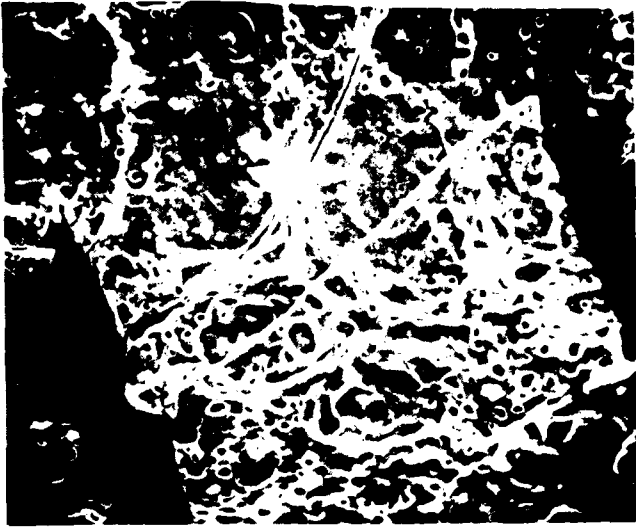


Figure 7. Substrate face of non-filled epoxy after etching for 7 hr at 70°C (3000X).

There are two possibilities for the observed differences between the filled and non-filled epoxies. There may be differences between the morphology or microstructure of the epoxy in the filled and non-filled systems. Also, there may be physical differences on the macroscopic level. These differences may include channels in the filled systems which may allow transport of permeating species into the interior of the bulk epoxy. The SEM micrographs showed that the epoxy encased the filler particles, but was not bonded to it.

Another study of Zn-filled epoxies took advantage of the reaction,  $Zn + 2HCl = ZnCl_2 + H_2$ . Zn-filled epoxies (epoxy to polyamide ratios were 2.0 and 3.0) were totally immersed in the 0.5M HCl. Some samples were partially immersed, only the substrate side or the exposed side was in contact with the acid solution. Sample treatment was for 24 hr at room temperature or for 4-7 hr at 70°C. Using SEM-EDS analysis (with X-ray mapping), it was possible to trace the permeation of the HCl through the filled epoxies by monitoring the X-ray signals for Zn and Cl (Fig. 8). The Cl signal was always detected in the presence of Zn, but Zn was detected in the absence of Cl. Cl was not detected on the Zn particles, but was found in high concentrations at the zinc-epoxy interface. In most cases the Cl traversed a path from one Zn particle to the next; however, in some instances Cl appeared to accumulate in regions between the filler particles. This study proposes the possible path that permeating species may take in the failure of the film and the subsequent corrosion.

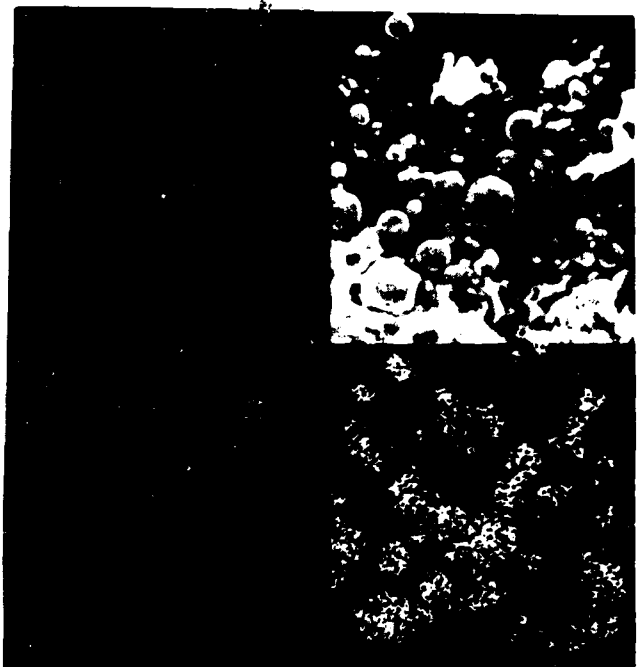


Photo 1

Photo 2

Photo 3

Figure 8. Photo 1 of Zn-filled epoxy after treatment with 0.5M HCl. Substrate side is down. Photo 2, X-ray map of Zn signal. Photo 3, X-ray map of Cl signal.

Non-filled epoxies were subjected to solvent etching. The solvent used was butyl cellosolve and the epoxy films were formulated with epoxy to polyamide ratios of 2.0, 2.75, and 3.5. Samples were cured at room temperature for 24, 48, 168 and 336 hr. Also, the samples were post cured at 120°C for 24 hr following the room temperature cures. These samples were then placed in the solvent for 24, 72 and 163 hr. These samples were then examined in the SEM. No characteristic morphology was observed (maximum magnification attained was 20,000X).

Following the solvent etch, the above samples were subjected to a Cr<sub>2</sub>O<sub>3</sub> etch at 70°C for 4-7 hr. SEM-EDS analysis indicated similar trends in Cr permeation as reported previously for other samples. The Cr signal was stronger throughout the fracture surface, relative to those samples without the solvent etch. In some of the two-to-one ratio samples, the substrate side was visually darker, and subsequent EDS analysis showed this region to be very high in Cr.

OsO<sub>4</sub> stained samples were thin sectioned and observed in the transmission electron microscope (TEM). Sodium oleate, an eighteen carbon chain with a double bond at the ninth carbon, was added at various times during the cure. It was hoped that

this long chain sodium salt of oleic acid would aggregate in higher concentrations in the low crosslinked regions. Subsequent staining with  $\text{OsO}_4$  would reveal these high concentration regions. Due to the brittleness which developed as a result of the staining, we have not been able to consistently make thin sections by ultramicrotomy for transmission electron microscopy. There were, however, sections that seemed thin enough (less than 1000  $\text{\AA}$ ) for TEM observation. At 100,000X there appeared in samples, where the sodium oleate was added 4 or more hr after the onset of cure, the existence of nodular regions. For samples where the sodium oleate was added immediately, these nodular regions did not exist. Due to the inconsistency of the thin sections, no conclusion is drawn.

Collaborative work with Dr. Henry Leidheiser was conducted concerning ion permeation. Films of 20  $\mu\text{m}$  to 40  $\mu\text{m}$  thickness of both polybutadiene and epoxy (two-to-one ratio epoxy to polyamide) were cast on cold rolled steel. A pin point defect was made through the thickness of the film. The samples were immersed in electrolyte solutions of LiCl, NaCl, KCl, or CsCl. When a cathodic voltage was applied, delamination occurred in the area surrounding the pin point defect. Since CsCl gave the fastest delamination (most area delaminated per period of time), it was used extensively as the electrolyte solution. Following delamination the affected area was easily removed from the substrate. The area examined was the cross section of the area cutting through the defect, Figure 9. Through SEM-EDS analysis we obtained the following information. Within the defect, both Cs and Cl were detected, Cl having a slightly "stronger signal. However, EDS analysis of the cross-sectional area moving away from either side of the defect showed a steadily decreasing signal for Cl and no signal for Cs.

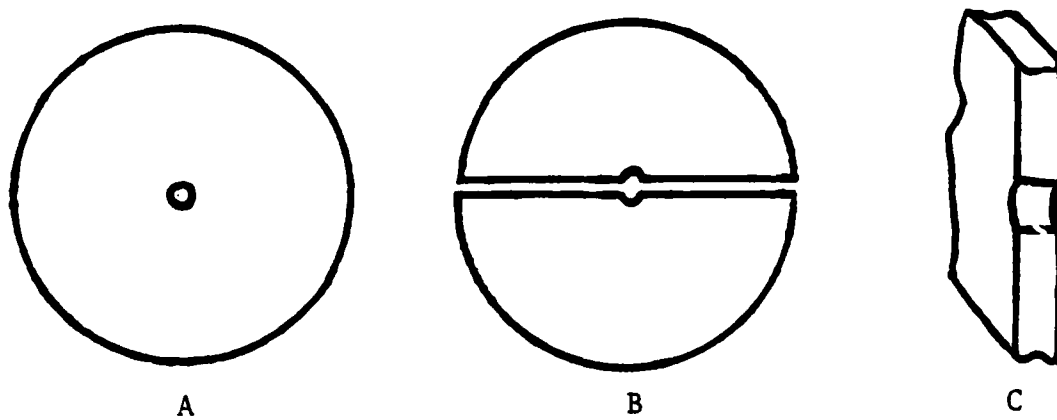


Figure 9. (A) Removed area of delaminated film. (B) Area of film cut through the defect. (C) Cross-sectional view of film including the defect.

In another study the procedure was terminated at the onset of delamination. Since the area of delamination was small, the film was not removed from the substrate. The coating-substrate samples were cut through the defect exposing the small area of delamination, thus revealing the coating-substrate interface. Analysis of the coating-substrate interface revealed the presence of Fe, Cs, and Cl; X-ray signals for only Fe were obtained from the substrate. Examination of the cross section within the defect revealed two distinct regions of interest. The region near the substrate-coating interface was higher in Cs and Cl than the region above. In both regions the Cl signal was stronger than the signal for Cs. When delamination was allowed to continue until a large area of film had delaminated, no regional differences within the defect were found.

## DISCUSSION

Through the course of this study we have examined many samples which were subjected to various corrosive conditions. Regardless of the epoxy formulation and cure conditions (including the specific samples of polybutadiene), the trends of permeating species were consistent for all samples. The films all fail in the same area; the protective coating in contact with a surface, e.g. a filler particle or substrate, is the least resistant to corrosion or the most susceptible to the permeation of corroding elements.

There are limitations to SEM-EDS analysis. The observability of subtle differences in morphology, manifested as topographical differences, is limited by the resolution of the instrument. As reported earlier, epoxies have density domains of approximately 10-60 nm. The maximum resolution of the SEM is 20 nm. In addition, the EDS X-ray analysis is qualitative only, with a detectability of one thousand parts per million and 25-50% possible error. It at best will only give relative quantities.

Transmission electron microscopy has been done on both filled and non-filled ( $\text{OsO}_4$  stained) samples. The drawback of this technique lies in the sample preparation. ultramicrotomy is needed to obtain a workable sample. In the case of the Zn-filled samples, the shear action deforms the filler particle and tears it away from the epoxy matrix, thus distorting the true image of the filler-matrix interface. It has been reported [11] that the density domains, as described earlier, are not visible in the thin sections as viewed in the TEM. The problems with the stained non-filled samples have already been mentioned.

In order to quantitatively examine the films which have been subjected to corrosive conditions and etching solutions, scanning transmission electron microscopy (STEM), with a resolution of  $10 \text{ \AA}^\circ$ , should be exploited. Once again, there is the problem of thin sectioning, but bulk samples can be examined as well.

## REFERENCES

- [1] R. J. Morgan and J. E. O'Neal, *J. Mater. Sci.* 12, 1966 (1977).
- [2] R. J. Morgan and J. E. O'Neal, *Polym. Plst. Tech. and Eng.* 10(1), 49 (1978).
- [3] R. J. Morgan and J. E. O'Neal, *Org. Plast. Coat., Preprints (ACS)* 38, 485 (1978).
- [4] R. J. Morgan and J. E. O'Neal, *J. Mater. Sci.* 14, 109 (1979).
- [5] J. L. Racich and J. A. Koutsky, *J. Appl. Polym. Sci.* 20, 2111 (1976).
- [6] R. Blockland and W. Prins, *J. Polym. Sci.*, A2, 7, 1595 (1969).
- [7] R. E. Cuthrell, *J. Appl. Polym. Sci.* 11, 1495 (1967).
- [8] A. S. Kenyon and L. E. Nielson, *J. Macromol. Sci.-Chem.* A3(2), 275 (1969).
- [9] H. H. M. Balyuzi and R. E. Burgi, *Nature* 227, 489 (1970).
- [10] L. Gallacher and F. A. Bettelheim, *J. Polym. Sci.* 58, 697 (1962).
- [11] J. L. Racich and J. A. Koutsky, "Chemistry and Properties of Crosslinked Polymers", S. S. Labana, Ed., p.303, Academic Press, New York, 1977.
- [12] S. C. Misra, J. A. Manson and L. H. Sperling, *ACS Symposium Series No. 114*, 157 (1979).
- [13] R. J. Morgan and J. E. O'Neal, *J. Polym. Sci. (Polym. Phys. Ed.)* 14, 1053 (1976).
- [14] J. L. Kardos, *Trans. N.Y. Acad. of Sciences* 11, 35(2), 136 (1973).
- [15] J. L. Racich and J. A. Koutsky, *Bull. Am. Phys. Soc.* 20, 456 (1975).
- [16] J. L. Racich, J. A. Koutsky, *J. Appl. Polym. Sci.* 20, 2111 (1976).
- [17] J. L. Kardos, *Trans. N.Y. Acad. Sci.* 11, 35(2), 136 (1973).
- [18] R. M. Kessenikh, *Polym. Sci. USSR* 14, 466 (1972).

- [19] C. A. Kumins, J. Coat. Tech. 52, 39 (1980).
- [20] W. D. Bascom, "Composite Materials", Academic Press, N.Y. 1974, L. J. Broutman and R. J. Krock, Eds., Vol. 6, Chapter 3.
- [21] T. K. Kwei, J. Polym. Sci. A3, 3229 (1965).
- [22] C. A. Kumins and J. Roteman, J. Polym. Sci. A1, 527 (1963).

Program #13. Preparation of Colloidal Iron Sols by  
(a) Aqueous Precipitation and  
(b) by Dispersion

BACKGROUND

The purpose of this work is to develop a fundamental understanding of the application of coatings to corroded steel surfaces after removal of only the loose surface rust. In such a case, the coating must wet the corrosion products of iron and penetrate through the porous rusted layer to bind firmly to the underlying solid substrate. The approach taken is to prepare the eight reported corrosion products of iron in the form of colloidal sols and determine the adsorption of suitable polymer molecules on the surfaces of these colloidal particles. The very large surface area of the colloidal iron corrosion particles allows accurate measurement of the polymer adsorption. Interpretation of the adsorption results using the acid-base interaction scheme proposed by Fowkes et al. [1,2] allows the characterization of the iron corrosion products as Lewis acids or bases and the selection of polymer candidates for practical coatings systems on the same basis. Two approaches have been taken to study these interactions: (i) preparation of the pure iron corrosion products as colloidal sols by aqueous precipitation reactions, followed by transfer of colloidal particles to organic media for the polymer adsorption experiments; (ii) dispersion of commercial iron corrosion products in aqueous and organic media for characterization and polymer adsorption studies.

Part (a). Preparation of Iron Corrosion Products  
as Colloidal Sols

Introduction

The preparation of colloidal sols of  $\alpha\text{-Fe}_2\text{O}_3$  (K-129-11),  $\beta\text{-FeOOH}$  (K-1151-1), and  $\text{Fe}_3\text{O}_4$  (K-107-1) by aqueous precipitation reactions in closed systems at high temperatures was described earlier [3]. These colloidal sols were cleaned by serum replacement and characterized. X-ray diffractograms of the recovered solids were compared with those of the corresponding commercial products as well as literature standards. X-ray diffractograms of commercial  $\gamma\text{-Fe}_2\text{O}_3$  and  $\alpha\text{-FeOOH}$  were also compared with literature standards.

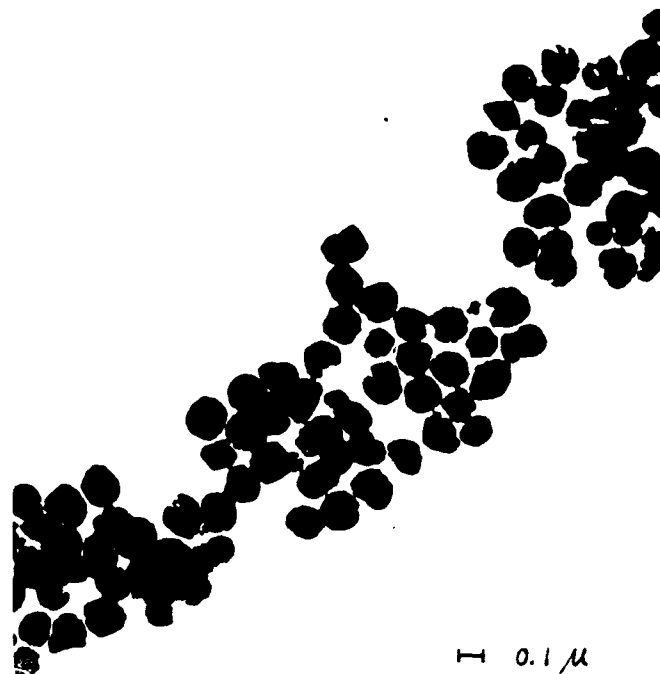
The morphology of the particles produced in these earlier, preliminary precipitations was characterized by transmission electron microscopy. Later preparations using standardized procedures gave particles that were characterized by both transmission and scanning electron microscopy. Figures 1-3 show both transmission and scanning electron micrographs of  $\alpha$ -Fe<sub>2</sub>O<sub>3</sub>,  $\beta$ -FeOOH, and Fe<sub>3</sub>O<sub>4</sub>, respectively. The morphologies of the primary particles were well-characterized by these two methods, the  $\alpha$ -Fe<sub>2</sub>O<sub>3</sub> particles being spheroidal, the  $\beta$ -FeOOH particles acicular or needlelike, and the Fe<sub>3</sub>O<sub>4</sub> particles cubic or block-like.

The effects of surfactants on the particle nucleation and growth steps of emulsion polymerization are well known: the number of particles formed increases strongly with increasing surfactant concentration. To apply this concept to the preparation of iron oxide sols, a series of  $\alpha$ -Fe<sub>2</sub>O<sub>3</sub> sols was prepared using the K-129-11 method in the presence of increasing concentrations of Triton X-100 (nonionic octylphenol-ethylene oxide adduct with 9-10 moles ethylene oxide; Rhom & Haas Co.). This surfactant was chosen because of its known ability to stabilize colloidal dispersions in water by steric stabilization. The only effect observed was the generation of a negligibly small number of prolate-spheroidal particles (in addition to the usual spheroidal particles) at Triton X-100 concentrations of  $5.0 \times 10^{-3}$  g/100 ml or greater. The settling behavior (in tall graduated cylinders) was the same independent of Triton X-100 concentration, although transmission electron micrographs of the samples containing  $1.2 \times 10^{-2}$  and  $2.44 \times 10^{-2}$  g/100 ml showed a greater degree of particle flocculation on the submicroscopic scale.

The experimental procedures used for the preparation of the foregoing colloidal sols gave only limited amounts of solid particles. For example, the solids content (determined by drying to constant weight at 100°) of a  $\alpha$ -Fe<sub>2</sub>O<sub>3</sub> sol prepared using the K-129-11 method was only 0.14%, that of a  $\beta$ -FeOOH sol prepared using the K-115-1 method only 0.23%, and that of a Fe<sub>3</sub>O<sub>4</sub> sol prepared using the K-107-1 method only 0.27%. These low solids contents meant that large volumes of colloidal sols must be prepared to give enough particles for the characterization and polymer adsorption studies.

An alternative approach tried was to adapt the commercial processes to prepare these colloidal sols to the laboratory-size apparatus. Thus far,  $\alpha$ -Fe<sub>2</sub>O<sub>3</sub>,  $\alpha$ -FeOOH, and  $\gamma$ -FeOOH have been prepared in larger quantities using this approach. This report describes the preparation, cleaning, and characterization of colloidal particles prepared in this way, as well as the transfer of these particles from aqueous media to organic media (flushing) and preliminary acid-base characterization by adsorption of polymers.

TEM



— 0.1 μ

SEM



Figure 1. Transmission and scanning electron micrographs of cleaned  $\alpha$ - $\text{Fe}_2\text{O}_3$  particles (K-129-11).

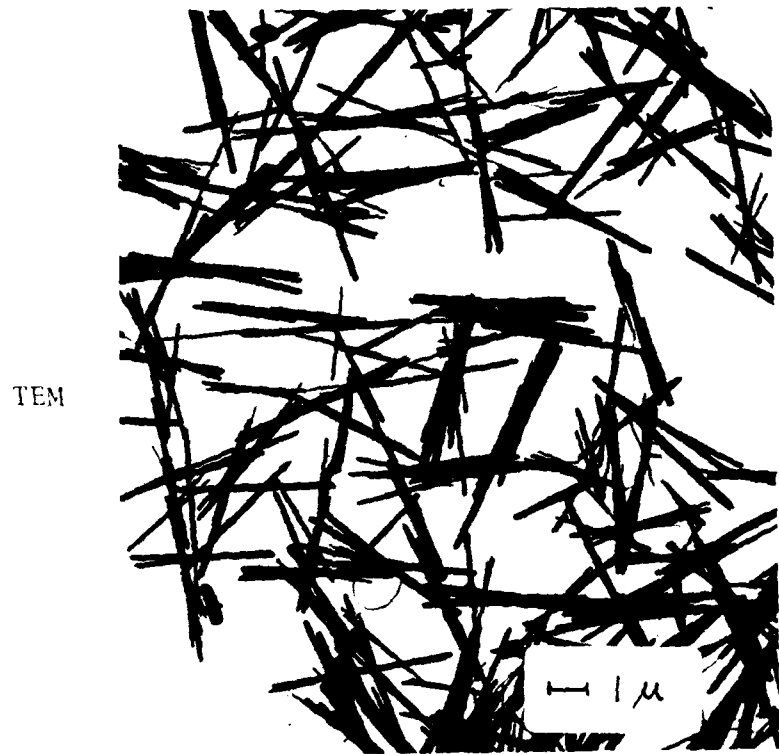
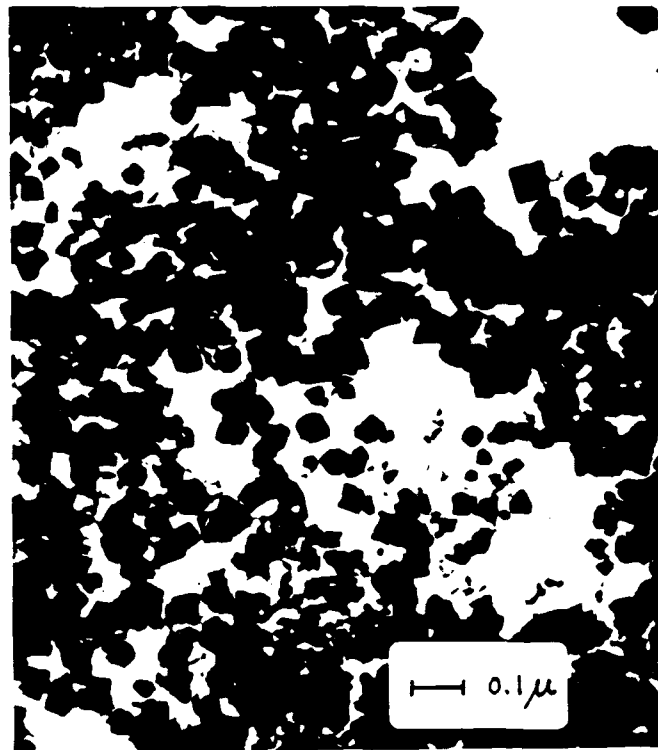


Figure 2. Transmission and scanning electron micrographs of cleaned  $\beta$ -FeOOH particles (K-115-1).

TEM



SEM

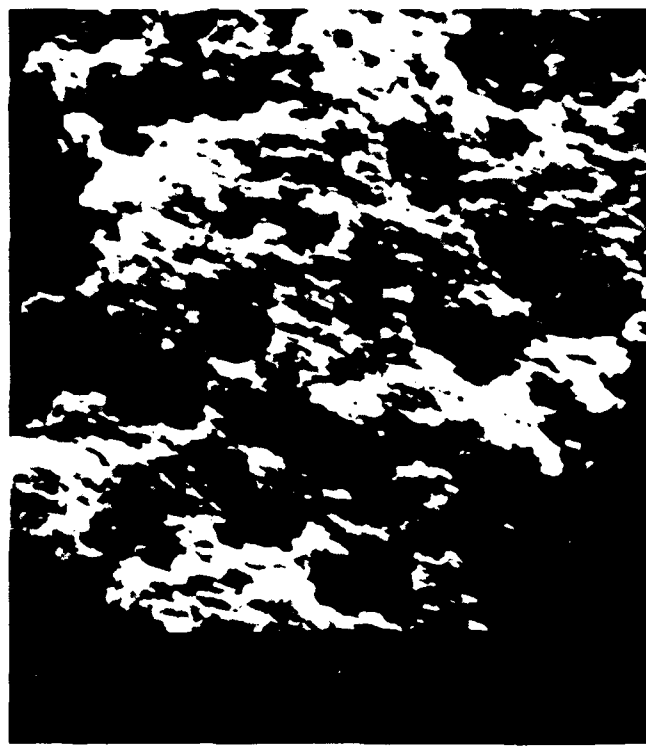


Figure 3. Transmission and scanning electron micrographs of cleaned  $\text{Fe}_3\text{O}_4$  particles (K-107-1).

### Experimental Details

The adaptation of commercial processes to prepare the requisite colloidal particles used stirred 4-l glass beakers as reactors. The sheet iron used was degreased in naphtha vapor and boiled for 10 min in hydrochloric acid. A Plexiglas rack was constructed to hold the folded sheet of iron in the beaker. A looped Tygon tube with holes drilled in it was positioned in the bottom of the beaker to serve as an oxygen sparger.

To prepare the  $\alpha\text{-Fe}_2\text{O}_3$  particles, a solution of  $\text{FeSO}_4 \cdot 7\text{H}_2\text{O}$  (Matheson Coleman and Bell, reagent-grade) in sulfuric acid containing the immersed folded iron sheets was heated at 82° for 10 hr, with oxygen bubbled through the reaction mixture at 1.5 standard ft<sup>3</sup>/hr.

The  $\alpha\text{-FeOOH}$  and  $\gamma\text{-FeOOH}$  particles were prepared using a two-step process, the generation of seed particles followed by their growth to larger size. The seed particles were prepared by stirring the appropriate iron salt solution after addition of sodium hydroxide, with oxygen bubbled through the reaction mixture at ca. 2 standard ft<sup>3</sup>/hr. The seed particles thus produced were then grown to larger-size particles in the presence of the folded iron sheet at 75-80°, also with oxygen sparging. The  $\alpha\text{-FeOOH}$  particles were prepared using a solution of  $\text{FeSO}_4 \cdot 7\text{H}_2\text{O}$  and the  $\gamma\text{-FeOOH}$  particles using a  $\text{FeCl}_2$  solution prepared by dissolving cleaned sheet iron in hydrochloric acid.

The foregoing preparations gave aqueous dispersions of the desired particles. Samples of these dispersions were cleaned by serum replacement using distilled deionized water or centrifugation-decantation. The cleaned sols were flushed to transfer the particles from the aqueous medium to the organic medium required for the polymer adsorption studies. For water-immiscible solvents (e.g. toluene), the cleaned sols were poured into a mixture of the desired solvent with sufficient ethanol to make the aqueous medium compatible with the water-immiscible solvent. The diluted sol was then placed in a Buchler Flash-Evaporator and the water-ethanol azeotrope was distilled off until both were completely removed. During this process, more of the water-immiscible solvent was added periodically to keep the particles in dilute suspension. The removal of water and ethanol was checked by shaking a given volume of the supernatant layer of the sol with an equal volume of water until no significant change in volume of either layer was observed. The water-miscible solvents used all had boiling points higher than 100°. Therefore, the solvents were added to the cleaned colloidal sols without ethanol, and the distillation was continued until the water was removed completely. These treatments gave colloidal dispersions of the iron compounds in the desired organic media; these dispersions were then used for the polymer adsorption studies.

The polymer adsorption studies used standard polymers recommended by Fowkes et al. [1,2] and Manson [4]: basic polymethyl methacrylate (Lucite 4F; E. I. du Pont de Nemours & Co.) and acidic post-chlorinated polyvinyl chloride (Geon 627x563; BFGoodrich Co.; 67% Cl;  $M_n$  40000). In addition, Epon 1001F epoxy resin (Shell Chemical Co.; epoxide equivalent weight 450-550) and Emerez 1511 curing agent (General Mills; amine equivalent weight 230-246) chosen as standards in the ONR Corrosion Program were also used.

The polymer adsorption isotherms were determined by weighing a given amount of iron oxide into an 8-oz. polypropylene bottle and adding a given amount of polymer solution. The basic polymethyl methacrylate was dissolved in the neutral carbon tetrachloride or toluene solvent and the acidic chlorinated polyvinyl chloride in neutral methylene chloride or 1,4-dioxane solvent. The Epon 1001F was dissolved in diethylene glycol monobutyl ether. The iron oxide-polymer solution mixture was agitated by adding glass beads to the bottle and rolling it on rollers to simulate ball-milling. At predetermined times, the dispersion was shaken vigorously, and a sample of the mixture was withdrawn and centrifuged to separate the iron oxide; then a 10-ml aliquot of the supernatant layer was dried to constant weight under vacuum to determine the concentration of unadsorbed polymer. The samples containing polymethyl methacrylate and chlorinated polyvinyl chloride were allowed to dry in an air oven to remove the bulk of the solvent and then were heated under vacuum for 48 hr at 120-125° to achieve constant weight. The samples containing Epon 1001F epoxy resin were dried for 24 hr at 100° in an air oven; further drying for 48 hr at 60° under vacuum gave no change in weight. The first experiments comprised determination of the time required to achieve adsorption equilibrium using a given polymer solution concentration; later experiments, the determination of the adsorption isotherms using polymer solutions of different concentration.

### Results and Discussion

The solids contents of the colloidal sols prepared using the laboratory adaptation of the commercial processes were much higher than those of the colloidal sols prepared using the classical methods. These solids contents were determined by titration of Fe(III) at the end of the preparation. Typical values obtained were 9.60 g/100 ml for  $\alpha$ -Fe<sub>2</sub>O<sub>3</sub>, 5.38 g/100 ml for  $\alpha$ -FeOOH, and 3.97 g/100 ml for  $\gamma$ -FeOOH. Of course, in each case, the solids content could have been increased by allowing the reaction to proceed further before stopping it. The extent to which the reaction was allowed to proceed was determined by the time required to produce a sufficiently large surface area for the polymer adsorption studies, yet not so long as to produce too large a particle size or particles of ill-defined shape. Therefore, the solids contents were controlled at values considered to be suitable.

Figure 4 shows transmission electron micrographs of these three samples. The  $\alpha$ - $\text{Fe}_2\text{O}_3$  (Fig. 4A) particles were spheroidal, similar in shape but smaller in size than those produced by the K-129-11 method (Fig. 1). The  $\alpha$ - $\text{FeOOH}$  particles (Fig. 4B) and  $\gamma$ - $\text{FeOOH}$  particles (Fig. 4C) were acicular, similar in shape but smaller in size compared with the  $\beta$ - $\text{FeOOH}$  particles prepared using the K-115-1 method (Fig. 2). Scanning electron micrographs, now in preparation, will confirm the morphology of these particles.

Mössbauer spectroscopy [5] showed that both the  $\alpha$ - $\text{FeOOH}$  and  $\gamma$ - $\text{FeOOH}$  particles were essentially pure (Fig. 5). Titration of the Fe(III) in the  $\text{Fe}_2\text{O}_3$  sample showed a purity of 92.5%. Mössbauer spectra of this sample will also be obtained.

Serum replacement was used to clean the sols prepared using the methods described earlier. For example, samples of an  $\alpha$ - $\text{Fe}_2\text{O}_3$  sol (K-129-11) containing 0.07, 0.28, 0.97, 1.02, 1.50, and 4.50 g particles were cleaned in a 400-ml serum replacement cell equipped with a 0.5  $\mu\text{m}$  Nuclepore filtration membrane without significant loss of solids due to flocculation. The cleaning of the highest-concentration sol took 300 hr and 10 l of distilled deionized water. The cleaning process was monitored by the conductance of the effluent stream; in each case, the conductance eventually reached a constant value, which was 2.5 times that of the distilled deionized water. Presumably this conductance was representative of an equilibrium electrolyte concentration in the presence of the colloidal  $\alpha$ - $\text{Fe}_2\text{O}_3$  particles.

The serum replacement method proved efficient for the lower-concentration sols prepared using the methods described earlier. However, it was more difficult to apply to the higher-concentration sols prepared using the laboratory adaptation of the commercial processes. Therefore, these sols were cleaned by repeated centrifugation and decantation, followed by redispersion in distilled deionized water.

The adsorption isotherms of polymethyl methacrylate, chlorinated polyvinyl chloride, Epon 1001F, and Emerez 1511 on the  $\alpha$ - $\text{Fe}_2\text{O}_3$ ,  $\alpha$ - $\text{FeOOH}$ , and  $\gamma$ - $\text{FeOOH}$  samples were determined. The polymethyl methacrylate and chlorinated polyvinyl chloride reached the equilibrium plateau values in 12 hr, the Epon 1001F and Emerez 1511 in 2 hr. The difference in the time required to reach adsorption equilibrium is attributed to the much lower molecular weight of the Epon 1001F and Emerez 1511 oligomers as compared with the higher molecular weight polymethyl methacrylate and chlorinated polyvinyl chloride.

Ullman [6] claimed that electron microscopy showed that the surfaces of iron oxide particles are smooth and that the adsorption of polymer molecules is nearly instantaneous. In this work, the surface smoothness has not yet been demonstrated unequivocally by transmission electron microscopy. Also, the relationship

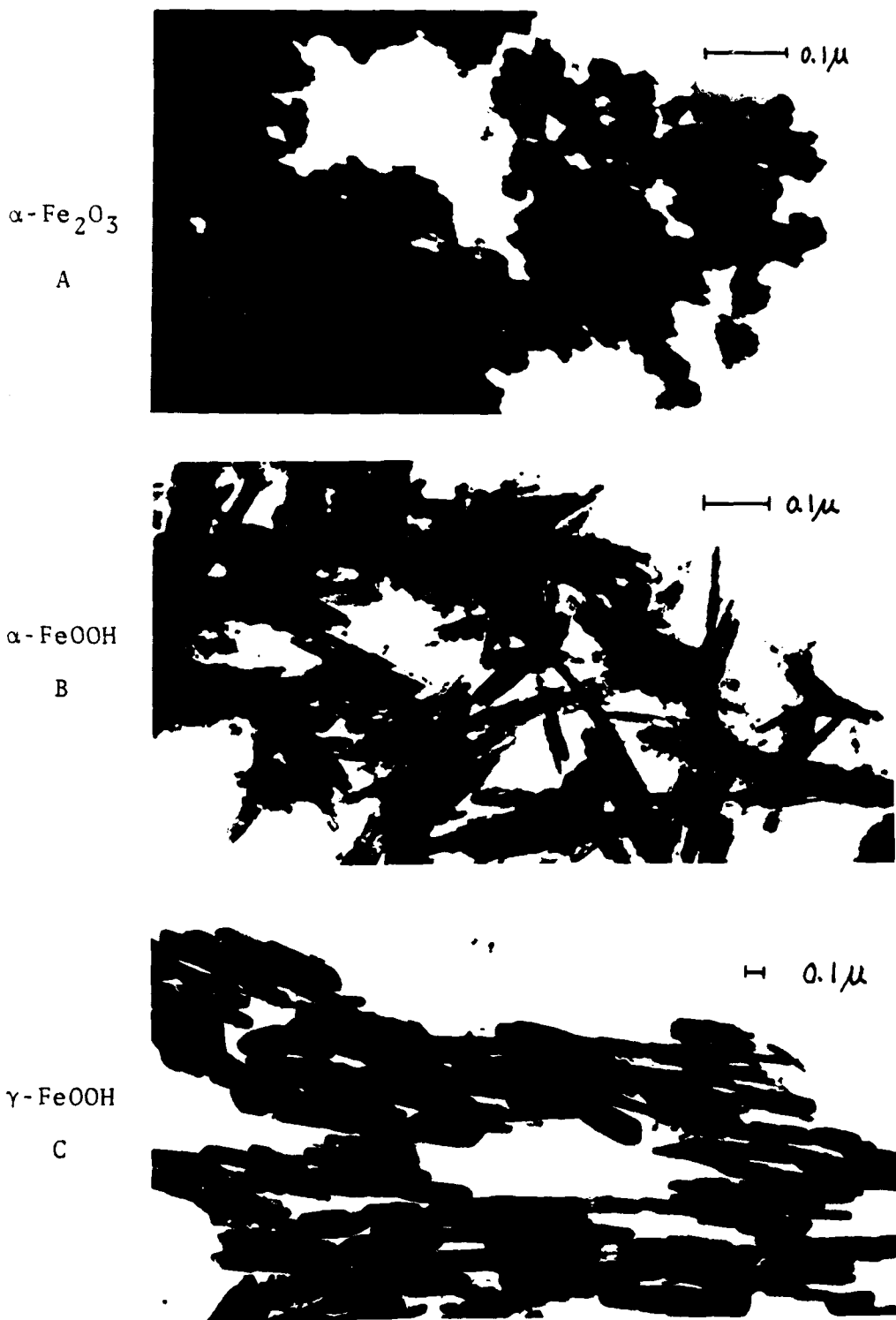


Figure 4. Transmission electron micrographs of iron oxide particles prepared in larger quantities: A.  $\alpha$ - $\text{Fe}_2\text{O}_3$ ; B.  $\alpha$ - $\text{FeOOH}$ ; C.  $\gamma$ - $\text{FeOOH}$ .

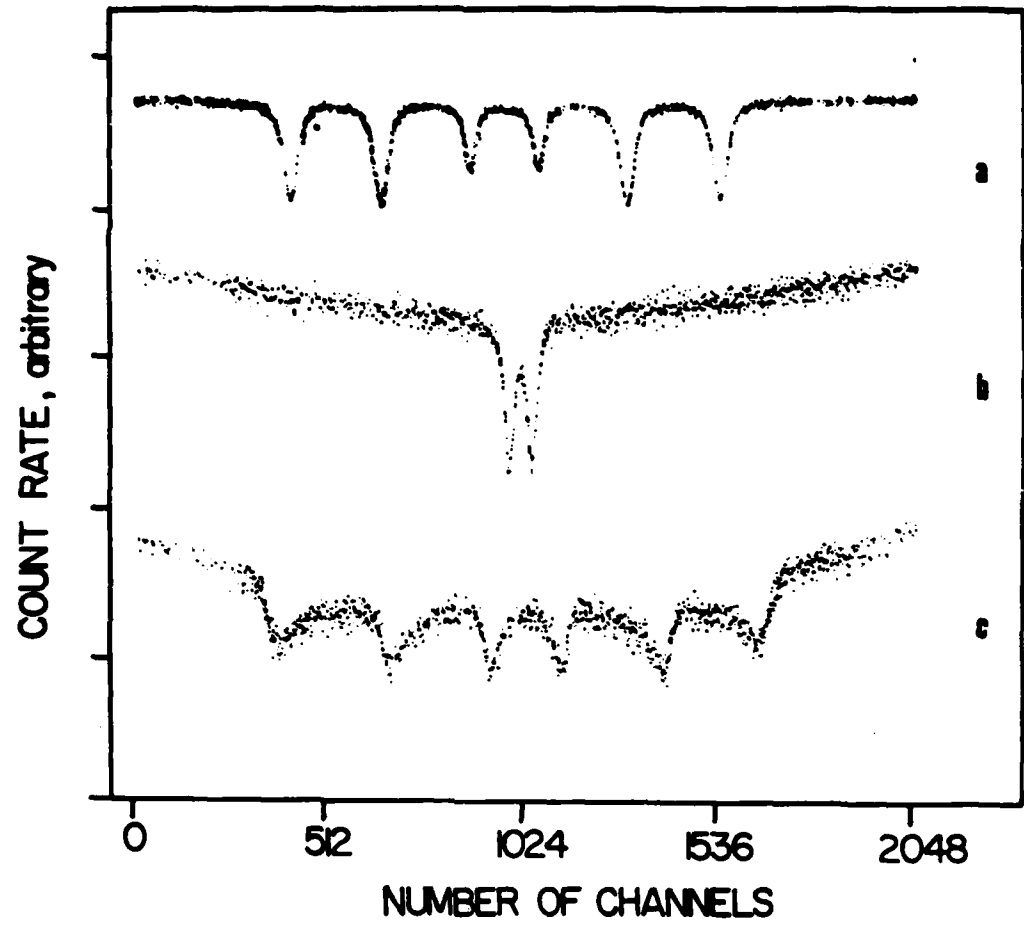


Figure 5. Mössbauer spectra of: A. alpha iron (standard);  
B.  $\gamma$ -FeOOH measured at room temperature;  
C.  $\alpha$ -FeOOH measured at room temperature.

between surface smoothness and rate of adsorption has not yet been defined. However, the shorter time required for the adsorption of the oligomeric Epon 1001F is expected because entropy effects are considered dominant in adsorption of polymer molecules from solution.

Figure 6-8 show the adsorption isotherms for  $\alpha\text{-Fe}_2\text{O}_3$ ,  $\alpha\text{-FeOOH}$ , and  $\gamma\text{-FeOOH}$ , respectively, as the variation of g polymer adsorbed/g substrate with equilibrium polymer concentration in g/100 ml. The adsorption isotherms should be expressed in terms of g polymer adsorbed/m<sup>2</sup> substrate, but this requires the specific surface areas, which are now being measured. Nevertheless, the adsorption isotherms show that all three iron oxides are amphoteric, i.e., they contain both acidic and basic surface groups. Moreover, the amounts of polymer adsorbed are greater than for the corresponding commercial  $\alpha\text{-Fe}_2\text{O}_3$  and  $\alpha\text{-FeOOH}$  samples (see Table III), the results for which are also shown in Figures 6 and 7. These results suggest that these prepared samples have higher specific surface areas than the corresponding commercial samples.

Table I gives the equilibrium plateau values in terms of the number of polymer segments adsorbed/g substrate. For the  $\alpha\text{-Fe}_2\text{O}_3$ , the adsorption of Emerez 1511 is inordinately high relative to the order observed for the commercial  $\alpha\text{-Fe}_2\text{O}_3$ . For the  $\alpha\text{-FeOOH}$ , the order is the same as for the commercial  $\alpha\text{-FeOOH}$ . Further conclusions must await the completion of the specific surface area determinations, but these results suggest that the surface characteristics of the prepared  $\alpha\text{-Fe}_2\text{O}_3$  and  $\alpha\text{-FeOOH}$  samples may be different from those of the corresponding commercial samples.

Table I  
Number of Polymer Segments Adsorbed/Unit Weight Substrate

Iron Oxide	Number of Polymer Segments Adsorbed/g Substrate, $\times 10^{-20}$			
	Cl-PVC	PMMA	EP 1001	EM 1511
$\alpha\text{-Fe}_2\text{O}_3$	33	22	12	55
$\alpha\text{-FeOOH}$	77	64	18	24
$\gamma\text{-FeOOH}$	28	53	25	38
<hr/>				
$\alpha\text{-Fe}_2\text{O}_3^*$	8.6	6.6	1.2	1.5
$\alpha\text{-FeOOH}^*$	9.3	6.0	0.45	0.77

\*Commercial samples (see Table III).

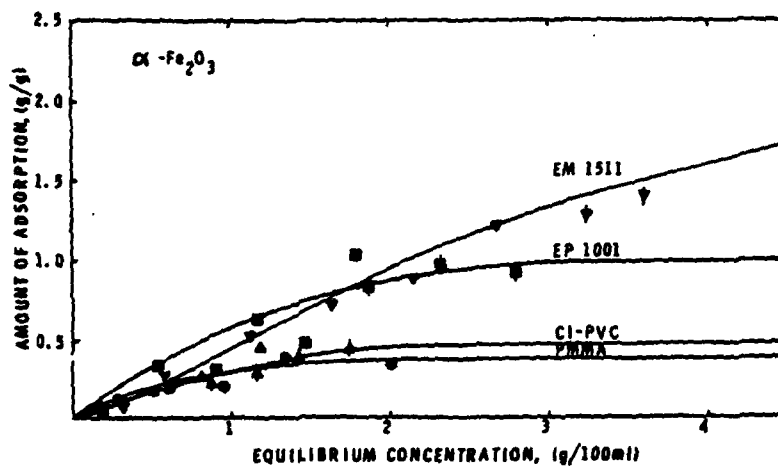


Figure 6. Adsorption isotherms of different polymers on  $\alpha\text{-Fe}_2\text{O}_3$ .

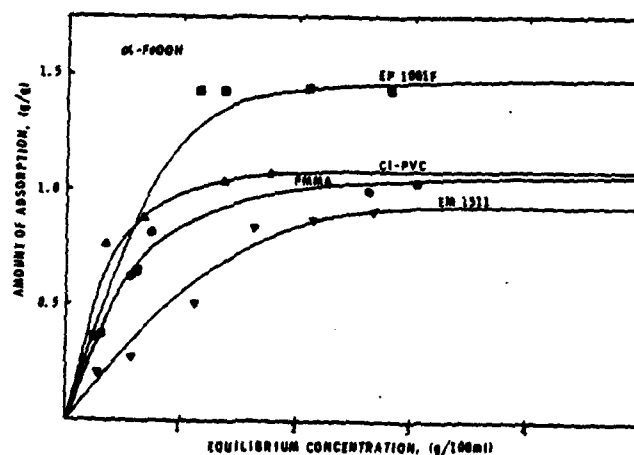


Figure 7. Adsorption isotherms of different polymers on  $\alpha\text{-FeOOH}$ .

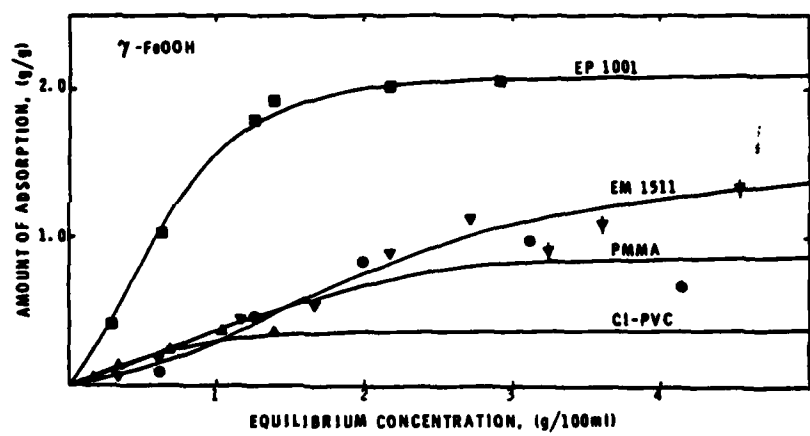


Figure 8. Adsorption isotherms of different polymers on  $\gamma$ -FeOOH.

## Part (b). Dispersions of Commercial Iron Oxides

### Introduction

This approach used commercial iron oxides dispersed in aqueous media for characterization and in organic media for polymer adsorption studies. Of the eight corrosion products of iron, four were available commercially. These were obtained from Pfizer Inc., Pigment and Metals Division, Easton, Pa. (Table II). These iron oxide samples were used as received. However, transmission electron microscopy showed possible contamination of the  $\alpha$ -FeOOH, so additional samples were obtained from Pfizer, the seed from which the oxide was produced and a sample of production material removed before the surface treatment. Transmission electron microscopy of these samples showed the same morphology, so the original sample was used.

Table II  
Commercial Iron Oxides

<u>Iron Oxide</u>	<u>Sample Designation</u>	<u>Lot Number</u>
$\alpha$ -Fe <sub>2</sub> O <sub>3</sub>	R-2199	#E9036
$\gamma$ -Fe <sub>2</sub> O <sub>3</sub>	MO-2228	#E9460
Fe <sub>3</sub> O <sub>4</sub>	BK-5000	#E9516
$\alpha$ -FeOOH	YLO-2288-D	#F9006

### Experimental Details

All four samples were characterized as to morphology by transmission electron microscopy, and their specific surface areas, relative porosities, and relative adsorption energies were measured by argon gas adsorption (Table III). The specific surface areas of all four samples were great enough for the polymer adsorption experiments. The high BET "C" values (the average energy of adsorption is an exponential function of C) showed that, with the possible exception of  $\alpha$ -FeOOH, the particle surfaces were crystalline. Also, the adsorption isotherms showed that the samples were nonporous.

Table III  
Argon Gas Adsorption on Iron Oxides

<u>Iron Oxide</u>	<u>Specific Surface Area, m<sup>2</sup>/g</u>	<u>BET "C" Value</u>
$\alpha\text{-Fe}_2\text{O}_3$	9.96	3589
$\gamma\text{-Fe}_2\text{O}_3$	19.80	1158
$\text{Fe}_3\text{O}_4$	5.72	$\infty$
$\alpha\text{-FeOOH}$	10.66	445

Transmission electron microscopy [3] showed that all four samples had a broad distribution of particle sizes. The  $\gamma\text{-Fe}_2\text{O}_3$  and  $\alpha\text{-FeOOH}$  particles were acicular, and the  $\alpha\text{-Fe}_2\text{O}_3$  and  $\text{Fe}_3\text{O}_4$  particles were spheroidal.

Aqueous dispersions of the four iron-oxide samples were prepared in 250-ml polypropylene bottles containing 13 mm Burundum grinding cylinders; the bottles were capped and allowed to roll on the rollers to simulate ball-milling. Samples were taken at various times, and the settling times were measured. Transmission electron micrographs showed that there was no change in crystal structure upon dispersion.

The dispersions were cleaned by serum replacement in a 2000-ml glass cell shown in Figure 9. The large volume of the cell allowed the cleaning of a large volume of dispersion. The filtration membrane was a 0.1  $\mu\text{m}$  Nuclepore membrane supported by a perforated Teflon disc. The ground-glass joints were sealed with Dow Corning high vacuum sealant. Distilled deionized water was pumped through the cell until the effluent pH matched that of the distilled deionized water (pH 6.8); then an additional 200 ml distilled deionized water was pumped through to complete the cleaning.

The oxides as received were not easily wetted by organic solvents. Their hydrophilic surfaces were attributed to the presence of an adsorbed layer of water on the iron oxide surfaces. Washing the particles with ethanol, followed by xylene-ethanol mixtures and later by xylene (good solvent for Epon 1001) gave dispersions that were still partially flocculated. Drying the iron oxide at 100° under vacuum for 24 hr enhanced its dispersion in water by ball-milling and, following cleaning by serum replacement, its dispersion in organic solvents. Finally, to obtain the iron oxide samples for the polymer adsorption studies, the aqueous iron oxide dispersions in water were allowed to settle and the supernatant

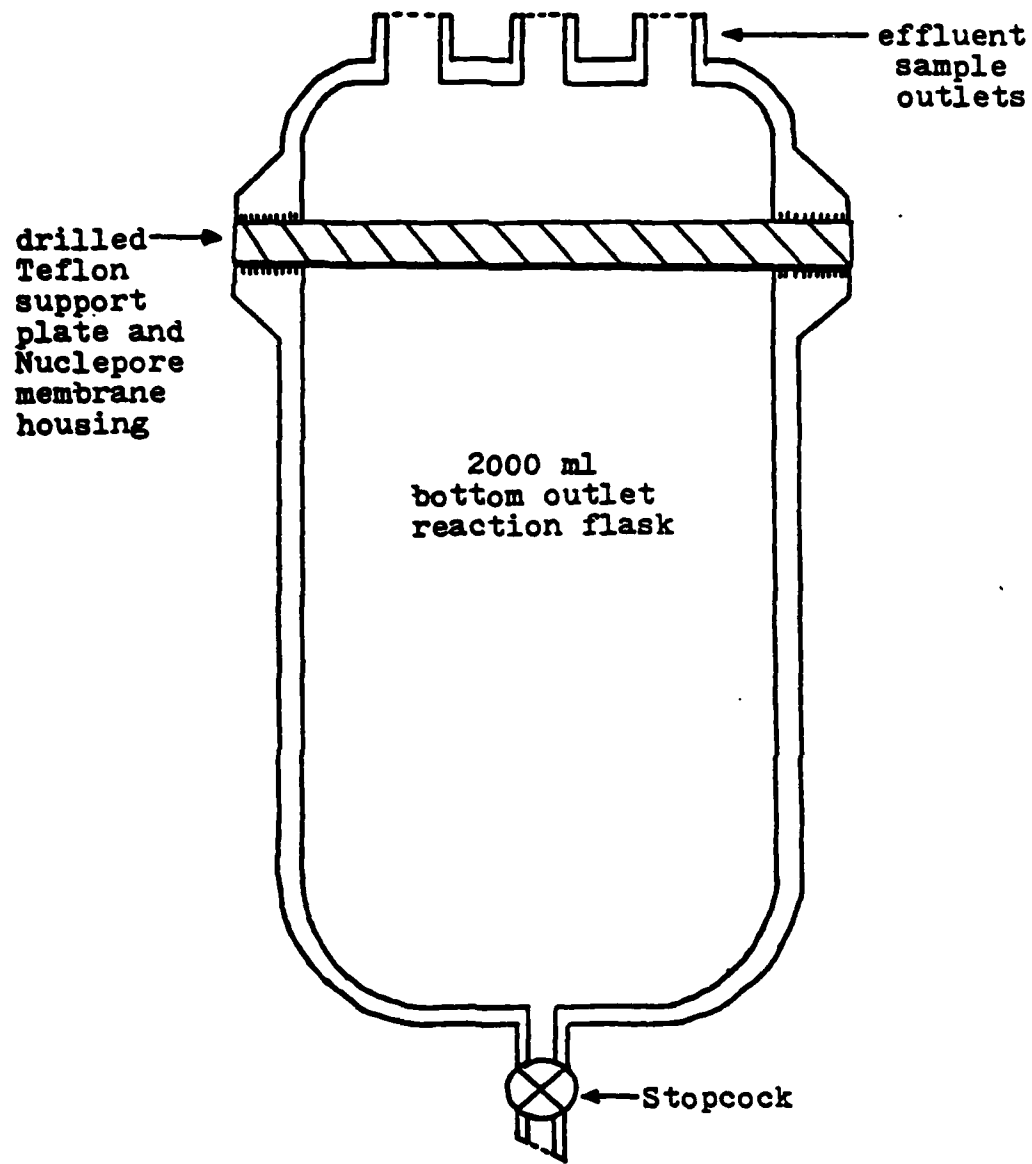


Figure 9. Schematic representation of apparatus used for serum replacement of iron oxide sols.

layer was decanted; this process was repeated several times, and the slurries of resuspended iron oxide particles were dried at 100° under vacuum for 24 hr. The dried samples were kept in tightly sealed bottles to hinder the adsorption of moisture. These iron oxide samples were easily dispersable in the organic solvents and therefore were added directly to the polymer solutions.

Weighed amounts of the iron oxides were added to the polymer solutions in polypropylene bottles and rolled on the roller mill; the samples were then centrifuged to sediment the iron oxide, and an aliquot of the supernatant layer was dried to apparent dryness in a hood and then dried to constant weight in an air oven at 100°. This technique gave poor results, principally because the solvents migrated through the polypropylene bottles. Therefore, 8-oz flint glass bottles were substituted for the polypropylene bottles; the bottle screw caps were lined with aluminum foil to prevent contamination from the vinyl cap liners.

The polymer adsorption on the iron oxide samples was complete in 3 days, so all experiments were run for that period of time. The iron oxide-polymer mixture was shaken for 3 min on the Red Devil Paint Shaker and rolled on the roller mill for 72 hr. Double samples of each iron oxide were run, and calibrations were obtained from polymer solutions run without iron oxides.

### Results and Discussion

For the aqueous iron oxide dispersions, the degree of dispersion was followed by measuring the time required for complete settling of the dispersion. Table IV shows that the settling time increased with increasing milling time over the 120-hr period, indicating that the degree of dispersion increased (or the average particle size decreased) as the milling progressed. At the same time, the pH of the aqueous phase increased for all samples except the  $\text{Fe}_3\text{O}_4$ . For the three  $\alpha\text{-FeOOH}$  samples, the settling times for the commercial sample and the final sample without surface treatment were about the same, but were greater for the  $\alpha\text{-FeOOH}$  seed; since the seed particles were smaller than the final particles, longer settling times are expected. Also, the final pH of all three samples was the same within experimental error, but the initial pH was different, being lowest for the commercial sample which had been subjected to surface treatment, much higher for the seed sample, and slightly higher than that for the final sample without surface treatment. The surface treatment is not known, but obviously involves a compound with a lower isoelectric point.

All of the foregoing samples settled as if they were stable dispersions, i.e., the sample soon showed a phase boundary with particle movement back and forth across this boundary, followed by the formation of a settled oxide layer which slowly increased

Table IV  
Settling Times and pH of Aqueous Iron Oxide Dispersions

<u>Iron Oxide</u>	<u>Milling Time, hrs</u>	<u>Settling Time, hrs</u>	<u>pH</u>
$\alpha\text{-Fe}_2\text{O}_3$	24	2.5	6.7
	72	4.0	7.1
	120	6.5	8.3
$\gamma\text{-Fe}_2\text{O}_3$	24	0.33	7.8
	72	0.50	8.2
	120	0.75	8.8
$\text{Fe}_3\text{O}_4$	24	1.0	8.8
	72	1.0	8.8
	120	1.5	8.8
$\alpha\text{-FeOOH}$	24	1.75	6.6
	72	3.0	7.2
	120	4.75	9.0
$\alpha\text{-FeOOH seed}$	24	0.50	7.7
	72	3.25	8.7
	120	10.5	8.9
$\alpha\text{-FeOOH final}$ without surface treatment	24	3.0	8.1
	72	1.5	8.4
	120	4.75	9.0

in depth and an opaque supernatant layer which slowly became less opaque. After the samples had settled for 60 days, they were redispersed, but these redispersed samples settled as if they were unstable, i.e., the sample initially showed no phase boundary, but instead the formation of a thin settled oxide layer which slowly compacted, a thick layer of a gelatinous flocculated particle structure which settled only slightly, and a small clear supernatant layer which increased only slowly and never comprised more than a small part of the total height. Transmission electron microscopy showed no changes in crystal structure before and after 60 days' settling. The initial samples which showed an increase in pH upon milling also showed a thin white film on the water surface; this film was removed by sedimentation and decantation followed by redispersion in distilled deionized water or by serum replacement; however, the pH of the aqueous phase was unchanged by this treatment and transmission electron microscopy showed the film to be polymeric, indicating that the white film may have been part of the polypropylene bottles that was abraded away during the milling and that the final pH is an inherent property of the dispersed iron oxide particles.

Polymer adsorption experiments were carried out using polymethyl methacrylate in toluene, chlorinated polyvinyl chloride in 1,4-dioxane, and Epon 1001F epoxy resin and Emerez 1511 curing agent in diethylene glycol monobutyl ether solution with all 4 iron oxides, for a total of 16 adsorption systems. The adsorption experiments were carried out as described earlier, i.e., by mixing dried iron oxide powder in the polymer solution for three days, then centrifuging and measuring the concentration of unadsorbed polymer in the supernatant layer. At least 4 different concentrations of polymer were used in each adsorption system. The adsorption data were obtained in g adsorbed polymer/g iron oxide; these values were expressed as mg adsorbed polymer/m<sup>2</sup> iron oxide surface using the specific surface areas determined by argon adsorption. These values were then plotted against the equilibrium polymer concentration in the continuous organic phase to give the adsorption isotherms. Figures 10-13 show the adsorption isotherms for  $\alpha$ -Fe<sub>2</sub>O<sub>3</sub>,  $\gamma$ -Fe<sub>2</sub>O<sub>3</sub>, Fe<sub>3</sub>O<sub>4</sub>, and  $\alpha$ -FeOOH, respectively. For the  $\alpha$ -Fe<sub>2</sub>O<sub>3</sub>, Fe<sub>3</sub>O<sub>4</sub>, and  $\alpha$ -FeOOH, the equilibrium plateau values were greatest for the chlorinated polyvinyl chloride and decreased progressively for polymethyl methacrylate, Epon 1001F, and Emerez 1511. For  $\gamma$ -Fe<sub>2</sub>O<sub>3</sub>, the order was similar but with the polymethyl methacrylate and Epon 1001F interchanged. Table V gives the equilibrium plateau values in terms of the number of polymer segments adsorbed/100 Å<sup>2</sup> substrate surface area.

Table V  
Number of Polymer Segments Adsorbed/Unit Surface Area

Iron Oxide	Number of Polymer Segments Adsorbed/100 Å <sup>2</sup>			
	Cl-PVC	PMMA	EP 1001	EM 1511
$\alpha$ -Fe <sub>2</sub> O <sub>3</sub>	85	65	13	15
$\gamma$ -Fe <sub>2</sub> O <sub>3</sub>	51	19	5.7	2.3
Fe <sub>3</sub> O <sub>4</sub>	168	57	9.0	13
$\alpha$ -FeOOH	86	58	9.0	7.4

These results show that all four iron oxides are amphoteric, i.e., the substantial adsorption of both the acidic chlorinated polyvinyl chloride and the basic polymethyl methacrylate shows that the polar surface sites are both basic and acidic. The substantial amounts adsorbed correspond to a thickness much greater than a monolayer of polymer segments. Substantial adsorption of Epon 1001F and Emerez 1511 was also observed, but amounts adsorbed are closer to a monolayer adsorption.

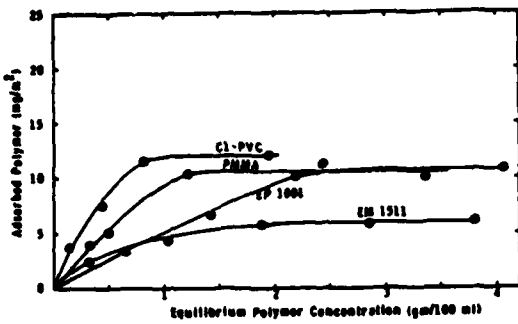


Figure 10.

Adsorption isotherms of different polymers on commercial  $\alpha\text{-Fe}_2\text{O}_3$ .

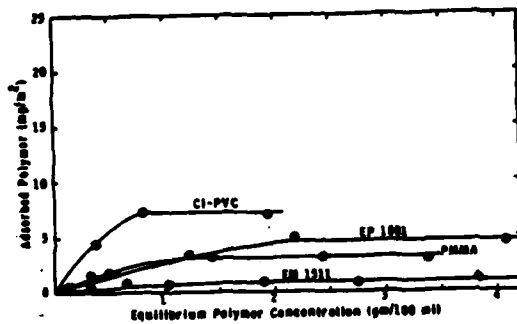


Figure 11.

Adsorption isotherms of different polymers on commercial  $\gamma\text{-Fe}_2\text{O}_3$ .

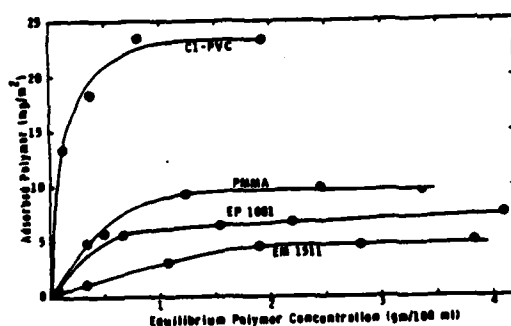


Figure 12.

Adsorption isotherms of different polymers on commercial  $\text{Fe}_3\text{O}_4$ .

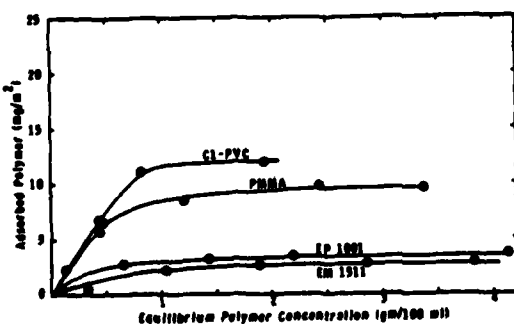


Figure 13.

Adsorption isotherms of different polymers on commercial  $\alpha\text{-FeOOH}$ .

The number of polar sites per unit surface area was also determined for  $\alpha$ -Fe<sub>2</sub>O<sub>3</sub> and Fe<sub>3</sub>O<sub>4</sub> (measurements of the other samples are in progress) by adsorption of water vapor on the dried iron oxides. This method does not distinguish between acidic or basic surface sites, but merely gives the total number of such sites. The number of such sites/100 Å<sup>2</sup> was 7.2 for  $\alpha$ -Fe<sub>2</sub>O<sub>3</sub> and 10.7 for Fe<sub>3</sub>O<sub>4</sub>. These values are at, or close to, the ca. 10 water molecules/100 Å<sup>2</sup> concentration that corresponds to a saturated monolayer. The values determined by water vapor adsorption are in good agreement with the number of adsorbed polymer segments for Epon 1001F and Emerez 1511. If the Epon 1001F is difunctional in epoxide groups and the Emerez 1511 difunctional in amine groups, the number of polymer segments adsorbed corresponds to adsorption of both functional groups on the  $\alpha$ -Fe<sub>2</sub>O<sub>3</sub> surface but adsorption of only a single functional group on the Fe<sub>3</sub>O<sub>4</sub> surface. This difference in the mode of adsorption may be due to the Fe(II) in the Fe<sub>3</sub>O<sub>4</sub> as compared with the Fe(III) in the  $\alpha$ -Fe<sub>2</sub>O<sub>3</sub>.

The number of polymer segments adsorbed/100 Å<sup>2</sup> is much greater for the chlorinated polyvinyl chloride and polymethyl methacrylate than for Epon 1001F and Emerez 1511. This difference is attributed to the much higher molecular weights of the chlorinated polyvinyl chloride and polymethyl methacrylate, which allow adsorption of individual segments on a polar site, with loops and chain ends of the polymer extending out into the medium. In contrast, the Epon 1001F and Emerez 1511 are oligomers which can arrange themselves in a packed surface layer without extending far out into the medium. The number of polymer segments adsorbed is significantly greater for the chlorinated polyvinyl chloride than for the polymethyl methacrylate; this is attributed to the greater flexibility of the chlorinated polyvinyl chloride chains as compared with the relatively stiff polymethyl metacrylate chains. The much greater adsorption of chlorinated polyvinyl chloride on Fe<sub>3</sub>O<sub>4</sub> than on the other three iron oxides is attributed speculatively to the Fe(II) in the Fe<sub>3</sub>O<sub>4</sub> and the Fe(III) in the other three iron oxides.

It is of interest that, for chlorinated polyvinyl chloride, the number of polymer segments adsorbed/100 Å<sup>2</sup> increased with decreasing specific surface area (increasing average particle size), i.e., the larger the iron oxide particles, the thicker the layer of adsorbed polymer. The same variation was observed for polymethyl methacrylate with a lesser spread of values, but not with Epon 1001F or Emerez 1511. The thinner adsorption layers of the smaller particle size iron oxides are attributed speculatively to their smaller radii of curvature as well as possibly their greater surface roughness and porosity.

In any event, these four iron oxides adsorb substantial-but-different concentrations of both the model acidic and basic polymers as well as the prototype ingredients of a practical coatings system. Thus far the results are consistent with those for the iron oxides prepared in the laboratory. Further experiments are required to complete these adsorption studies and define each corrosion product of iron in terms of its surface properties.

## CONCLUSIONS

The iron corrosion products prepared as colloidal sols and purchased commercially are both amphoteric, i.e., their surfaces comprise both acidic and basic groups as determined by adsorption of basic polymethyl methacrylate and acidic chlorinated polyvinyl chloride standards. However, the proportion of acidic and basic groups may vary significantly from one compound to another. Thus far all compounds studied adsorb substantial-but-different proportions of Epon 1001F and Emerez 1511 (candidates for practical coatings systems). Further experiments are required to define completely the adsorption characteristics of these systems.

## PERSONNEL

Graduate student M. H. Kang carried out the preparation and characterization of the colloidal sols of iron corrosion products and the corresponding polymer adsorption measurements. Graduate student D. W. Timmons carried out the characterization and polymer adsorption experiments for the commercial iron oxide samples. Graduate student T. C. Huang assisted in the polymer adsorption measurements beginning the summer of 1981. Mr. L. M. Bennetch served as consultant and helped in the preparation of pure iron oxide sols. Visiting scientist Dr. M. J. Cantow supervised the work of M. H. Kang and D. W. Timmons from the beginning of the project until June 1980. Staff member Ms. O. L. Shaffer carried out the electron microscopy. Faculty member Dr. F. J. Micale carried out the argon and water adsorption experiments and assisted with the other experiments as did faculty member Dr. M. S. El-Aasser.

## REFERENCES

- [1] M. J. Marmo, M. A. Mostafa, H. Jinnai, F. M. Fowkes, and J. A. Manson, I&EC Prod. Res. Dev. 15 (3), 206 (1976).
- [2] F. M. Fowkes and M. A. Mostafa, I&EC Prod. Res. Dev. 17 (1), 3 (1978).
- [3] First Annual Report, ONR Project, 1980.
- [4] J. A. Manson, private communication, 1981.
- [5] Mössbauer spectrometry carried out by S. Music.
- [6] R. Ullman, Encyl. Polym. Sci. Tech. 1, 551 (1964).

## Program #14. Mössbauer Studies of Iron Oxides

### ABSTRACT

Mössbauer spectroscopy has been used to investigate the precipitates formed by hydrolysis of 0.1M solutions of  $\text{Fe}(\text{NO}_3)_3$ ,  $\text{FeCl}_3$ ,  $\text{Fe}_2(\text{SO}_4)_3$ , and  $\text{NH}_4\text{Fe}(\text{SO}_4)_2$  at 90°C. The isomer shifts, electric quadrupole splittings and nuclear magnetic splittings were used for the qualitative and quantitative identification of the hydrolysis products. Proposals were made concerning the mechanism of formation of the oxides and hydroxyoxides of iron. Hydrolysis in the nitrate and chloride solutions proceeds by the formation of monomers and dimers of iron(III) ions, followed by the formation of polymeric species. The polymers formed in the nitrate solution are not presumed to include the nitrate ion in the polymer chain, whereas the polymers formed in the chloride solution contain some chloride ions in place of the hydroxyl ion. The next step in the precipitation process is the formation of oxybridges and the development of  $\alpha\text{-FeOOH}$  and  $\beta\text{-FeOOH}$  structures. This step is followed by loss of water and internal crystallization of  $\alpha\text{-FeOOH}$  to  $\alpha\text{-Fe}_2\text{O}_3$  in nitrate solution or by dissolution of  $\beta\text{-FeOOH}$  and growth of  $\alpha\text{-FeOOH}$  in chloride solution. In sulfate solutions the formation of a  $\text{FeSO}_4^+$  complex suppresses the polymerization process and the formation of oxyhydroxides and oxides. Basic Fe(III) sulfates are formed instead.

### INTRODUCTION

The investigation and understanding of structural transformations of iron hydroxides and oxides are important, since they are common in nature and have great industrial importance (to corrosion and protection, catalysis, pigments, magnetic tapes, cooling water treatment, etc.).

The composition and structures of iron(III) (hydr)oxide precipitates depend on the  $\text{Fe}^{3+}$  concentration, the nature of the anion present, pH, temperature, time of aging and other topochemical parameters [1,2]. Difficulties in the investigation of these precipitation systems result from two facts. First, small differences in the values of the parameters change the composition,

structure and morphology of the precipitate. Second, the experimental methods used in previous studies, e.g. potentiometry, ultracentrifugation, electron microscopy, visible spectrophotometry, IR spectrophotometry and X-ray diffraction have limitations and cannot follow all stages of the overall precipitation process. The stage least susceptible to study is the characterization of the precipitate in the colloidal dimension range, where the hydroxy polymers, small iron(III) (hydr)oxide particles of complex composition, and so-called amorphous iron(III) hydroxide form.

The use of  $^{57}\text{Fe}$  Mössbauer spectroscopy permits a study of each of the steps involved in the precipitation of iron hydroxyoxides and their subsequent transformation. Mössbauer spectroscopy of frozen solutions has been used previously to investigate the initial stages of hydrolysis and polymer formation [3]; however, the formation of solid phase complicated the situation since  $^{57}\text{Fe}$  atoms of all components contributed to the spectrum. In this study the solid phase was separated from mother liquor in order to avoid this problem. In such a way, it was possible to record the spectra at room temperature and to determine the composition and structures of the hydrolysis products of  $\text{Fe}(\text{NO}_3)_3$ ,  $\text{FeCl}_3$ ,  $\text{Fe}_2(\text{SO}_4)_3$  and  $\text{NH}_4\text{Fe}(\text{SO}_4)_2$  solutions.

The hydrolysis experiments described herein were carried out at 90° in the absence of a base. The formation of iron oxides under these conditions has special pertinence to the so-called "hot water test" in which the adherence of organic coatings to a steel substrate is determined after exposure to water at 80-100°. Corrosion and precipitation of iron oxides at the coating/substrate interface sometimes occur under these conditions.

## EXPERIMENTAL

Merck AnalaR grade  $\text{Fe}(\text{NO}_3)_3 \cdot 9\text{H}_2\text{O}$ ,  $\text{FeCl}_3 \cdot 6\text{H}_2\text{O}$ ,  $\text{Fe}_2(\text{SO}_4)_3 \cdot 9\text{H}_2\text{O}$ , and  $\text{NH}_4\text{Fe}(\text{SO}_4)_2 \cdot 12\text{H}_2\text{O}$  and bidistilled water were used. The precipitates were produced from 0.1M solutions of  $\text{Fe}(\text{NO}_3)_3$ ,  $\text{FeCl}_3$ ,  $\text{Fe}_2(\text{SO}_4)_3$ , and  $\text{NH}_4\text{Fe}(\text{SO}_4)_2$  by heating in closed flasks at  $90 \pm 1^\circ\text{C}$ . Solutions were not stirred during precipitation periods up to 24 hr. Filtrations of the precipitates were carried out using Schleicher und Schull 0.1-0.2  $\mu\text{m}$  filters or filter papers (blue) of the same firm. The precipitates were subsequently washed free from mother liquor solution with bidistilled water and ethanol. Samples were dried in air for 2 hr at 60°C. Mössbauer spectra were recorded using a constant-acceleration spectrometer of standard design in conjunction with a multi-channel analyzer. The spectrometer was calibrated using a thin iron foil.  $^{57}\text{Co}/\text{Pd}$  or  $^{57}\text{Co}/\text{Pt}$  source was used. The spectra were recorded at room temperature ( $22^\circ\text{C}$ ) or liquid nitrogen temperature using a transmission geometry. Folded spectra have been

evaluated by fitting a sum of Lorentzian lines using a least squares SIRIUS program (Central Physical Research Institute, Budapest, Hungary) and its modification [4]. All chemical shifts are given with respect to metallic iron.

## RESULTS

### Precipitation from $\text{Fe}(\text{NO}_3)_3$ Solution

Mössbauer spectra of the precipitates formed by hydrolysis of 0.1M  $\text{Fe}(\text{NO}_3)_3$  solution for different times of heating at 90°C are shown in Figures 1-4. Mössbauer parameters obtained by computer evaluation of all measured spectra are summarized in Table I. The precipitate produced from 0.1M  $\text{Fe}(\text{NO}_3)_3$  solution after 80 min of heating was in the form of a stable colloidal dispersion. Half of the dispersion was removed by filtration (sample 41) and the other half was aged for 2 additional days at room temperature (sample 41a). The Mössbauer spectrum of sample 41 shows only a quadrupole doublet Q at room temperature and a magnetic splitting component  $M_1$  with very broad lines at liquid nitrogen temperature. The spectrum indicates that there is superposition of several magnetic components and the value of the internal magnetic field  $H_{5/2} = 453$  kOe represents only a mean value. The Mössbauer spectrum of sample 41a shows a quadrupole doublet Q at room temperature (Fig. 1a) and three relatively well resolved magnetic components ( $M_1, M_2, M_3$ ) at liquid nitrogen temperature (Fig. 1b). The parameters of component  $M_1$  are ascribed to  $\alpha\text{-FeOOH}$  (goethite), and components  $M_2$  and  $M_3$  with small values of internal magnetic field  $H_{5/2} = 416$  kOe and  $H_{5/2} = 353$  kOe at liquid nitrogen temperature are ascribed to iron(III) hydroxy polymers. In Table I the values A(%) represent the percentages of each component in the sample investigated assuming similar values for the Debye-Waller factor. The values for internal magnetic field  $H_{5/2}$  near 470 kOe obtained at liquid nitrogen temperature are slightly less than those for  $\alpha\text{-FeOOH}$  (goethite) [5-8].

The precipitate produced by hydrolysis of 0.1M  $\text{Fe}(\text{NO}_3)_3$  for 6 hr at 90°C (sample 43) yields a different Mössbauer spectrum at room temperature than that observed for shorter hydrolysis times. This spectrum shows the superposition of a central quadrupole doublet Q and two magnetic splitting components ( $M_1, M_2$ ) with values  $H_{5/2} = 477$  kOe for  $M_1$  and  $H_{5/2} = 338$  kOe for  $M_2$  (Fig. 2). Two magnetic splitting components ( $M_1, M_2$ ) with values  $H_{5/2} = 528$  kOe for  $M_1$  and  $H_{5/2} = 492$  kOe for  $M_2$  appear in the spectrum recorded at liquid nitrogen temperature (Fig. 3). The Mössbauer parameters of component  $M_1$  correspond to hematite ( $\alpha\text{-Fe}_2\text{O}_3$ ) and of component  $M_2$  correspond to goethite ( $\alpha\text{-FeOOH}$ ). The spectrum of sample 39 prepared in  $\text{Fe}(\text{NO}_3)_3$  containing 0.05M  $\text{HNO}_3$  does not show a central quadrupole doublet at room temperature.

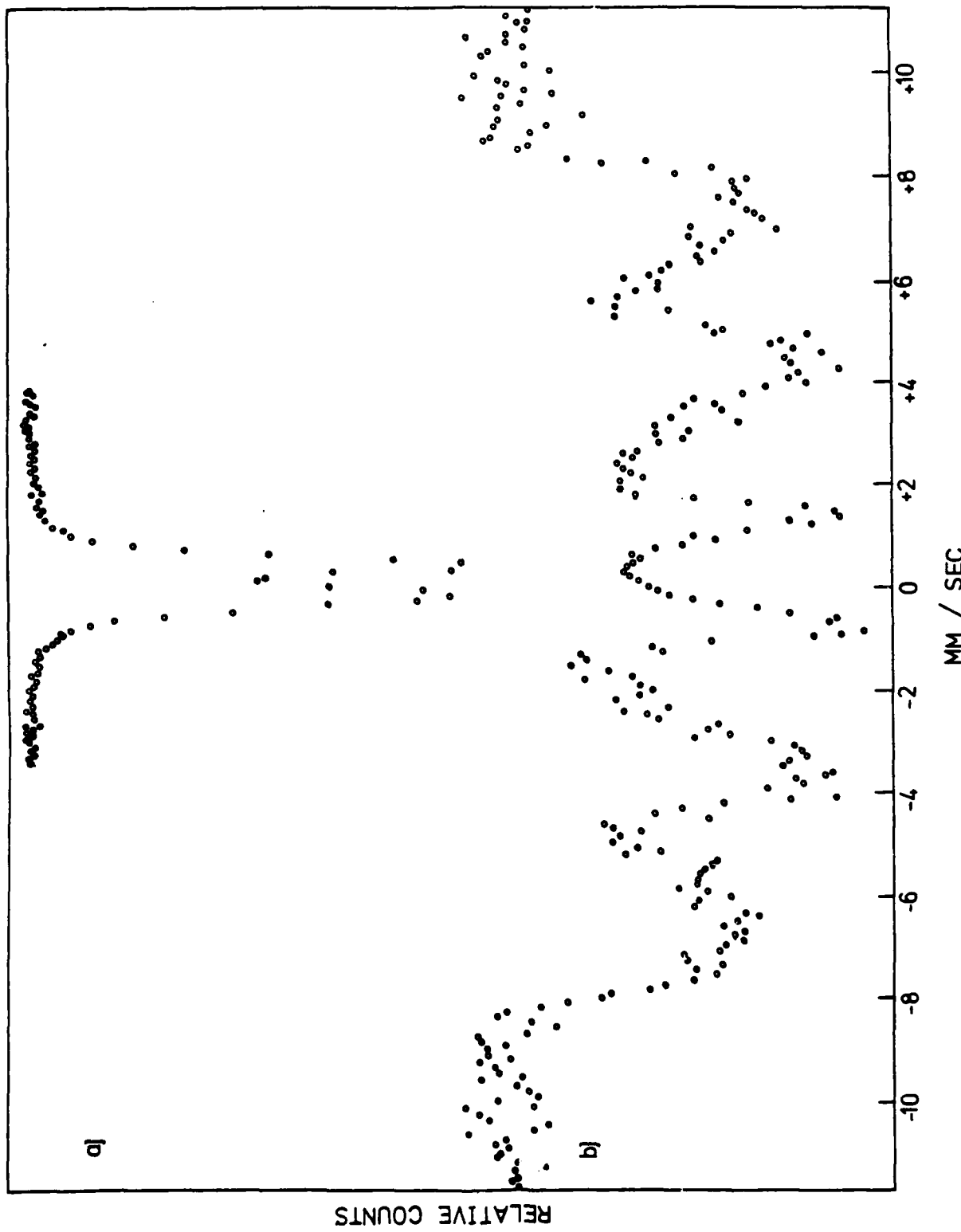


Figure 1. Mössbauer spectra of the precipitate formed by hydrolysis of 0.1M  $\text{Fe}(\text{NO}_3)_3$  solution for 80 minutes at 90°C (sample 41a)  
 (a) room temperature spectrum; (b) 77 K spectrum.

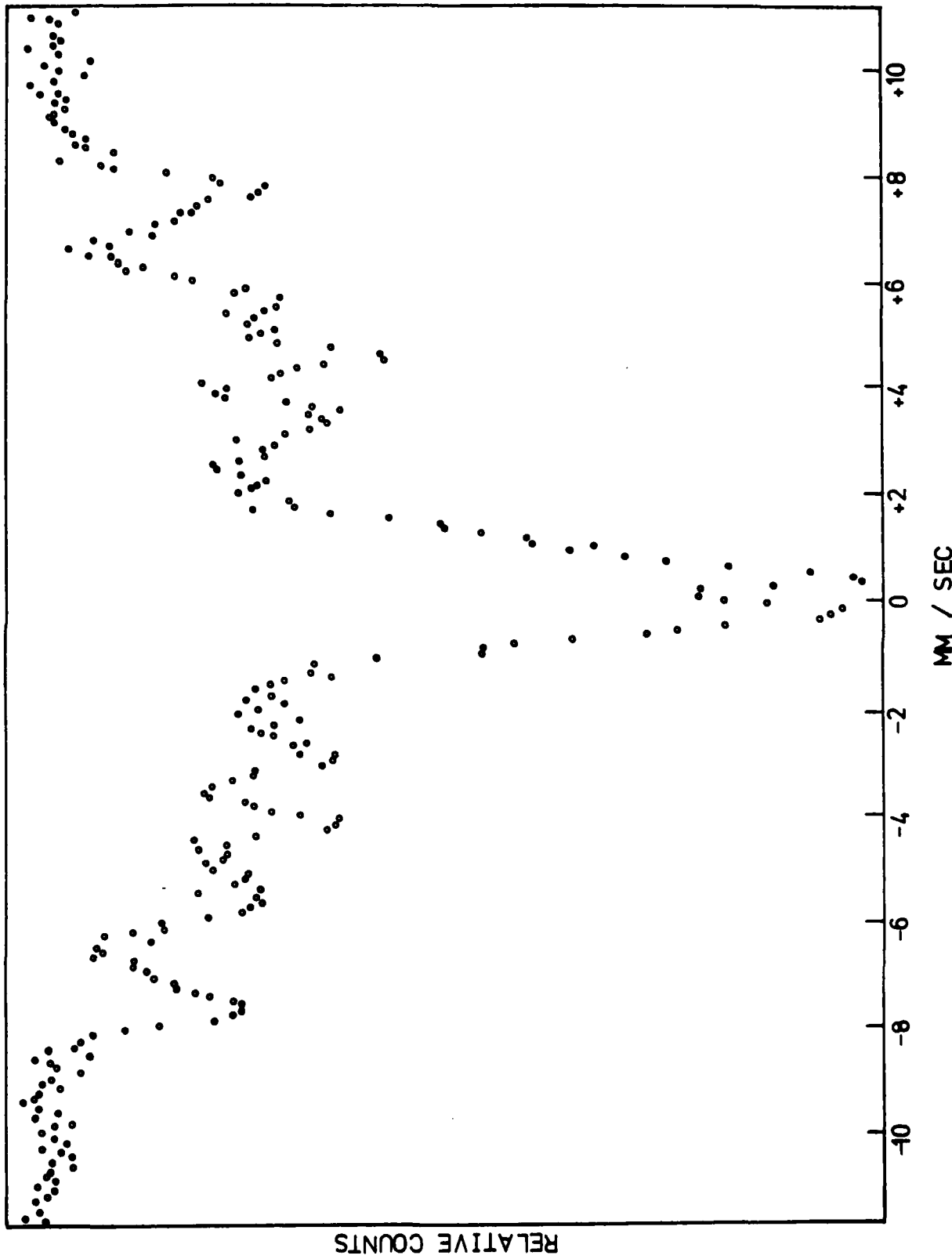


Figure 2. Mössbauer spectrum (room temperature) of the precipitate formed by hydrolysis of 0.1M  $\text{Fe}(\text{NO}_3)_3$  solution for 6 hours at 90°C (sample 43).

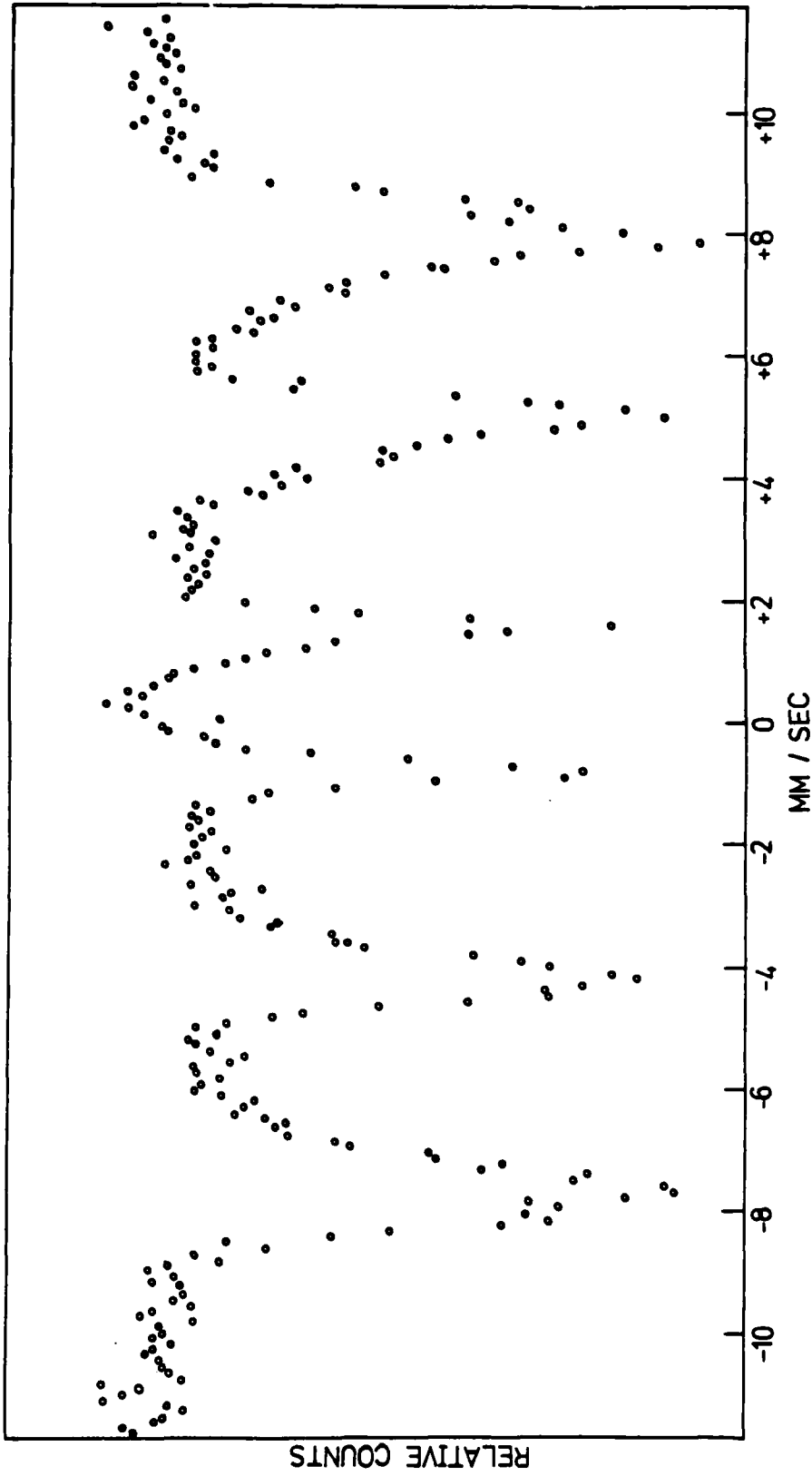


Figure 3. Mössbauer spectrum (77 K) of the precipitate formed by hydrolysis of 0.1M  $\text{Fe}(\text{NO}_3)_3$  solution for 6 hours at 90°C (sample 43).

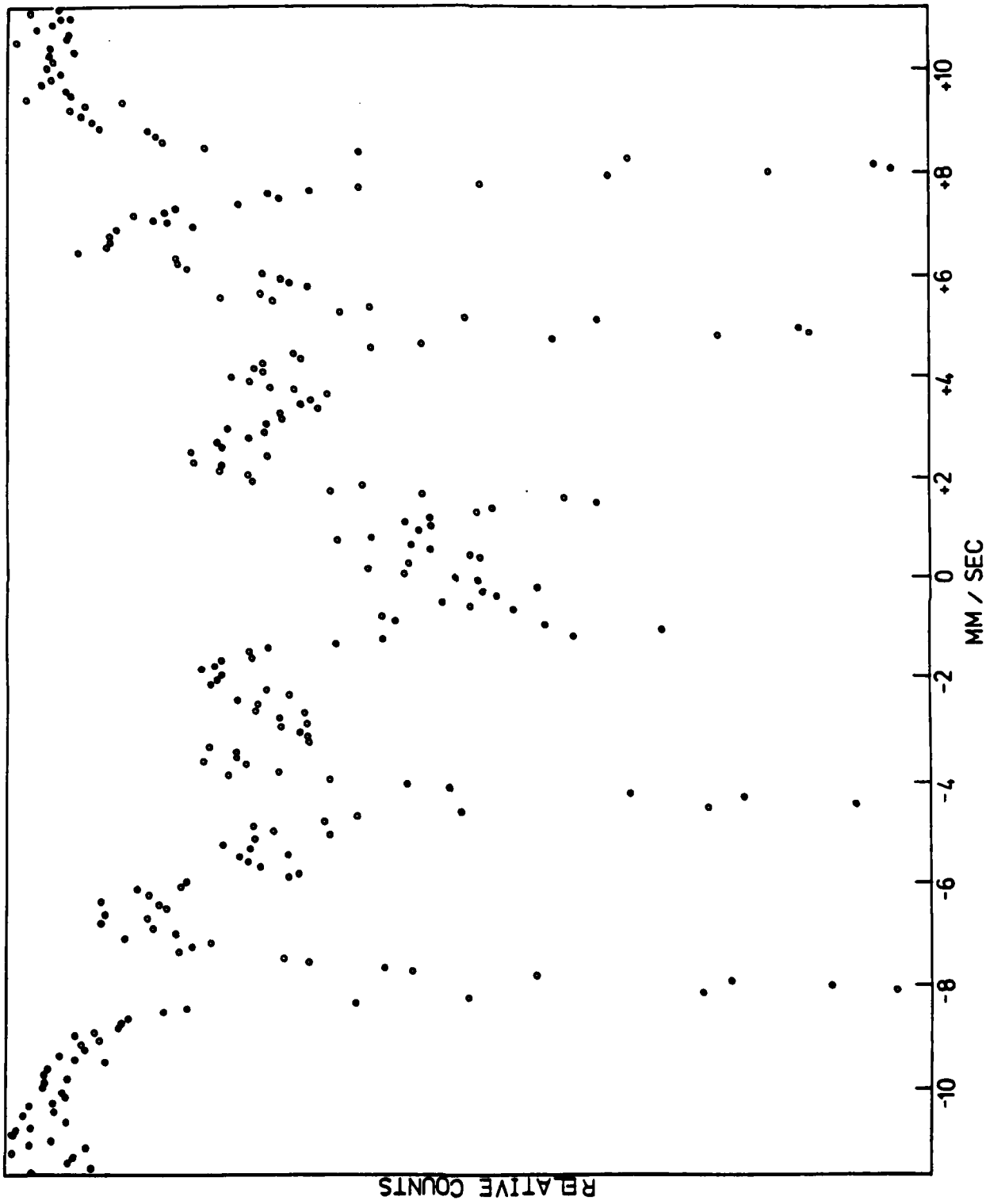


Figure 4. Mössbauer spectrum (room temperature) of the precipitate formed by hydrolysis of 0.1M  $\text{Fe}(\text{NO}_3)_3$  solution for 24 hours at 90°C (sample 40).

in contrast with the spectrum of sample 40 (Fig. 4). The measured effective magnetic fields ( $M_1, M_2$ ) can be ascribed to  $\alpha\text{-Fe}_2\text{O}_3$  of higher and lower crystallinity, respectively.

#### Precipitation from $\text{FeCl}_3$ Solution

Mössbauer spectra of the precipitates formed by hydrolysis of 0.1M  $\text{FeCl}_3$  solution (samples 15, 44, 51) show a quadrupole doublet ( $Q$ ) at room temperature and two magnetic splitting components ( $M_1, M_2$ ) at liquid nitrogen temperature. The Mössbauer parameters of component  $M_1$  are ascribed to  $\alpha\text{-FeOOH}$  and of component  $M_2$  to  $\beta\text{-FeOOH}$ . No  $\alpha\text{-Fe}_2\text{O}_3$  was detected.

#### Precipitation from $\text{Fe}_2(\text{SO}_4)_2$ Solution

The Mössbauer spectra of the precipitates (samples 16, 30, 46) formed by hydrolysis of 0.1M  $\text{Fe}_2(\text{SO}_4)_3$  solution at 90°C show a quadrupole doublet ( $Q$ ) at room and liquid nitrogen temperatures. The precipitate formed by hydrolysis for 3 hr (sample 16) has Mössbauer parameters  $\delta = 0.369 \text{ mm/s}$  and  $\Delta = 1.012 \text{ mm/s}$  at room temperature. From Table I it is seen that Mössbauer parameters of samples 16 and 30 (yellow precipitate) are close to those of sample 46 (brown precipitate) with the exception of the quadrupole splitting value of sample 46, which was 0.689 mm/s at room temperature and 0.736 mm/s at liquid nitrogen temperature. This difference can be attributed to different compositions of the basic iron(III) sulfate formed.  $\text{Fe}(\text{OH})\text{SO}_4$  is formed at short times by hydrolysis of  $\text{Fe}_2(\text{SO}_4)_3$  solution at 90°C and there is transformation to other relatively complex forms of basic iron(III) sulfate (brown precipitate) at long times of hydrolysis.

The Mössbauer spectrum of sample 85 prepared by hydrolysis of 0.1M  $\text{NH}_4\text{Fe}(\text{SO}_4)_2$  solution for 6 hr at 90°C shows one quadrupole doublet with parameters  $\delta = 0.396 \text{ mm/s}$  and  $\Delta = 1.101 \text{ mm/s}$ , values which are comparable with those obtained for the precipitate produced by the hydrolysis of 0.1M  $\text{Fe}_2(\text{SO}_4)_3$  solution (Table I).

#### DISCUSSION

On the basis of earlier studies the hydrolysis of Fe(III) solution occurs by a sequence of stages which includes the formation of monomer and dimer hydrolysis species, their polymerization, formation of a precipitate and subsequent transformation of the precipitate to oxides of known composition and

TABLE I  
 $^{57}\text{Fe}$  Mössbauer Parameters of the Precipitates Formed by Hydrolysis of Iron(III) Salt Solutions at 90°C

Sample	Temp.	Lines	$\delta^{*, **}$ (mm/s)	$\Delta E_q$ (mm/s)	$H_{5/2}^{**}$ (kOe)	$\Gamma$ (mm/s)	A (%)	Experimental Conditions for the Precipitate Preparation	pH start	pH final
41	RT	Q	0.311	0.689			100	0.1M $\text{Fe}(\text{NO}_3)_3$ solution was hydrolyzed for 80 minutes	1.66	1.48
	77 K	M <sub>1</sub>	0.480	0.060	453	very broad	100			
41a	RT	Q	0.369	0.644			100	Sample 41 was hydrolyzed additionally for two days at room temperature	1.66	1.43
	77 K	M <sub>1</sub>	0.497	-0.136	469.1	0.956	35.1			
42	RT	M <sub>2</sub>	0.532	-0.062	416.3	0.956	37.5			
		M <sub>3</sub>	0.483	0.010	353.4	0.956	27.4			
42	77 K	M <sub>1</sub>	0.468	-0.224	467.7	0.685	31.4	0.1M $\text{Fe}(\text{NO}_3)_3$ solution was hydrolyzed for 2 hours	1.66	1.44
		M <sub>2</sub>	0.418	-0.144	425.7	0.910	42.6			
43	RT	M <sub>3</sub>	0.388	-0.376	345.7	1.280	26.0			
		Q	0.335	0.650			100			
43	77 K	M <sub>1</sub>	0.389	-0.156	477	1.409	27.1	0.1M $\text{Fe}(\text{NO}_3)_3$ solution was hydrolyzed for 6 hours	1.66	0.92
		M <sub>2</sub>	0.384	-0.238	338	1.735	42.5			
77 K	M <sub>1</sub>	0.471	-0.242	528.0	0.312	19.4				
	M <sub>2</sub>	0.470	-0.250	491.9	0.690	80.6				

TABLE I (continued)

Sample	Temp.	Lines	$\delta^{*,**}$ (mm/s)	$\Delta E_q$ (mm/s)	$H_{5/2}^{**}$ (kOe)	$\Gamma$ (mm/s)	A (%)	Experimental Conditions for the Precipitate Preparation	pH start	pH final
40	RT	$\Omega$ $M_1$ $M_2$	0.385 0.367 0.396	0.700 -0.214 -0.164	498.8 352.4	0.571 0.571	11.9 70.0	0.1M $Fe(NO_3)_3$ solution was hydrolyzed for 24 hours	1.66	0.79
	77 K	$M_1$ $M_2$	0.465 0.480	-0.204 -0.242	531 493.7	0.363 0.551	64.2 35.8			
39	RT	$M_1$ $M_2$	0.366 0.303	-0.236 -0.208	516.1 495.6	0.396 0.629	66.0 34.0	0.1M $Fe(NO_3)_3$ in 0.05M $HNO_3$ solution was hydro- lyzed for 24 hours	0.75	
	77 K	$M_1$ $M_2$	0.475 0.478	-0.198 -0.224	530.3 498.4	0.394 0.516	67.9 32.1			
15	RT	$\Omega$	0.378	0.641			100	0.1M $FeCl_3$ solution was hydrolyzed for 3 hours and additionally aged for one day at room temperature		
	77 K	$M_1$ $M_2$	0.498 0.477	0.020 -0.244	470.9 456.5	0.245 0.623	4.8 95.2			
44	RT	$\Omega$	0.345	0.670			100	0.1M $FeCl_3$ solution was hydrolyzed for 6 hours		
	77 K	$M_1$ $M_2$	0.492 0.449	-0.120 -0.398	479.4 457.8	0.456 0.562	67.6 32.4			

TABLE I (continued)

Sample	Temp.	Lines	$\delta^{*,**}$	$\Delta E_q$	$H_{5/2}^{**}$	$\Gamma$	A	Experimental Conditions for the Precipitate Preparation	pH start	pH final
51	RT	Q	0.394	0.648				0.1M $FeCl_3$ solution was hydrolyzed for 24 hours	1.85	0.95
	77 K	$M_1$ $M_2$	0.488 0.458	-0.074 -0.324	472.6 448.5	0.573 0.557	84.9 15.1			
16	RT	Q	0.369	1.012				0.1M $Fe_2(SO_4)_3$ solution was hydrolyzed for 3 hours and additionally aged for one day at room temperature	1.77	after one day
	77 K	Q	0.400	0.965						
30	RT	Q	0.369	1.012				0.1M $Fe_2(SO_4)_3$ solution was hydrolyzed for 8 hours	1.65	1.38
	77 K	Q	0.461	1.012						
46	RT	Q	0.382	0.689				0.1M $Fe_2(SO_4)_3$ solution was hydrolyzed for 24 hours	1.65	1.38
	77 K	Q	0.507	0.736						
85	RT	$Q_1$	0.396	1.101				0.1M $NH_4Fe(SO_4)_2$ solution was hydrolyzed for 6 hours at 90°C		

\*Isomer shifts are given relative to alpha iron.

\*\*Errors:  $\pm 0.005$  mm/s and  $\pm 1$  kOe.

structure. The monomeric and dimeric  $\text{Fe}^{+3}$  complexes have been well characterized [3,9]. Formation of iron(III) hydroxy polymers from  $\text{Fe(III)}$  salt solutions has earlier been investigated by several methods [10-17]. Spiro and co-workers [10] reported an investigation of  $\text{Fe}(\text{NO}_3)_3$  hydrolysis with gel chromatography. They concluded that high molecular weight ferric-hydroxy polycations are in the form of 7 nm spheres having the empirical formula  $[\text{Fe(OH)}_x(\text{NO}_3)_{3-x}]_n$ ,  $2.3 < x < 2.5$ , with  $M_w$  near 140,000. The stages in the hydrolysis of  $\text{Fe(III)}$  salt solutions were recently confirmed with pH titration of acidified iron(III) nitrate solution in the temperature range from 24° to 90°C [11], light scattering, ultracentrifugation and electron microscopy [12]. The precipitates formed by the hydrolysis of  $\text{Fe(III)}$  salt solutions under various experimental conditions were identified as  $\alpha\text{-FeOOH}$  (goethite),  $\gamma\text{-FeOOH}$  (lepidocrocite), and  $\beta\text{-FeOOH}$  using X-ray diffraction [13]. Ferric-hydroxy polycations formed in partially neutralized  $\text{Fe}(\text{NO}_3)_3$  solutions have been characterized using electron microscopy and ultracentrifugation techniques [14,15]. The authors concluded that the anion present during the formation of the polycations didn't affect the structure of the polycations, but did affect subsequent aging processes. Mössbauer spectroscopic characterization of frozen ferric perchlorate solutions suggests that a significant proportion of the hydrolysis product is hydroxy polymer molecules [16,17].

The results of these papers indicate that the polymerization of iron(III) ions is an important stage in the process of the formation of oxyhydroxides and oxides. However, it is difficult to correlate these results because they were obtained under varying experimental conditions, using several techniques of differing capabilities. The experimental conditions utilized in this work made it possible to follow all transformations from iron(III) hydroxy polymers to well crystallized  $\alpha\text{-Fe}_2\text{O}_3$  end product by using Mössbauer spectroscopy. The formation of iron(III) oxyhydroxides and oxides has mainly been studied by adding a base to  $\text{Fe(III)}$  salt solution. It is well known that  $\text{Fe}^{3+}$  ion is characterized by high hydrolyzability and deprotonation of its water complexes can easily be achieved at elevated temperatures and more slowly at room temperature. This characteristic of  $\text{Fe}^{3+}$  ion was used in the present study to produce iron(III) oxyhydroxide and (hydr)oxide precipitates from various  $\text{Fe(III)}$  salt solutions without adding the base and, in such a way, to simplify these precipitation systems, generally known as very complicated. On the basis of the Mössbauer spectroscopic measurements it was possible to make qualitative and quantitative analysis of all hydrolysis products of  $\text{Fe(III)}$  salt solutions at elevated temperature. These data will be used in the following discussion to elucidate the mechanism of the formation of iron(III) oxyhydroxides and (hydr)oxides from different iron(III) salt solutions.

### Precipitation from $\text{Fe}(\text{NO}_3)_3$ Solution

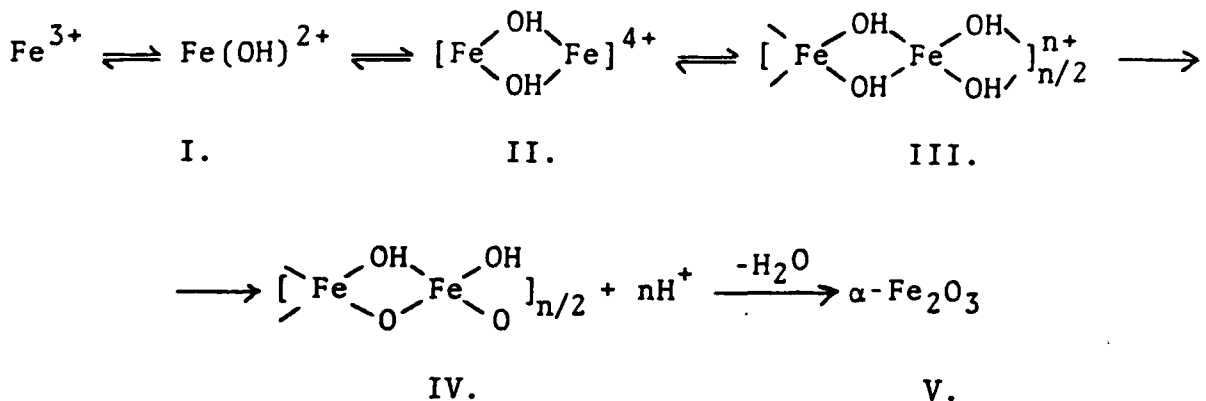
The Mössbauer spectra of the hydrolysis products of  $\text{Fe}(\text{NO}_3)_3$  solution formed between 80 and 120 min indicate the presence of three magnetic splitting components (Samples 41a and 42, Fig. 1b). The value of  $H_{5/2}$  near 470 kOe obtained at liquid nitrogen temperature and the isomer shift and quadrupole splitting can be ascribed to superparamagnetic  $\alpha\text{-FeOOH}$  (goethite) of poor crystallinity [18] or nonstoichiometry.\* The low values of the internal magnetic field (416 kOe and 353 kOe) in the precipitates obtained after 80 min of heating of  $\text{Fe}(\text{NO}_3)_3$  solution were attributed to iron(III) hydroxy polymers with the general formula  $[\text{Fe}(\text{OH})_x(\text{NO}_3)_{3-x}]_n$ . The amount of nitrate in the polymers decreases with the time of heating and further hydrolysis occurs. These polymers are proposed to be embedded in laterally arrayed islands of primary  $\alpha\text{-FeOOH}$  particles. The primary particles are rod-like ( $\sim 5$  nm) as confirmed by electron microscopy [20]. Also primary particles are uniform and monodisperse. These results are in accordance with the general rule which says that in the case of hydrolysis of easily hydrolyzable metal cations at room or elevated temperatures, the colloid particles are, in principle, uniform with a narrow particle-size distribution.

The spectra of the precipitate produced by hydrolysis for 6 hr, as measured at room and liquid nitrogen temperatures, indicate the presence of superparamagnetic  $\alpha\text{-Fe}_2\text{O}_3$  and  $\alpha\text{-FeOOH}$  with a narrow particle size distribution (Figs. 2 and 3). On the basis of Mössbauer parameters given in Table I and in accordance with the literature data [5-8], it can be calculated that  $\alpha\text{-Fe}_2\text{O}_3$  particles in this sample are between 7.0 nm and 12.0 nm and the  $\alpha\text{-FeOOH}$  particles are approximately 20-50 nm in average dimension. After 24 hr of hydrolysis,  $\alpha\text{-Fe}_2\text{O}_3$  becomes the dominant species as seen from the increase in the  $M_1$  component ( $\alpha\text{-Fe}_2\text{O}_3$ ) in Figure 4 and from  $A(\%)$  values in Table I. In the Mössbauer spectra of the precipitate produced by hydrolysis for 24 hr in 0.05M  $\text{HNO}_3$  there is no central quadrupole doublet indicating that particles in the sample are greater than 50 nm in average dimension.

The shape of the spectra shown in Figures 1-4 can be interpreted as a common effect of narrow particle size distribution and superparamagnetism. The paramagnetic phase completely disappeared at liquid nitrogen temperature owing to the narrow size distribution [16].

\*Superparamagnetism, poor crystallinity and stoichiometric defects can decrease the effective magnetic field. Below the magnetic transition temperature ultrafine particles of ferro- and antiferromagnetic materials show a paramagnetic behavior. This phenomenon known as superparamagnetism is manifested as a drastic change in shape of the Mössbauer hyperfine spectrum [3,19].

On the basis of the Mössbauer measurements, the formation of solid phase by hydrolysis of  $\text{Fe}(\text{NO}_3)_3$  solution at elevated temperature can be schematically described as follows:



Scheme 1.

In the first step there is the formation of simple hydrolysis products of iron(III), such as monomers (I) and dimers (II). The next step is the formation of iron(III) hydroxy polymers (III). Oxybridges form with prolonged time of heating or aging, and the  $\alpha\text{-FeOOH}$  structure (IV) develops. The final step is loss of water and internal crystallization of  $\alpha\text{-FeOOH}$  to  $\alpha\text{-Fe}_2\text{O}_3$  (V).

#### Precipitation from $\text{FeCl}_3$ Solution

The influence of chloride ions on the formation of iron(III) oxyhydroxide and oxide has been extensively studied. Only in the case of slow hydrolysis of  $\text{FeCl}_3$  solution near room temperature has it definitely been shown that the end product is completely in the  $\alpha\text{-FeOOH}$  form [21-23]. Also, it is known from previous studies [15, 18, 24-27] that the presence of chloride ions during the precipitation of iron(III) oxyhydroxide and oxide may markedly influence the structure and composition of the solid phase. Studies of crystal nucleation and growth during hydrolysis in  $\text{FeCl}_3$  solutions ( $\text{OH}/\text{Fe}$  mol ratio - 0-2.75) has shown that the transformations,  $\beta\text{-FeOOH} \rightarrow \alpha\text{-Fe}_2\text{O}_3$  and  $\beta\text{-FeOOH} \rightarrow \alpha\text{-FeOOH}$  at pH 1-2, proceed by dissolution and reprecipitation and the precipitation process is promoted by adding seed crystals [24]. The course of these reactions is strongly dependent on the structure of the solvated iron species before the precipitation. The polymerization of Fe(III) ions is confirmed even in very concentrated aqueous  $\text{FeCl}_3$  solutions [28, 29].

Mössbauer spectra of the precipitates formed by hydrolysis of  $\text{FeCl}_3$  solution for 3 and 24 hr at 90°C show the presence of

two components ( $\alpha$ -FeOOH and  $\beta$ -FeOOH) as summarized in Table I. No evidence for the presence of  $\alpha$ -Fe<sub>2</sub>O<sub>3</sub> was observed in these samples. With prolonged time of heating there is gradual increase in the amount of  $\alpha$ -FeOOH as it is seen from A(%) values in Table I. The precipitation of oxyhydroxides by hydrolysis of FeCl<sub>3</sub> solution at 90°C can be interpreted similarly as in the case of the precipitation from Fe(NO<sub>3</sub>)<sub>3</sub> solution. Iron(III) hydroxy polymers formed as precipitate precursors in chloride solution very probably include some chloride ions in the polymer chain instead of OH<sup>-</sup> groups. This conclusion is in accord with the results of the investigation of the polymeric species in FeCl<sub>3</sub> acid solutions [28]. The chief difference in comparison with the polymers formed by hydrolysis of nitrate solution is in the fact that nitrate ions are not included in the polymer chain (see Scheme 1) and they serve only for the compensation of polymer positive charge. Results of a previous Mössbauer spectroscopic study of the hydrolysis of iron(III) salt solution showed that chloride and sulfate ions occupy the first ligand sphere of iron(III), whereas nitrate and perchlorate ions do not [3,30,31]. The process of polymerization is followed by the incomplete elimination of chlorides in the course of the precipitation and the formation of the  $\beta$ -FeOOH structure. Here it can be mentioned that an investigation of the  $\beta$ -FeOOH precipitate showed that there is a minimum chloride content (~2%) in the precipitate which cannot be washed out [32]. The Mössbauer spectra of the precipitate formed after 24 hr of hydrolysis showed only a quadrupole doublet at room temperature and two magnetic splitting components at liquid nitrogen temperature.

The results suggest the formation of  $\alpha$ -FeOOH nuclei (free from Cl<sup>-</sup>) in the course of the formation of oxybridges. With prolonged time of heating  $\beta$ -FeOOH recrystallizes via dissolution and  $\alpha$ -FeOOH crystals grow on preformed nuclei. The percentage of  $\beta$ -FeOOH after 24 hr of heating is high (15.1%) and this fact is in accord with the high stability of  $\beta$ -FeOOH and its slow dissolution in the pH range investigated. In contrast to this behavior the formation of  $\alpha$ -FeOOH, or more precisely  $\alpha$ -FeOOH and  $\alpha$ -Fe<sub>2</sub>O<sub>3</sub> from "amorphous" iron(III) hydroxide gel, is a faster process [33-37].

#### Precipitation from Fe<sub>2</sub>(SO<sub>4</sub>)<sub>3</sub> or NH<sub>4</sub>Fe(SO<sub>4</sub>)<sub>2</sub> Solution

The influence of sulfate ions on the precipitation process from Fe<sub>2</sub>(SO<sub>4</sub>)<sub>3</sub> solution has been investigated in earlier studies [28-42]. The formation of Fe(OH)SO<sub>4</sub>, [Fe(OH)<sub>2</sub>]<sub>2</sub>SO<sub>4</sub> and Fe<sub>4</sub>(SO<sub>4</sub>)<sub>10</sub> compounds by heating of acidic Fe<sub>2</sub>(SO<sub>4</sub>)<sub>3</sub> solution has been observed [38]. Also, monodispersed basic iron(III) sulfate sols of composition Fe<sub>3</sub>(SO<sub>4</sub>)<sub>2</sub>(OH)<sub>5</sub>·2H<sub>2</sub>O have been reported [39]. Generally, the composition and crystal structure of basic iron(III) sulfates strongly depend on the preparation conditions (pH, temperature, time of heating, concentration of sulfates).

Mössbauer spectra and calculated Mössbauer parameters (Table I) of precipitates produced by hydrolysis of  $\text{Fe}_2(\text{SO}_4)_3$  or  $\text{NH}_4\text{Fe}(\text{SO}_4)_2$  solution for different times at 90°C indicate a markedly different influence of sulfate ions on the formation of iron(III) oxyhydroxides and oxides in comparison to the hydrolysis products formed in  $\text{Fe}(\text{NO}_3)_3$  and  $\text{FeCl}_3$  solutions. After 24 hr, the  $\text{Fe}(\text{OH})\text{SO}_4$  compound formed in short times of hydrolysis at 90°C transforms to basic iron(III) sulfate of complex composition. The precipitation process by hydrolysis of  $\text{Fe}(\text{SO}_4)_3$  or  $\text{NH}_4\text{Fe}(\text{SO}_4)_2$  solution at 90°C cannot be interpreted as in the cases of precipitation from  $\text{Fe}(\text{NO}_3)_3$  and  $\text{FeCl}_3$  solutions. Evidently, the formation of the dominant  $\text{FeSO}_4^+$  complex [9] suppresses the formation of iron(III) hydroxy polymers and subsequent formation of iron(III) oxyhydroxides and oxides.

#### REFERENCES

- [1] A. L. Mackay in "Reactivity of Solids", Proc. of the Fourth Int. Symp. on the Reactivity of Solids, p.571-583 (J. H. de Boer et al., Eds.) Elsevier, Amsterdam, 1960.
- [2] E. Matijević, Progr. Colloid Polymer Sci. 61, 24 (1976).
- [3] A. Vértes, L. Korecz, and K. Burger, "Mössbauer Spectroscopy", Elsevier Pub. Co., Amsterdam, 1980.
- [4] S. I. Nagy and T. W. Weir, The SIRIUS Evaluating Program (The manual for internal use), CSCR, Lehigh University, Bethlehem, Pa., 1980.
- [5] D. S. Kulgawczuk, Nukleonika 14, 777 (1969).
- [6] A. M. van der Kraan, Mössbauer Effect Studies of Superparamagnetic  $\alpha\text{-FeOOH}$  and  $\alpha\text{-Fe}_2\text{O}_3$ , Ph.D. Thesis, Technical High School, Delft, 1972.
- [7] W. Meisel, Kem. Kozlem. 48, 41 (1977).
- [8] L. H. Bowen, "Mössbauer Spectroscopy of Ferric Oxides and Hydroxides" in Mössbauer Effect Data Index, 1979, p.76-94.
- [9] J. Bjerrum, G. Schwarzenbach, and L. G. Sillen, "Stability Constants of Metal-Ion Complexes", No. 17, Spec. Publ. Chem. Soc., London, 1964.

- [10] T. G. Spiro, S. E. Allerton, J. Renner, A. Terzis, R. Bils, and P. Saltman, *J. Amer. Chem. Soc.* 88, 2721 (1966).
- [11] J. Dousma and P. L. de Bruyn, *J. Colloid Interface Sci.* 56, 527 (1976).
- [12] J. Dousma and P. L. de Bruyn, *J. Colloid Interface Sci.* 64, 154 (1978).
- [13] P. J. Murphy, A. M. Posner, and J. P. Quirk, *Aust. J. Soil Res.* 13, 189 (1975).
- [14] P. J. Murphy, A. M. Posner, and J. P. Quirk, *J. Colloid Interface Sci.* 56, 270 (1976).
- [15] P. J. Murphy, A. M. Posner, and J. P. Quirk, *J. Colloid Interface Sci.* 56, 312 (1976).
- [16] A. Vértes, M. Ranogajec-Komor, and P. Gelencser, *Acta Chim. Acad. Sci. Hung.* 77, 55 (1973).
- [17] I. Dezsí, V. D. Gorobchenko, M. Komor, I. I. Lukashevich, A. Vértes, and K. F. Tsitskishvili, *Acta Chim. Acad. Sci. Hung.* 70, 329 (1971).
- [18] K. Kauffman and F. Hazel, *J. Inorg. Nucl. Chem.* 37, 1139 (1975).
- [19] R. L. Cohen, "Application of Mössbauer Spectroscopy", Vol. I, Academic Press, New York-San Francisco-London, 1976.
- [20] S. Musić, unpublished results.
- [21] S. Musić, I. Nagy-Czakó, and A. Vértes, *Colloid Polymer Sci.* 258, 469 (1980).
- [22] J. H. L. Watson, R. R. Carell, Jr., and W. Heller, *J. Phys. Chem.* 66, 1757 (1962).
- [23] R. H. H. Wolf, M. Wrätscher, and J. Šipalo-Zuljević, *Kolloid-Z. Z. Polymere* 215, 57 (1967).
- [24] R. J. Atkinson, A. M. Posner, and J. P. Quirk, *Clays Clay Minerals* 25, 49 (1977).
- [25] J. Dousma, T. J. van den Hoven, and P. L. de Bruyn, *J. Inorg. Nucl. Chem.* 40, 1089 (1978).
- [26] E. Matijević and P. Scheiner, *J. Colloid Interface Sci.* 63, 509 (1978).
- [27] Y. Ujihira and M. Ohyabu, *J. Physique* 40, C2-347 (1979).

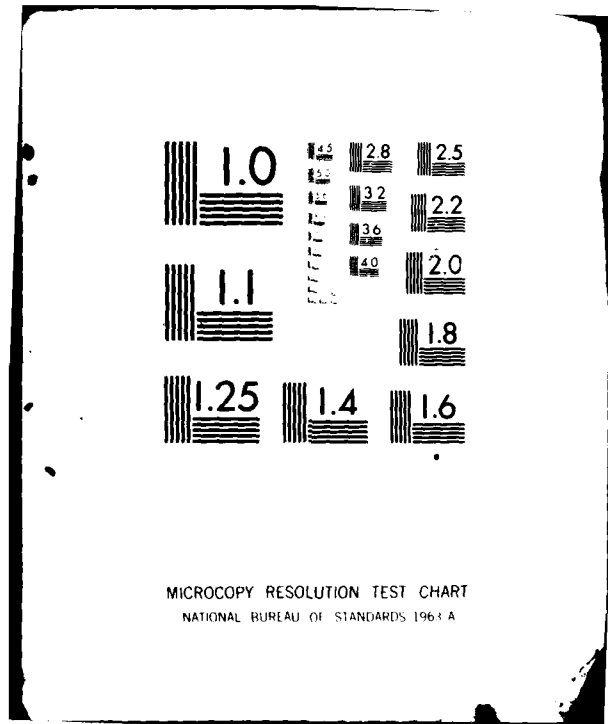
AD-A109 606

LEHIGH UNIV BETHLEHEM PA CENTER FOR SURFACE AND COATINGS ETC F/0 11/3  
CORROSION CONTROL THROUGH A BETTER UNDERSTANDING OF THE METALLI-ETC(U)  
NOV 81 M LEIDHEISER, E M ALLEN, M S EL-AASSER N00014-79-C-0731  
ML

UNCLASSIFIED

3x3  
Searle

END  
DATE FILMED  
1-82  
NTIC



- [28] G. W. Brady, M. B. Robin, and J. Varimbi, Inorg. Chem. 3, 1168 (1964).
- [29] S. Balt, J. Inorg. Nucl. Chem. 29, 2307 (1967).
- [30] A. Vértes, M. Suba, M. R. Komor, Ann. Univ. Sci. Budapest Rolando-Eötvös Nom., Sect. Chim. 12, 69 (1971).
- [31] A. Vértes, M. R. Komor, M. Suba, Ann. Univ. Sci. Budapest Rolando-Eötvös Nom., Sect. Chim. 12, 79 (1971).
- [32] J. Ellis, R. Giovanoli, and W. Stumm, Chimia 30, 194 (1976).
- [33] R. H. H. Wolf, M. Mirnik, and B. Težak, Kolloid-Z. Z. Polymere 205, 111 (1965).
- [34] S. Okamoto, H. Sekizawa, and S. I. Okamoto, Proc. 7th Int. Symp. on the Reactivity of Solids, p.341 (Eds. J. S. Anderson, M. W. Roberts, F. S. Stone) Chapman and Hall Ltd., London 1972.
- [35] W. R. Fischer and U. Schwertmann, Clays Clay Minerals 23, 33 (1975).
- [36] A. Vértes, K. Lazar, K. Keleman, and L. Bognar, Radiochem. Radioanal. Lett. 3, 375 (1970).
- [37] A. A. van der Giessen, Chemical and Physical Properties of Iron(III)-Oxide Hydrate, Ph.D. Thesis, Technical University, Eindhoven, The Netherlands, 1968.
- [38] T. V. Arden, J. Chem. Soc. 350 (1951).
- [39] E. Matijević, R. S. Sapieszko, and J. B. Melville, J. Colloid Interface Sci. 50, 567 (1975).
- [40] K. H. Lieser, Z. Elektrochemie Berichte Bunsen phys. Chemie 63, 661 (1959).
- [41] R. S. Sapieszko, R. C. Patel, and E. Matijević, J. Phys. Chem. 81, 1061 (1977).
- [42] J. Dousma, D. den Ottelander, and P. L. de Bruyn, J. Inorg. Nucl. Chem. 41, 1565 (1979).

## Program #15. Characterization of the Surface Properties of Iron Oxides

### INTRODUCTION

The development of protective coatings for corrosive materials requires a knowledge not only of the physical properties of the coating, but also the nature of the interaction of the coating with the substrate and the affinity of the metal oxide/coating interface for water. Water plays an essential role in the corrosion of iron. The experimental approaches used in this phase of the program to study the surface properties of materials require high-surface-area, small-particle-size samples. Mössbauer spectroscopic and X-ray diffraction techniques have shown that  $\alpha$ -FeOOH,  $\gamma$ -FeOOH,  $\alpha$ -Fe<sub>2</sub>O<sub>3</sub>, and Fe<sub>3</sub>O<sub>4</sub> are present as corrosion products on iron exposed to atmospheric conditions. High-purity, high-surface area powders of a number of these iron oxides have been obtained commercially and have been precipitated from solution in other phases of this program.

The objectives of this research approach, therefore, are concerned with the characterization of the intrinsic surface properties of corrosion products, and the extent and manner in which the surface properties can be changed by pretreatment conditions such as high temperature and chemisorption of surface active materials. The solid/liquid interfacial properties of the iron oxide samples were investigated by electrophoretic mobility measurements as a function of pH where the acid-base character of the surface groups was evaluated. The solid/gas interfacial properties were investigated by water adsorption isotherms where the surface polar site concentration on different iron oxides was determined as a function of activation temperature and chemical treatment of the surface with hexamethyl-disilizane, HMDS, which interacts quantitatively with surface hydroxyl groups.

### EXPERIMENTAL

The iron oxide samples used in this study were Fe<sub>3</sub>O<sub>4</sub> and  $\alpha$ -Fe<sub>2</sub>O<sub>3</sub> obtained from Pfizer Inc. and a series of iron oxides precipitated from solution according to experimental techniques described in Section 13 of this report. Although the bulk of results is reported on the Pfizer samples, the current effort is primarily directed towards the samples precipitated in this laboratory.

The argon gas adsorption isotherms for specific area determination were obtained at liquid nitrogen temperatures using a classical BET volumetric vacuum rig. The residual pressure of  $10^{-6}$  Torr was monitored by an ion gauge. A capacitive electronic manometer equipped with a 1000 Torr differential pressure transducer (Datametrics, Inc.) was used to measure the argon gas pressure with a sensitivity of  $10^{-3}$  Torr. Specific areas were calculated for argon molecular cross-section of  $17 \text{ \AA}^2$ . The water adsorption isotherms were measured on a quartz spring (Worden Quartz Co.) balance with a sensitivity of  $10 \mu\text{g/g}$  of sample. The equilibrium water vapor pressure was measured with a 100 Torr capacitive differential manometer (Datametrics, Inc.).

The iron oxide samples were prepared for electrophoretic mobility measurements by ultrasonic dispersion in the medium of interest. Three electrophoresis systems were used in this study: Rank Brothers Mark II, Pen Kem Model 500, Pen Kem System 3000. The latter instrument was completely automated and allowed rapid measurements to be made (less than 5 min per determination) so that the results could be followed as a function of time. The results included in this report were found not to vary with time. General agreement, including measurements at high electrolyte levels, between the three instruments was established.

## RESULTS AND DISCUSSION

### Solid/Gas Interface

Water adsorption isotherms have been measured on  $\alpha\text{-Fe}_2\text{O}_3$  and  $\text{Fe}_3\text{O}_4$  samples which have been activated at 25, 100, 200, 300, and  $400^\circ\text{C}$ . Although the work included in this report is for these two samples, gas adsorption isotherms are currently being determined on iron oxide samples prepared in this laboratory and presented in Section 13 of this report. The experimental approach adopted here is designed to determine the surface hydrophilicity of iron oxides under different conditions of high temperature activation. The procedure measures the weight loss as a function of activation temperature, the water adsorption isotherms at  $25^\circ\text{C}$  after activation at the specified elevated temperature, and a second series of isotherms which follows the previous series after activation at  $25^\circ\text{C}$ . The intent was to compare the weight loss results to the amount of irreversibly adsorbed water after each isotherm, and also the decrease in monolayer capacity of the second isotherm activated at  $25^\circ\text{C}$  compared to the first isotherm which was activated at the elevated temperature. Since the intrinsic surface properties of the iron oxide samples are sought in this approach, the specific surface area, as determined from a BET analysis of argon adsorption isotherms at  $-195^\circ\text{C}$ , was measured as a function of activation temperature.

Tables I and II summarize the gas adsorption results on  $\alpha\text{-Fe}_2\text{O}_3$  and  $\text{Fe}_3\text{O}_4$ , respectively. The results show that the specific surface area for  $\alpha\text{-Fe}_2\text{O}_3$  decreases nearly linearly with increasing activation temperature above 100°C. The results for  $\text{Fe}_3\text{O}_4$ , by contrast, show that the specific surface area increases with increasing activation temperature. Although there was no evidence of porosity from an analysis of the shape of the argon adsorption isotherms on both iron oxides, these results do suggest that for  $\text{Fe}_3\text{O}_4$  high temperature activation leads to a small increase in surface porosity.

The water adsorption results for  $\alpha\text{-Fe}_2\text{O}_3$  in Table I are shown in Figures 1 and 2. Figure 1 presents the weight loss, amount of irreversibly adsorbed water, and the difference between the first and second water adsorption monolayer value all as a function of activation temperature. The results show that the weight loss above 200°C is due to desorbed water primarily from the bulk since it cannot be accounted for from analysis of the water adsorption isotherms. The correlation between the difference in monolayer values between the first and second isotherms and the irreversibly adsorbed water, both of which are attributed to strongly adsorbed water on surface hydroxyl groups, is in good agreement. The indication is that the surface hydroxyl concentration does not change much with activation temperature up to 400°C. An analysis of the monolayer values, which are presented in Figure 2 in terms of water molecules/ $100 \text{ \AA}^2$  as a function of activation temperature, is based upon the assumption that a water molecule has a cross-sectional area of  $10 \text{ \AA}^2$ . The degree of surface hydrophilicity, which is proportional to the surface hydroxyl concentration, appears to increase with increasing activation temperature.

The  $\text{Fe}_3\text{O}_4$  results, which are summarized in Table II, are presented in Figures 3 and 4. The weight loss results in Figure 3 indicate that the water loss at activation temperatures above 100°C is due primarily to water loss from the bulk. The irreversible water and difference in monolayer values between the first and second isotherms are almost constant over the entire temperature range. The water monolayer values for the first and second isotherms as a function of activation temperature, Figure 4, show that the first monolayer values increase with increasing activation temperature up to 200°C followed by a decrease, while the second isotherm monolayer values decrease with increasing activation temperature over the entire temperature range. The interpretation of these results is that below 200°C, strong physically adsorbed water is removed, and there is evidence that partial dehydroxylation occurs above 200°C. Heats of immersion experiments as a function of activation temperature are currently being planned in order to verify the conclusions concerning dehydroxylation of water from the iron oxide surfaces.

Another approach to hydrophobe iron oxides is by chemical treatment of the surface. Since surface hydroxyl groups on iron oxides are primarily responsible for the adsorption of water, the approach was to treat chemically these hydroxyls so as to render them hydrophobic. Silanes, in general, are known to react with the proton of hydroxyls whether they are part of the

Table I  
Gas Adsorption Results on  $\alpha\text{-Fe}_2\text{O}_3$

Activation Temp., °C	Specific Surface Area ( $\text{m}^2/\text{g}$ )	Wt. Loss mg/g	$W_{m1}^*$		$W_{m2}^{**}$		$W_{m1} - W_{m2}$		Irreversibly Adsorbed Water mg/g
			mg/g	100 Å <sup>2</sup>	mg/g	100 Å <sup>2</sup>	mg/g	100 Å <sup>2</sup>	
25	10.9	--	2.12	6.56	--	--	--	--	--
100	10.6	0.48	2.35	7.44	1.82	5.78	0.52	1.66	0.86
200	9.8	0.69	2.42	8.32	1.87	6.43	0.55	1.89	0.72
300	8.8	2.77	2.45	9.32	2.00	7.61	0.45	1.71	1.03
400	8.2	9.00	2.42	9.88	1.75	7.13	0.67	2.75	0.80

\* First water adsorption isotherm monolayer at 25°C after indicated activation temperature.

\*\* Second water adsorption isotherm monolayer at 25°C after activation at 25°C.

Table II  
Gas Adsorption Results on Fe<sub>3</sub>O<sub>4</sub>

Activation Temp., °C	Specific Surface Area (m <sup>2</sup> /g)	Wt. Loss mg/g	W <sub>m1</sub> * molecules/ 100 Å <sup>2</sup>		W <sub>m2</sub> ** molecules/ 100 Å <sup>2</sup>		W <sub>m1</sub> - W <sub>m2</sub> molecules/ 100 Å <sup>2</sup>		Irreversibly Adsorbed Water mg/g
			mg/q	100 Å <sup>2</sup>	mg/q	100 Å <sup>2</sup>	mg/q	100 Å <sup>2</sup>	
25	7.2	--	1.82	8.46	--	--	--	--	--
100	7.7	0.76	2.15	9.41	1.77	7.77	0.37	1.64	0.51
200	8.5	2.12	2.42	9.60	1.67	6.63	0.75	2.97	0.91
300	8.8	9.90	1.72	6.55	1.52	5.81	0.19	0.74	0.82
400	9.7	14.86	1.95	6.76	1.55	5.38	0.40	1.39	0.97

\* First water adsorption isotherm monolayer at 25°C after indicated activation temperature.

\*\* Second water adsorption isotherm monolayer at 25°C after activation at 25°C.

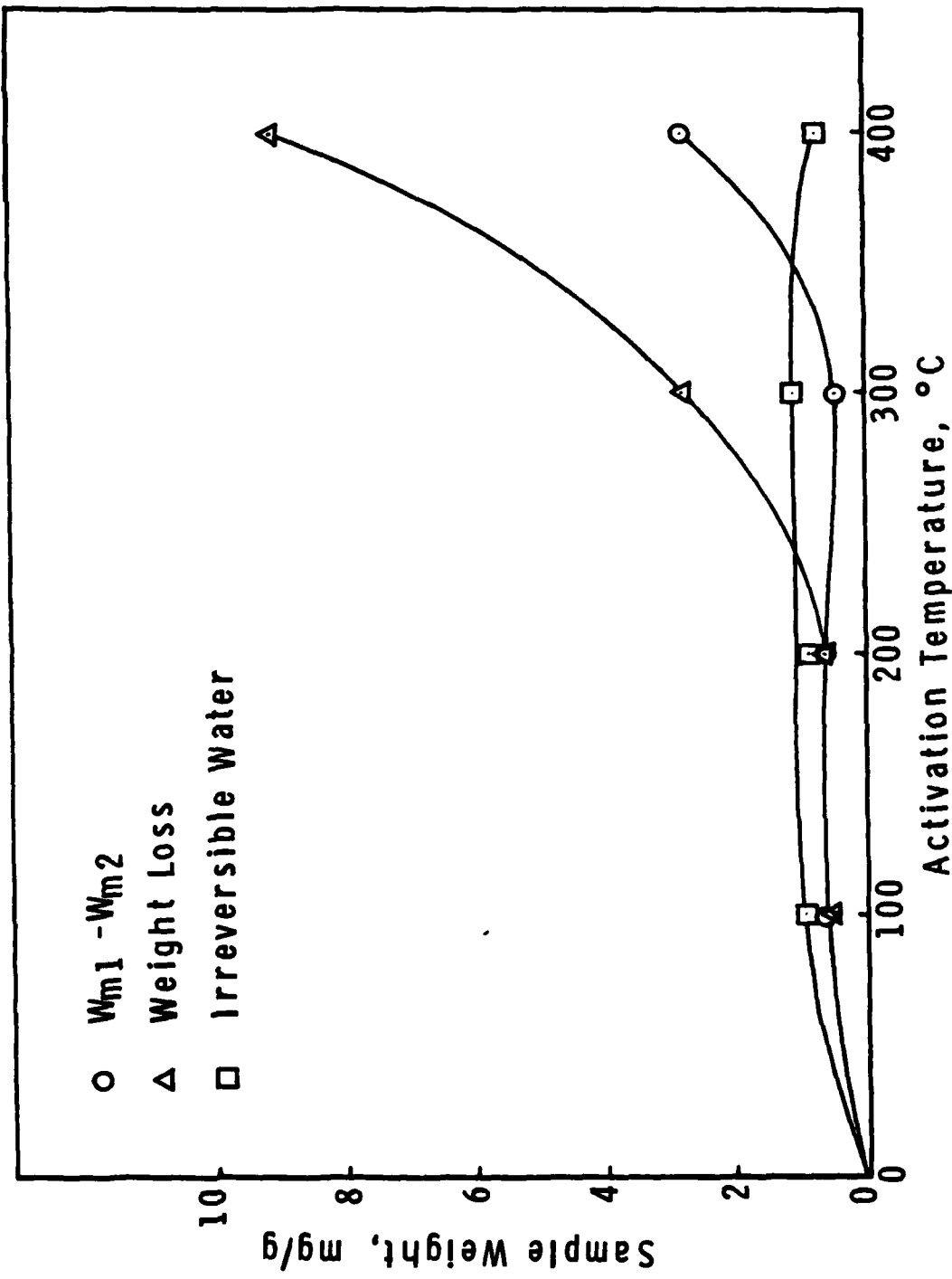


Figure 1. Adsorption results as a function of activation temperature for  $\alpha$ -Fe<sub>2</sub>O<sub>3</sub>.

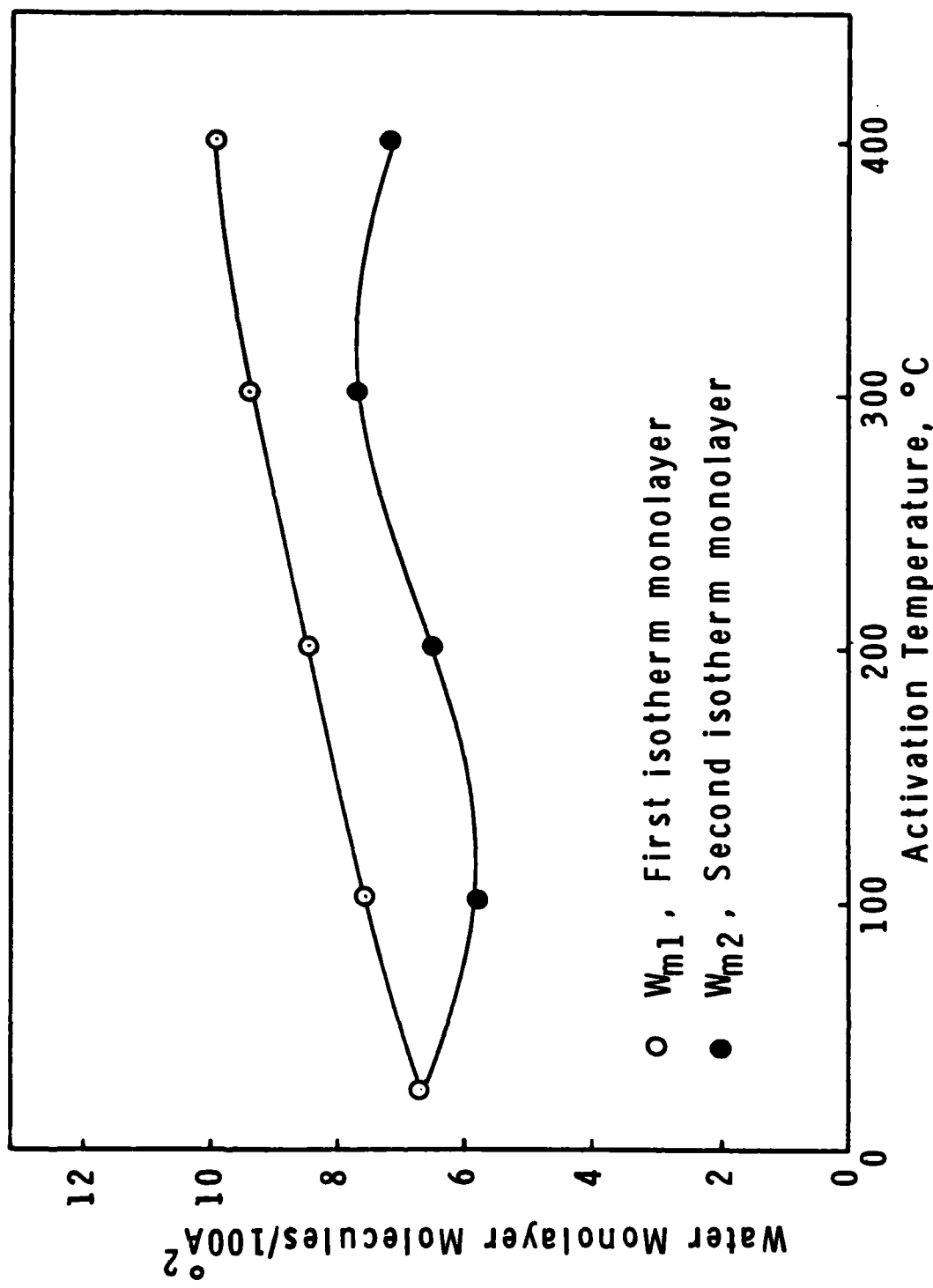


Figure 2. Water monolayer results as a function of activation temperature for  $\alpha$ -Fe<sub>2</sub>O<sub>3</sub>.

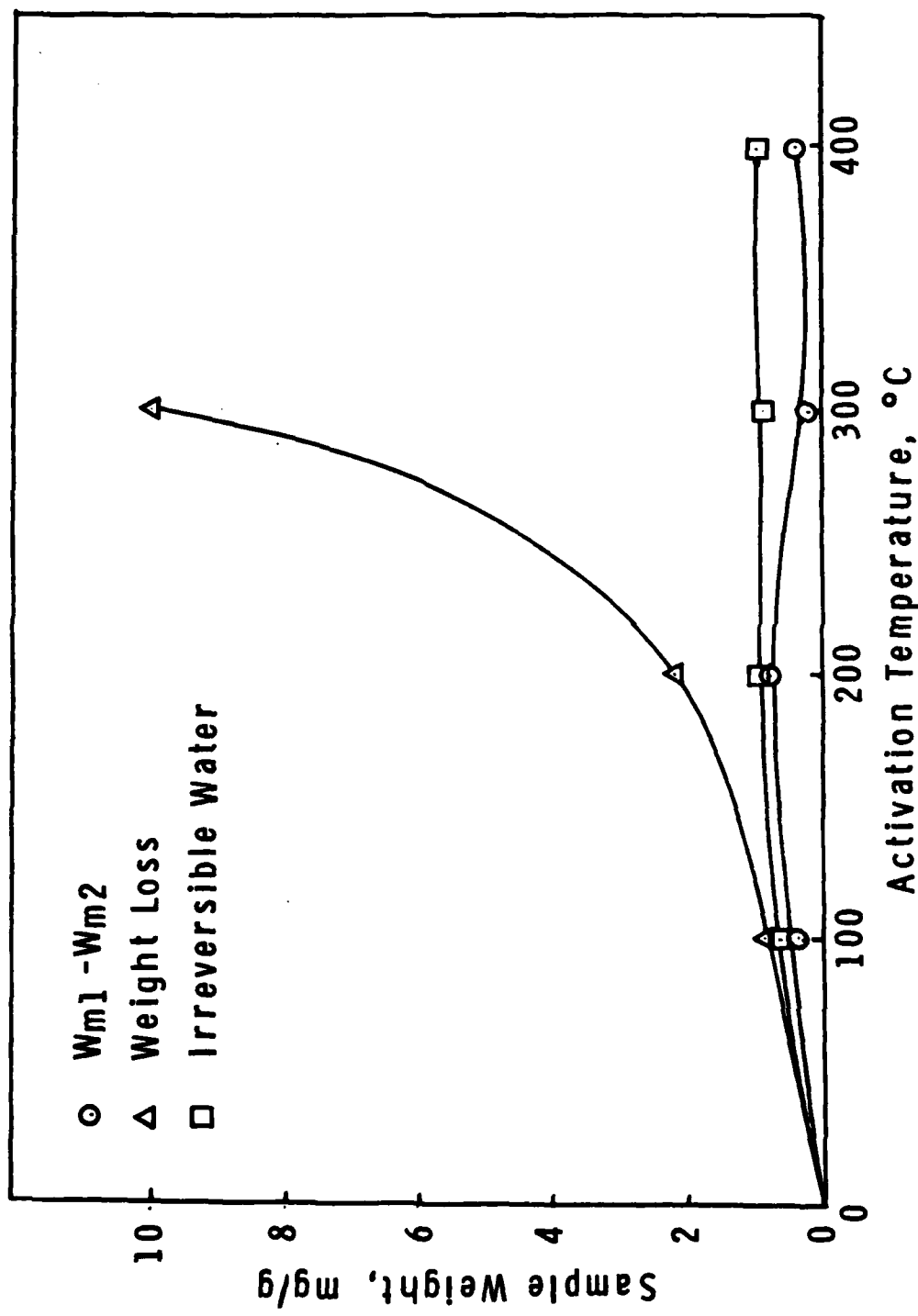


Figure 3. Adsorption results as a function of activation temperature for  $\text{Fe}_3\text{O}_4$

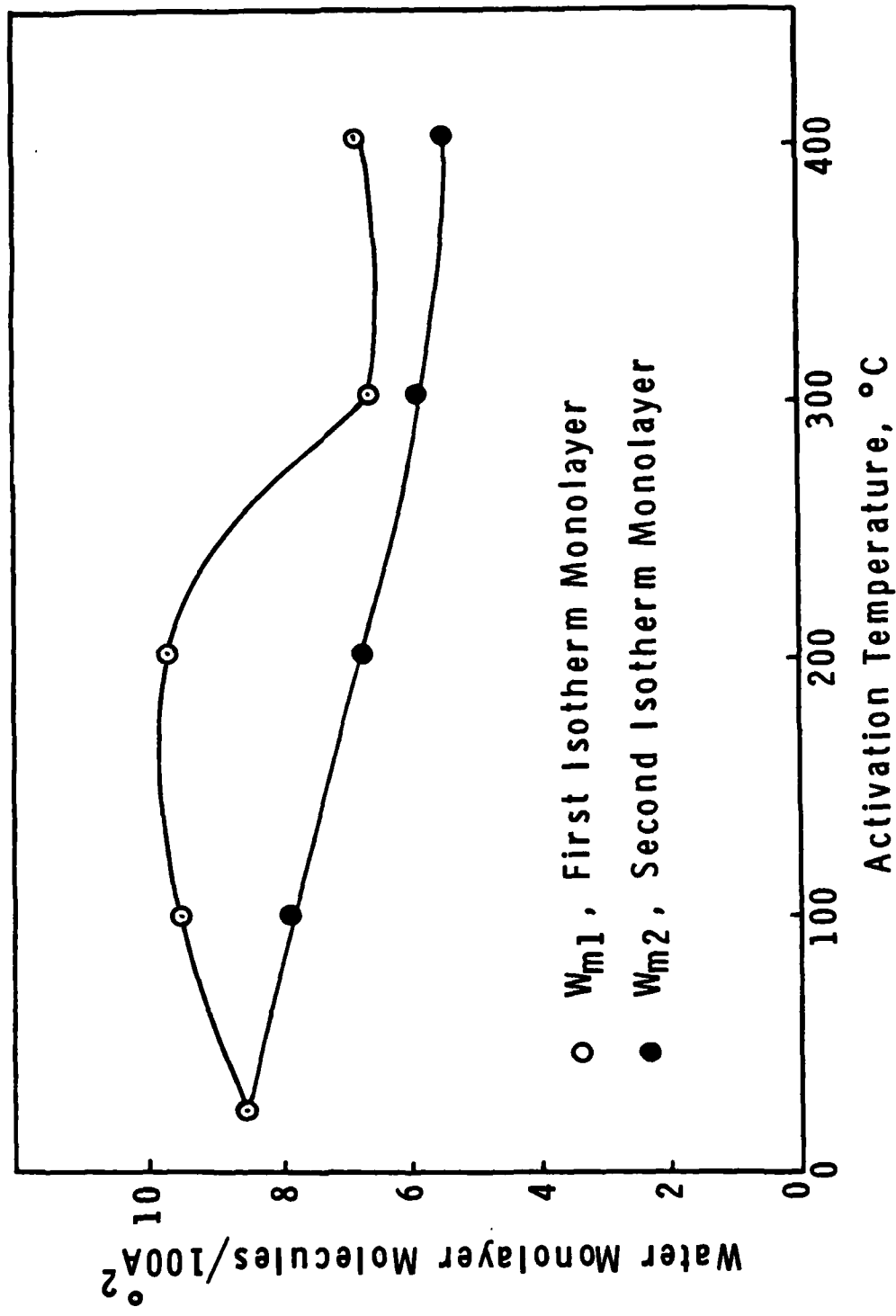
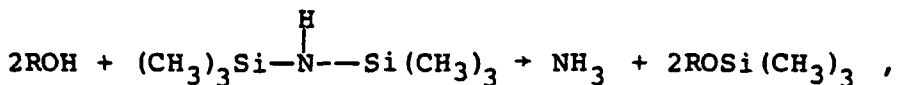


Figure 4. Water monolayer results as a function of activation temperature for  $\text{Fe}_3\text{O}_4$ .

surface, or of an organic or inorganic molecule. Hexamethyldisilizane, HMDS, was used to treat  $\alpha$ -Fe<sub>2</sub>O<sub>3</sub> according to the following reaction:



where R represents the iron oxide surface. Adsorption isotherms were measured on  $\alpha$ -Fe<sub>2</sub>O<sub>3</sub> after activation at 100 and 400°C. The results, Figure 5, show that the adsorption is more pronounced after the 400°C activation where there is also evidence of a "stepped" isotherm. Water adsorption isotherms were measured on these samples after the HMDS treatment and the results, with and without the HMDS treatment, are summarized in Table III. Since it is assumed that the chemisorbed HMDS occurs according to the above chemical reaction, the amount of HMDS adsorbed in Figure 5 is expressed in terms of trimethylsilicon groups/100 Å<sup>2</sup>. This measurement is not strictly accurate because adsorption above the inflection point is expected to occur by physical adsorption of the HMDS molecule. The irreversibly adsorbed HMDS, however, is expected to be due to chemisorbed trimethylsilicon, and was found to be 1.04 and 5.45 trimethylsilicon groups/100 Å<sup>2</sup> for the 100 and 400°C activated sample, respectively.

The first and second water adsorption isotherms for the HMDS-treated and untreated  $\alpha$ -Fe<sub>2</sub>O<sub>3</sub> activated at 100°C are presented in Figure 6. The monolayer results in Table III show that there is only a small decrease in the water monolayer values after HMDS treatment. The monolayer values for the second isotherms,  $W_{M2}$ , show a decrease of 0.87 molecules/100 Å<sup>2</sup>, which is in good agreement with the irreversibly adsorbed, or chemisorbed, HMDS. Another significant feature of the water adsorption isotherms in Figure 6 is that there is a decrease in adsorption in the multi-layer region for the HMDS-treated sample. Figure 7 presents the water adsorption isotherms for the HMDS-treated and untreated  $\alpha$ -Fe<sub>2</sub>O<sub>3</sub> activated at 400°C. The irreversibly, or chemically, adsorbed HMDS is much greater for this sample, 5.45 trimethylsilicon groups/100 Å<sup>2</sup>, and the result is a much greater reduction in the amount of adsorbed water. The reduction in the second water monolayer value, 4.08 molecules/100 Å<sup>2</sup>, is in good agreement with the irreversibly adsorbed HMDS value of 5.45 trimethylsilicon groups/100 Å<sup>2</sup>. It is also significant to note from the water adsorption results in Figure 7 that the amount adsorbed is much less for the HMDS-treated sample in the multi-layer region.

#### Solid/Liquid Interface

The electrophoretic mobility of Fe<sub>3</sub>O<sub>4</sub> was measured as a function of pH for samples which had been activated in vacuum up to 400°C in order to determine the effect of temperature on

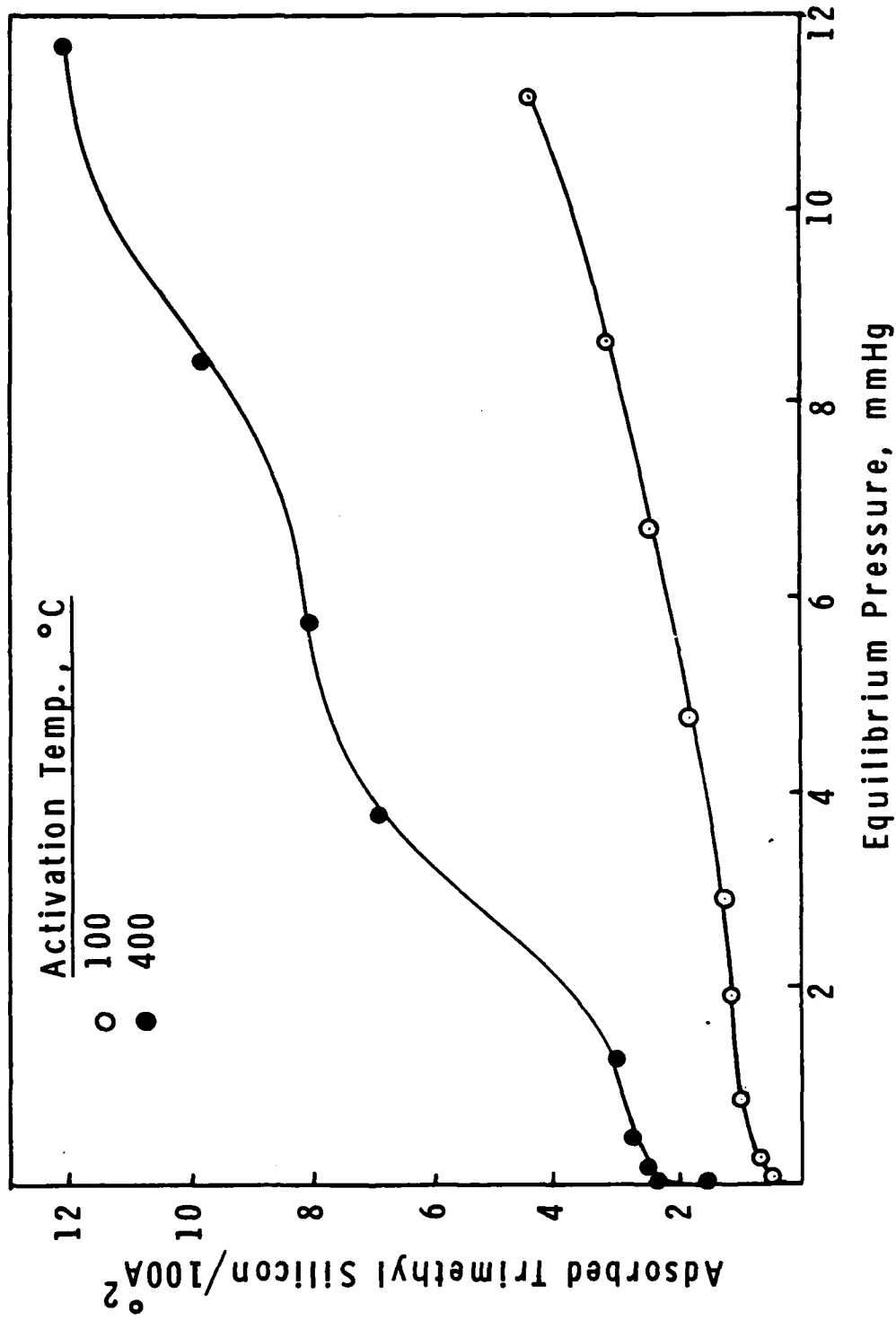


Figure 5. Adsorption isotherm of HMDS on  $\alpha\text{-Fe}_2\text{O}_3$  after activation at 100 and 400°C.

Table III  
Gas Adsorption Results on  $\alpha\text{-Fe}_2\text{O}_3$  Treated with  
HMDS after High Temperature Activation

Activation Temp., °C	Treatment after Activation	$\text{Si}(\text{CH}_3)_3/\text{100 A}^2$	Irreversibly Adsorbed HMDS		$W_{m1}^{**}$ molecules/ 100 $\text{A}^2$	$W_{m2}^{**}$ molecules/ 100 $\text{A}^2$	$\frac{W_{m1} - W_{m2}}{\text{mg/g}}$ molecules/ 100 $\text{A}^2$
			mg/g	100 $\text{A}^2$			
100	none	--	2.35	7.44	1.82	5.78	0.53
100	HMDS	1.04	2.22	7.04	1.55	4.91	0.67
400	none	--	2.42	9.88	1.75	7.13	0.67
400	HMDS	5.45	1.82	7.43	0.75	3.05	1.07
							4.38

\* First water adsorption isotherm monolayer at 25°C after indicated activation temperature and treatment.

\*\* Second water adsorption isotherm monolayer at 25°C after activation at 25°C.

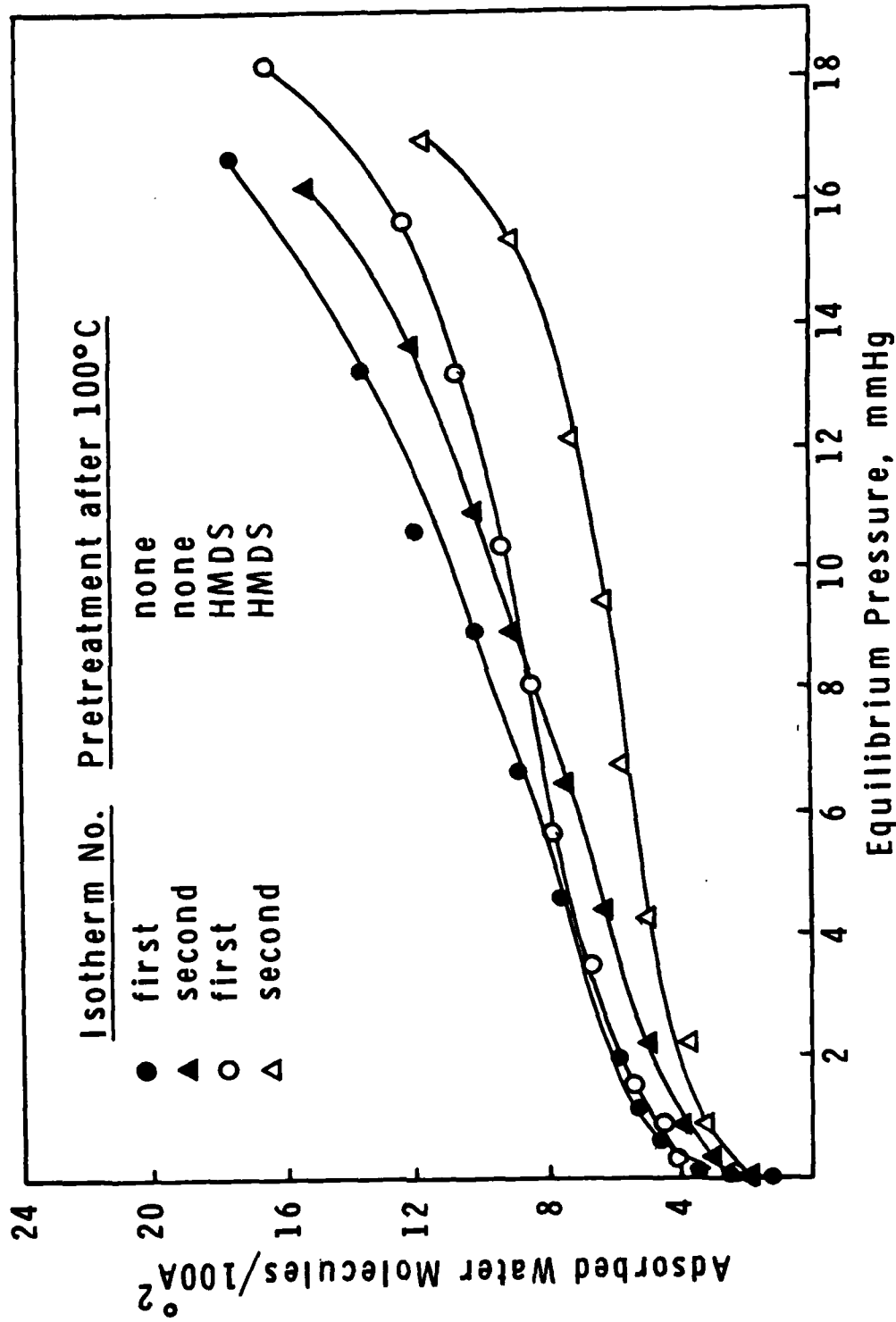


Figure 6. Water adsorption isotherm on  $\alpha\text{-Fe}_2\text{O}_3$  after activation at 100°C and with and without pretreated HMDS.

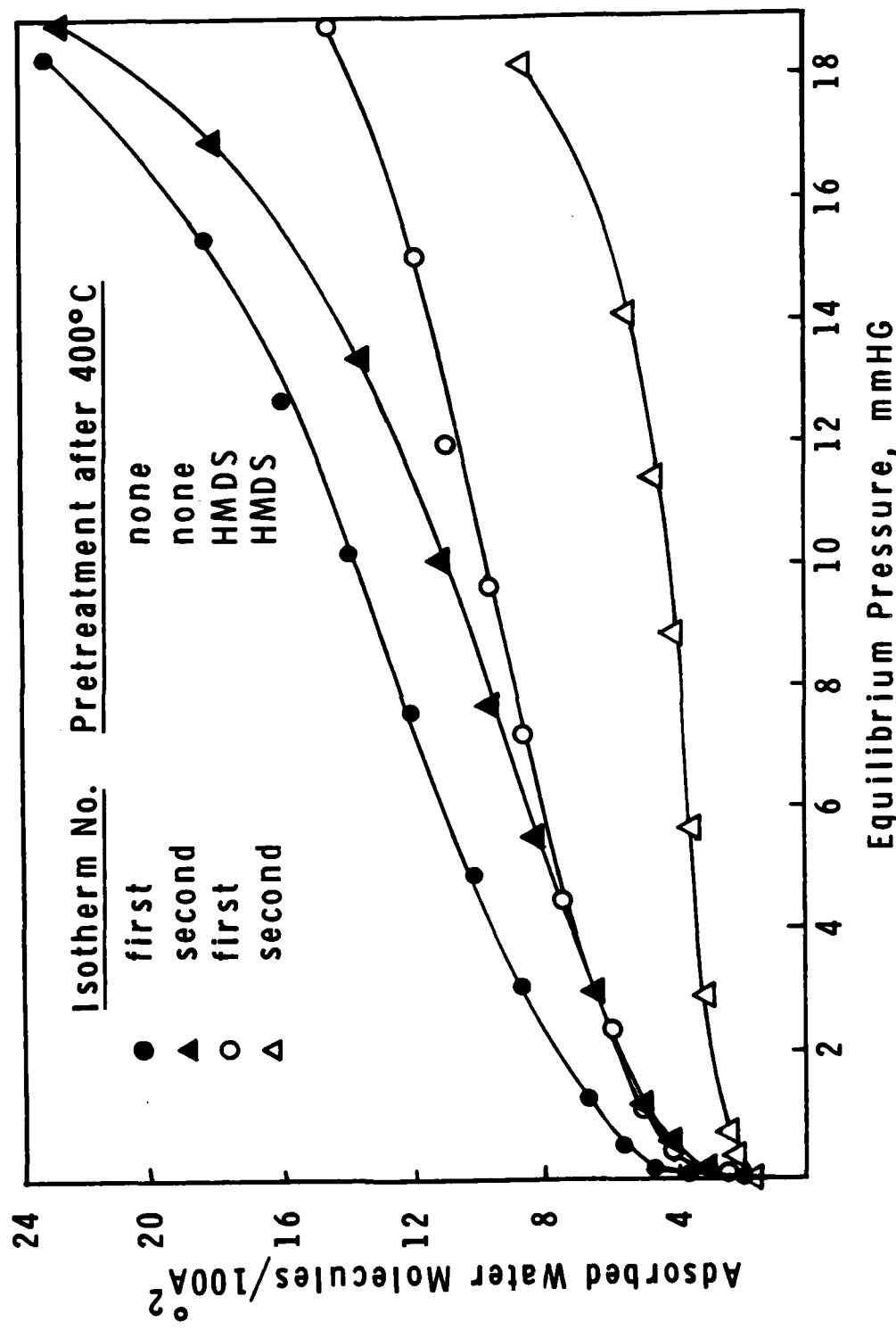


Figure 7. Water adsorption isotherm on  $\alpha\text{-Fe}_2\text{O}_3$  after activation at 400°C and with and without pretreated HMDS.

the positive or negative character of the surface, i.e., the proton donor or acceptor tendencies of surface functional groups. Surface hydroxyl groups which are amphoteric are known to be present on this surface, and high temperature can either dehydroxylate the surface to Fe-O-Fe or change the electronegativity of the surface oxygen due to bulk changes in the crystal lattice. Dehydroxylation of the surface to Fe-O-Fe results in a surface which is a proton acceptor, and hence an increase in the positive character of the surface. The electrophoresis results in Figure 8 show that the isoelectric point, IEP, i.e., the pH where the electrophoretic mobility is equal to zero, decreases with increasing activation temperature. The interpretation of these results is that significant dehydroxylation of the surface does not occur at activation temperatures up to 400°C, which is consistent with the water adsorption results, but that the oxygen of the surface hydroxyls becomes more electropositive with increasing activation temperature and thus becomes stronger proton donors.

Electrophoresis measurements were made as a function of pH on a number of iron oxide compounds which were prepared by Dr. Svetozar Music and subsequently analyzed by him with Mössbauer spectroscopic techniques. Although the interpretation of results is not yet complete, the results do point out some interesting trends and the utility of electrophoresis as an analytical technique to investigate surface properties. The samples investigated were  $\text{Fe(OH)}\text{SO}_4$ ,  $\alpha\text{-Fe}_2\text{O}_3$ , a mixture of 19.4%  $\alpha\text{-Fe}_2\text{O}_3$  and 80.6%  $\alpha\text{-FeO(OH)}$ , and a mixture of 64.2%  $\alpha\text{-Fe}_2\text{O}_3$  and 35.8%  $\text{FeO(OH)}$ . The results, Figure 9, show that  $\alpha\text{-Fe}_2\text{O}_3$  has an IEP at a pH of 5.7, which is in good agreement with previous measurements. The hydroxylation of this sample is entirely on the surface, while  $\text{Fe(OH)}\text{SO}_4$  and  $\sim\text{FeO(OH)}$  have hydroxyls in the crystal structure. The  $\text{Fe(OH)}\text{SO}_4$  has the IEP at the lowest pH value compared to the other samples. The results for the other two samples, which contain a mixture of  $\alpha\text{-Fe}_2\text{O}_3$  and  $\alpha\text{-FeO(OH)}$ , show that when  $\alpha\text{-Fe}_2\text{O}_3$  is the dominant component, the IEP is close to that of the pure material. Likewise, when  $\alpha\text{-FeO(OH)}$  is dominant, the IEP is close to that of compounds containing OH groups in the crystal lattice. These results suggest that it is possible to use electrophoresis as a tool for qualitatively distinguishing the surface composition of corrosion products.

## CONCLUSIONS

The gas adsorption results indicate that both  $\alpha\text{-Fe}_2\text{O}_3$  and  $\text{Fe}_3\text{O}_4$  are relatively hydrophilic surfaces with  $\text{Fe}_3\text{O}_4$  being the more hydrophilic. High temperature activation of  $\alpha\text{-Fe}_2\text{O}_3$  above 100°C results in the desorption of strong physically adsorbed water which does not appear to increase with increasing temperature. The strong physically adsorbed water is assumed to adsorb through hydrogen bonding with surface hydroxyls. There is no

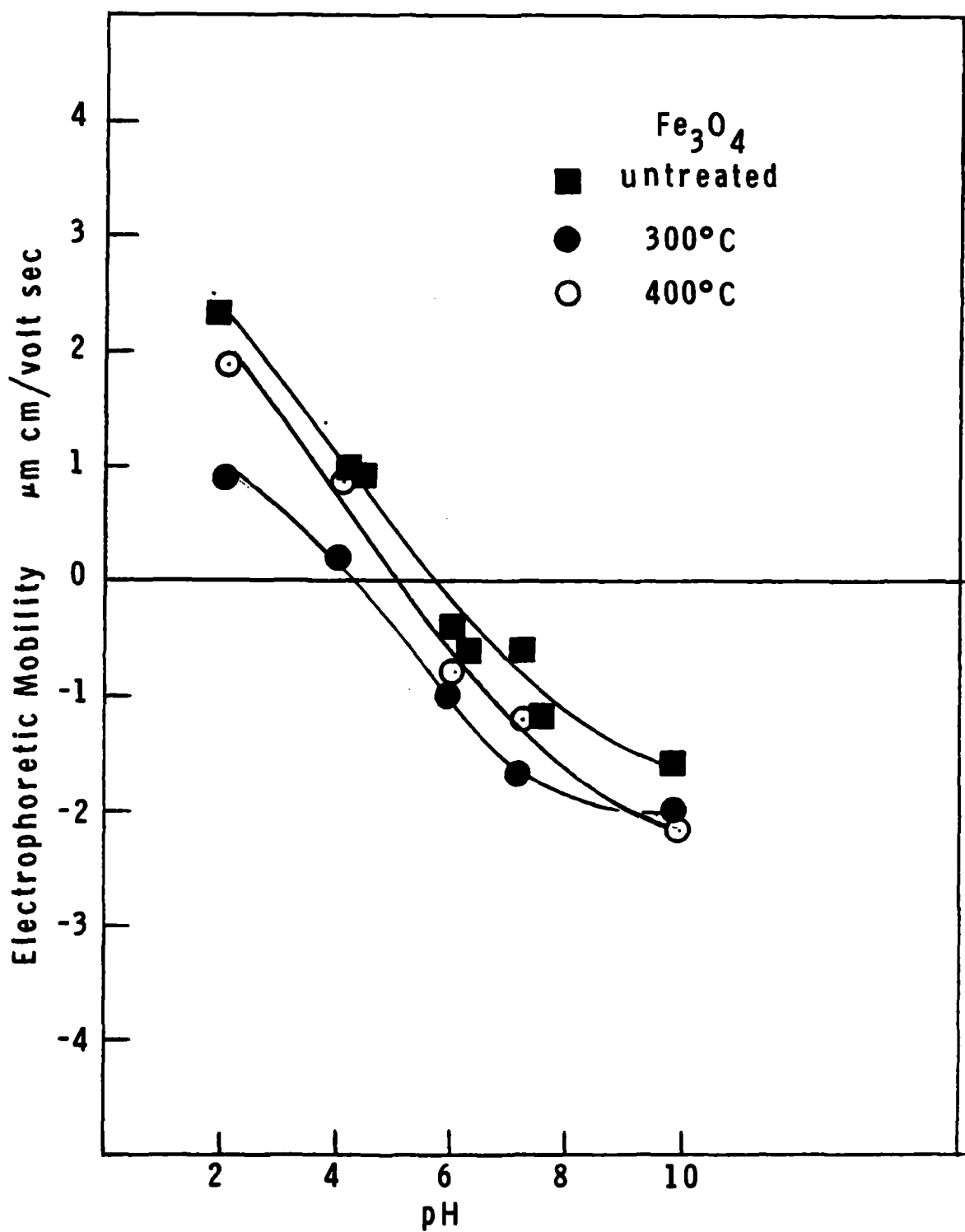


Figure 8. Electrophoretic mobility of  $\text{Fe}_3\text{O}_4$  before and after 300° or 400°C activation as a function of pH.

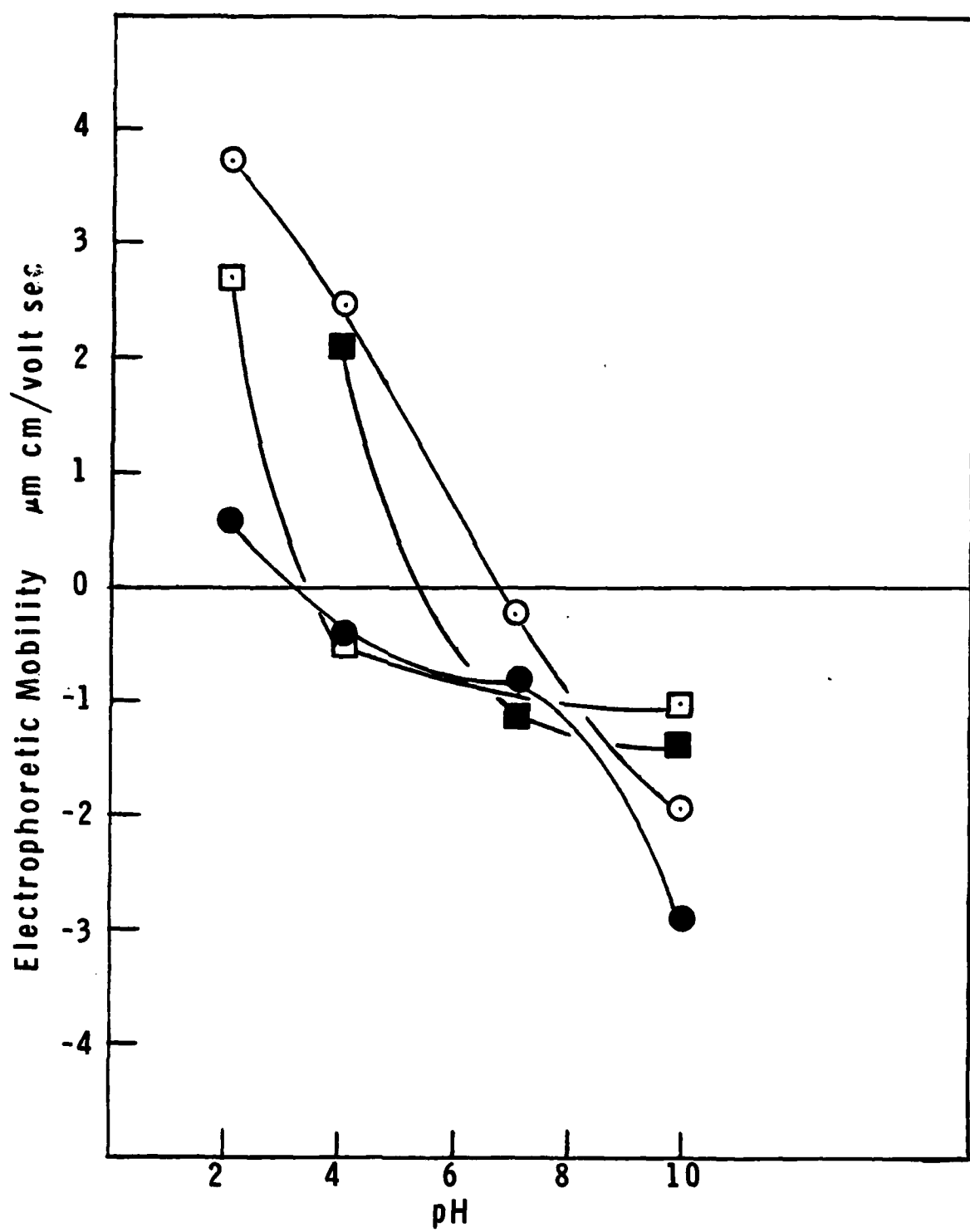


Figure 9. Electrophoretic mobility of  $\text{Fe(OH)}\text{SO}_4$  ( $\bullet$ ),  $\alpha\text{-Fe}_2\text{O}_3$  ( $\blacksquare$ ), mixture of 19.4%  $\alpha\text{-Fe}_2\text{O}_3$  and 80.6%  $\alpha\text{-FeO(OH)}$  ( $\square$ ), and mixture of 64.2%  $\alpha\text{-Fe}_2\text{O}_3$  and 35.8%  $\alpha\text{-FeO(OH)}$  in the particle ( $(\circ)$ ).

evidence of dehydroxylation of the  $\alpha$ - $\text{Fe}_2\text{O}_3$  surface at activation temperatures up to 400°C. The  $\text{Fe}_2\text{O}_3$  surface shows similar behavior in that high temperature activation up to 400°C also shows signs of desorption of strong physically adsorbed water. The first and second water monolayer values,  $W_{m1}$  and  $W_{m2}$  respectively, however, show a definite decreasing trend with increasing activation temperature. This is interpreted as an irreversible decrease in the surface hydroxyl concentration with increasing temperature. This decrease may be expressed as 8.46 water molecules/100 Å<sup>2</sup> for the sample activated at 25°C to 5.38 water molecules/100 Å<sup>2</sup> for the sample activated at 400°C. It is interesting to note that for the unactivated samples,  $\text{Fe}_3\text{O}_4$  is more hydrophilic than  $\alpha$ - $\text{Fe}_2\text{O}_3$ , and for the 400°C activated samples,  $\alpha$ - $\text{Fe}_2\text{O}_3$  is more hydrophilic than  $\text{Fe}_3\text{O}_4$ .

The HMDS treatment has a pronounced effect on decreasing the surface hydrophilicity of  $\alpha$ - $\text{Fe}_2\text{O}_3$ , and probably by replacing the proton of the surface hydroxyl with a trimethylsilicon group. This effect is much more pronounced for the sample activated at 400°C than 100°C due to the fact that the irreversible adsorption of HMDS is greater at the higher temperature. There appears to be close to a one-to-one correlation between the concentration of irreversibly adsorbed trimethylsilicon and the decrease in the surface hydroxyl concentration as determined from analysis of the water adsorption isotherms.

DATE  
FILMED

28